Mechanical, Microstructural, and Corrosion Characterizations of Similar & Dissimilar Induction Assisted Friction Stir Welding of Inconel 718 & Stainless Steel

A Thesis Submitted in Partial Fulfillment of the Requirement for the Degree of

DOCTOR OF PHILOSOPHY

by

Sanjay Raj

(Roll No. 176103110)

DEPARTMENT OF MECHANICAL ENGINEERING
INDIAN INSTITUTE OF TECHNOLOGY GUWAHATI
GUWAHATI– 781039, INDIA.

August, 2023

Dedicated to

My Parents

Mrs. Devanti Devi,

Mr. Shanker Prasad Chourasia,

&

My Beautiful Wife, Mrs. Bandana Kumari,

&

My Loving Son, Sumit, and Aadvik

&

My Loving Family Members

for their **LOVE**, **SUPPORT**, and **PATIENCE**

DEPARTMENT OF MECHANICAL ENGINEERING
INDIAN INSTITUTE OF TECHNOLOGY GUWAHATI
GUWAHATI-781039, ASSAM

DECLARATION

I hereby declare that the information presented in the dissertation "**Mechanical, Microstructural, and Corrosion Characterization of Similar & Dissimilar Induction Assisted Friction Stir Welding of Inconel 718 & Stainless Steel**" submitted to "Indian Institute of Technology Guwahati" for the degree of "Doctor of Philosophy" is a work of pure authenticity carried out under the supervision of Prof. Pankaj Biswas. Any part of this work has not earlier been submitted for the award of any degree, diploma, associateship, fellowship, or equivalent to any institution. All text and figures are my own.

Date:

Sanjay Raj
Roll No. 176103110
Department of Mechanical Engineering
Indian Institute of Technology Guwahati
Assam-781039, India.

DEPARTMENT OF MECHANICAL ENGINEERING
INDIAN INSTITUTE OF TECHNOLOGY GUWAHATI
GUWAHATI-781039, ASSAM

CERTIFICATE

It is certified that the work contained in the thesis entitled "**Mechanical, Microstructural, and Corrosion Characterization of Similar & Dissimilar Induction Assisted Friction Stir Welding of Inconel 718 & Stainless Steel**" submitted by **Mr. Sanjay Raj**, a student in the Mechanical Engineering Department, Indian Institute of Technology Guwahati, Guwahati, Assam, India for the award of the degree of Doctor of Philosophy has been carried out under my supervision. This work has not been submitted previously elsewhere for the award of any other degree or diploma.

Date:

Prof. Pankaj Biswas
Department of Mechanical Engineering
Indian Institute of Technology Guwahati
Guwahati, Assam-781039, INDIA

ACKNOWLEDGEMENTS

First and foremost, I would like to express my deep appreciation to everyone who contributed to making my doctoral research work achievable. Before presenting my research work, I am deeply indebted to humbly acknowledge all of them for their kind support.

I want to express my deepest gratitude to my supervisor Prof. Pankaj Biswas for allowing me to work under his supervision. His exceptional organization, planning, management skills, and persistent patience taught me a lot. I am also grateful for his valuable advice, friendliness, and guidance in the moment of difficulties in research work. I appreciate all his contributions, time, and ideas to make my doctoral research productive and challenging.

I would like to thank my doctoral committee members, Prof. Sukhomay Pal, Prof. Prasenjit Khanikar, and Prof. S. K. Majumder, for their valuable suggestions and encouragement during the period of my research work.

I sincerely thank the former and present departmental heads, Prof. S.K. Dwivedy and Prof. K. S. R. Krishna Murthy, for extending various facilities in the Mechanical department during the tenure of my doctoral program. I am also grateful to all the Mechanical engineering department faculty members and office staff for giving me a comfortable and friendly environment for pursuing my research.

I also like to express my heartful gratitude to the Director, all Deans, and the Mechanical Engineering department for providing financial support for this research work.

Further, I would also like to thank Mr. N. K. Das, assistant workshop superintendent, and all members of the central workshop, especially Mr. Sanjib. Sarma, Mr. S. Ahmed, Mr. Dilip Chetri, Mr. Dipak K. Deka, Mr. N. Borah, and Mr. Nidul Saikia, for extending help in conducting experimental work.

I wish to express my gratitude to the Central instrument Facility (CIF), IIT Guwahati, for providing a facility for material characterization instruments. Also, thanks to the chemical engineering department for allowing me to perform corrosion testing.

I am thankful to my senior researcher Dr. Avinish Tiwari, Dr. Sagar Hanamant Pawar, Dr. Saurav Suman and Dr. Deepak Kumar, for stimulating discussions and motivating me to overcome any problem, either in work or otherwise. I sincerely thank my lab mates, Mr. Pardeep Pankaj, Mr Ankan Das, and Mr. Rituraj Bhattacharjee for brotherhood and all our fun.

Most importantly, I owe all I am or hope to be to my parents. I would like to thank my father, Mr. Shanker Prasad Chourasia, and my mother, Mrs. Devanti Devi, for their love, unconditional support, and encouragement during my research work. I want to thank all my family members for their encouragement, especially my elder brother (Ajay Kumar), younger brother (Dilip Kumar), and my sister (Leela Devi) for encouraging me to go still further at every point in life. I would also thank my in-laws, Mr. Ranjit Kumar Modi (Papa), Mrs. Anjani Devi (Mummy), and brother and sister-in-law Santosh Kumar and Khushboo Kumari for their love and support through the years in pursuing my Ph.D in a modest stipend.

Apart from that, I am head over heels indebted to my dear wife Mrs. Bandana Kumari, who is at one with me throughout my research work, travails, fits of anger, and impatience. From the depth of my heart, thank you for your encouragement and for being the most caring mother of our kids Mr. Sumit Kumar and Mr. Aadvik Kumar, throughout my Ph.D. pursuit. She also supported my family during of my doctoral studies. Thank you for being my research paper's best friend and typos checker.

I want to express my gratitude to Dr. Tej Pratap, Dr. Anurag Kumar, Dr. Dharmendra Kumar Dheer, Dr. Shuja Ahmed, Dr. K. Sajun Prasad, Mr. Sunil Kumar Biswal, Mr. Vivek Kumar, and my other hostel mates and colleague, for their moral support. I shall forever be grateful to all my friends and well-wishers.

I am privileged and fortunate to work at the Indian Institute of Technology Guwahati.

Finally, I bow my head to God almighty in profound gratitude and seek blessings.

August 2023 **Sanjay Raj**

ABSTRACT

Among different joining techniques, friction stir welding (FSW) is a solid-state welding process in which joining occurs below the melting point temperature. The significant frictional heat and stirring effect generated between the tool and workpiece result in plastic deformation and intermixing of materials. Unlike conventional fusion welding of Inconel 718 and steel, FSW of these materials overcomes several problems associated with the high heat input, such as liquation cracking, solidification cracking, and formation of a brittle intermetallic compound in the fusion zone. Friction stir welding (FSW) of high-strength materials like Inconel 718 and steel is also more challenging than welding softer materials for several reasons, including high tool degradation and the potential for defective joint formation. The high temperature and mechanical stresses during the welding process cause severe wear and damage to the FSW tool, affecting the weld quality and the tool's lifespan. And also, of their high strength, high melting point, and low thermal conductivity, a high level of process control and optimization is required to ensure proper heat input and material flow. However, the demand for joining high-strength materials using the FSW technique is growing in industries such as nuclear plants, petrochemical, aerospace, submarine, and hydraulic power plant. This technique requires more development, modification, and modification improvement of the existing FSW techniques.

The present study explored similar and dissimilar joining of Inconel 718 and stainless-steel materials under the conventional FSW and induction-assisted FSW process using tungsten carbide tool material. For the comparison of the conventional FSW process with external energy-assisted FSW, a setup for the induction-assisted FSW was developed, and experiments were carried out. It was found that tool life was significantly affected by the application of induction preheating. Various process parameters like weld traverse speed, tool rotational speed, plunge force, and preheating temperature affect the weld quality. From the experimental investigation of joining Inconel 718 by the FSW, it was found that an optimum traverse speed of 300 rpm and a low traverse speed of 90 mm/min resulted in refined grain microstructure, high microhardness, and high strength of the weld joint. The utilization of an induction preheating system in the FSW process resulted in improved weld quality at a high welding speed of 140 mm/min. The results also revealed that preheating affected the process temperature, lowering the axial force and frictional heat and improving the tool life.

Additionally, the FSW and I-FSW processes were used to conduct an experimental investigation on dissimilar Inconel 718 coupled with AISI 204/SS316L. In the dissimilar FSW of Inconel 718 and AISI 204Cu using a WC-10wt.% Co tool a successful joint with high-strength at medium traverse speed (i.e., 70–90 mm/min) under the observed rotational speed of 300 rpm. The application of FSW led to grain refinement in the nugget zone, resulting in an increment of hardness value, which was directly proportional to the traverse speed. These features were attributed to dynamic recrystallisation. The weldments obtained at a traverse speed of 70 mm/min showed a higher ultimate and yield strength, which was higher than the Inconel 718 parent metal but lower than the AISI 204Cu parent metal.

Moreover, a successful joint of dissimilar Inconel 718 with SS316L was obtained at a constant rotational speed of 300 rpm and 70 mm/min with conventional and at 140 mm/min with induction preheating assisted process. Preheating reduces the axial force experienced by the tool by 24% under 140 mm/min traverse speed. Induction preheating reduced the tool wear by 62% due to the reduction of axial force and material softening. Besides mechanically intermixing, an increase in temperature during the I-FSW process led to increasing the width of the diffusion zone at the interface layer; however, no intermetallic compound layer was found at the interface region.

The corrosion test of dissimilar Inconel 718/SS316L joint revealed a lower level of corrosion resistance in all the samples when exposed to 1M HCl solution compared to 3.5 wt.% NaCl solution. The corrosion resistance of the dissimilar joint was higher than the base SS316L, which was highly affected by the grain size and presence of the carbide particles. High pitting corrosion with the HCl solution in the region of SS316L was mainly related to the refined $M_{23}C_6$ carbide particles in the nugget zone, which act as cathodes relative to the ϒ-austenite matrix.

Keywords: Friction stir welding; induction preheating; Inconel 718; stainless steel; similar and dissimilar welding; material characterization.

CONTENTS

List of Figures

List of Tables

CHAPTER 1

1. Introduction

1.1 General background

Welding is a joining process whereby two or more parts are joined permanently using heat, pressure or both on the materials up to a suitable temperature with or without the application of filler material [1]. Various parts or components are fabricated to mitigate the complexity of manufacturing large structures in the joining process. There are various classifications of welding processes available based on the source of heat, the composition of joints, phases/ filler materials, application of pressure, mechanisms, etc. [2]. Modern methods of joining are classified, depending on the state of the material during welding, as follows (a) fusion welding and (b) solid-state welding techniques.

Fusion welding is a form of joining two or more metals using heat and pressure by melting them together and then bonding them with the help of filler metal. Due to the many advantages of the fusion welding technique, like its high strength, low thermal expansion, and good corrosion resistance, many industries generally prefer this technique. Apart from this benefit, some problems associated with the conventional fusion welding process, like it requires several consumables filler metal and fluxes, become more expensive than other types of welding, and release toxic and harmful gases that adversely affect the environment. Additionally, the large heat input associated with the process alters the microstructure and mechanical properties, leading to residual stress in the weld zone. Defects like hydrogen embrittlement, segregation of alloying elements, slag inclusion, microfissuring in the heat-affected zone (HAZ), formation of a brittle intermetallic compound, and incomplete penetration are found in the fusion zone [3]. The problem associated with conventional fusion welding processes has stimulated researchers to develop alternate joining technology in recent years. Thus, some of the above-stated problems associated with fusion welding, particularly high heat input, can be solved using the solid-state welding technique.

Solid-state welding is an important category of welding processes in which joining is achieved below the melting point of the base materials. In recent years, the solid-state joining technique has attracted huge attention for joining similar and dissimilar materials. The friction stir welding (FSW) process is one of the solid-state joining techniques invented by Thomas et al. [4] at The Welding Institute (TWI), Cambridge, UK, and patented in 1991. This technique was

developed to join softer materials like aluminium (Al), copper (Cu), and its alloy, and found that it has significant advantages over conventional welding technology. In the solid-state joining process, the joining can be performed at room temperature and also at elevated temperatures without melting the materials being joined. In the FSW process, a rotating cylindrical tool is inserted into the workpiece, generating sufficient frictional heat that deforms the welded material. After this, the tool goes along the weld line, producing a solid-state joint below the material's melting point. The thermomechanical effect of the rotating tool in the workpiece produces severe plastic deformation, and intermixing these materials generates high-strength metallurgical joints [5]. Since the temperature of welding goes to 80% of the melting temperature of the base material, it is also known as the hot working process. The energy supplied during the friction stir welding process is through pressure and/or friction. Initially, it was developed to join low melting point materials (i.e., Al, Mg alloys). However, after the development of high wear and toughness tool materials (i.e., pcBN, WC-Co and Si_3N_4 tool), it has been successfully investigated on high-strength materials like steels, Ni-alloys, copper and titanium.

Figure 1.1 (a) depicts the schematic diagram of the various steps involved in the FSW process. Step 1 shows that before performing FSW, the base material is first rigidly clamped on a welding fixture in such a way that faying surfaces are close enough at the joint line so that plates do not spread during welding. Afterwards, the tool is clamped firmly onto the adopter and aligned along the joint line. The next step (step 2) is plunging and dwelling, in which a non-consumable rotating tool (which is harder than the base material) is plunged into the weld line with a specific force until the shoulder contacts the base material. After the plunging, the tool is rotated at the same place for few times to make the material soften due to frictional heat, known as a dwelling. Sufficient heat should be generated since a part of the generated heat is conducted to the anvil and the surrounding material. Step 3 involved joining and tool traverse, in which, after plunging and dwell period, the tool is traversed along the weld line to produce the weld joint. During the traversing of the tool, heat is generated by friction force and plastic deformation of the material, which maintains sufficient heat for the material flow around the tool pin. The material ahead of the traversing tool first starts preheating and then plastically deformed by the rotating tool. The material adjacent to the tool pin is extruded around it and forged by the tool shoulder behind it. As the tool starts moving along the weld line, the fresh material from the front side of the tool pushes the old rotating material and replaces it to participate in welding, and a welding mixture is left behind the tool. After completing the

joining process, the final step 4 is retarding, in which the rotating tool is retracted from the abutted surfaces and generates a keyhole in the BM. In the FSW process, the proper selection of the process parameters, such as tool rotational speed, traverse speed, tool plunge depth, tool offset, tool geometry, and tool tilt angle, play an important role in obtaining a defect-free joint [6]. In the joining and tool traverse step, a set of complex deformation processes and their interactions at high temperatures, high strains and strain rates conditions determine the weld zone microstructures [7]. The cross-sectional view of the weld area reveals three distinct regions characterized by their microstructure: the SZ, the thermomechanically affected zone (TMAZ), and the HAZ, as illustrated in Figure 1.1 (b). The stir zone (SZ), also called the nugget zone, is a dynamically recrystallized zone of the joints. This is a central region of the weld which is characterized by grain refinement subjected to intense material stirring in this zone. TMAZ occurs on either side and adjacent to SZ. In this region, the strain and temperature are lower than that of the nugget zone, resulting in a comparatively minor impact of welding on the microstructure. Heat affected zone in the FSW process is similar to the heat-affected zone of the fusion welding process, which is subjected to a thermal cycle only but not deformed during the welding. The region out of the weld zone is called base metal (BM) [8]. The terminology advancing and retreating sides used in this process are based on the welding direction and tool motion. The side of the weld where tool rotation and translation are in the same direction is called the advancing side. The other side of the weld, where the tool rotation and weld direction are opposite, is called the retreating side [7], as shown in Fig. 1.1 (b).

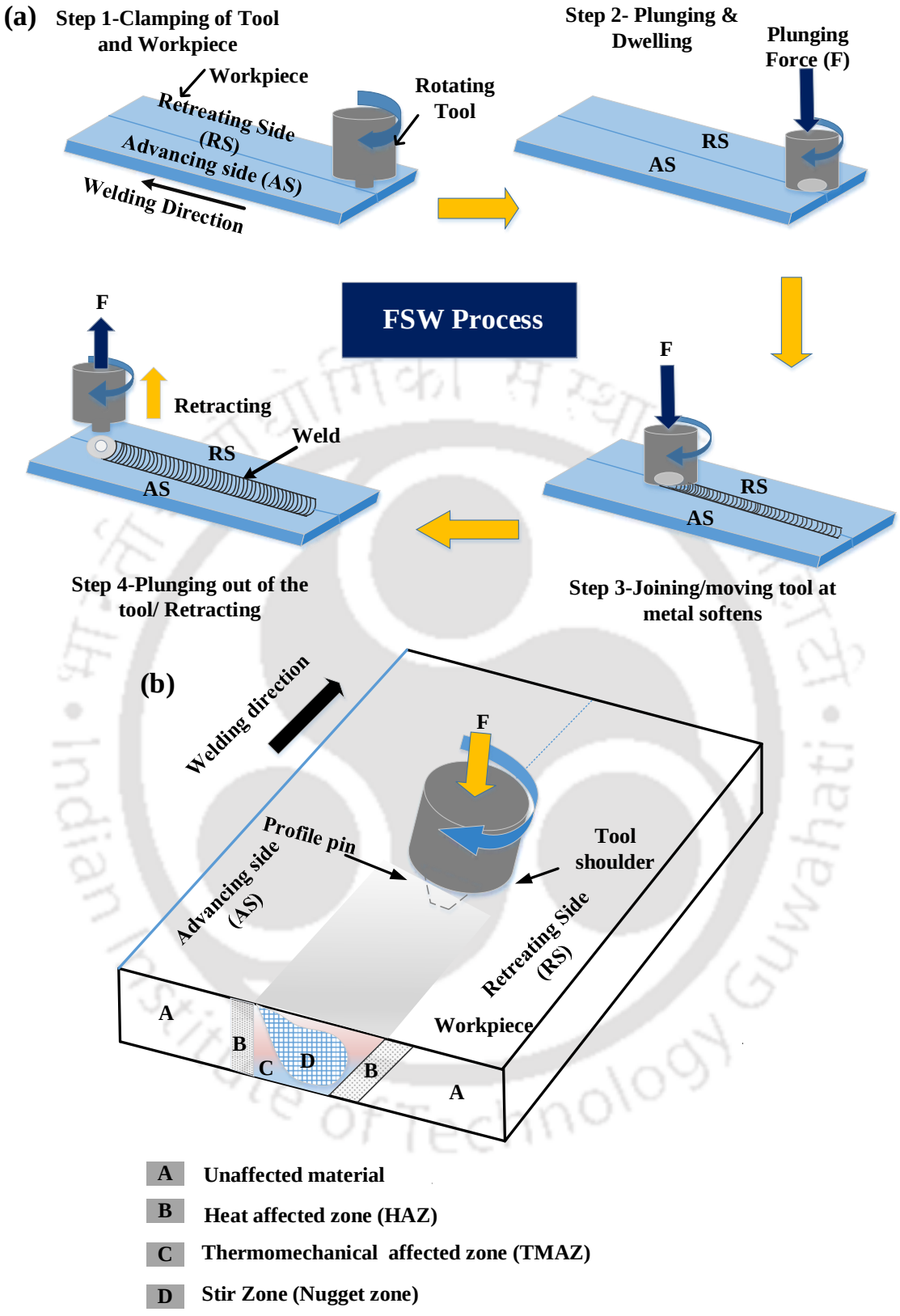

Fig 1.1 Different steps involved in (a) the FSW process and (b) generated different weld zone.

1.2 Motivation

Inconel 718, an age-hardened Ni-Fe-Cr-based alloy, is a primary industrial material in high-temperature and high-strength applications. The added demands for Inconel 718 in the nuclear plant, petrochemical, aerospace, submarines and hydraulic power plant industries are very high because of its excellent properties like mechanical strength, impact toughness, corrosion resistance and thermal fatigue resistance within the temperature range of −250 °C to 700 °C [9,10]. Due to the presence of sluggish age-hardening precipitates such as gamma prime (ϒ'-Ni_3Al) and gamma double prime (ϒ"- Ni_3Nb), this particular Ni-base superalloy exhibits remarkable resistance to strain age cracking. This attribute contributes to its excellent weldability compared to other alloys in the same category [11]. Thus, Inconel 718 is one of the most popular high-temperature application alloys used where other materials like aluminium and steel fail in the adverse working environment. With the growing interest in Ni-based superalloys for the critical components in an adverse environment, the present work is motivated to investigate the weldability of Inconel 718 in a similar and dissimilar mode.

In manufacturing industries, joining dissimilar materials to achieve flexible design considerations with characteristic properties and higher economic efficiency is continuously demandable. Therefore, low-cost material with high mechanical strength, Ni-free austenitic stainless steel (Fe-Cr-Mn), is highly demandable in construction industries, food processing, biomedical applications and body parts of automobile industries [12]. Due to the high cost of Ni, the use of the alternative substitution element manganese (Mn) with nitrogen (N) in austenitic stainless steel has found excellent mechanical properties [13]. The substitution elements function as stabilizers of austenite in the austenitic stainless steel (series 200) at both high and low temperatures. It has also been recognized that the incorporation of copper (Cu) reduces the work hardening rate [12,14]. Due to their outstanding mechanical and formability properties, Inconel 718 and AISI 204Cu materials are in high demand across industries. This has prompted us to research the weldability of these material combinations.

Similarly, the combination of Inconel 718 (IN718) superalloy and austenitic stainless steel 316L (SS316L) in dissimilar joints have found numerous applications in aerospace and high-temperature corrosive environments such as chemical power plants, submarines, and the gas and oil industries. This is because of their exceptional strength and impressive corrosion resistance. [15]. The particular use of bimetallic joints of IN718 and SS316L was stated by Henderson et al. [16] and Locci et al. [17] in the gas turbine engine part and the hot-side heat

exchanger of the power conservation system and the components for the international space station, respectively. Generally, stainless steel and Ni-based alloys are utilized in severe environments where high corrosion resistance and high-temperature mechanical properties are required. Locci et al. [17] and Ferretti et al. [18] have reported that in the hybrid structure, Inconel 718 can be used in the hot section part because of exhibits superior properties up to 1500 ^{o}C in relation to excellent mechanical properties, high toughness and high corrosion resistance. In contrast, austenitic stainless steel 316L (SS316L) can be used in the relatively low-temperature (about 800 ^{o}C) part as a result of its great strength and good corrosion resistance. The supercritical water oxidation (SCWO) system components are made with stainless steel and nickel-based alloys carrying organic wastes, causing a severe corrosion environment. The working fluid of the SCWO system is supercritical water which contains a corrosion environment of chloride, acidity, salts and oxygen, making a severe environment for component materials [19,20]. Because of the high concentrations of elements nickel (Ni), chromium (Cr), and molybdenum (Mo), both alloys are extremally resistant to corrosion and oxidation [21]. The unique combination, such as excellent formability, high tensile strength, good creep resistance, and high corrosion resistance at elevated temperatures, makes IN718 and SS316L materials highly demandable in industries which motivated us to investigate the weldability and corrosion resistance of the joint of these combinations.

In general, joining various Ni-based superalloys and stainless-steel parts in manufacturing industries is employed using the fusion welding technique, conventionally through tungsten inert gas welding, gas-shielded metal arc welding, micro plasma arc welding, and electron beam welding. However, there are some problems associated with high heat input during fusion welding of Inconel 718, such as solidification cracking, segregation of chromium (Cr) element at the grain boundaries causing liquation cracking, poor penetration, microfissuring in the heat-affected zone (HAZ) and separation of niobium (Nb) rich phase (i.e., Laves phase) which forms a brittle compound in the fusion zone upon solidification [22]. The above difficulties associated with fusion welding mainly affect fracture toughness, tensile strength, ductility, creep-rupture properties, and corrosion resistance. Similarly, due to contrasts within the chemical and physical properties of dissimilar joining of Ni-alloy with stainless steel, the selection of proper filler materials is quite difficult. In addition, solidification and liquation cracks in the weld zone, porosity and blowholes defects, and segregation of Nb rich phase (i.e., Laves phase) in the weld zone generate unfavourable results on weldability and mechanical properties of the dissimilar joint.

Therefore, to avoid and eliminate the challenges associated with the fusion welding of Inconel 718 and stainless steel and to control the high heat input, the advanced joining technique, friction stir welding (FSW), having low heat input, has been introduced in this work. A number of potential advantages of the FSW process over the conventional fusion welding process have been identified [23]. The solid-state FSW process removes the melting and solidification-related defects and causes fewer metallurgical changes in the HAZ. Because of the refinement of grain structure, it shows good mechanical as well as corrosion resistance of the joint. The use of FSW leads to savings in post-weld processing, reductions in inspection costs, reduced energy requirements, elimination of consumable material, and provides superior weld quality [5]. The FSW process is an environmentally friendly technology due to the absence of shielding gas, harmful emissions, and ultraviolet or electromagnetic hazards during welding. It is called green welding technology [24].

Although initially FSW process was developed for joining low melting point materials (i.e., Al, Mg alloys) [25]. The main reason for the success of FSW of softer alloys was because of lower peak temperature and low process loads during the welding and an abundance of reusable tools. However, after the development of high-strength and high-wear resistance tool materials (i.e., pcBN, WC-Co, and Si_3N_4 tool) at an elevated temperature, researchers tried to join the high-strength and high melting point materials. During FSW of high-strength materials like Ni-based alloy and steel, the downward force, the peak temperature, and spindle torque on the tool either lead to premature failure of the tool or excessive wear during welding. Moreover, a limited choice of tool materials is available, which are highly expensive and difficult to manufacture. Furthermore, the variations in the mechanical, thermal, and chemical characteristics of the tool material also alter the weld quality [26]. During the FSW of Ni-based alloy, tool performance, durability, and high production cost are major issues that need to be resolved.

The rapid degradation of the tool motivated us to find a potential solution for the improvement of tool life. Several methods have been applied in the recent past to reduce wear and break off the tool, increase the tool life, and improve the weld quality of high-strength materials. In this field, the main effort applied by researchers is to modify the tool geometries, maintain slow plunge rates, create a pilot hole at the plunge position, and preheat the materials. However, these strategies do not completely resolve the problem, so more in-depth knowledge is essential. Among this effort, preheating the material is extensively used to reduce tool wear and increase productivity. For preheating the materials to soften and reducing the plunging

force, some researchers [27,28] have used different external energy sources called Hybrid/Assisted friction stir welding techniques. In the Hybrid friction stir welding technique, many local preheating sources have been investigated, such as plasma, laser, electrical, back heating, and induction preheated FSW developed to improve tool life and enhance weld quality. Though, only a few preheating sources have been employed for FSW of Inconel 718 and high-strength steel. Among these, induction preheating is another source of external heat input for upgrading the FSW process. Induction heating is a non-contact heating process that uses an eddy current to heat the conducting material [29]. Due to many advantages of induction heating, such as providing a quick and uniform temperature, less setup time, focused heat, clean and energy-efficient, and safety benefits compared to other preheating sources such as open flame and resistance heating, it becomes more usable. Maintaining a preheating temperature suitable to make the defect-free joint is also noteworthy. Preheating and welding parameters have complex interactions that affect the peak temperature of welding, heat generation rate, microstructure, mechanical properties, and tool force during the assisted FSW process. Although process control has significantly improved, the availability of depth knowledge is still insufficient. Also, the study about using induction heating as a preheating source during FSW of high-strength materials is still insufficient.

1.3 Induction heating process

Induction heating is a non-contact heating process that heats electrically conductive materials by eddy currents which are produced by electromagnetic induction through the object [29]. The essential components of the induction heating process are an induction coil, an alternating-current power source, and the workpiece to be heated, as shown in Fig. 1.2. Applying a high-frequency alternating current to an induction coil produces an alternating magnetic field, which induces eddy currents. The induced eddy current heats the workpiece, which is placed inside the magnetic field, without touching the coil. It is generally used in process heating before metalworking, heat treatment, welding, and melting of metals.

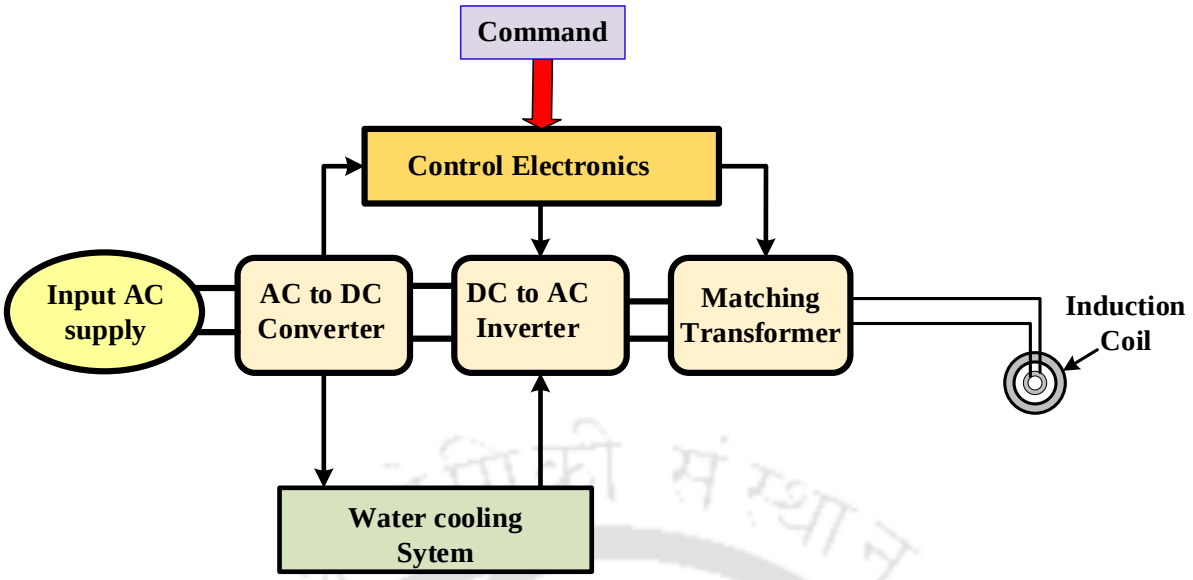

Fig 1.2 Power supply block diagram of induction heating machine.

The mechanisms of energy dissipation in the induction heating process are based on two factors, the first is energy losses due to Joule heating which is associated with the resistance of the material, and the second is energy losses associated with magnetic hysteresis. When the induction heater provides high-frequency alternating current to the induction coil, then an invisible force field (electromagnetic or flux) generates around the induction coil, and this force field induces an equal and opposing electric current in the workpiece. Because of the flow of high-intensity induced current (also called eddy current) into the workpiece, heat is generated. This heat generates because of the material's resistance, which opposes the current flow, also called the joule heating effect. No contact is required between the coil and the workpiece, which is also restricted to localized areas for inducing an electric current into the workpiece. The heating rate of the workpiece depends on the frequency of the induced current, the intensity of the induced current, the magnetic permeability of the material, the specific heat of the material and the material's resistance.

Another factor of the energy dissipation in the induction heating of magnetic materials such as steel, nickel, and a few other metals is losses associated with magnetic hysteresis. Hysteresis loss usually happens in ferromagnetic materials when they are magnetized and demagnetized. This is because the atoms in a ferromagnetic material combine in groups to form regions called magnetic domains. These magnetic domains are like small magnets because there have their own polarity and are affected by any external magnetic field. The alternating magnetic flux field causes the magnetic dipoles of the material to oscillate as the magnetic poles change their

polar orientation every cycle. This oscillation is called hysteresis, and a minor amount of heat is produced due to the friction produced when the dipoles oscillate. When the magnetic materials are heated above the Curie temperature, they become nonmagnetic, and hysteresis ceases. The basic nature of induction heating for Ni-based alloy and steel is fulfilled and becomes useful for heating.

1.4 Research objectives

The main objective of this work is to develop the experimental setup for induction-assisted friction stir welding and determine the process conditions that lead to the successful application on the Inconel 718 and stainless steel 204Cu and SS316L FSW. The primary objective of this research work is divided into the following subpart for the accomplishment.

- Feasibility study of FSW of Inconel 718 and determining the process parameters for successful application of this process.
- Development of induction-assisted FSW process, characterization of weld quality and tool wear during FSW of similar welding of Inconel 718.
- Investigations of FSW of dissimilar Inconel 718 and AISI 204Cu steel at different welding speeds.
- Comparative study of conventional and induction-assisted FSW of dissimilar high-strength alloy, i.e., Inconel 718 and SS316L.
- Investigations of corrosion behaviour of Inconel 718 and SS316L dissimilar joints formed with and without induction-assisted FSW.

1.5 Structure of the Thesis

This thesis is organized into 9 different chapters, closely reflecting the scope of work defined in the previous section.

Chapter 1 provides a brief introduction along with the working principle and motivation of the present research work.

Chapter 2 deals with an extensive literature review of the work of previous researchers, which is focused on the FSW of Inconel 718, stainless steel AISI 204Cu and SS316L, along with auxiliary energy-assisted FSW. The performed research on the mechanical and microstructural examination and corrosion properties was discussed.

Chapter 3 reveals the procedures and methods used for conducting the experiments.

Chapter 4 presents preliminary experimentation to find the operating parameters and their effect on mechanical as well as microstructural properties during FSW of Inconel 718 alloy. (**Published**)

Chapter 5 deals with the experimental investigation of joining Inconel 718 plates performed by induction preheating-assisted hybrid FSW. **(Published)**

Chapter 6 deals with joining dissimilar alloys, i.e. stainless steel (AISI 204Cu) and Inconel 718. **(Published)**

Chapter 7 deals with the effect of induction preheating during the FSW of dissimilar alloys, i.e., stainless steel 316L and Inconel 718. **(Published)**

Chapter 8 presents the experimental investigation of the corrosion behaviour of the dissimilar joint of Inconel 718 and SS316L formed by FSW. **(Published)**

Chapter 9 represents the conclusions and scope of future work, followed by a list of publications and references.

……..*……..*…….. :

CHAPTER 2

2. Literature Review

2.1 Introduction

The previous chapter discussed detailed information regarding the friction stir welding process and induction heating system. This chapter contains an extensive literature review on the FSW of Inconel 718 in similar and dissimilar configurations (with SS316L and AISI 204Cu) using conventional and assisted FSW techniques. The initial section of this chapter provides information regarding the available literature on the FSW process applied to high-strength materials like Ni-alloy and steel. Furthermore, a detailed literature survey explores the effect of FSW and I-FSW process parameters on joint performance. The current thesis primarily focuses on using an external heat source to save tool life during the FSW of similar and dissimilar materials. Therefore, the literature related to the auxiliary energy-assisted FSW technique is studied in more detail. Afterwards, tool material, geometry, and defects generated during various parameters were discussed. This chapter also contains a detailed literature review on the corrosion properties of dissimilar welded joints of Ni-alloy and stainless-steel material. Finally, the major research gaps from the literature review of the present thesis work are outlined.

2.2 FSW of similar Ni-based superalloy

Inconel 718 alloy is a Ni-base superalloy with excellent corrosion and oxidation resistance, which has outstanding mechanical properties within the temperature range of −250 °C to 700 °C [30]. It is a highly desirable alloy in many industrial fields such as aerospace, oil field, nuclear engineering, marine engineering, turbine engine, and cryogenic tankage fields. Generally, the fusion welding technique is employed to join Ni-base superalloys such as gas tungsten arc welding, gas-shielded metal arc welding, and laser beam welding [31,32]. In this field, Mei et al. [33] used the electron beam welding (EBW) technique to join Inconel 718 and studied the effect of base metal and welding speed. They found that the largest amount of the microsegregation of Laves phase in the center of the weld pool and hot cracking of the HAZ was mainly due to the effect of variation of the base metal microstructure and welding speed. Ram et al.[32] and Anbarasan et al. [34] employed the gas tungsten arc welding (GTAW) process for welding of Inconel 718 and worked on controlling the undesirable Laves phase in

the weld zone, which was found to be detrimental to the mechanical properties of the joint. Li et al. [35] researched the laser welding characteristics of the Inconel 718 under reduced ambient pressure. They reported that welding joints appeared without defects when the ambient pressure was 4×10^{-3} Pa.

However, there are some difficulties associated with high heat input during fusion weldings of Inconel 718, such as solidification cracking, poor penetration, microfissuring in the heat affected zone (HAZ), Cr segregation at the grain boundaries causing liquation cracking and separation of Nb upon solidification, which forms a brittle compound (i.e., $(Ni, Cr, Fe)_2(Nb, Mo, Ti)$) in the fusion zone [11,22]. Generally, Ni-alloy faces cracking problems during fusion welding in the welded region due to excessive heat input, which mainly affects fracture toughness, tensile strength, ductility, creep-rupture properties, and corrosion resistance [36]. Therefore, to minimize major drawbacks associated with the fusion welding of Inconel 718 and to control the high heat input, some researchers used an advanced joining technique, friction stir welding (FSW), having low heat input. In the field of a similar FSW process of Ni-based alloy, Song et al. [37], Ye et al. [38], and Ahmad et al. [39] successfully joined Inconel 625, Inconel 600, and Inconel 718 materials, respectively. Song et al. [40] performed FSW using a WC-Co tool on Inconel 718 alloy sheet and found a defect-free weld at a 150 mm/min traverse speed. An enhancement in weld strength and microhardness values in the SZ was observed due to high grain refinement and homogenous microstructure. They also studied post-heat treatment, which enhanced the weld strength and microhardness values. Due to post-heat treatment of the welded joint, the formation of a precipitate hardening compound found which was improved the weld strength and hardness compared to without a heat-treated weld joint. Lemos et al. [41] used a threaded pcBN tool with a W-Re binder in the FSW process and studied the effect of welding parameters on the residual stress of Inconel 625. They found more grain refinement at low rotational speed (i.e., 200 rpm), resulting in the lowest residual stress in the SZ. They also observed a difference in the residual stress on the retreating side (RS) compared to the advancing side (AS) due to the variation in tool rotational speed. The residual stresses were high at a high rotational speed and slightly changed at a low rotational speed. Ahamed et al. [39] investigated the effect of varying traverse speed on mechanical and microstructural properties during the welding of Inconel 718 using silicon nitride FSW tool material. At low traverse speed, particle precipitation and grain refinement were observed high in the center of the weld. Sato et al. [42] successfully joined a 4.8 mm-thick Inconel 600 alloy using of polycrystalline cubic boron nitride (pcBN) tool and reported that grain refinement

produces defect-free joints along with enhanced mechanical and microstructural properties. Also, an adverse effect on corrosion resistance was reported in the weld region. Similarly, Hanke et al. [43] used a pcBN tool to join a 3.2 mm Inconel 625 alloy. They investigated the effect of welding parameters on tool wear mechanisms and their impact on microstructure. Tool wear was maximum at high rotational speed by the diffusion process. In review articles by Lemos et al. [44], important issues like tool materials, process parameters and tool wear in FSW of Ni-based alloys are discussed. The peak temperature and weld quality are significantly influenced by the rotational speed and traverse speed.

2.3 FSW of dissimilar Ni-based alloy and stainless steel

In manufacturing industries, joining dissimilar materials is an important consideration because it provides a range of benefits, including flexible design considerations with characteristic properties and higher economic efficiency. In the field of joining dissimilar Ni-alloy with stainless steel material, traditional fusion welding techniques like Laser welding [45–49], GTAW [50–56] and Plasma welding [15] have been applied. The dissimilar welding faces some problems like stress corrosion cracking, hydrogen embrittlement, hot cracks, the rapid growth of grains, porosity, blowholes, alloying elements segregation and heat-affected zone softening, etc., due to their different material properties, melting points, improper selection of filler materials and thermal conductivity [57,58]. The excellent properties of the dissimilar joint, including minimal distortion and high-quality weld formed by the FSW process, make it advantageous over other welding processes. Researchers reported that the defect-free joint of dissimilar Ni-based alloy with stainless steel formed by the FSW process was achieved by careful selection of welding parameters, tool design, and pre-and post-weld treatments.

A few important findings from the previous studies of friction stir welding of dissimilar Ni-based alloys with stainless steel have been discussed. Kangazian et al. [59] successfully joined dissimilar Inconel 825 and SAF 2507 plates with a WC-based tool. They reported that positioning of super duplex steel on the advancing side resulted in good weld strength. They found toughness value of the weld zone was higher than the Ni-alloy and lower than the super duplex stainless steel due to the dynamic recrystallization and grain refinement. Rodriguez et al. [60] applied the FSW process on the Inconel 625 and mild steel for dissimilar joining. They found six different zones in the weld region generated due to dynamic recrystallization and deformation. Shamanian et al. [61] studied the FSW welding parameters during the dissimilar joining of Inconel 825 and stainless steel 316 L. They obtained defect-free weld at 24 mm/min

welding speed and rotational speed of 500 rpm. Song et al. [62] joined Inconel 600 with SS 400 and obtained a defect-free lap joint at 100 mm/min welding speed and tool rotational speed of 200 rpm using a WC-Co tool. They stated that applying FSW was highly effective for diminishing the grain measure of the weld nugget zone. Landell et al. [63] explored the microstructure and mechanical properties of the FSWed ASTM 572 steel plate with cladded Inconel 625. They observed that the two-pass welding procedure improved the mechanical and microstructure properties resulting in enhanced weld quality. Aghaei et al. [64] investigated the effect of welding parameters on the mechanical and microstructure properties of Monel 400 and stainless steel 316 joined by the friction stir welding process. Sound welds were obtained at the low rotating speed of 400 rpm with 50 to 100 mm/min welding speeds.

However, the FSW of dissimilar high-strength materials has not been widely used because of the problems associated with tool wear. Vicharapu et al. [65] reported a progressive wear mechanism of the pcBN tool caused by softening and diffusion of the W-Re binder phase and mechanical wear mechanism observed at varying process parameters. During the FSW of high-strength materials, the generated high temperature and load cause the degradation of the FSW tool, which affects the depth of weld penetration, microstructure, the strength of the weld joint, and manufacturing costs [66].

2.4 Auxiliary energy-assisted FSW technique

The FSW process was initially developed to weld softer or hard-to-weld aluminium alloys. After the successful application of this process on low melting point material, industries have shown remarkable interest in welding high melting/strength material because of the numerous applications and advantages of the FSW process, as discussed in the previous section.

It is commonly observed that the produced heat is insufficient to soften and plasticize the material during the welding of high melting/strength, such as steel and Ni-based alloys, resulting in defective joints. Countering this problem, researchers [67,68] suggested that during the welding, a significant increase in tool rotational speed and/or a decrease in welding speed and an increase in downward axial force is required to produce adequate heat. However, increasing the downward axial force and decreasing the tool traverse speed resulted in major difficulties like unpredictable tool breakage and severe tool wear, leading to an increase in production cost as well as reduced joint efficiency.

To overcome these difficulties, several methods have been applied in the recent past to reduce wear and break-off tools, increase tool life, and improve the weld quality of high-strength materials. In this field, the main effort applied by researchers is to modify the tool geometries and preheat the materials. Under the preheating methods, additional heat is given to harder alloys before and during the welding process to reduce the amount of work required by the FSW tool, which results more remarkably than the other methods. For preheating the materials to soften and reduce the downward load, some researchers have used different external energy sources called hybrid/auxiliary/assisted friction stir welding techniques. These hybrid FSW processes could be classified as mechanical and thermal-assisted processes based on different external energy sources. Under the mechanical-assisted category, only ultrasonic-assisted friction stir welding (UAFSW) has been significantly used to join softer materials. The laser [27], plasma [28], arc [69], electrical [70], back heating [71], and induction [72] preheating processes are categorized as thermal-assisted processes. The following subsections, 2.4.1 to 2.4.6, systematically summaries the available literature review of the major hybrid FSW technique, the details of the experimental setups, and the effects of the auxiliary energy on the FSW process.

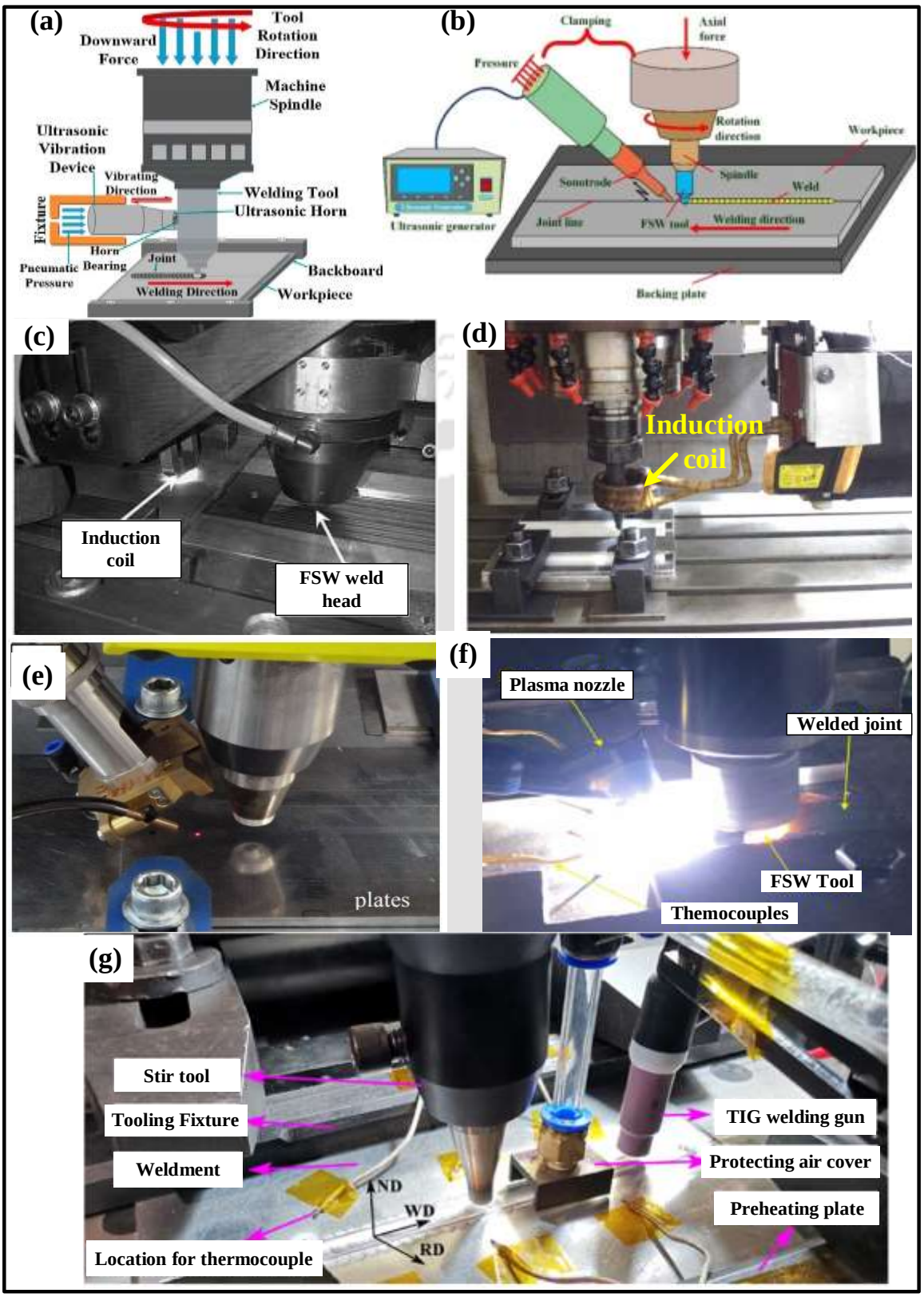

Fig. 2.1 Experimental setup of (a-b) Ultrasonic assisted FSW [73], (c-d) Induction-assisted FSW [74,75], (e) Laser assisted FSW [76], (f) Plasma assisted FSW [77], and (g) TIG assisted FSW [78].

2.4.1 Ultrasonic-assisted hybrid FSW

The high-frequency ultrasonic vibration assisted-FSW (UASFW) process is the only variant of the mechanical-assisted process, which is used to soften metallic materials without obvious temperature rise. Figures 2.1 (a-b) show the schematic experimental setup diagram of the ultrasonic-assisted FSW. Generally, there are two modes of transfer of ultrasonic vibrations to the workpiece has been used, one executed energy through the tool [73] and another transfer directly to the workpiece in the weld zone [79], as shown in Fig. 2.1 (a) and Fig. 2.1 (b), respectively. This process consists of the ultrasonic energy source, including a vibration tool, amplitude transformer, and transducer, integrated with a conventional FSW machine. Earlier literature mentioned that using ultrasonic energy helped reduce the chance of forming weld defects and improve the material flow.

In this field, Zhang et al. [80] used ultrasonic vibration in the conventional FSW machine to weld 6-mm thick 7N01-T4 aluminium alloy plates. They have compared the material flow behaviour in these conventional and assisted FSWs. They reported that using ultrasonic vibration significantly increased the welding speed, improved surface quality, and reduced axial force compared with conventional FSW. Zhao et al. [73] studied the effect of ultrasonic vibration on the contact state at the tool/workpiece interface. They developed the coupled model of the UAFSW process to analyze the ultrasonic field and thermal behaviour. They reported that using ultrasound effectively reduces the interfacial friction stress, acoustic softening of base material, and friction reduction at the tool/material interface. Ahmadnia et al. [81] investigated the effect of ultrasonic vibration on tensile strength and formability. They determined the major parameter effects, which were applied to the friction stir tool during the welding of AA6061 materials. They reported that using ultrasonic vibration power of 400 W, a rotational speed of 1000 rpm, a welding speed of 40 mm/min, and an axial force of 12 kN gives maximum tensile strength with minimum surface roughness. Ma et al. [82] joined aluminium alloy 6061 with the ultrasonic-assisted FSW and compared it with the conventional FSW. They reported that the use of ultrasonic vibration hardness and tensile strength increased with increasing ultrasonic energy. Similarly, in the field of dissimilar friction stir welding, Zhong et al. [73] joined AA6061-T6 to AA2024-T3 using ultrasonic vibration ahead of the FSW tool and found that the use of ultrasonic vibration lowers the traverse force, tool torque and axial force. Liu et al. [83] used ultrasonic-assisted stationary shoulder friction stir welding to join dissimilar 6061-T6 Al and AZ31B Mg alloys. They reported that induced vibration and

acoustic streaming helped to break the continuous IMCs layer near the thermo-mechanically affected zone into pieces, improving weld quality and tensile properties.

2.4.2 Induction-assisted hybrid FSW

Induction heating is a non-contact process that uses an eddy current to heat the conducting material. When an electrically conducting material is placed inside the variable magnetic field, the eddy current in the material is generated according to the Faraday law. This generated current produces heat into the workpiece due to the material's resistance [84]. Induction preheating is another source of external heat input for upgrading the FSW process. Due to many advantages of induction heating, such as providing a very fast and uniform temperature, less setup time, clean and energy-efficient, and safety benefits compared to other preheating sources such as open flame and resistance heating, it becomes more usable [85]. Álvarez et al. [86] used the induction-assisted friction stir welding (I-FSW) process to join super duplex stainless steel. In this setup, the FSW machine and the induction coil were fixed separately so that the induction coil first heated the weld line, as shown in Fig. 2.1 (c). Another setup in which an induction coil heated the tool to join the thermoplastics [75] is shown in Fig. 2.1 (b). The use of induction pre-heating generally increases the material flow, reducing the plunging force and improving processing time. Oeystein et al. [87] patented a modified FSW process setup and investigated the effect of induction coil preheating on the joining of medium-strength AA 6082 T5 Al-alloy and ferrous alloys. The result shows that the downward force on the tool was reduced by 50%, along with the increase in welding speed and improvement in joint mechanical properties. Sun et al. [88] used a high-frequency-assisted spot FSW process for joining S12C steel plates. The effect of preheating improved grain structure in the weld nugget zone and resulted in improved weld quality. They also reported that preheating resulted in reduced downward axial force, and tool rotational speed caused enhanced tool life. Álvarez et al. [86] successfully welded super duplex stainless steel using high-frequency induction preheated FSW technique and analyzed a comparative study with and without the effect of preheating. They confirmed that the use of induction preheating reduced applied load by up to 31% and doubled the welding speed due to material softening. Similarly, Cheon et al. [72] also reported reducing vertical load by 26% and increasing welding speed by 40% using a 4 kW induction preheating source during the FSW of carbon steel. Vijendra and Sharma [75] used an induction coil around the tool, and they found that an induction-assisted tool softens the base material (BM) and is easily stirred for welding. They reported optimum tool-pin temperature and

rotational speed were 45 °C and 2000 rpm, respectively, for the maximum joining strength of thermoplastic. However, the study about using induction heating as a preheating source during FSW of high-strength materials is still very limited.

2.4.3 Laser-assisted FSW

Laser-assisted FSW (LAFSW) is the most commonly used hybrid FSW process in which a laser heat source preheats the workpiece before joining. Figure 2.1 (e) shows the experimental setup of LAFSW, which incorporates the conventional FSW machine accompanied by a laser heat source. In this process, the laser heat source focuses on the area of the workpiece where the tool is plunged, and afterwards, the laser keeps on preheating the workpiece before the tool passes from that area. Throughout this process, focal point of the laser maintains a constant distance from the tool. This additional non-contact local preheating source minimises the reaction force on the tool, reduces the deflection in the fixture, and gives higher weld speeds [89]. Additionally, one major advantage is that this laser-assisted FSW can be used to join both conductive and non-conductive materials. Various experimental research has been undertaken for LAFSW of low and high-melting temperature alloys. Palm et al. [90] patented laser-assisted FSW in 2004 and studied tool life improvement by softening the workpiece with the laser preheat technique. In the field of laser-assisted FSW, Sun et al. [27] successfully welded S45C steel plates and studied the influence of laser position on mechanical and microstructure properties. Due to the laser preheating, welding speed increased by two times compared with normal FSW, and laser positioning on the retreating side gives maximum heat input. Song et al. [91] also observed that the welding speed of laser-assisted FSW was 1.5 times higher than the normal FSW when joining Inconel 600 plates. The effect of laser preheating improved mechanical strength due to grain refinement in the stir zone (SZ). Ahmad et al. [92] numerically developed a thermodynamic coupled model for the laser preheating and FSW process for the joining of structural steel by LAFSW. They found that the application of laser at a distance of 20 mm from the rotational tool reduced the reaction force on the tool up to 55% compared with the conventional FSW. Casalino et al. [76] designed an experimental setup for the LAFSW of Aluminium 5754 alloy and investigated the influence of the preheat on the weld quality. They reported that laser avoids the formation of cracks and increases process speed with high surface finish quality. Similarly, Campanelli et al. [93] used fiber laser-assisted FSW for the joining of 6 mm thick 5754H111 aluminium alloy. They found that laser pre-heating positively affects the joining of aluminium alloys, such as the benefits of this innovation for low tool wear, higher

welding speeds, and lower clamping force. Merklein et al. [94] reported that conventional FSW of steel and aluminium alloys shows poor weld quality in dissimilar joining. In contrast, using laser preheating enhanced the weldability and the welding feed and reduced the tool's wear. Similarly, Fei et al. [95] investigated the effect of pre-hole offset during the LAFSW of the steel and aluminium alloys. Results showed that a pre-hole offset distance influences the IMC layer of the interface in such a way that when the pre-hole offset distance was suitable, iron-abundant inter-metallic compounds were obtained; otherwise, aluminium-abundant inter-metallic compounds were formed. Although LAFSW is a widely studied process among all the auxiliary energy-assisted FSW, it also has some disadvantages like the low energy efficiency of laser, bulky setup, high cost, and requirement of a skilled operator.

2.4.4 Arc assisted FSW (AAFSW)

The most effective preheating method for joining materials of low melting points or high strength is the arc-assisted friction stir welding (AAFSW) system. This method incorporates preheating sources such as a plasma arc [96] or a tungsten inert gas (TIG) welding arc [97] in combination with the conventional FSW process, as shown in Figs 2.1 (f-g).

Kou and Cao [98] invented the arc-assisted FSW process, in which an electric arc torch is applied directly to the workpiece. It was reported that joint strength and tool life were improved due to greater plastic flow of material by employing a supplementary arc heat source during welding. Under joining dissimilar materials, the preheating arc is typically aimed at harder materials to compensate for the mismatch in melting points between the materials.

The plasma arc is used as a preheating source in the FSW process in which a plasma torch transfers concentrated arc with the direct current, which consequently plasticizes the workpieces. Yaduwanshi et al. [28] reported that plasma preheating reduced the cooling rate in welded joints and average plunging force by 22-28%. Reduction of the plunging force improved the tool's life. In the field of plasma, preheating Pankaj et al. [99] and Tiwari et al. [96] also investigated the effect of preheating on material flow and tool life. The thermal and material flow behavior results were compared between numerical simulations and experimental findings. A numerical model was also created by Yaduwanshi et al. [100] to analyze the time-temperature history and determine the isotherm of the nugget zone in plasma-assisted FSW.

In the AAFSW system, several researchers have used a tungsten inert gas (TIG) welding arc source as a preheating with the conventional FSW process. It found that the total heat input in

the AAFSW was higher than the conventional FSW; this brings down the materials' mechanical strength and causes softening of the material, reducing the downward axial force. Bang et al. [97] utilized a gas tungsten arc welding preheating source during the dissimilar FSW of aluminum (Al6061 -T6) alloy with stainless steel (ST304), as shown in Fig. 2.1 (g). They reported that preheating increases the weld strength more than the FSW joint strength, possibly due to enhanced material flow and partial annealing effect in the weld zone. Mehta et al. [101] utilized preheating source of TIG welding during the FSW for dissimilar Al-Cu systems and found a minor improvement of tensile strength at a low preheating current of 40 amp as well as maximum strength achieved at cooling under the water system. Yi et al. [78] used the TIG arc preheating system during the FSW of 2519 aluminium alloy and reported enhanced tensile strength and elongation of the joint. The use of preheating reduced the hole defects and onion ring area resulting in enhanced mechanical properties. Patel et al. studied the effect of the TIG preheating source on the mechanical and microstructure properties of FSW-joined aluminium and titanium materials. They reported that the strength of the heat-assisted joint reduced due to the inclusions of the Al–Ti intermetallic and grain coarsening.

2.5 Mechanical properties and process parameters

The process parameters like welding speed, tool rotational speed, tool tilt angle, tool offset, downward force, and tool design are important variables that can affect the quality and properties of the weld produced by the FSW process [5]. The rotation and welding speed of the tool is one of the most important process parameters in FSW, which affect the heat generated during welding, the material flow, and the quality of the joint. The optimal parameter varies depending on the welded material and tool design. The downforce applied by the tool to the material also affects the heat generated during welding and the quality of the joint. By adjusting these process parameters, FSW can be optimized to produce high-quality welds with specific properties such as weld strength, ductility, and heat-affected zone properties.

Ahmed et al. [6] studied the welding parameters in joining AA6061-T6 sheets and compared suitable parameters based on the weld tensile strength. They reported that high tool rotational speed (1900 rpm) combined with a high speed of tool travel (150 mm/min) and low plunge depth (0.10 mm) was found to be suitable welding parameters in micro-FSW. Miyano et al. [102] used variable welding speeds of 50, 100, 200, and 300 mm/min and a constant tool rotating speed of 400 rpm for FSW of 2 mm thick high nitrogen-containing stainless steel. Full-penetrated and defect-free butt joints were obtained at an optimum welding speed of 100

mm/min, and under this, the best mechanical properties were recorded. Lakshminarayanan et al. [26] joined AISI 409M ferritic stainless-steel plates and incorporated the process parameters like rotational speed, welding speed, and tool shoulder diameter with the tensile strength and impact toughness of the friction stir welded joints. They reported that the welding speed significantly influences tensile strength and impact toughness, followed by rotational speed and tool shoulder diameter. Du et al. [103] stated that cavity defect at the advancing side of the TA5 alloy weld was observed under improper rotation and welding speeds and affected tool wear behavior. Apart from the tool rotational and traverse speed, the tool tilt angle and tool offset influence the process variables related to material transport and heat transfer. In practice, the tool is tilted toward the behind side of the weld at an appropriate angle ($1^o – 3^o$) to achieve high-quality welds with optimal material flow and minimal tool wear. The specific tool tilt angle used in FSW can vary depending on a number of factors, including the material being welded, the material's thickness, and the tool's rotational speed. Meshram et al. [104] studied the effect of tool tilt angle on material flow and weld defects. An intermediate tool tilt angle ($1^o – 2^o$) generates weld without microscopic defect in 7 mm thick AA2219. Zhai et al. [105] reported that an increase in tool tilt angle increases the temperature at the shoulder/workpiece interface point increasing the flowability of the material toward the advancing side. Kumar et al. [106] investigated the influence of tool tilt angle ($0^o – 3^o$) on the metallographic and mechanical properties of FSWed AISI 316L austenitic stainless-steel butt joints. They reported that the weld joint strength against the tool tilt angle depicts a parabolic trend and was maximum at an angle of 1.5^o.

In the dissimilar joining, the effect of tool offset on the amount and distribution of the heat generated during the welding process is important. When the tool is offset from the centerline of the joint, it causes more heat to be generated on one side of the weld than the other. This results in uneven material flow and may cause defects such as voids or lack of fusion. Tool offset also affects the size and shape of the weld and the wear and longevity of the welding tool. Muhammad et al. [107] studied the effect of tool offset on the joint quality of dissimilar Al-Cu welds and found shifting toward the Al side gives a thick IMC layer. Tiwari et al. [108] joined AISI 304 stainless steel with mild steel and studied the tool offset and rotational speed effect on the microstructure and mechanical properties. Joint obtained at a rotational speed of 875 rpm and 1.2 mm offset toward SS304 gives maximum strength. Similarly, in the dissimilar FSW of stainless steel with Ni-based alloy, Kangazian et al. [59], Shamanian et al. [109], and Aghaei et al. [64] have used WC-based tool alloy for joining. They reported that placing high-

strength material on the advancing side and using low tool rotational and traverse speed generate defect-free joints with high weld strength. Although, the detailed study of process parameters during the dissimilar FSW of Ni-based alloy and stainless steel still lacks to complete understanding of the underlying mechanism of how the tool parameters affect the material flow and the heat transfer in the FSW process. The welding parameters also affect the mechanical properties, like the hardness value of the weld joint. It was observed that both rotational and transverse speeds significantly affect hardness results [108]. Further research is needed to fully understand these interactions and optimize the process parameters for the best possible weld quality and properties.

2.6 Microstructural study

Microstructural analysis of an FSW joint refers to examining the weld structure at a microscopic level, which aids in identifying the weld's characteristics. Typically, the microstructural analysis of the FSW joint involves using techniques such as optical microscopy, scanning electron microscopy (SEM), and transmission electron microscopy (TEM) to examine the weld zone. The weld zone, which is the joint region subjected to material processing, involves combinations of the highest levels of deformation (i.e., strain) and heat that produce desired shape and microstructure [110]. The material in this region often has a refined grain and homogeneous structure due to phenomena such as recovery, recrystallization, and grain growth which depend upon the working temperature and degree of deformation [2]. During the FSW process, high temperature and heavy deformation occur, leading to the material's recovery and recrystallisation. The temperature during the FSW process reached quite high, assumed to be a hot working process that results in the dynamically recrystallized microstructure.

The macroscopic view of the weld zone typically looks like a basin shape. Mishra et al. [5] reported basin-shaped and elliptical-shaped weld zones at low and higher rotational speeds, respectively. The FSW weld zone is based on the grain size divided into four zones. A center of the weld known as the stir zone (SZ), adjacent to the stir zone, is the thermo-mechanically affected zone (TMAZ), beside it is the heat-affected zone (HAZ) and the rest part as a base material (BM) [111]. Shamanian et al. [109] also reported the presence of different regions during the study of dissimilar FSW joints of Inconel 825/SS316L. Although some researchers [91,109] reported that the presence of a heat-affected zone (HAZ) was not clearly seen under

the weld zone of high-strength material. This could be the combined effect of the fast cooling rate during FSW and the physical properties of the parent metals.

The effect of process parameters highly influences the weld quality. The insufficient heat input and improper material intermixing generate different kinds of defects in the weld zone. Higher heat input generates intermetallic compounds, excess weld flash, and surface galling. In contrast, low heat input creates insufficient softening, an increase of flow stress, tunnelling defect, kissing bond (KB), and hooking defects, as shown in Fig. 2.2. Moussawi et al. [112] studied the defects associated with the FSW process of DH36 and EH46 steel and found that the defects formation such as voids, weld root defects, and kissing bonds occur due to high tool traverse speed. Albannai et al. [24] reviewed and stated that defects like solidification or liquation cracking are not able to exist during FSW since it is a solid-state welding process. If the wrong process preparation and/or incorrect weld parameter is used, then defects can be found in the produced joint and alter the weld quality. Pardeep et al.[113] studied the parametric effect on the weld quality and reported that defects like wormholes, high flash generation, and incomplete weld penetration were observed at the high rotation speed and very low traverse speed.

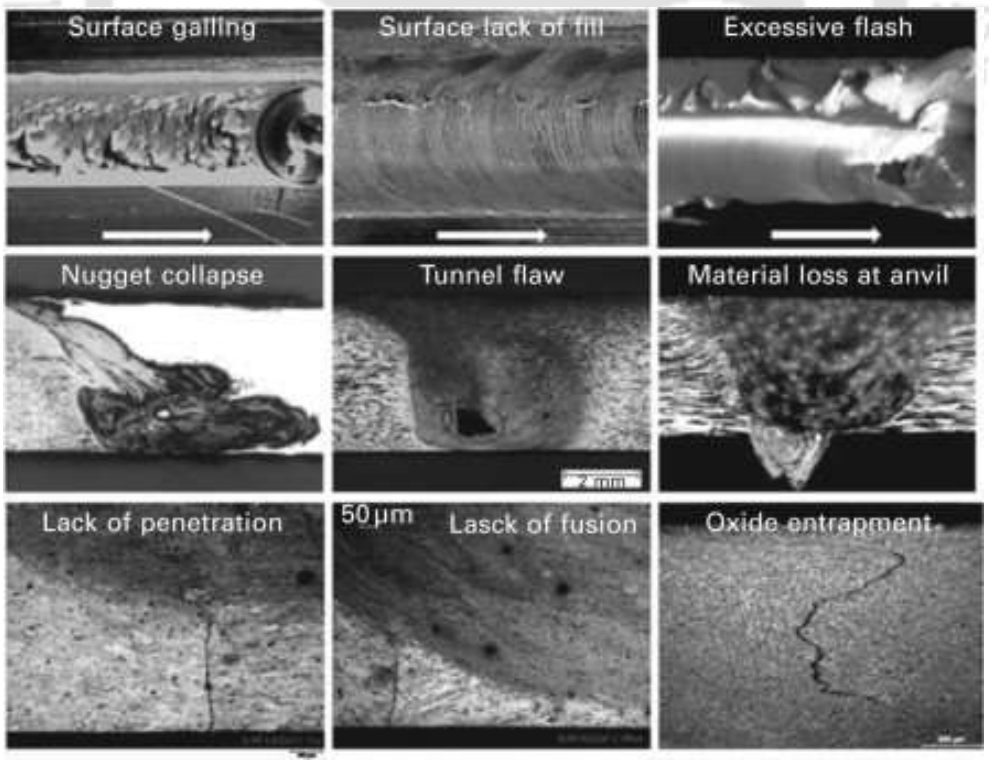

Fig. 2.2 Different types of defects during the FSW process [114].

The FSW process involves several complex phenomena, such as phases, microstructure, and weld metallurgy. The friction stir welded joints' microstructure and phases depend on base materials and process parameters. Song et al. [62] investigated the microstructure properties of the FSWed lap joint of Inconel 600/SS 400. The application of FSW effectively reduced the grain size of Inconel 600 from 20 µm to 8 µm in the nugget zone (NZ). They reported that the MC carbides with a size of 50 nm were partially formed in the region of the lap joint interface in Inconel 600. Ahmed et al. [115] studied the effect of welding speed on the microstructure of the Inconel 718 using electron backscattering diffraction (EBSD). They reported that low-resolution EBSD scans across the NG showed a great reduction in grain size, and high-resolution EBSD scans showed that the NG region is dominated by a dynamically recrystallized grain structure with very fine grains. Kangazian et al. [116] studied the microstructure of dissimilar FSWed joints of Inconel 825 and supper duplex stainless steel 2507. They found that NZ showed higher hardness than the base metal due to dynamic recrystallization and the subsequent refinement of the microstructures. Sato et al. [42] reported that the application of FSW on Inconel 600 produced a refined grain structure in the SZ which enhanced the mechanical properties of the joint but exhibited slightly lower corrosion resistance.

The microstructure of the FSWed joint is also affected by the application of the external preheating source. Sun et al. [27] applied an external laser preheating source during the FSW of the S45C steel and studied their effect on the microstructure. They reported that the application of preheat reduced the formation of the brittle martensite phase in the nugget zone at a welding speed of less than 600 rpm. Song et al. [91] joined Inconel 600 through the application of laser-assisted FSW. They found that the application of the preheat is effective in increasing the extent of grain refinement and improving the mechanical properties. Similarly, Tiwari et al. [96] and Yaduwanshi et al. [100] used plasma preheating during the FSW process and reported that additional material softening reduces tool wear and axial force. Applying preheating in the FSW process increases the joint's cooling time, resulting in a small increment of the grain structure.

When dissimilar materials such as aluminium and magnesium or steel and aluminium are joined using FSW, it is common to observe the formation of intermetallic compounds (IMCs) at the interface between the two materials [117]. The formation of IMCs is influenced by several factors, including the composition of the materials being welded, the welding parameters (such as the rotational speed and traverse speed), and the thermal history of the weld. In the case of dissimilar aluminium and magnesium joints, the formation of IMCs is

typically less pronounced than in steel and aluminium welding. This is because aluminium and magnesium have similar melting temperatures and are more compatible with each other compared to steel and aluminium, which have a larger difference in their melting temperatures [118]. Mypati et al. [119] and Muhammad et al. [107] investigated the use of FSW to join aluminium (Al) and copper (Cu) and found that the process resulted in the formation of intermetallic compounds (IMCs) at the interface, which altered the mechanical properties of the joint. Kaushik et al. [120] conducted a microstructural study on dissimilar aluminium and steel joints. The formation of the IMCs with variable thicknesses ranging from 1 μm to 4 μm was detected. Shi et al. [121] performed FSW on dissimilar aluminium/ magnesium (Al/Mg) and investigated the formation of IMCs in the banded structure (BS) zone and their effect on mechanical properties. The presence of the IMCs of the $Al_{12}Mg_{17}$ layer makes the BS zone a weak/critical zone. The formation of IMCs affects the strength and ductility of the weld, so it is important to control their formation during the welding process. However, in the case of Ni-alloy and steel, the formation of the IMCs not reported. Shamanian et al. [109] reported that intermetallic phases formed in the SZ of dissimilar FSWed when the materials had high affinity to each other, like Al/Ti pair. The dissimilar material rich in Fe and Ni generally forms a solid solution phase in a wide range of chemical compositions, and unlikely that intermetallic phases formed in the SZs.

Overall, the microstructural analysis of an FSW joint is important in understanding the characteristics of the weld and its properties, such as strength, ductility, and fatigue resistance.

2.7 Tool material and geometry

The FSW tool is a critical component of the process, and its material and geometry play an important role in determining the quality of the weld and its efficiency. The FSW tool material must have high wear resistance, strength, and thermal conductivity. The tool material should also be able to withstand high temperatures and resist chemical reactions with the workpiece material [66]. The most commonly used materials for FSW tools are tungsten, molybdenum, and tool steels. Other materials such as ceramics, diamond, and polycrystalline cubic boron nitride (pcBN) have also been used for FSW tools, but they are less commonly used due to their higher cost and lower toughness [96]. Although, in recent years, after the progress in high abrasion resistive and excellent toughness tool materials such as polycrystalline cubic boron nitride (pcBN) tool, cemented tungsten carbide (WC-Co) tool, tungsten-rhenium (W-25%Re) tool and silicon nitride (Si_3N_4) tool), many researchers have been applied to join high strength

and high melting point materials like steel, Ni-alloy and titanium alloy. In this field, Song et al. [40], Ahmed et al. [115], and Sato et al. [42] have used the WC-Co tool, Si_3N_4 tool, and pcBN tool, respectively, during the similar FSW of Ni-based alloy. Similarly, in the dissimilar FSW of stainless steel with Ni-based alloy, Kangazian et al. [59], Shamanian et al. [109], and Aghaei et al. [64] have used WC-based tool alloy for joining the material.

However, the FSW of high-strength materials has not been widely used because of the problems associated with tool wear. Hanke et al. [43] and Vicharapu et al. [65] reported a progressive wear mechanism of the pcBN tool caused by softening and diffusion of the W-Re binder phase and mechanical wear mechanism observed at varying process parameters. Tiwari et al. [122] employed the WC-Co tool during the FSW process's joining of the DH36 steel plates and reported a progressive degradation of the tool. They observed that abrasion, adhesion, diffusion, crack initiation, and oxidation was the main cause of the degradation of the tool. Rotational and transverse motion of the tool causes continuous rubbing and exposure to high temperatures which lead to wear and degradation of the tool material because of reduction of yield strength of material at high temperature. The FSW tool experiences significant mechanical and thermal stresses during the welding process. These stresses result in plastic deformation, fatigue, or even cracking of the tool, leading to wear and reduction of tool life. During the FSW of high-strength materials, the generated high temperature and axial load on the tool cause the degradation of the FSW tool, which affects the depth of weld penetration, microstructure, the strength of the weld joint, and manufacturing costs [66]. Many researchers have worked on modifying tool geometry [120,123,124] to improve tool life and overcome the tool degradation problem.

The FSW tool geometry is equally important as the tool material. The geometry of the tool determines the heat input, the stirring effect, and the pressure applied to the workpiece during the welding process. The tool geometry is designed based on the thickness and type of material being welded [125]. Critical parameters of the FSW tool geometry, including shoulder diameter, pin geometry, and thread pitch, play an important role in defect-free joints. As the probe side of the tool wears, its geometry and dimensions may change. This can affect the quality and consistency of the weld, leading to variations in joint strength, porosity, or defects. The worn probe may also have reduced stirring and mixing capability, affecting the overall weld quality [126]. Also, as wear progresses, the remaining tool material has to bear higher loads and forces, leading to accelerated wear rates and potential tool failure. This can result in a shorter tool life and the need for frequent tool replacement or reconditioning.

However, the variation of tool geometry in the use of joining of steel and Ni-alloy are limited due to severe tool degradation. Pradeep et al. [113] used a conical pin with a flat shoulder tool during the FSW of steel. Kaushik et al. [120] reported that straight cylindrical pin geometry compared with tapered cylindrical pin with minimum interference with the steel plate is best for dissimilar Al-steel joining. Quintana et al. [127] stated that the tool pin has a significant influence on torque generation in the FSW process. Buffa et al. [128] investigated the effect of pin angle on weld quality and reported that the overall temperature in the weld zone increases with the increase of pin angle, and the use of a conical pin in FSW produces a helical movement in the weld zone. A tool with a concave shoulder and conical pin had shown the minimum tool degradation as compared to other profiles. Kumar et al. [129] studied the tool geometry during the joining of aluminium alloy and stated that the tool with the chamfered shoulder having a frustum-shaped rounded-end pin resulted in a better-quality weld. Lemos et al. [44] presented valuable insights on various aspects of tool design in joining high-strength Ni-based alloys. The right combination of tool material and geometry can produce high-quality, defect-free welds with high efficiency and consistency.

2.8 The corrosion resistance of the joint formed by friction stir welding

Corrosion is one of the most common phenomena affecting the desirable properties of the metal in a severe environment, whereas corrosion resistance is a critical factor in determining its long-term durability and performance. Generally, the corrosion resistance of a joint formed by FSW depends on various factors, including the type of material being welded, the welding process used, and any post-weld treatments applied [130]. However, FSW joints generally exhibit better corrosion resistance than other welded joints due to reduced heat input, improved microstructure, no filler material, and a smooth surface finish [131]. The investigation of the corrosion properties of the FSWed joints is also important because the welded joint exhibits different zone, which resulted in an inhomogeneous structure across the joint. Moreover, when dissimilar alloys with different corrosion potentials are welded together, the joint has different corrosion properties. Jayaraj et al. [132] reported that the mixing of two dissimilar metals with the FSW process formed an intercalated microstructure which led to the creation of micro-galvanic corrosion cells in the weld, which may alter the weld properties. West et al. [133] investigated the corrosion properties of the weld zone in 3.5 wt.% NaCl solution and reported that moderately inferior corrosion resistance of dissimilar welds was observed compared to individual base metals. Wang et al. [134] studied the effect of microstructure on the corrosion

behavior of dissimilar FSWed steels and reported that low-angle grain boundaries deteriorated the corrosion resistance on the SS304 side of the joint.

Generally, stainless steel and Ni-based alloys are utilized in severe environments such as aerospace, nuclear engineering, oil and gas production parts, and submarine parts, where high corrosion resistance and high-temperature mechanical properties are required. The working fluid of the supercritical water oxidation SCWO) the system is supercritical water which contains a corrosion environment of chloride, acidity, salts, and oxygen, making a severe environment for component material [19,20]. Similarly, gas turbine engine components made with Ni-alloy faced localized corrosion attacks under an acidic environment created when ingested air contaminants react with moisture [135]. However, very few studies have focused on the corrosion behaviour of friction stir welded Ni-alloy and stainless-steel joints. In this field, Lemos et al. [136] explored the intergranular corrosion of the FSWed Inconel 625 joint and observed the existence of $M_{23}C_6$ and M_6C carbide particles at the grain boundaries diminished the corrosion resistance. Sato et al. [42] also joined Inconel 600 plates by the FSW process and reported that welded section showed the minimum corrosion resistance under the ferric sulfate acid test. Similarly, in the field of corrosion properties of FSWed stainless steel, Sarlak et al. [137] investigated the corrosion behaviour of the duplex stainless-steel joints and found that the corrosion resistance of the nugget zone was enhanced with increasing welding speed, and it was higher than the parent metal. Li et al. [138] successfully joined nickel-free austenitic steel by the FSW technique. According to the report, the presence of carbide and ferrite particles in the nugget zone of the joint was found to have a slightly negative effect on its corrosion resistance. Atapour et al. [139] investigated the pitting corrosion behavior on the FSWed lean duplex stainless steel joint. Based on the cyclic polarization, the result showed the higher welding speed led to an increase in the number of pits and a decrease in the size of pits.

2.9 Major research gaps from the literature review

From the above-detailed literature review, it is observed that the number of publications on FSW to Ni-based alloys remains limited, probably because of the practical difficulty of such welding. Very limited literature is available on the similar and dissimilar FSW of Inconel 718 and austenitic stainless steel (SS416L/AISI 204Cu) using the tungsten carbide WC-10wt.%Co tool. The commercialization of FSW for Inconel 718 and steel has not yet been feasible due to the high tool cost, limited availability of tool materials, and significant tool wear. More modifications in the FSW technology are required to achieve such implementation. However,

a number of researchers have described how this challenge has been overcome. Detailed analysis of the welding parameters, such as traverse speed and rotational speed, on the mechanical and microstructural properties of the Ni-based alloy and stainless steel explained. Moreover, previously investigated researchers didn't focus on the effect of welding parameters on the similar Inconel 718 and dissimilar Inconel 718 with AISI 204Cu/SS316L. Researchers rarely worked on the effect of external preheating on the microstructure, mechanical properties, temperature distribution, axial force, tool life, and corrosion properties of the FSWed joint. The selection of tool material and optimizing the tool design to reduce wear and deformation during FSW of high-strength material still need to investigate. Although a lot of issues have been addressed in FSW of similar/dissimilar steel, the available knowledge on FSW of dissimilar Ni-based alloys and steel is very limited. So, based on the literature survey, the significant research gaps are outlined as follows:

- Previous investigations were only focused on the feasibility of FSW on Inconel 718. Optimizing process parameters like rotational and traverse speeds and their effect on mechanical and microstructural properties were not studied systematically.
- Studies about using induction heating as a preheating source during FSW of high-strength materials are rarely found. There is no research work found on the joining of Inconel 718 using induction-assisted FSW.
- In the field of external preheating sources, induction preheating during the dissimilar FSW between Inconel 718 and SS316L/AISI 204Cu has not been found in the available literature.
- The survey revealed very limited information regarding the dissimilar friction stir welding of Ni-based alloys and stainless steel. There is no published research on the corrosion behavior of joints made of dissimilar friction stir welded Inconel 718 and SS316L.
- No systematic study is focused on investigating the degradation of tungsten tools during FSW of Inconel 718 and stainless steel. There is a need for targeted investigations on tool wear and degradation to evaluate the effectiveness of tool materials and designs.

……..*……..*…….

CHAPTER 3

3. Methodology

3.1 Introduction

This chapter explains the experimental procedures, methods, and mathematical models followed during the thesis work. In accordance with each objective, it provides the sequence in which work has been performed. The first section explains the experimental details include: material selection and experimental setup. The second section contains detailed information about the test and analysis part of the microstructure, mechanical, and corrosion analysis. The later section explains the mathematical model to study the temperature distribution and stress evaluation during the dissimilar FSW.

3.2 Experimental and testing procedures

3.2.1 Material selection

In this experimental work, 3 mm thick metal sheets of Inconel 718, austenitic stainless steel AISI 204Cu, and 316L were used. The average chemical composition (in wt.%) and mechanical properties of the material mentioned by the manufacturer are presented in Table 3.1. The received base materials were examined with the Energy Dispersive X-Ray Spectroscopy (EDS) and tensile testing to confirm the material properties. In this experimental work, three different high-strength materials were chosen to demonstrate the reliability of the FSW and I-FSW processes. The reason for the selection of the Inconel 718 alloy was its wide range of industrial applications. This alloy is commonly used in the power generation, petrochemical industries, marine industries, aerospace industries, and cryogenic industries because of its high corrosion resident, high toughness, and excellent mechanical properties in the working range of −250 ◦C to 720 ◦C, makes highly demandable in industries [30]. The presence of gamma prime (ϒ’-Ni_3Al, Ni_3Ti and Ni_3(Ti, Al)) and gamma double prime (ϒ”-Ni_3Nb) in the Ni-based superalloy Inconel 718 make this alloy highly strengthened and corrosion resistance at elevated temperatures [11].

The joining of dissimilar materials is continuously demandable in manufacturing industries during the production of multi-component systems. Reducing material costs with flexible design considerations in industries is highly considerable. Therefore, two types of high-

strength materials were selected, one AISI 204Cu and another SS31L. Austenitic stainless steel AISI 204Cu is a Ni-free, low-cost, high-strength and moderate corrosion-resistant (Fe-Cr-Mn) material [12]. Due to the high cost of Ni, the use of the alternative substitution element manganese (Mn) with nitrogen (N) in austenitic stainless steel has found excellent mechanical properties [13]. The unique combination of excellent mechanical properties and good formability makes Inconel 718 and AISI 204Cu materials highly demandable in industries.

Similarly, the reason for selecting stainless steel 316L (SS316L) alloy is due to its numerous applications in the chemical, aerospace, oil, and nuclear industries because of its outstanding strength and good corrosion resistivity [15]. However, the dissimilar joining of IN718 alloy with the SS316L has been noted to achieve a flexible design with desirable properties and reduce the cost in nuclear power plants and aerospace industries [21,140].

3.2.2 Selection of tool material and design

The selection of FSW tool material/design was a challenging issue for the successful welding of high-strength/temperature alloys. During the FSW of high softening alloys, the temperature reaches above 900 ^{o}C; at this temperature, tool material must have outstanding characteristics such as high strength, some fracture toughness, and high fatigue life. Apart from the good mechanical properties at elevated temperatures, tool material must be resistant to chemical wear. In addition to the above properties, tool material should be cost-effective and easy availability [141]. The three primary classes of tool material: super abrasive tool material (ex. pcBN), refractory metals (ex. tungsten (W) and molybdenum (Mo) based) material, and superalloys tool material (Ni-based or Co-based) have been used from over the past decade. Out of the three main categories of tool materials, in this study, tungsten carbide-based (WC-10wt.%Co) tool materials were chosen for the FSW of Inconel 718 and stainless steel while taking into consideration the material properties, cost, and availability. The details of tool properties provided by the supplier are summarized in Table 3.2. The fabrication of the tool was based on the powder metallurgy process as per the supplier. The tool design was based on minimizing tool wear during the FSW process and maintaining constant weld quality. The heat generated during the FSW is directly proportional to the contact area of the tool surface and the workpiece. Liu et al. [23], Kaushik et al. [120] and Buffa et al. [128] reported that the use of a minimum diameter (20-25 mm) of the tool shoulder with tapered cylindrical pin geometry results in desirable microstructures in the weld, consequently improving the strength of the joint. In this experimental investigation, a cylindrical WC-10wt.%Co FSW tool having a flat

shoulder, with a diameter of 25 mm, containing a tapered cylindrical pin length of 2.7 mm with a root diameter of 7 mm and free end diameter of 5 mm, was selected in all the welding processes, as shown in Fig. 3.1.

Table 3.1 The nominal chemical composition (in wt.%) and physical properties of the used material.

Chemical composition (wt.%)											
Materials	Ni	Fe	Cr	Mn	Mo	Nb	Ti	Cu	N	Al	C
Inconel 718	52.2	19.1	18.8	-	3.4	5.8	1.1	-	-	0.5	0.05
AISI 204Cu	1.5	70.6	15.1	10.2	-	-	-	2.4	0.05	-	0.16
SS316L	9.5	69.7	17.7	0.4	2.0	-	-	-	0.1	-	0.03

Mechanical properties				
Materials	Tensile strength (MPa)	Yield Strength (MPa)	Elongation (%)	Hardness ($HV_{0.5}$)
Inconel 718	741	310	60	210
Annealed Inconel 718	948	455	33	260
AISI 204Cu	856	465	36	280
SS316L	688	289	70	195

Table 3.2 Properties of WC-Co tool material.

Properties	**Details**
Composition (wt.%)	Tungsten carbide/cobalt (WC-10wt.%Co)
Rupture Stress	3740 N/mm^2
Rockwell Hardness	81 HRC

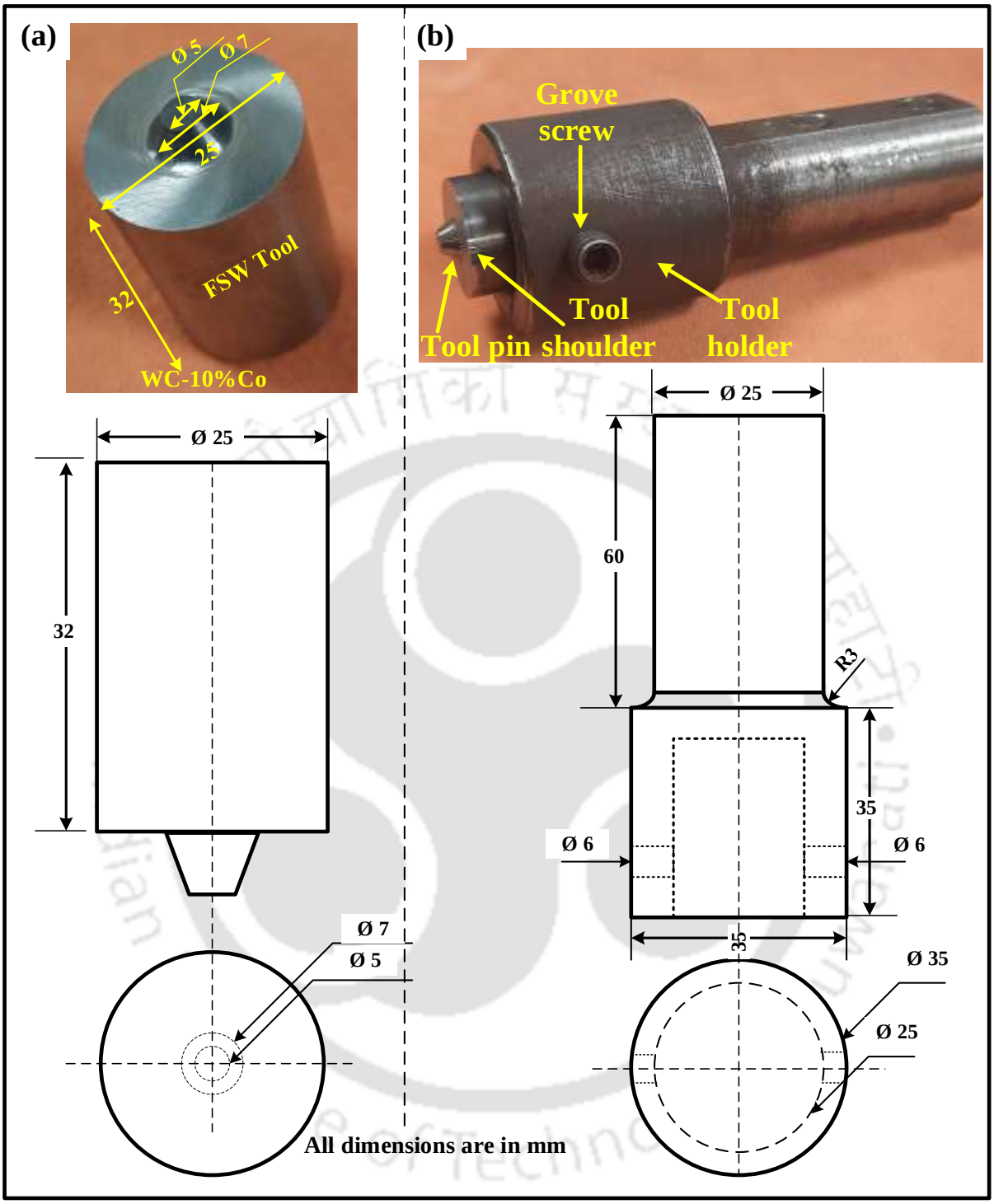

Fig. 3.1 FSW tool dimensions and tool holder dimensions.

3.2.3 Experimental setup

Welding experiments were performed on a modified 25 HP heavy-duty vertical milling machine (FSW machine) fitted with the auxiliary induction preheating system, as shown in Fig. 3.2. In order to deliver a maximum z force of 55–58 kN (working range) during welding, a hydraulic power pack system was installed. The spindle speed of this machine was in the range of 300 to 1800 rpm, and the traverse speed of the bed was 20 to 300 mm/s. A robust milling fixture was used to prevent the movement of the plates during the plunging and translational movement of the tool. The fixture was made of a low-carbon steel plate with centrally rectangular-shaped grooves (200 mm × 160 mm × 3 mm) that were secured with work-holding fixtures on the strain gauge-based force-dynamometer situated on the machine traverse table. A strain gauge-based force dynamometer connected with a strain data logger was used to measure the axial force with and without induction FSW. On the rectangular-shaped groove, a hardened steel back plate was used during the welding process to reduce the heat extraction from the weld line and hold a sufficient forging force. The horizontal clamp restricted the vertical movement of the plate. The design aimed to constrain the work plate's motion in vertical, horizontal, and traverse directions.

At the start of the process, the FSW tool was first fixed in the tool holder made up of high-tool steel with the help of a grove screw. The assembled tool with the tool holder was clamped in the arbor of the machine with the grove screw.

For the I-FSW setup, a high-frequency induction heating machine was mounted on the fixed vertical stand on the machine traverse table, as depicted in Fig. 3.2 The arrangement was such that there was no contact between the vertical stand and with traverse table. The maximum output power of the induction machine was 20 kW with a working range of 100 to 120 kHz. The pancake-type water-cooled induction heating coil made of copper material was used to preheat the workpiece. For cooling the heating coil, an external water supply arrangement was installed. The heating coil was placed 5 mm above the base plate and at a 20 mm distance from the FSW tool holder to the coil end edge in the direction of welding. As per fundamental electromagnetic induction heating law, the applied alternating current to the induction coil produces the electromagnetic field on the surface of the workpiece, which generates the eddy current that consequently heats the workpiece [85]. After the completion of the welding process, the workpiece was allowed to cool down at ambient temperature. All the experiments were conducted under normal atmospheric temperature and pressure. The positioning of

material on the AS and RS in the dissimilar welding was decided on the strength of the material. High-strength material (i.e., Inconel 718 or AISI 204Cu) was placed on the AS, whereas SS316L was placed on the RS in different welding conditions. Based on the previous investigations [116], positioning higher tensile strength material (i.e., stainless steel) on the advancing side gives good strength.

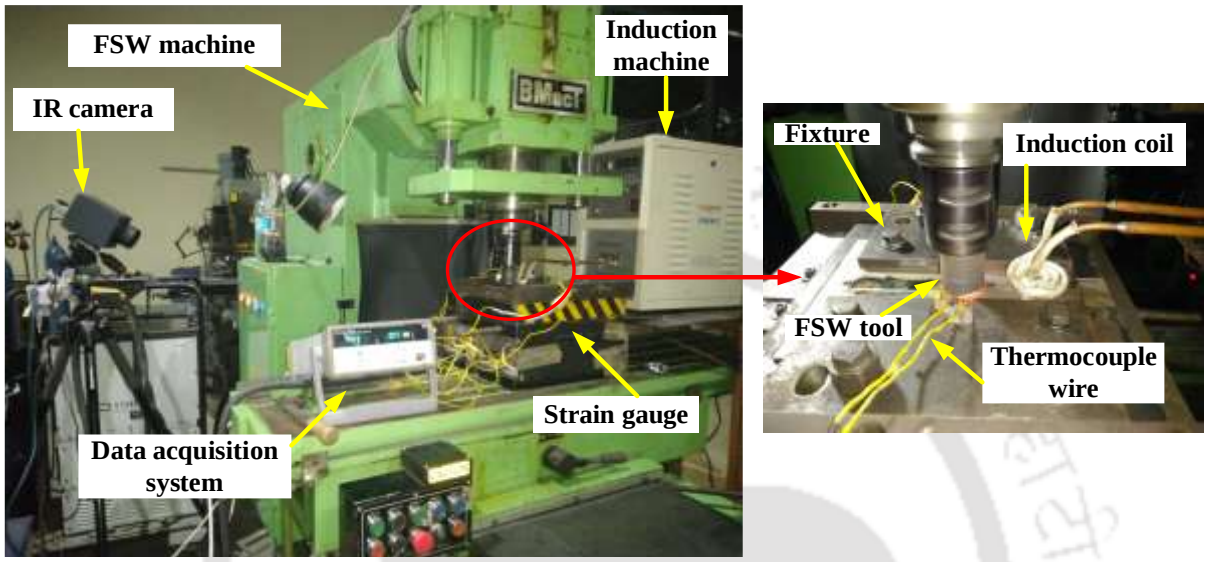

Fig. 3.2 Induction-assisted hybrid FSW experimental setup.

3.3 Test and analysis

3.3.1 Microstructural characterization

Investigation of the microstructure of the weld joints and comparative study with the base metal is significant to understand the microstructural evaluation of the FSW and I-FSW butt joints of the Ni-alloy and steel after the welding. The microstructure of a material influences its physical properties, which help to determine how the material performs in a given application. Different techniques described below were used to provide the chemical and physical information of the material with the sub-micron resolution.

In order to evaluate the microstructure of the weld joints, it is essential to prepare the test sample carefully. The sample preparation for microstructural examination started with selecting a representative sample of the materials, followed by sectioning, mounting, grinding, polishing, and etching steps, as per ASTM-E3. In this work, samples from the proper welded joint material were chosen for the grain size and general microstructural examination. After the selection of the proper welded joint material, test samples were carefully sectioned from

the weldments using wire electrical discharge machining, as shown in Fig. 3.3. After extraction of samples which are in a convenient size mounted in epoxy material under the cold mounting process to facilitate handling and polishing steps. Under the molding step, the cross-section of the weld was kept in the upper face for the grinding. Mechanical grinding was performed on the water-lubricated rotary abrasive wheels using an abrasive grit series from rough (200 grit) to finer (2500 grit) to provide a flat surface. The principle is that the material is removed from the surface using abrasive particles with progressively smaller grain sizes until the desired outcome is achieved. The final polishing step was performed by cloth polishing with alumina powder (0.05 µm) which removed the final thin layer of the deformed metal. After final polishing, kalling's reagent (2 g $Cucl_2$ + 40 ml CH_3OH + 35 ml HCL) for Inconel 718; 2% nital solution for AISI 204Cu; and 30 ml HCl + 10 ml HNO_3 + 20 ml glycerine for SS316L was used as an etchant for reveal microstructure and the constituent phases.

In addition, transmission electron microscopy (TEM) operated at 200 kV was used to study the morphology and microstructure of the nugget zone in detail. The sample preparation for the transmission electron microscopy (TEM) analysis was started by cutting thin slice specimens perpendicular to the weld direction from the weld nugget zone. The initial specimen size was less than 200 µm, obtained by the high-speed linear precision saw equipped with the diamond-wafering blade and then mechanically polished to less than 100 µm. Once the specimens were thinned to their final size, they were punched into a diameter of 3mm using a disc cutter for the TEM specimen holder. The final thinning of polished 3 mm diameter specimens was carried out with a Twin-jet electropolisher using a solution of Perchloric acid solution: Ethanol (1:9) at −20 °C and 30 V.

The characterization of etched welded specimens to examine microstructural features and fracture morphology analysis of weld cross-sections was performed using optical microscopy (OM) and scanning electron microscopy (SEM) equipped with energy-dispersive X-ray spectroscopy (EDS). The digital microscope was used to capture the macro-structural images. After taking the microstructure images, the grain size was measured as per ASTM E112-13 standard using the mean linear intercept (MLI) method in the 'ImajeJ' analyzer software. The presence of external elements due to tool wear during the welding and phase identification in the weld zone was studied using x-ray diffraction (XRD) with Cu-Kα radiation. The scan rate and range used in this work were 0.5 ^{o}/min and 25^{o} to 95^{o}, respectively. Moreover, the

compositions of the passive film formed during the corrosion test on the FSW/I-FSW samples were analyzed by X-ray photoelectron spectroscopy (XPS) (PHI5000 Versaprobe system).

3.3.2 Mechanical characterization

Mechanical testing or engineering test of the welded sample was performed to determine the mechanical properties of the joint, such as strength, ductility, hardness and toughness were evaluated at ambient temperature. In this experimental work, the samples were extracted from the properly welded joint (smooth top welded surface) for mechanical testing in the traverse direction of the weld line.

To measure the tensile properties of weld joints, sub-sized transverse tensile samples were extracted from the welded joint according to the ASTM E8/8M using wire electric discharge machining (W-EDM), as shown in Fig. 3.3 Tensile tests were performed on the Instron 8801 universal testing machine at a cross-head speed of 1 mm/min at room temperature. The test was also conducted for the base metal to assess and compare the strength of the weld joints.

To test the impact strength of the weld joints and base metal, V-notch Charpy sub-sized specimens were extracted from the welded plate according to the ASTM E23 standard. The V-notch was positioned in the center of the weld to ensure it struck the weld nugget zone. Impact testing was performed at room temperature using a universal impact tester.

The microhardness distribution along the transverse cross-section of the weldment was measured with a Vickers pyramidal indenter using a standard load of 0.5 kgf and a dwell time of 20 sec, as per ASTM-E92-17 stander. Three lines from the top cross-section were marked to measure the variation of microhardness of the joints. Three lines were marked from the top of the cross-section at equal distances to measure the microhardness variation on the joint's cross-section.

After the mechanical tests, the fractured tensile and toughness samples were characterized using scanning electron microscopy to examine the fracture mode. Three trials of the tensile and toughness tests in each welding parameter were established to confirm the repeatability and consistency of the results.

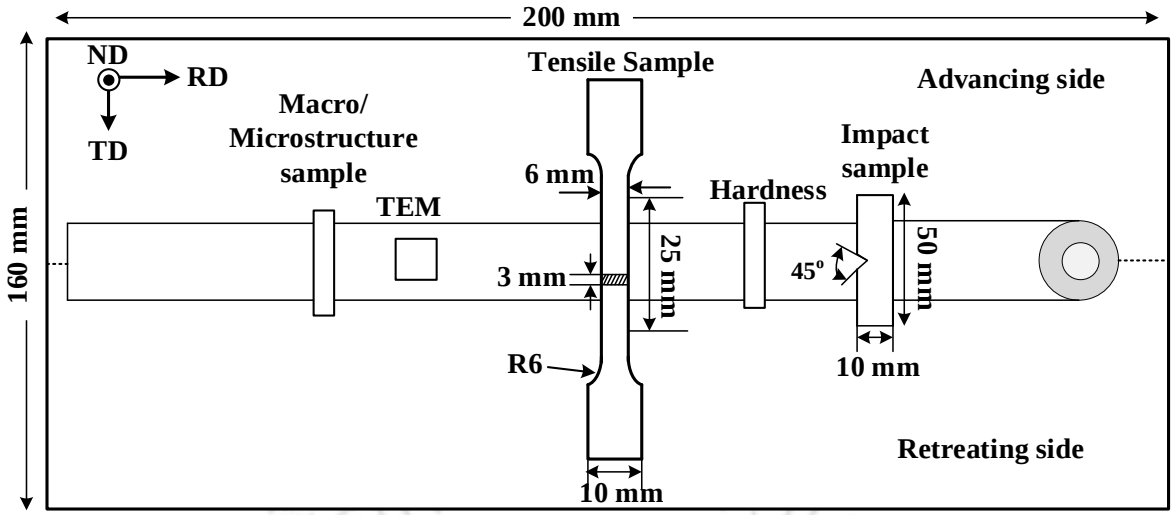

Fig. 3.3 Schematic diagram of extraction of testing specimens.

3.4 Corrosion analysis

In this experimental work, the electrochemical studies on the weldments obtained with and without the induction-assisted FSW of the Inconel 718 with stainless steel 316L along with the base metal (BM) were conducted in a conventional three-electrode cell arrangement. Before performing the corrosion test, all samples were prepared to mirror-polished surfaces with SiC paper up to 2000 grits. The experiments were performed in a designed corrosion cell (300 mL) which had a facility for connecting the working electrode, reference electrode, and counter electrode, as shown in Fig. 3.4. In three-electrode systems, the platinum wire as a counter electrode (cathode), the saturated calomel electrode (SCE) as a reference electrode and weld specimens along with BM (uncovered area of 1.32 cm^2) were used as working electrodes (anode). The electrochemical cell was filled with all the electrodes, and the working electrode was exposed to a solution medium at 22 ^oC ± 5 °C. In this electrochemical experiment work, two different solution media, 3.5 wt.% NaCl and 1 M HCl were used. Before performing the potentiodynamic polarization (PDP) and electrochemical impedance spectroscopy (EIS), the open circuit potential (OCP) of the working electrodes was recorded for 60 minutes. The experiment was conducted with a potentiostat/galvanostat instrument (Autolab - PGSTAT302N). The potential was scanned under ± 250 mV (vs. Ecorr) with a scan rate of 1 mV/s. Each experiment was run at least three times to ensure that electrochemical measurements were accurate.

An immersion test was also carried out in 1M HCl and 3.5 wt.% NaCl at room temperature for 240 h (10 days) to study corrosion morphology and weight reduction measurements. The morphology of the corroded samples was examined using optical microscopy. Micro-balance with great precision (0.1 mg) was used to weigh the samples before and after the immersion test. After the immersion test, all the samples were cleaned as per the ASTM G1 standard with acetone and distilled water. The following relation was used to compute the weight loss after 240 hours.

$$w = w_o - w_1 \tag{1}$$

where w is the weight loss in g, w_o is the initial weight before the test in g, and w_1 is the weight after the corrosion test in g.

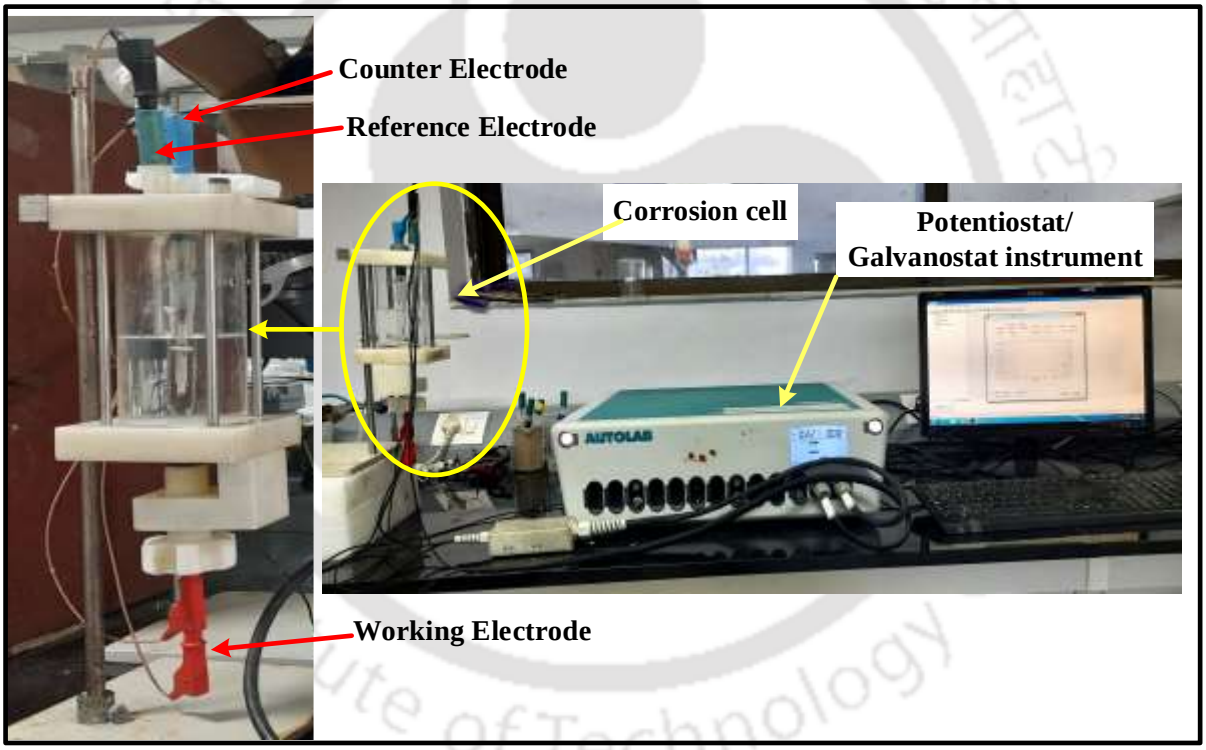

Fig. 3.4 Experimental setup for measurement of corrosion test.

The information mentioned above broadly describes the experimental procedures,including the selection of materials, tool materials, FSW and induction-assisted FSW machine setup, backing plate material, FSW fixture, and corrosion test setup. The specifications of the various machines used in this experimental work are summarized in Appendix A.

……..*……..*……

CHAPTER 4

4. FSW of Inconel-718 Alloy Using a Tungsten Carbide Tool

4.1 Introduction

In this chapter, the experiment has been conducted to join similar Ni-based superalloy (Inconel 718) plates by the FSW process using a tungsten carbide tool. The primary interest is joining similar Inconel 718 plates and investigating the effect of varying process parameters, such as traverse and rotational speeds, on mechanical and microstructural properties. In addition, the effect of process parameters on the axial force, weldments' thermal history, and toughness properties have been studied. The optimum welding parameters have been determined with experimental trials, leading to successful joining with high strength and no defects.

4.2 Materials and methodology

In this study, Inconel 718 sheets of dimensions 200 mm × 80 mm × 3 mm in the hot rolled condition were used to perform butt joints. The average measured values of the chemical composition along with the mechanical properties of Inconel 718, are discussed in section 3.2.2. A cylindrical tungsten carbide-based (WC-10wt.%Co) FSW tool with a tapered pin was used in the present experimental investigation. The details of the tool properties and its dimensions and experimental setup with the working principle are discussed in section 3.2.3. Before welding, the joining edges of the sheets were prepared as a right-angle butt joint, and then the sheets were clamped onto a rigid fixture with a backing plate to keep joint edges fixed.

Initially, the experiment was performed at a constant tool rotational speed of 300 rpm with varying traverse speeds from 40 mm/min to 140 mm/min to optimize the traverse speed. After fixing a medium traverse speed of 90 mm/min at which a smooth weld surface without defect was observed, the experiment was performed with varying rotational speeds varied from 300 pm to 600 rpm. Based on the preliminary studies and published literature [115,142]. Table 4.1 displays the six sets of welding operating parameters selected for this investigation to determine the optimal FSW parameters. The plunge depth of the shoulder was kept 0.2 mm, and the tool tilt angle was 2^{o}, fixed for all sets of experiments.

Table 4.1 Welding parameters and their effect on weld quality.

Weld no.	Tool Rotational speed (rpm)	Traverse speed (mm/min)	Maximum tensile strength (MPa)	Weld surface quality
Weld 1	300	40	654	Poor
Weld 2	300	70	701	Medium
Weld 3	300	90	733	Excellent
Weld 4	300	140	229	Poor
Weld 5	450	90	233	Poor
Weld 6	600	90	30	Poor

After welding, test samples were cut in the transverse direction, using wire electrical discharge machining (Wire EDM) (JK-machine EC032) for mechanical tests and metallographic analysis. The details of the methodology for metallographic and mechanical tests are explained in section 3.3. The transient temperature distribution of the weld samples during FSW was measured by an Agilent data acquisition system using K-type thermocouples. The thermocouple wire positions on the welding specimens are shown in Fig. 4.1. The transient temperature distribution on the advancing side (AS) and retreating side (RS) during the welding process were recorded using four K-type thermocouples (i.e., TC1, TC2, TC3, and TC4) and a Data Acquisition System. Thermocouples were spot-welded onto either side of the weld line, two at RS (TC1 and TC2) and the other two at AS (TC3 and TC4) on the upper surface of the sheet.

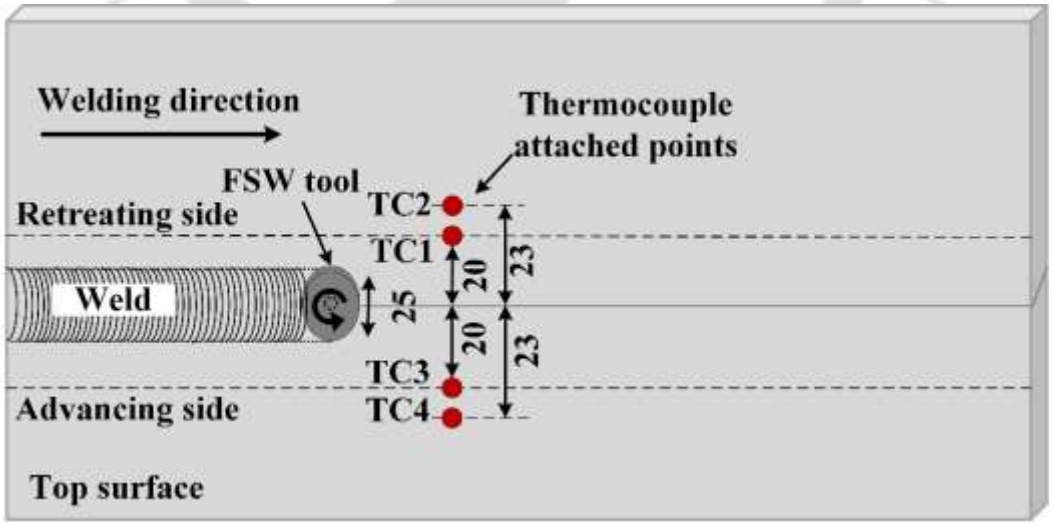

Fig. 4.1 Position of thermocouples for determining transient temperature distribution during FSW of Inconel 718.

4.3. Results and discussion

Characterization results of friction stir welded joints are discussed in the following subsections.

4.3.1 Analysis of axial force

Among the heat generation process parameters, the axial force during welding significantly affects frictional heat generation due to contact between the tool shoulder and the workpiece. The axial force required during FSW of Inconel 718 for welding the sample Weld 3 at 300 rpm with 90 mm/min is mentioned in Fig. 4.2 (a), which contains the plunging zone, the dwell period zone, and the welding zone [143]. In the initial period, the pin of the tool touches the surface of the workpiece until the surface of the shoulder gets into contact with the workpiece. During this period, maximum axial forces are generated in the tool, leading to maximum temperature generation in the workpiece. After this, the tool remains rotating in the plunge position without any movement for 10 sec, known as the dwell period. The softening of the material during this period results in a small reduction in force values. Following this, the tool moves with an almost constant axial force in the welding period. The axial force generated during the welding period was used to calculate the average axial force. An average axial force of 28 kN was recorded during the welding period for the sample Weld 3. The variation in the axial force curve was observed during the welding period of ± 1.4 kN. The fluctuation of axial force during the welding stage was also observed by Tiwari et al. [144] in their force measurements study.

In the same way for other samples, the axial forces were calculated. Figs 4.2 (b-c) shows the variation of axial force with the welding parameters. During the study of axial force at constant rotational speed (300 rpm), it was noticed that the maximum axial force was observed at high traverse speed (140 mm/min) and it was minimum at low traverse speed (40 mm/min), as shown in Fig. 4.2 (b). The increase in traverse speeds results in the reduction of the tool stirring time and frictional heat input, which leads to less thermal softening and flow of material. Furthermore, it resulted in an increment of the average axial force.

Similarly, from Fig. 4.2 (c), the variation of axial force with the increase of rotational speed was observed. The increase in rotational speed results in high frictional heat input, which finally leads to the thermal softening of the material near the tool, which ultimately reduces the axial force. The influence of the variation of welding parameters resulted in temperature variation and a change in axial forces. The average axial force increases to 20.5% with an increase in

traverse speed from 40 to 140 mm/min. Similarly, the average axial force decreased to 7.8% with an increase in rotational speed from 300 to 600 rpm. Pankaj et al. [113] and Parida et al. [145] also mentioned the effect of welding parameters on the axial force during FSW in their work.

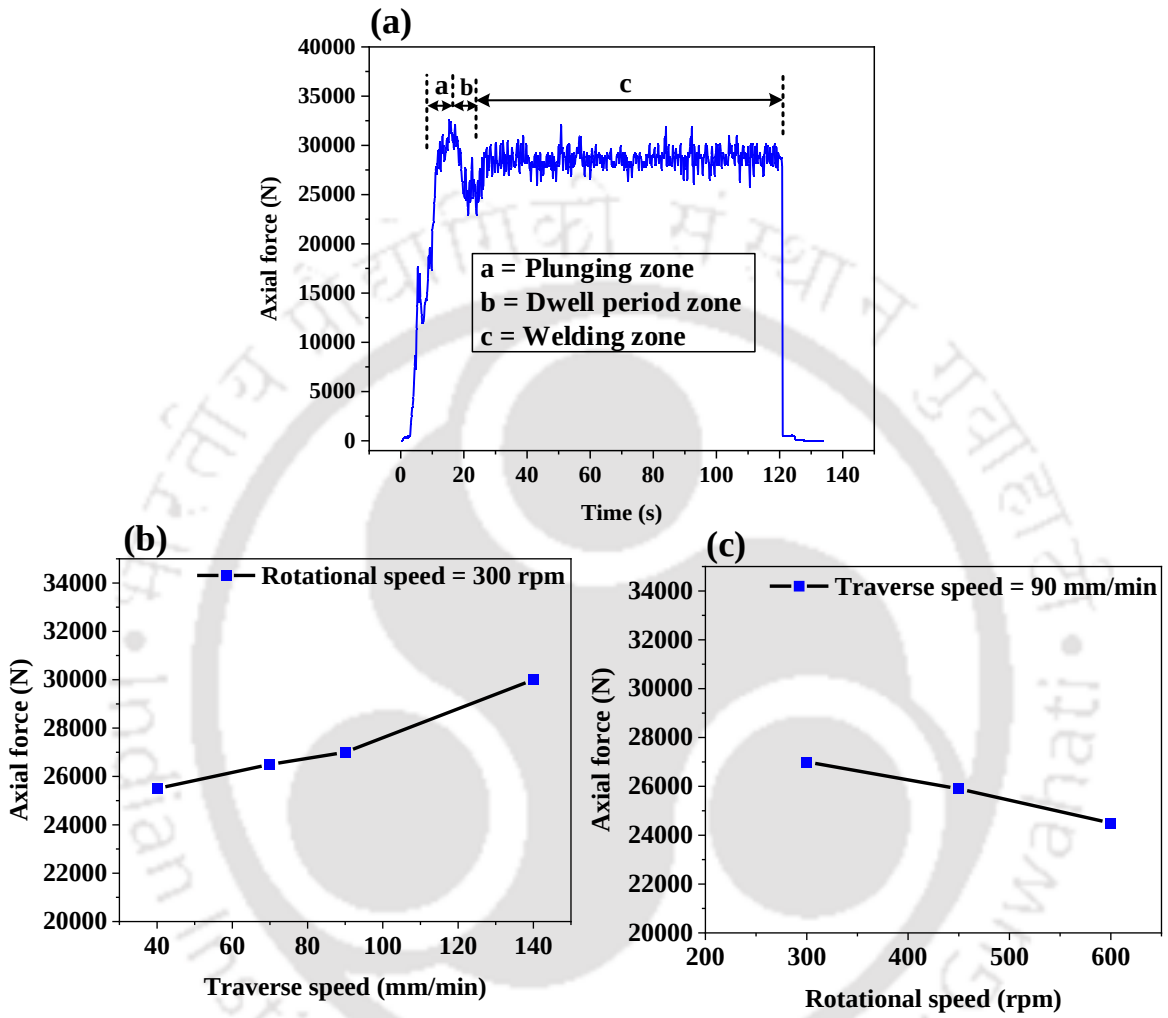

Fig. 4.2 (a) Generated axial force during FSW of Weld 3, and axial force variation with (b) traverse speed and (c) rotational speed.

4.3.2 Thermal history

The thermal history has a significant effect on both the mechanical and microstructural characteristics of FS-welded specimens**.** The variation of the transient temperature profile in AS and RS for the welded sample Weld 3 is shown in Figs. 4.3 (a-b). During welding, the peak temperatures attained at different thermocouple positions both on the AS and RS for different parameters are shown in Fig. 4.3 (c).

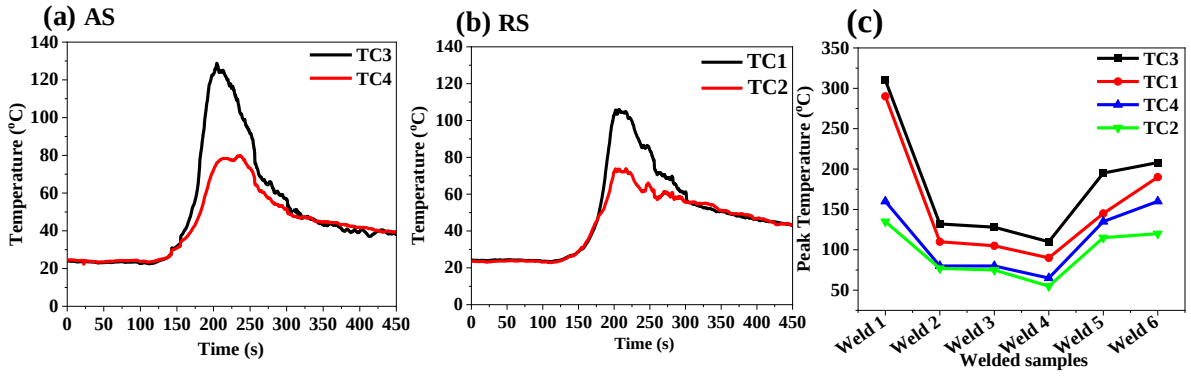

Fig. 4.3 Temperature distribution during FSW of sample Weld 3 in (a) AS and (b) RS, and (c) variation of peak temperature at varying welding parameters.

When the rotating tool approaches the thermocouple locations, the temperature at that position rapidly rises to its peak values, followed by a gradual decrease of temperature with time as the FSW tool moves away from the thermocouple locations.

The peak temperature on the advancing side (AS) of every weld sample was slightly more than the retreating side (RS). For example, in a welded sample Weld 3, the $T_{AS} > T_{RS}$ and the difference between the AS and RS temperature of TC3 & TC1, respectively, were TC3-TC1~23.2^{o}C, as shown in Fig. 4.3. The reason for the AS being higher temperature is mainly due to the deformation and flow of materials begins, which usually experience more friction in the AS. The direction vector of the peripheral velocity of the rotating tool coincides with the traverse velocity vector, leading to the generation of extra frictional heat. [146,147]. The process parameters significantly influence the variation of peak temperature during welding [145]. At a constant rotational speed of 300 rpm, the peak temperature of the weld sample decreases as the traverse speed increases, as shown in Fig. 4.3 (c). It is also observed that at a constant traverse speed of 90 mm/min, the peak temperature of the weld sample decreases as the rotational speed decreases. The increase in temperature at a low traverse speed is caused by a high rate of heat input and more string time of the material, whereas a high rotational speed creates higher frictional heat generation [43].

The measurement of temperature in the contact region of the tool and workpiece during FSW is challenging, using a thermocouple attachment. For this reason, an IR camera was used to measure the tool & workpiece contact region thermal history. The temperature distribution of the lowest traverse speeds (i.e., Weld 1) and highest traverse speeds (i.e., Weld 4) are shown in Fig. 4.4.

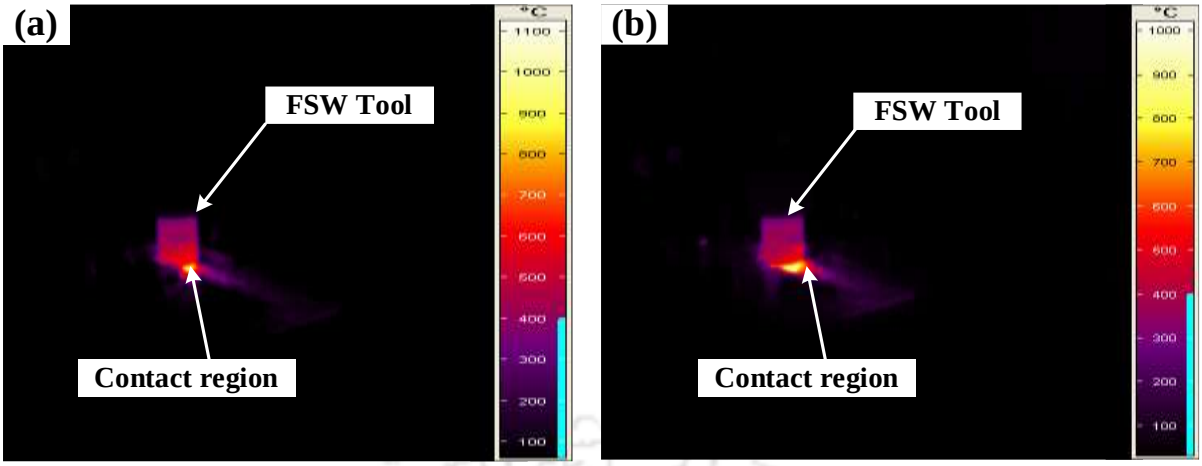

Fig. 4.4 Temperature distribution of (a) lowest (i.e., Weld 1) and (b) highest (i.e., Weld 4) traverse speed using IR Camera.

The peak temperature between the FSW tool & workpiece contact region of the weld sample Weld 1 (i.e., 40 mm/min) and Weld 4 (i.e., 140 mm/min) are around 1100 ºC and 1000 ºC, respectively. The measured contact temperature value was similar to the measured highest temperature in the weld nugget by Huang et al. [146], as shown in Fig. 4.4. It can be observed that the tool traverse speed has a significant effect on the temperature distribution during the FSW of Inconel 718 alloy.

4.3.3 Macro and microstructural characterizations

The top surface appearance of FS welded butt joints of Inconel 718 alloy sheets for different welding parameters are shown in Fig. 4.5. The proper selection of welding parameters is necessary to obtain a defect-free top surface. The top surfaces of most welded samples, except for the welded sample Weld 3 (welded at 300 rpm and 90 mm/min), have surface defects. The welded sample Weld 3 exhibited an excellent weld surface quality without any weld defects, like wormholes or cracks. From the current working ranges of FSW parameters, the tool rotational speed (i.e., at 300 rpm) with 90 mm/s traverse speed produced better weld surface quality. However, the welded samples Weld 5 and Weld 6 exhibited poor surface quality at a rotational speed higher than 300 rpm. The surface quality also deteriorated with lower traverse speed (i.e., 40 mm/min), as shown in Fig. 4.5. Weld 2 revealed moderate surface quality because a small defect appeared at the end of the weld line. In all-welded samples, a small volume of flash was evident, and a small weld thickness reduction was observed due to the combined effect of high axial force and plunge depth.

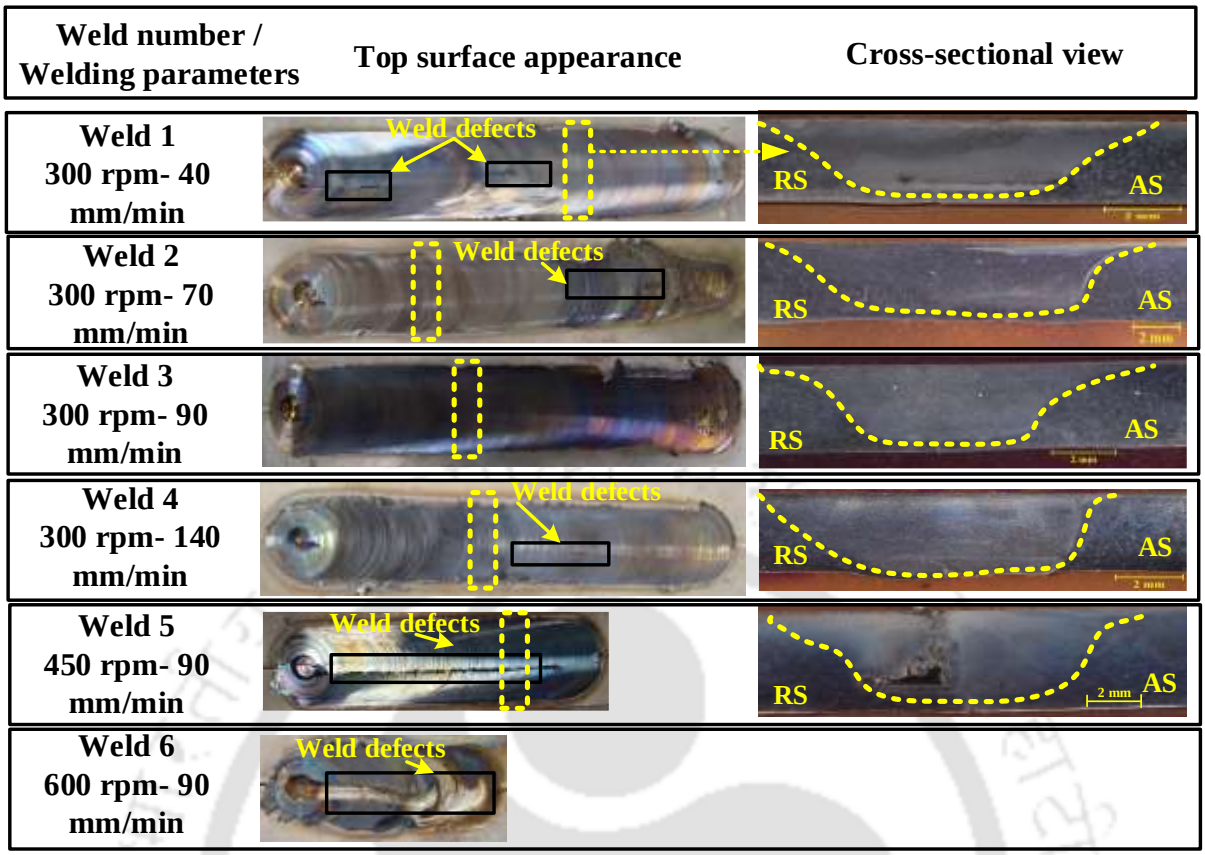

Fig. 4.5 Weld appearance and its cross-sectional view for different FSW parameters.

From the optical macrographs of low rotational speed (i.e., 300 rpm) welded samples (i.e., Weld 1, Weld 2, Weld 3, Weld 4 and Weld 5), the shape of the stir zone is a typical basin-shaped morphology produced. Song et al. [142] found similar morphology in their study of joining Inconel alloy by the FSW due to the contact material's intensive plastic deformation and the taper FSW tool pin, as shown in Fig. 4.5. During the welding, at a rotational speed of 300 rpm with traverse speeds 70, 90, and 140 mm/min, the depth of the stir zone from the top surface was almost the same as the material thickness. Some welded samples like Weld 1 and Weld 5 showed unwelded root notch and wormhole defects at low traverse speed (i.e., 40 mm/min) and high rotational speed (i.e., 450 rpm), respectively. In the welded sample Weld 5, a large wormhole was noticed at a high rpm of 450 rpm. The presence of defects such as a wormhole or large cavity was found due to abnormal mixing or insufficient plastic flow of materials. With a further increase in tool rotational speed (i.e., 600 rpm), the welded sample exhibited high flash with a large groove-like defect and high tool wear. The macrograph of Weld 6 could not be seen due to the presence of a large groove defect that produced an improper weld.

Ahmed et al. [115] reported that the macrograph view of welded Inconel 718 could be divided into four zones. A center of the weld known as the stir zone (SZ), adjacent to the stir zone, is the thermo-mechanically affected zone (TMAZ), beside it is the heat-affected zone (HAZ) and the rest part as a base material (BM). Figure 4.6 shows details of the optical macrographs of welded sample Weld 3, which was conducted at a traverse speed of 90 mm/min. Figure 4.6 (a) shows the cross-sectional view of welded sample Weld 3 in which the presence of a varied zone is observed, as highlighted in Figs. 4.6 (b-f). The difference in the grain structure and the material flow pattern allows for observing the presence of different microstructural zones.

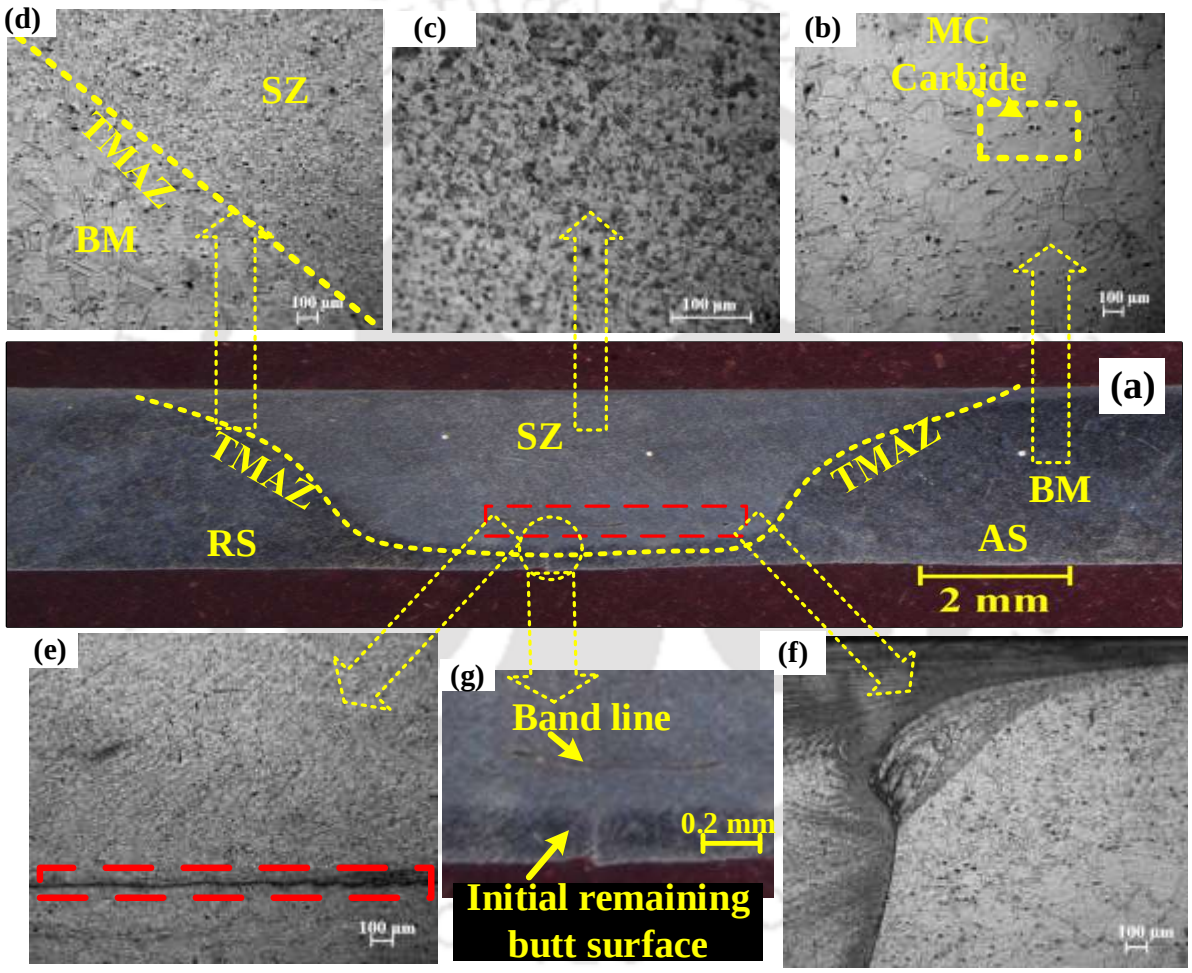

Fig. 4.6 Microscopic views and material flow behaviour in the weld sample number Weld 3 (a) cross-sectional view, (b) BM, (c) SZ, (d) TMAZ, (e) band of dark shade, (f) flow pattern view and (g) magnified view of initial remaining butt surface.

The effect of high temperature and stirring deformation resulted in dynamic recrystallization in the SZ. A small region of TMAZ was found at the interface between the BM and SZ, as shown in Fig. 4.6 (d). Grain growth near the TMAZ was not observed, resulting in the absence of the HAZs, which was a similar result reported by Song et al. [40]. In the TMAZ zone, the

deformed and slightly smaller grain microstructure than the BM was formed due to partial recrystallization and recovery. Figure 4.6 (e) shows a band of dark shade at the bottom of the SZ, which starts from the AS. Previous investigations [37,40] showed that tool wear in the SZ formed a band structure. Figure 4.6 (f) indicates the flow pattern of material near the bottom of the SZ. In the AS region, the high frictional heat generation observed from the temperature distribution graph caused high material deformation, resulting in a disruptive material flow pattern. A similar result was reported by Chen et al. [148] regarding the asymmetrical metal flow behaviour in AS and RS.

For the present range of operating parameters (at 300 rpm and 70 to 140 mm/min traverse speed), the presence of weld defects like large voids and tunnel defects was not observed except for the initial remaining butt surface at the bottom of the SZ, as shown in Fig. 4.6 (g). Sato et al. [42] also found a similar remaining butt surface during the FSW of Inconel 600. The grain size distribution in the BM was observed in the range of 23-158 µm, while the grain size range in the SZ and the TMAZ of the welded sample Weld 3 were 5-35 µm and 15-55 µm, respectively. Because of the material's dynamic recrystallization and stirring action, the average grain size of the SZ and TMAZ obtained was 10.38 µm and 18.5 µm, respectively, compared to the BM, where the average grain size was 74 µm. Figure 4.7 shows the microstructures of SZs obtained at different welding parameters that were analyzed by optical microscopy.

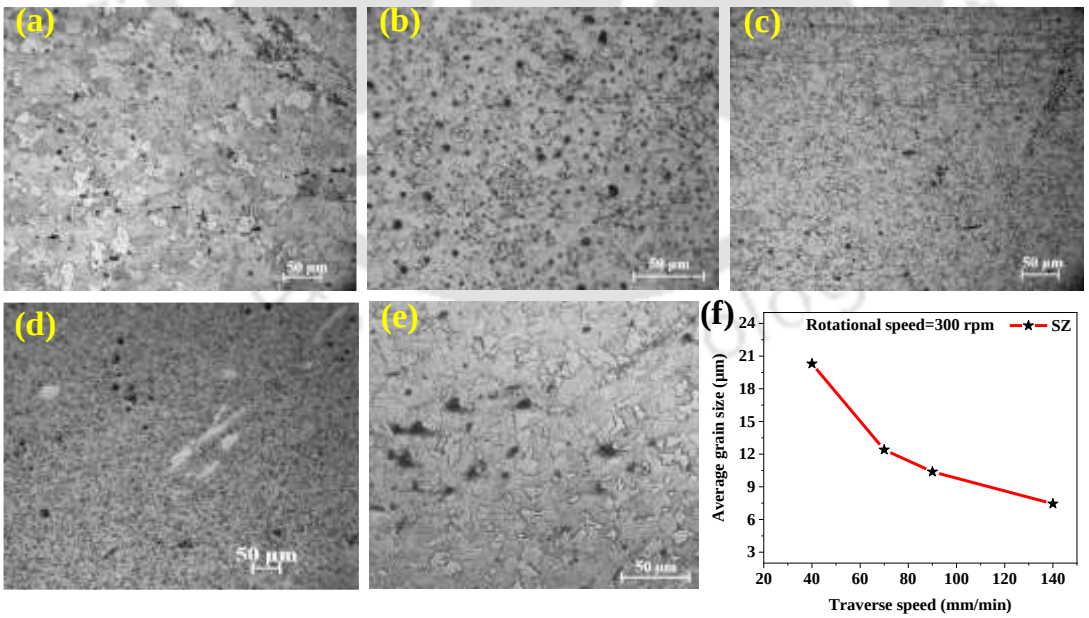

Fig. 4.7 Optical microstructural images of SZs of the welded samples (a) Weld 1 (b) Weld 2 (c) Weld 3 (d) Weld 4 (e) Weld 5 and (f) variation of grain size in SZ at different traverse speed.

Both rotational and traverse speeds have a significant effect on grain size refinement. With increasing traverse speed, the grain size decreases, and in all cases, the grain size is considerably smaller than the BM. The grain size variation obtained in the SZ is consistent with the published literature [115,142]. From Fig. 4.7, the presence of MC-type carbide particles in the SZ, similar to those at the BM, was also observed in all the welded samples. The size of these particles was more refined than the base material carbide particles. The measured temperature near the SZ was around 1000 ^{o}C, sufficient for the recrystallization of the base material grain. High grain refinement in the SZ was observed due to high heat input and strain rate during the FSW [149].

From Fig. 4.7 (d), the average grain size at high traverse speed (140 mm/min) was observed finest (i.e., 6.7 µm) due to relatively lower heat input and high cooling rate. The average grain size (i.e., 20 µm) distribution in the SZ at a rotational speed of 450 rpm and 90 mm/min traverse speed is shown in Fig. 4.7 (e). The SZ grain size and carbide particles were comparatively more considerable in high rotational speed than the other welding parameters observed. After fixing the tool rotational speed (i.e., 300 rpm), the average grain size variation in the SZ with varying traverse speed is shown in Fig. 4.7 (f).

The Field Emission Scanning Electron Microscope (FESEM) micrographs and Energy-Dispersive X-ray Spectroscopy (EDS) analysis results are shown in Fig. 4.8.

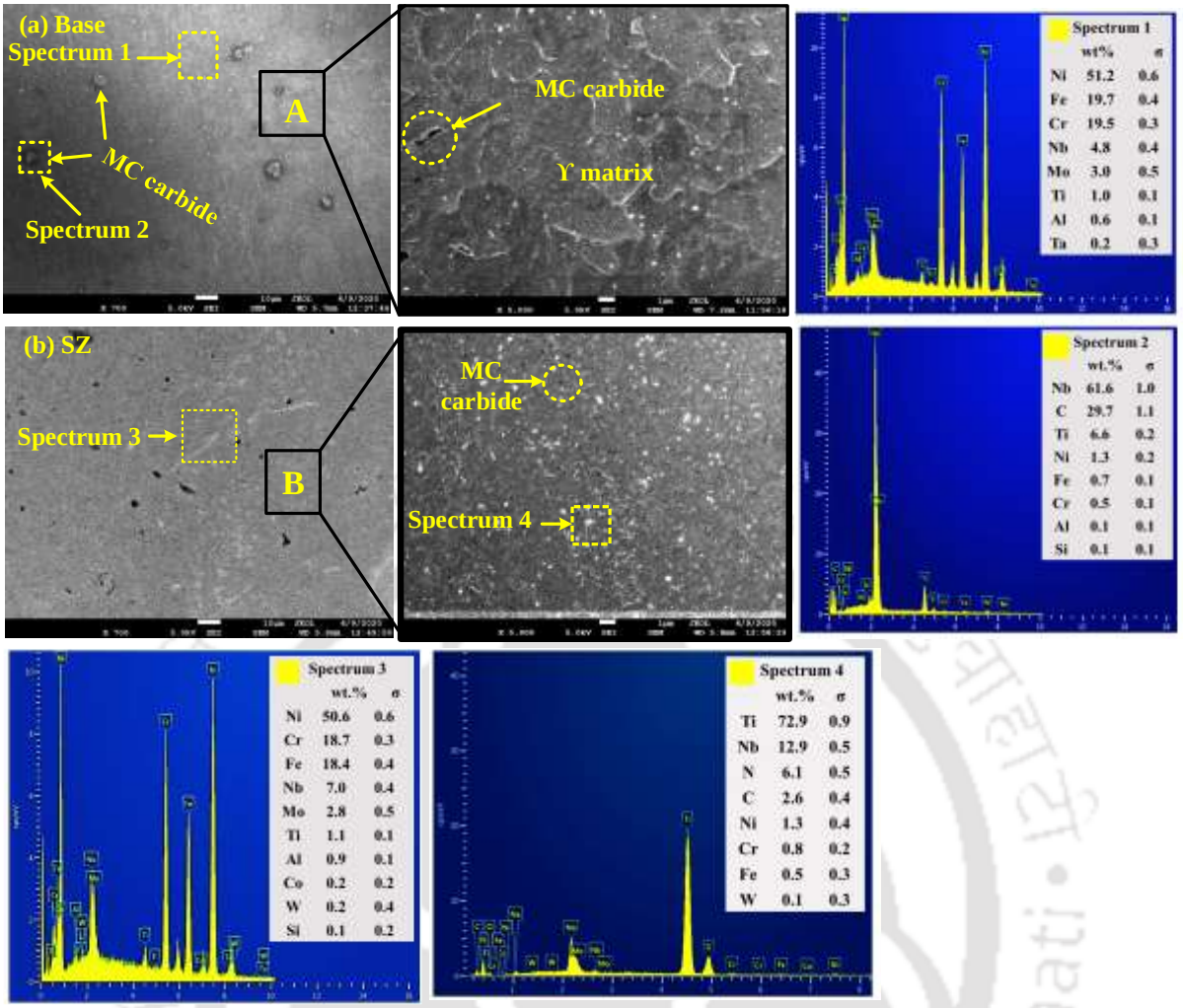

Fig. 4.8 FESEM micrograph and EDS analysis of Weld 3 at (a) BM region and (b) SZ region.

In the present investigation, the presence of MC carbides was observed in the BM and SZ of the Weld 3, as shown in Fig. 4.8 (a) and the magnified view of Fig. 4.8 (b), respectively. The carbide particles and some external elements were also observed from the EDS analysis. Magnified SEM images of regions A and B of BM and SZ, respectively, are shown in Fig. 4.8. The size of the carbide particle in the SZ was found fine and uniformly distributed in a range of 2 to 5 µm compared to the large carbide particle in a range of 5-25 µm in the BM. EDS spectrums 1 and 2 of the BM reveal the basic elements of Inconel 718 and a high percentage of Nb elements, respectively. The EDS spectrum 3 of the stir zone depicts the presence of W and Co elements in the SZ, which confirm the occurrence of wear of the tungsten carbide tool during the FSW of Inconel 718. Song and Nakata [40] also reported similar results for high tool wear during the FSW of a Ni-alloy. The presence of fine (Ti, Nb)C-type carbide observed in the SZ, which has a maximum amount (i.e., wt.%72) of Ti observed as shown in spectrum 4. The random distribution of the fine metallic carbide particles such as NbC and (Ti, Nb)C in

the grain and at the grain boundaries were observed in the magnified SEM image of SZ, as shown in Fig. 4.8 (b). According to some researchers [150], the discontinuous presence of carbide particles along the grain boundaries will hinder grain boundary cracking in deformation conditions.

The TEM study also observed the presence of carbide phases in the SZ. The bright-field TEM and selected area electron diffraction (SEAD) patterns of SZ of the Weld 3 are shown in Figs 4.9 (a-c). The presence of low-temperature carbides such as MC and $M_{23}C_6$ at the grain boundaries with average sizes of 40 nm was observed. $M_{23}C_6$ carbides form in the temperature range 760°C to 980°C, which mainly consists of Cr and C particles. Fig. 4.9 (d) shows the GATAN graph revealing the d spacing of the selected area of the high magnification TEM image (Fig. 4.9 (c)) is ~0.245 nm. Furthermore, the SAED patterns of the selected area show a diffraction ring pattern indicating crystalline nature with a face-centered cubic structure having (111), (110), (220), and (200) planes with the d-spacing value 2.082, 2.052, 1.82 and 1.804 Å, respectively, which is matched with the value found in the analysis of XRD.

The presence of niobium and titanium reach carbide particles in the nickel-chromium matrix affected the mechanical properties, such as the increase of yield and tensile strength of the welded sample and the increase of hardness in the SZ [42].

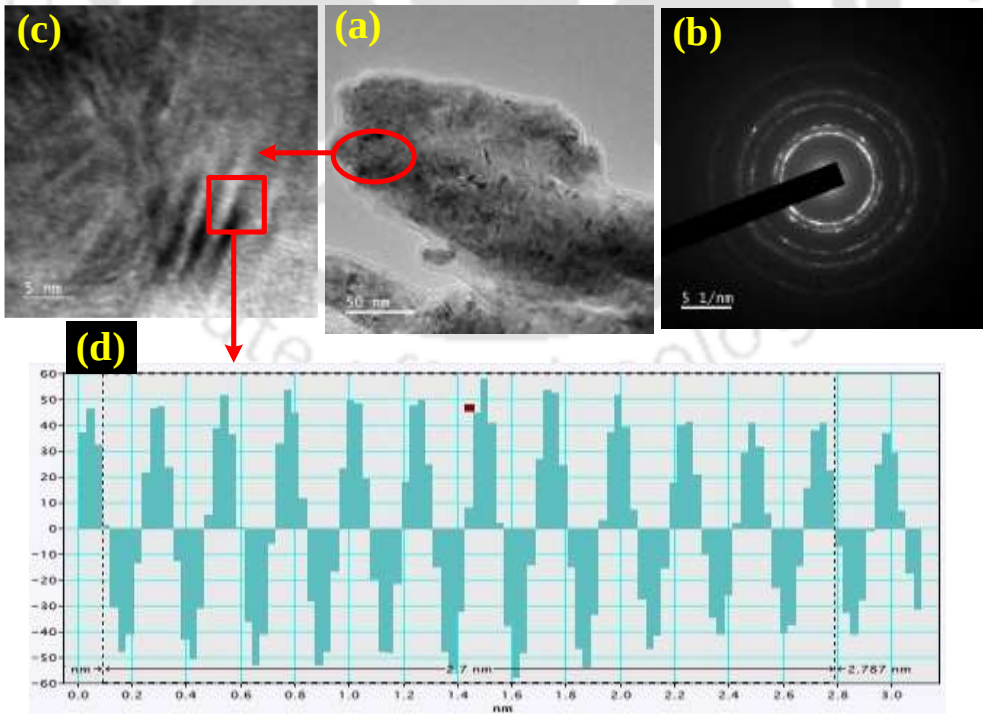

Fig. 4.9 (a) TEM image, (b) SAED pattern of SZ of the Weld 3, (c) high magnification TEM image and (d) GATAN graph for d-spacing.

4.3.4 XRD analysis

To examine the different phases, XRD analysis of the base metal (i.e., Inconel 718) and the Weld 3 was performed, which is shown in Fig. 4.10.

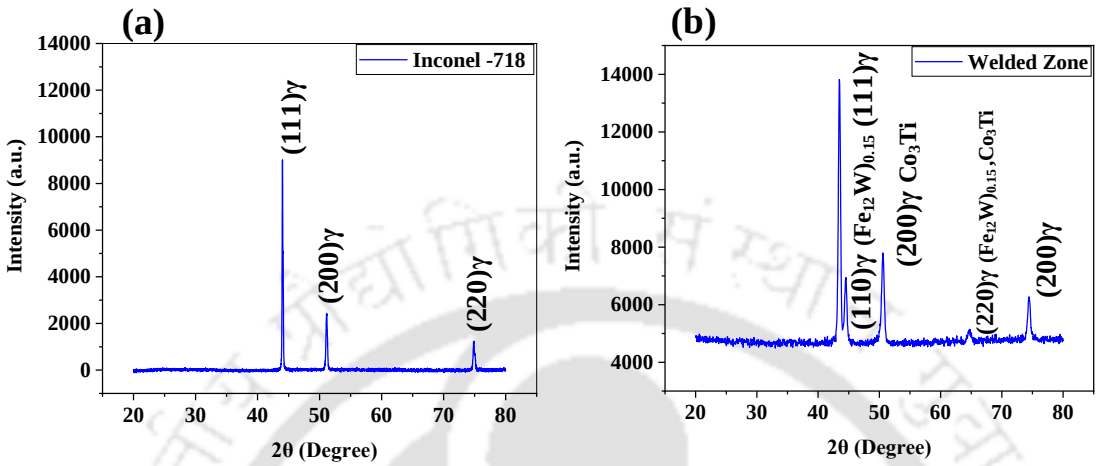

Fig. 4.10 XRD analysis of (a) Inconel 718 and (b) welded zone of sample Weld 3.

The base metal diffraction pattern exhibited only the austenitic ϒ-Ni matrix, as shown in Fig. 4.10 (a). In the XRD patterns of the SZ of the welded sample Weld 3, apart from austenitic ϒ-Ni matrix peaks, a clear indication of other major and minor peaks was found, shown in Fig. 4.10 (b). The presence of $(Fe_{12}W)_{0.15}$ and Co_3Ti phases were observed in the SZ of the sample Weld 3 at angles of $2\theta = 45^o$ and 65^o, respectively. The $(Fe_{12}W)0.15$ and Co_3Ti phases have an fcc structure with a lattice parameter a = 2.874 Å and a = 3.6034 Å, respectively. Thus, it confirmed the presence of W (Tungsten) and Co (Cobalt) elements in the SZ, proving that WC-Co tool wearing occurred during the FSW of Inconel 718. The presence of these elements has some advantageous effects on the weld joint quality (i.e., strengthening the weld region).

4.3.5 Mechanical characterizations

4.3.5.1 Tensile test

The top view of tensile specimens of the base material and welded joints obtained at different FSW parameters and their test results are shown in Fig. 4.11.

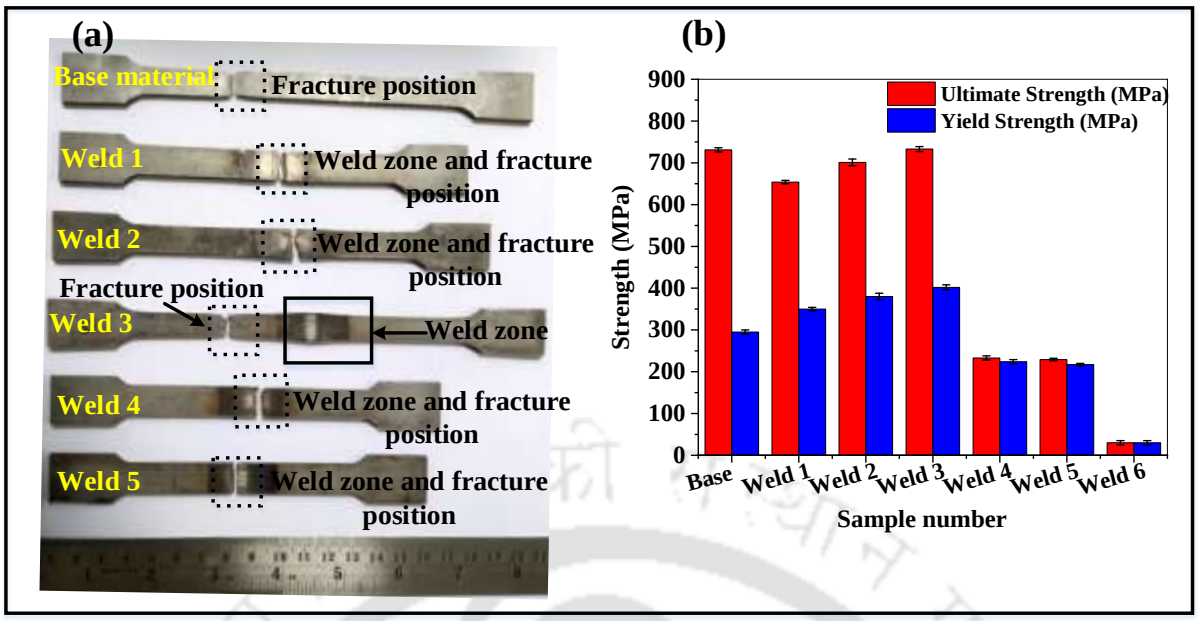

Fig. 4.11 (a) Top view of FSW welded tensile test specimens and (b) their respective tensile test results.

From the tensile specimens, it can be seen that the fracture position of most of the tensile test samples is at the weld nugget zone (NZ) except for Weld 3. The fracture location of Weld 3 is in the base material. Figure 4.11 (b) shows the average measured tensile and yield strength of all the welded specimens with corresponding error bands.

The ultimate tensile strength and yield stress of the BM were 731 MPa and 295 MPa, respectively. The ultimate strength of most of the welded samples is lower than the base material. However, based on the 0.2% of offset technique, the yield strength of the welded sample Weld 1, Weld 2, and Weld 3 was more than the base material, as shown in Fig. 4.11 (b). Higher yield strength may be due to the welding cycle thermal effect which significantly affects the grain size refinement in the SZ, strain hardening effect or phase precipitation at the grain boundary [5,151,152]. Furthermore, the yield strength of the high rotational speed welded sample Weld 4 and Weld 5 was lower than the base material. Due to coarse grain formation in both TMAZ and SZs at high rotational speed and the insufficient plastic flow of material, the yield strength decreases.

Weld parameters significantly affected the tensile properties of the welded specimens. At a constant rotational speed of 300 rpm, the ultimate strength of the weld specimen initially increased with increasing traverse speeds from 40 to 90 mm/min. After that, the ultimate strength decreased with a further increase in traverse speed, as shown in Fig. 4.11 (b).

The maximum ultimate tensile strength was observed in specimen Weld 3 (i.e., 733 MPa), which was slightly higher than the base material. Keeping all other parameters fixed, the ultimate strength of the weld specimen (i.e., Weld 4) decreased with increasing traverse speed, as shown in Fig. 4.11 (b). The decrease of tensile strength at a traverse speed of 140 mm/min was found due to low heat input results from improperly intermixing of the material, causing a band of dark shade and wormhole defects at the bottom side shown in the cross-sectional view in Fig. 4.5.

The tensile strength at higher rotation speeds in Weld 5 and Weld 6 was significantly lower compared to the base material due to improper weld formation and large groove defects formation during welding. The minimum tensile strength (i.e., 30 MPa) in Weld 6 was obtained at a tool rotational speed of 600 rpm. The optimum joint strength with excellent weld surface quality was in Weld 3, which was welded at a low rotational speed (i.e., 300 rpm) and medium traverse speed (90 mm/min). The main reasons for variations in tensile strength with the varying welding parameters are heat generation, grain size variations, uniformity of weld microstructure and complete bonding at the bottom region during the welding [115,153,154]. Formation of fine-grain size (i.e., 5-35 µm) and uniform weld microstructure in the SZ at medium traverse speed (i.e., 90 mm/min) with good weld quality resulted in high tensile strength. When the traverse speed increases, the reduction in heat input leads to a decrease in the plastic deformation of materials and the formation of internal wormhole defects that affect the mechanical strength of the welded sample. However, at higher tool rpm, the joint quality becomes poor because the higher magnitude of tool rotational speed leads to high heat generation, which results in insufficient mixing of material with some micro-voids formation, as shown in Fig. 4.12. The failure of tensile specimens of Weld 1, Weld 2, Weld 4, and Weld 5 was observed at the weld nugget because of some microvoids and a lack of proper bond formation in the weld root notch. Generally, the failure of the welded sample is observed in the weakest zone of the FSW joints. However, for welding parameters of 300 rpm with 90 mm/min, the welded tensile sample Weld 3 fractured in the base material with the highest tensile strength and percentage of elongation. The presence of the fine grain with uniform carbide particles and the absence of defects in the TMAZ and the weld nugget of Weld 3 resulted in maximum micro-hardness in the weld zone, which significantly enhanced the joint strength.

Furthermore, to investigate the localized fracture surface characteristics of tensile-test specimens, a FESEM analysis was carried out, shown in Fig. 4.13. The necking in the tensile test fracture surface of deformed welded sample Weld 3 was observed, like ductile materials,

as shown in Fig. 4.13 (a). The Position of the fracture surface was 30 mm away from the centre of a weld joint. The macro-morphology of the SEM micrograph of the fracture surface is shown in Fig. 4.13 (b). Figure. 4.13 (c) shows the inhomogeneous distribution of dimples, which proves that the quality of the fracture is ductile in nature. At the high magnification view of the marked zone A, shallow dimples and deep dimples were observed in the fracture surface, which is shown in Fig. 4.13 (d). The failure of Weld 3 in the base material was observed due to coarse grain size as compared to the SZ grain size. The cause of the initiation of cracks was the surface of the deep dimples acts as voids and cracks around the carbide particles, which are consecutively strained until the failure of the surface occurs [113,148].

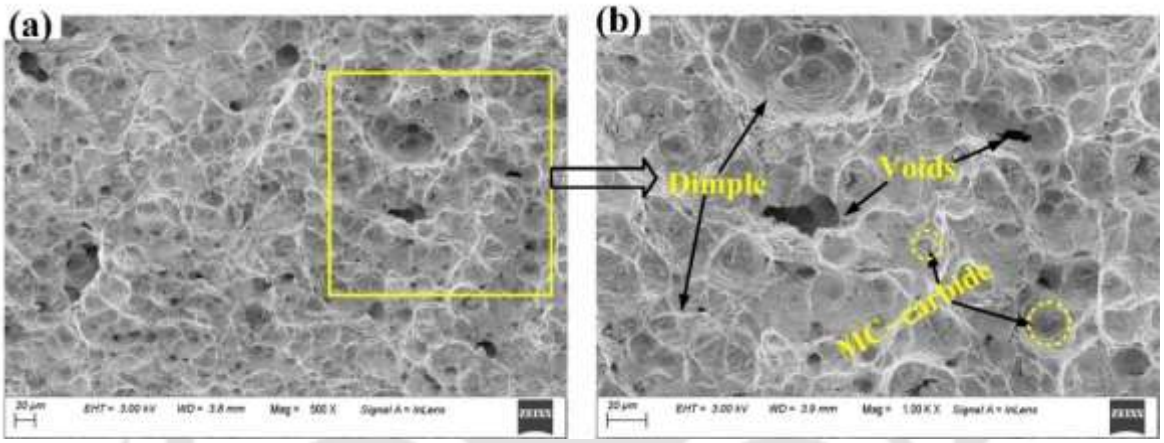

Fig. 4.12 SEM fractography of (a) tensile fractured sample Weld 5 and its (b) magnified view.

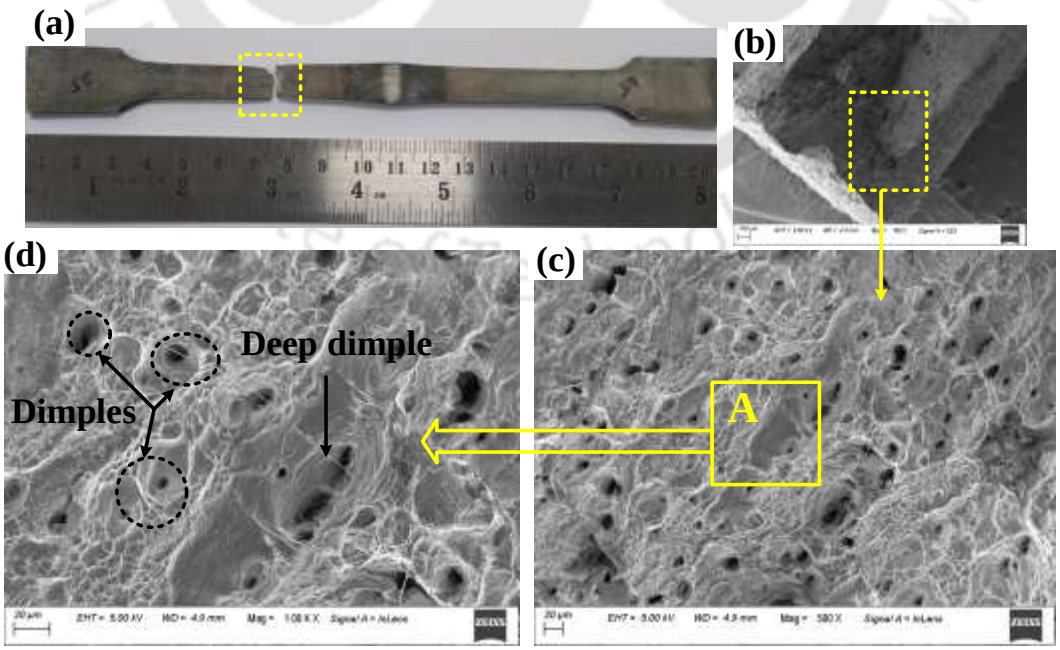

Fig. 4.13 A fractured cross-sectional view of a tensile specimen of welded sample Weld 3.

4.3.5.2 Hardness test

Vicker's microhardness tests were performed perpendicular to the weld line in the weld zone area. The microstructure variation in different weld zones strongly influenced the microhardness profile, identified in Fig. 4.6. It was observed that both rotational and transverse speeds significantly affect hardness results. A large microhardness variation was observed along the line perpendicular to the welding direction, shown in Fig. 4.14.

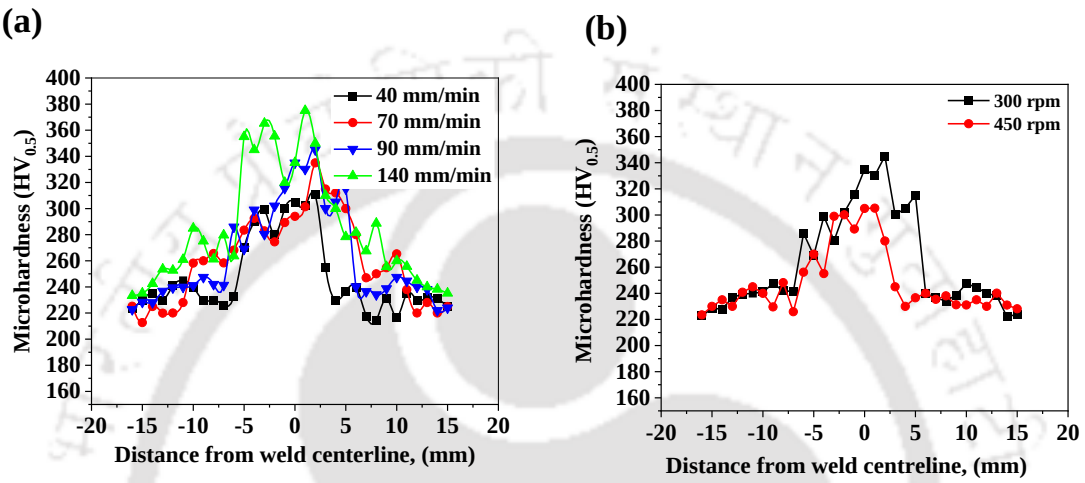

Fig. 4.14 Hardness distribution at (a) different traverse speeds and (b) different rotational speeds.

The measured microhardness values of the base material were between 220-230 HV. In the SZ of all the weld specimens, the microhardness magnitude was higher than that of the BM. Figure 4.14 (a) represents the variation of hardness distribution obtained for different traverse speeds keeping the rotational speed fixed (i.e., 300 rpm). It can be observed from Fig. 4.14 (a) that in the SZ, the microhardness values increased from 300 HV to 370 HV with increasing traverse speed from 40 to 140 mm/min. However, the magnitude of micro-hardness decreased from 345 HV to 295 HV with increasing rotational speed from 300 rpm to 450 rpm, as shown in Fig. 4.14 (b). The microstructural grain refinement was enhanced at high traverse and low rotational speeds. The higher microhardness value at the center of the weld zone was observed, which can be attributed to the fine-grained microstructure caused by the dynamic recrystallization and precipitates formation [148,155]. Due to the coarse-grained microstructure, the minimum hardness value in the SZ was observed for welded sample Weld 5. The maximum magnitude of hardness (i.e., 370 HV) was observed in sample Weld 4 due to the lowest grain size (i.e., the highest fine-grained microstructure) compared to other welded samples.

4.3.5.3 Toughness test

The Charpy impact tests were performed to evaluate the mechanical impact response of the FS-welded Inconel 718 alloy sheets. Visual inspection of fractured impact toughness samples showed that most samples were completely separated due to the impact test, except for the sample Weld 3, which is shown in Fig. 4.15 (a).

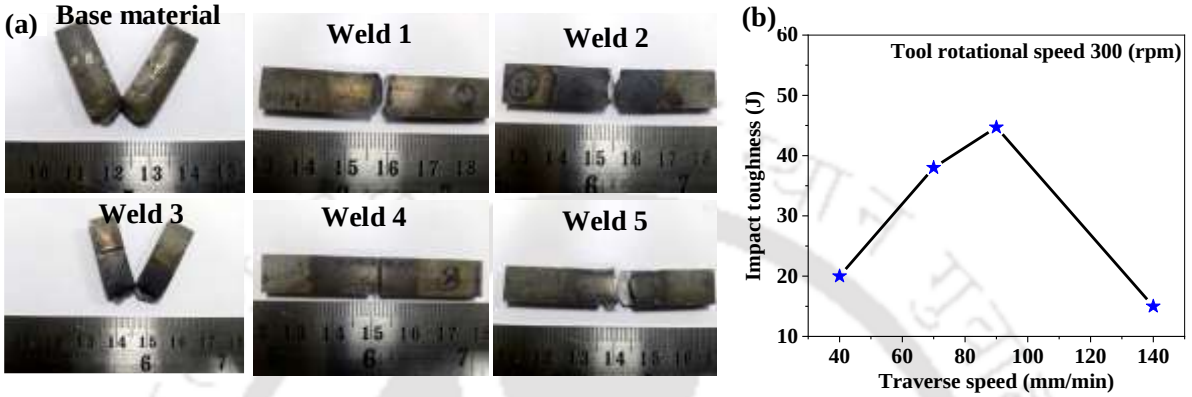

Fig. 4.15 (a) Fractured impact test samples of welded Inconel 718 and its (b) toughness values at increasing traverse speed.

The measured average impact toughness value of the base material at room temperature was 53 J. The variation of welding parameters, such as welding rotational and traverse speeds, significantly affect impact toughness values. The variation of impact toughness values with varying welding parameters is shown in Fig. 4.15 (b).

Keeping the rotational speed fixed, the impact toughness of samples Weld 1, Weld 2, and Weld 3 increased with increasing traverse speed from 40 to 90 mm/min, as shown in Fig. 4.15 (b). With a further increase in traverse speed, i.e., at a traverse speed of 140 mm/min, the impact toughness value of Weld 4 decreased drastically (i.e., 15 J). The increase in impact toughness value may be attributed to grain refinement at the weld zone, and suddenly, the decreased value obtained may be due to the presence of a wormhole and some micro-voids at the bottom portion of the SZ of Weld 5. The effect of rotational speeds on the impact toughness value was high. The impact toughness of Weld 3 was maximum (i.e., 44.7 J), and the minimum value was found in the sample Weld 6, which was welded at a high rotational speed. Improper weld at the bottom of the weld nugget and large wormhole defect in the AS resulted in minimum impact toughness values at a high rotational speed. This work also carried out SEM fractography analysis of the

fractured impact specimen. SEM fractography analysis results of both a good and bad quality Weld, i.e., samples Weld 3 and Weld 5, respectively, are shown in Fig. 4.16.

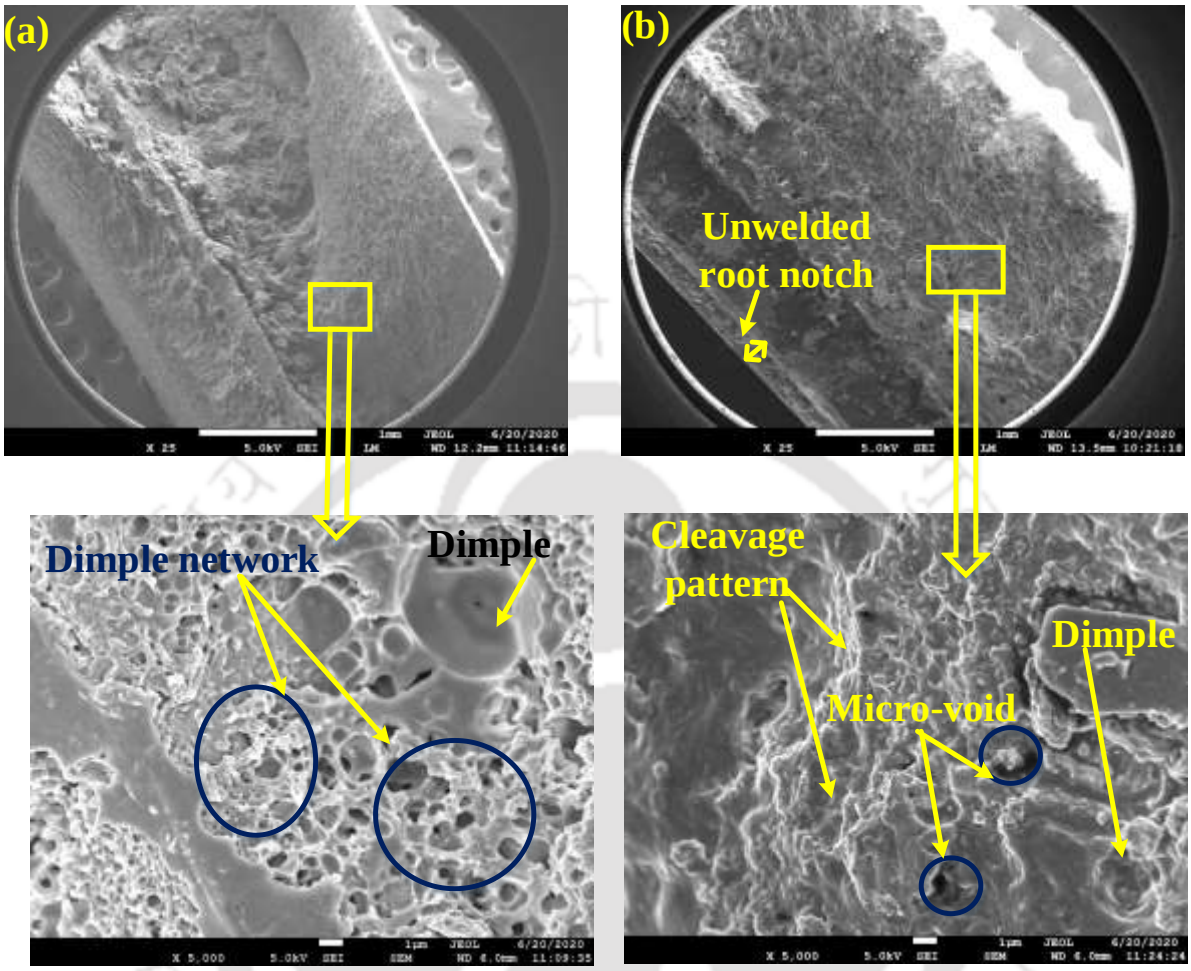

Fig. 4.16 SEM fractography of an impact-tested welded sample (a) Weld 3 and (b) Weld 5.

From SEM fractography image analysis of welded sample Weld 5, a small unwelded root notch surface was found in Weld 5, whereas it was not found in welded sample Weld 3, as shown in Figs. 4.16 (a-b). The unwelded root notch was observed at high rotational speed (more than 450 rpm) due to tool wear, resulting in a lack of penetration. From the high-magnification SEM fractography image of Weld 3, large-sized dimple and dimple networks were observed, resulting in the ductile type of fracture in nature. In contrast, the cleavage with voids and dimples results in a mixed mode of fracture in Weld 5. The toughness fractured part of Weld 5 has a shear-brittle type fracture topography. At higher rotational speeds, the material becomes softer due to high heat input, resulting in more flash formation caused by the reduction of weld thickness. Due to the high temperature and the corresponding flash out of material, the formation of microvoids was observed in the magnified SEM image, as shown in Fig. 4.16 (b).

The coarse grains at high rotational speeds were observed from microstructure analysis in the TMAZ, which decreased impact toughness. It should be noted that the presence of an unwelded notch root and the formation of microvoids in the weld zone lead to a decrease in the toughness value [26,156].

4.4 Brief scientific discussion

Scientific observation based on the change in microstructural properties with the parameters shows that the strength and microhardness of the weldment dependents on the heat input during the welding. The observed higher yield strength may be due to the welding cycle thermal effect which significantly affects the grain size refinement in the SZ, strain hardening effect or phase precipitation at the grain boundary. The main reasons for variations in tensile strength with the varying welding parameters are heat generation, grain size variations, uniformity of weld microstructure and complete bonding at the bottom region during the welding. Similarly, the higher microhardness value at the center of the weld zone was observed, which can be attributed to the fine-grained microstructure caused by the dynamic recrystallization and precipitates formation.

4. 5 Summary

In this study, FSW of Inconel 718 alloy was performed at varying process parameters using a WC-Co tool. The following outcomes can be drawn.

- The good surface appearance with proper weld joint was obtained at low rotational speed and medium traverse speed (i.e., at 300 rpm and 90 mm/min).
- The formation of internal weld defects such as wormhole and micro-voids was obtained at high rotational speed (i.e., more than 300 rpm) and high traverse speed (i.e., more than 90 mm/min) in the AS due to incomplete bonding between the TMAZ and the SZ during the welding.
- The average axial force was increased by 17.06% with an increase in traverse speed from 40 to 140 mm/min, whereas it was enhanced to 7.8% with a decrease in rotational speed from 600 to 300 rpm.
- The microstructure of the SZ of the welded sample Weld 3 revealed the presence of MC-carbide with (NbC) and (NbTi)C secondary phases in the SZ.
- Grain refinement in the SZ increased with increasing traverse speed and decreasing rotational speed due to stirring deformation accompanied by dynamic recrystallization.

- At 300 rpm rotational speed and 90 mm/min traverse speed, the ultimate tensile strength and yield strength were found to be 100.2% and 136.2% of the base material, respectively, which may be the presence of refined secondary phases, grain refinement, and homogeneous microstructure.
- With the increase of traverse speed from 40 to 90 mm/min, the grain refinement in SZ and TMAZ increases the yield strength and impact toughness of the welded joints. Further increasing the traverse speed (i.e., 140 mm/min), yield strength and toughness value decrease due to defects such as wormholes.
- The high rotational speeds, i.e., 450 rpm and 600 rpm, generate defects such as wormhole and coarse-grained microstructure in the weld zone, which results in the reduction of yield strength.
- The hardness values in the weld zone increased with increasing traverse speed and decreasing rotational speed due to grain refinement in this zone. The maximum hardness value, i.e., 370 $HV_{0.5}$, was observed in sample Weld 3 in the SZ, which is around 64% more than the BM hardness.

……..*……..*…….. :

CHAPTER 5

5. Experimental Investigation on Induction-Assisted Hybrid FSW of Inconel-718 Alloy

5.1 Introduction

Hybrid/Assisted friction stir welding is an advanced solid-state joining technique used to preheat high-strength materials to soften them and reduce the downward force acting on the tool during joining. Among the possible preheating sources, a high-frequency induction preheating source is a high-speed and uniform temperature provider with a unique combination of high stability and concentrated energy source. In the previous chapter, a conventional FSW process was used for joining Inconel 718 sheets, and their process parameters were established. This chapter discusses the development of an induction preheating setup with the conventional FSW machine. The joining of 3 mm thick Inconel 718 sheets is established with and without the induction-assisted FSW process (I-FSW). After conducting the welding process, a comparison study was carried out between the FSW and I-FSW of Inconel 718 alloy. The effect of induction preheating on microstructure, mechanical properties, axial force, and temperature distribution in the welded specimens has been investigated. In addition, tool wear has been analyzed in both cases with and without induction preheating during the FSW process.

5.2 Materials and methodology

Friction stir welding was performed on the commercially available as-hot rolled 3 mm thick Inconel 718 sheets in butt joint configuration. All sheets were prepared in the dimensions of 200 mm × 80 mm × 3 mm. The chemical compositions and physical properties of the Inconel 718 sheets and used taper tool materials are mentioned in chapter 3. The details of the experimental setup, working principle, and methodology used in the induction-assisted friction stir welding process are explained in chapter 3, section 3.2.3. A schematic representation of the induction preheating system is depicted in Fig. 5.1.

Before welding, the joining edges are prepared, such as making the right angle with the flatness and cleaning with acetone to remove any impurities. After preparation, the Inconel sheets were placed over the backing plate and rigidly clamped with a fixture for butt welding. The welding process in a position-controlled FSW machine starts with plunging the rotating cylindrical tool into the sample. After it, dwell time (10 sec) was allowed to warm up the material by frictional

heat. The induction heating source was started during the dwell period to provide additional heat for softening the surface area near the rotating tool. The temperature of the sample should be sufficient so that the material remains soft enough to be stirred easily with the tool. The welding surface heated with the induction heat source provided constant output power throughout the weld line. After welding up to the end line, the rotating tool was lifted up, the current supply into the coil was stopped, and the workpiece was allowed to cool down at ambient temperature. The K-type thermocouples were spot welded on the top surface of the workpiece to measure the transient temperature distributions. The spot position was at 20 mm (marked as TC1 & TC2) and 23 mm (marked as TC3 & TC4) from either side of the weld center line in the advancing side (AS) and retreating side (RS) are shown in Fig. 5.2. The optical-infrared temperature sensor was also used to measure the weld nugget temperature during the induction assisted FSW.

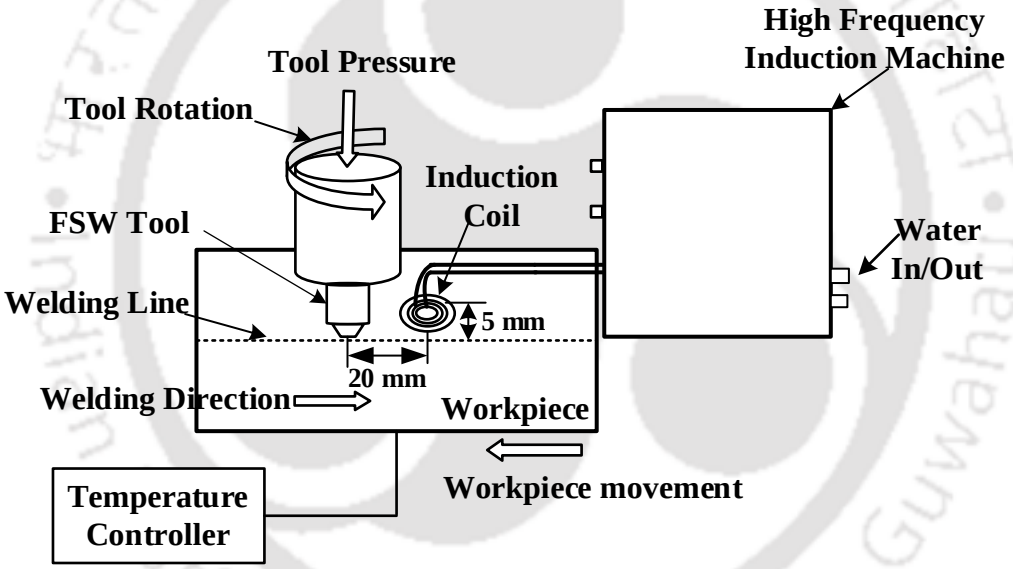

Fig. 5.1 Schematic diagram of induction-assisted FSW process.

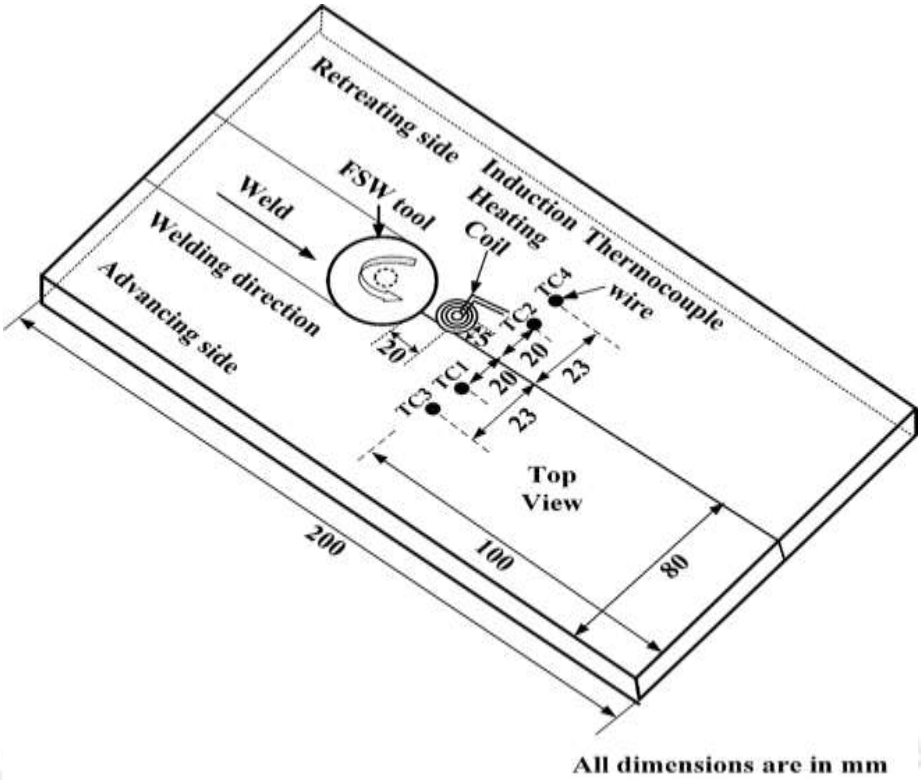

Fig. 5.2 Position of thermocouples used in the I-FSW process.

The FSW welding parameters for joining Inconel 718 were selected based on trial experiments and the authors' previous research [115]. The input parameters for the I-FSW were chosen based on the visual inspection and macrograph of the joints obtained in several experimental trials. The fixed rotational speed with variable traverse speed and the variable preheating temperature was used to optimize the welding parameters to check the effect of preheating temperature on tool life and weld quality, which are depicted in Table 5.1. All the experiments were performed with a fixed shoulder plunge depth of 0.2 mm and tool tilt angle of 2^{o}.

Table 5.1 Combination of welding parameters and preheating temperature.

Sr. no.	Tool rotation rate (RPM)	Welding speed (mm/min)	Plunge depth (mm)	Preheating temperature (^{o}C)		
				T_1	T_2	T_3
1	300	90	0.2	310	410	700
2	300	140	0.2	310	410	700

5.2.1 Test and analysis

After welding, the mechanical and microstructural characterization tests were performed on the welded joint samples. The testing methodology used in this experiment is explained in chapter 3, sections 3.3.1 and 3.3.2. To measure tool wear in terms of weight loss during conventional and induction-assisted FSW, a microbalance with high accuracy (1mg) was used. The weight loss and pin length shortage for analysis of tool wear in all the parameters were measured after 600 mm weld length (i.e., after 3rd weld length).

5.3 Results and discussion

Characterization results of induction-assisted friction stir welded joints are discussed in the following subsections.

5.3.1 Temperature distribution due to induction heating.

In order to evaluate the operating parameter of the high-frequency induction heating machine used in this experiment, firstly, we determined the variation of temperature profile with the variation of the output power of the induction machine. Figure 5.3 shows the variation in temperature profile obtained during the induction heating of the stationary Inconel plate surface, which was 5 mm below the coil surface. The experiments were carried out at three different output operating power, i.e. 7 kW, 12 kW, and 18 kW, with fixed heating time (30 sec), and found that the temperature was changed from 300 ^{o}C to 700 ^{o}C. From the temperature profile, it was found that the maximum temperature of the plate changed according to the output power of the induction machine. The variation of maximum temperature with rising time measurement results reveals that the time required to reach the rotating tool in preheated place was enough time to begin the FSW process with the induction heating.

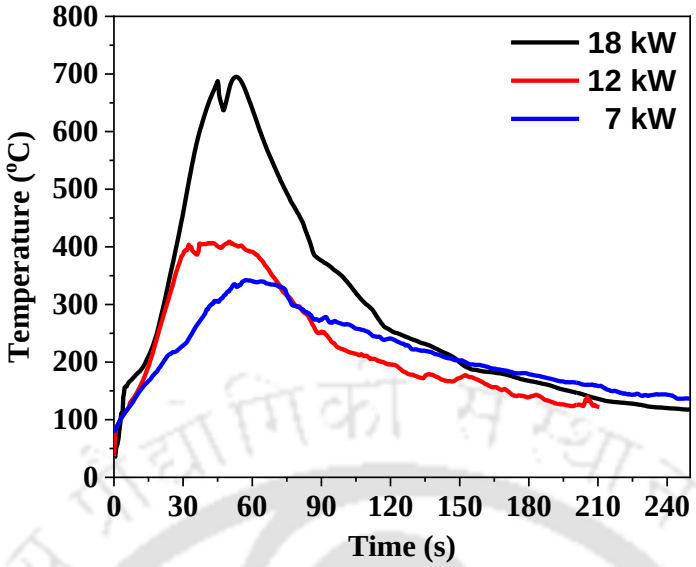

Fig. 5.3 Variation of the maximum temperature of the stationary plate with the interpretation of the output power of the induction machine.

After finding out the temperature variation of the stationary plate surface with the output parameter of the induction machine, we proceeded with this experiment with the varying FSW parameters (i.e., 90 and 140 mm/min) to find out the in-line preheating effect in this process. Figure 5.4 displays the recorded surface temperature of an Inconel plate for both conditions, with and without the use of the induction-assisted FSW process. The temperature was recorded at a constant tool rotational speed of 300 rpm and with varying transverse speeds of 90 and 140 mm/min. The obtained transient temperature profile at a distance of 20 and 23 mm from the weld centerline in conventional FSW is shown in Figs. 5.4 (a-b). Figs. 5.4 (c-d) shows the transient temperature profile obtained during the induction-assisted friction stir welding process. In this experiment, 7 kW induction output power for the welding parameters 90 mm/min and 140 mm/min was used to confirm the heating temperature goes above 310 ^{o}C. The yield strength of the Inconel 718 material began to decrease above 350 ^{o}C [157].

From the observation of the thermal history, the peak temperature of the advancing side (AS) was found higher than the retreating side (RS). The cause of higher temperature was additional frictional heat generation and transformation of solid material into semi-solid on the AS [158]. In the induction-assisted FSW process, Figs. 5.4 (c-d) shows existing of two peaks during the heating stage; the first is generated due to induction heating and the second due to FSW tool rotation. The use of induction heating during the welding at 90 mm/min and 140 mm/min

increased the peak temperature (Figs. 5.4 (c-d)) in the advancing side (i.e. TC1) by 1.5 times and 0.9 times, respectively, due to direct heat addition compared to the conventional FSW process (Figs. 5.4 (a-b)) at same parameters. The effect of process parameters on both the cases with/without induction-assisted FSW was observed to be highly affected by traverse speed. In all cases, the peak value of thermocouples at 90 mm/min was higher than the 140 mm/min because higher welding speed leads to less time of heat accumulation [113].

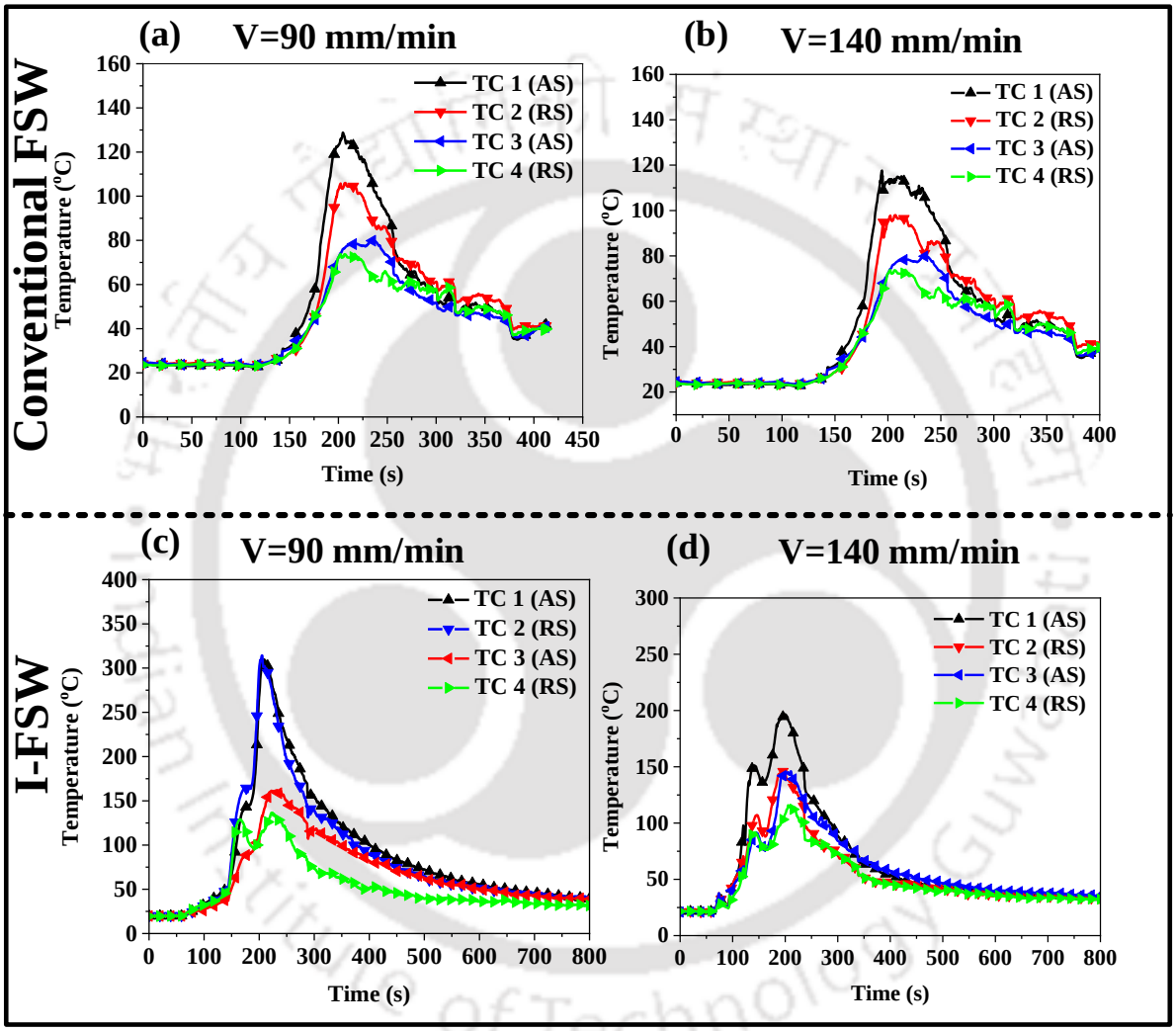

Fig. 5.4 (a) The temperature measurement during (a-b) conventional FSW process and (c-d) induction-assisted FSW process (I-FSW) at a preheating temperature of 310 °C.

Measuring the weld zone temperature with a thermocouple is a very challenging task. For this reason, the measurement of the weld zone temperature was carried out with an IR camera. The thermal history of with and without induction heated FSW are shown in Figs. 5.5 (a-b). The peak temperature between the FSW tool & workpiece contact region, at a traverse speed of 140 mm/min, was around 940 °C and 1060 °C during the conventional FSW and I-FSW process,

respectively. The measured contact temperature value during the preheating process was remarkably higher than the without-preheating process. The observed peak temperature was found to be consistent with the highest temperature recorded in the weld nugget by Huang et al. [146]. From the above observation, it can be said that the induction preheating significantly affects the temperature distribution during the FSW of Inconel 718 alloy.

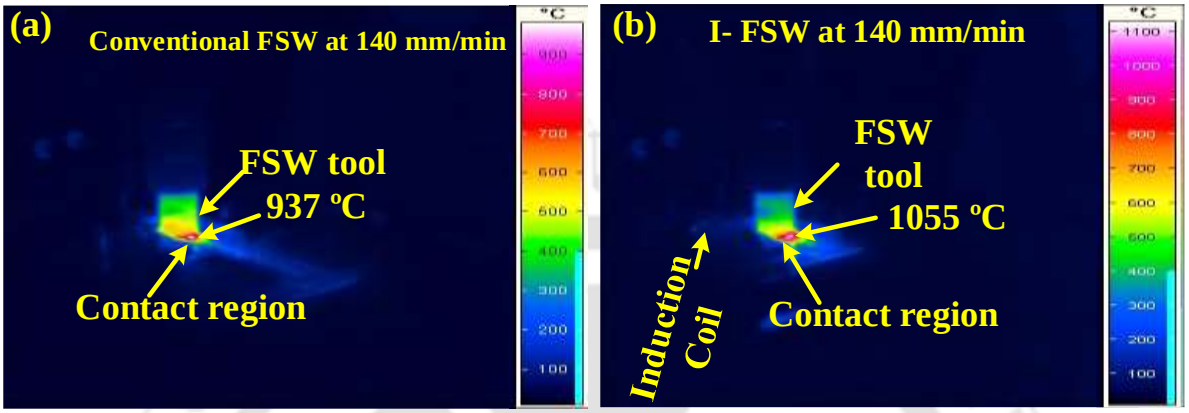

Fig. 5.5 Temperature distribution during (a) conventional FSW and (b) I-FSW.

5.3.2. Welded surface appearance and force evaluation

Figure 5.6 depicts the top surface appearance of the welded joint obtained at different parameters (as illustrated in Table 5.1) in conventional and induction-assisted FSW. Figure 5.6 (a) shows the good surface appearance of the welded joint obtained in the conventional FSW at 90 mm/min traverse speed. When the traverse speed increased by 140 mm/min, an internal cavity defect on the surface appeared because less heat input resulted in insufficient intermixing of materials, as shown in Fig. 5.6 (b). However, the effect of induction preheating was observed with sound weld at high traverse speed (i.e., 140 mm/min) and the thin flash generation (i.e. external material flow) from the weld surface. The preheating temperature and welding speed significantly affect the production of flash. Welding with constant rotational speed (i.e., 300 rpm) with preheating temperature 310 ºC appeared smooth welding surface with thin flash (thickness ~ 0.10 mm) at both traverse speeds (i.e., at 90 and 140 mm/min), as shown in Figs. 5.6 (c-d). As the preheating temperature increased above 410 ºC, a large groove defect with a thick flash (thickness ~ 0.25 mm) was observed. Welding was not observed at a high preheating temperature (i.e., at 700 ºC) due to the generation of a very thick flash (thickness ~ 0.34 mm) resulted in thinning of the plate. At high preheating temperatures, the tool pin touches the backing plate just after starting the welding, which results in breaking the tool pin and

generating the hole, as shown in Figs. 5.6 (g-h). Excess softening of material and high plunge load can be seen to generate a thick flash. The proper selection of preheating temperature and plunge load are essential parameters in a defect-free surface appearance.

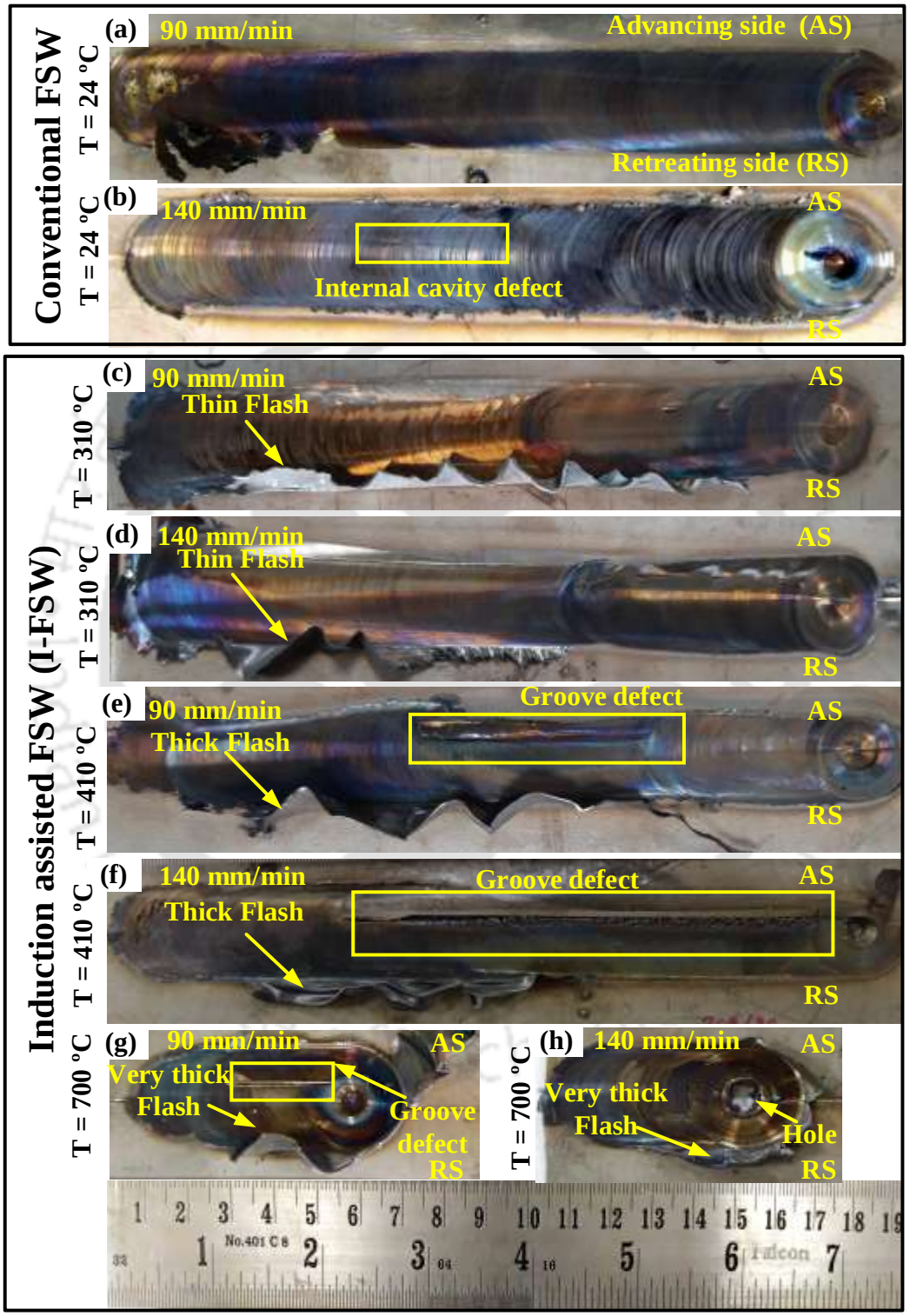

Fig. 5.6 The top surface appearances of welded plates obtained during (a, b) conventional FSW and (c-h) I-FSW process.

Figure 5.7 (a) shows the profile of the downward axial force generated during the FS welding of Inconel 718 with and without preheating under constant rotational speed (300 rpm) and 140 mm/min traverse speed. The generated axial force graphs over the weld time consist of three zones (i.e., plunge, dwell, and weld zone). Two peaks were generated during the plunging zone of the weld obtained in conventional FSW. The first peak was due to the initial plunging of the tool pin into the solid Inconel material, and the second peak was due to both the tool pin and shoulder plunge. Whereas in the preheating case, the first peak was not observed due to the effect of surface preheating. In preheating, the peak value of axial force (22 kN) in the plunging stage was lower than the without preheating (33 kN). The difference in peak value was observed due to the thermal softening of material by steady preheating. Following this, for some period of time, only a rotation of the tool occurs, known as the dwell period zone, which further softens the material, causing the decrease of axial force. The final zone is the welding zone, where almost constant axial force was observed in both cases. The steep fall-off in axial force can be seen once the weld is completed and the tool leaves the contact, as shown in Fig. 5.7 (a).

In the same way, the average axial forces for all the FSW process (with and without preheating) were calculated, as shown in Fig. 5.7 (b). During the study of generated axial force in conventional FSW, it was observed that at constant rotational speed (i.e., 300 rpm), the average force produced at traverse speed 90 and 140 mm/min was 27 kN and 30 kN, respectively. In all the cases, the average axial force value was higher at a higher traverse speed (i.e.,140 mm/min) than at a lower traverse speed (i.e., 90 mm/min). Tool stirring time and frictional heat input decrease at higher traverse speeds, leading to less thermal softening and material flow [77]. The average axial force generated during the I-FSW process at 310 ^{o}C was 21 kN and 22 kN at traverse speed 90 mm/min and 140 mm/min, which was decreased by 23% and 26% compared with conventional FSW (i.e., at 25 ^{o}C). It was 18.26 kN and 21.0 kN in the I-FSW process at 410 ^{o}C preheating temperature, which was reduced by 27% and 31%, respectively, compared with axial force generation at 25 ^{o}C. Similarly, the reduction of the axial force in the I-FSW process was observed at high preheating temperatures (i.e., at 700 ^{o}C). The use of induction preheating resulted in a decrease in the axial force. As a result, additional softening initiates the plastic flow of base material and is easily stirred in I-FSW compared to the conventional FSW. Some researchers have also reported a reduction of axial force using additional preheating in their literature during high-strength material welding [86,88].

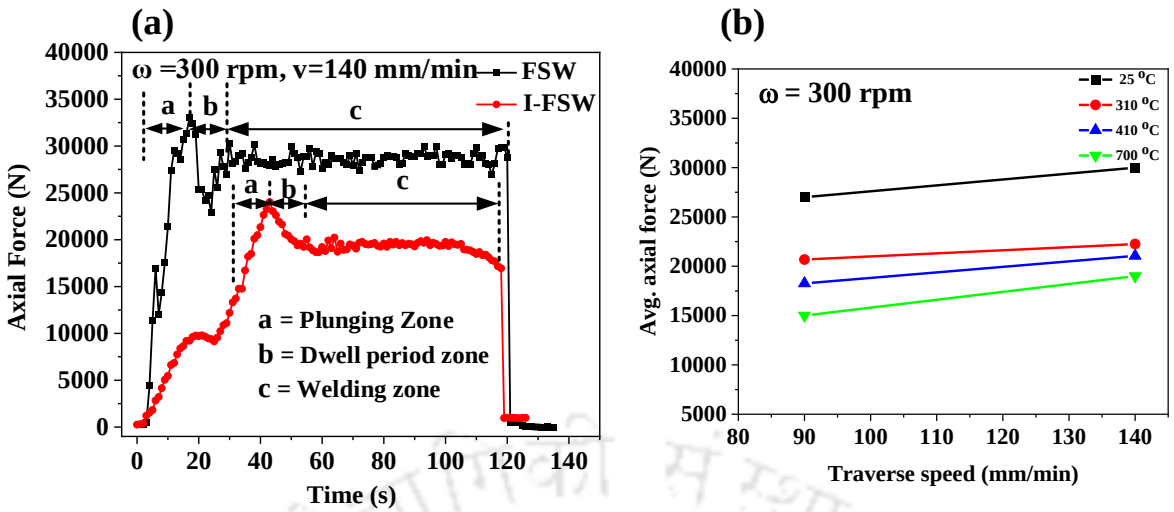

Fig. 5.7 Analysis of axial force generation during (a) conventional FSW and I-FSW process and (b) the average axial force at different preheating temperatures with varying traverse speeds.

5.3.3. Macro and microstructural characterizations

The cross-sectional macrostructure appearance of the joint obtained with and without induction preheated FSW are summarized in Fig. 5.8. All the optical macrographs of the nugget zone present basin-shaped due to the tapered shape of the tool pin. The obtained macrograph at traverse speed 90 and 140 mm/min shows full-penetration weld in all the preheating cases, whereas only the friction stir welded joint shows a lack of penetration. Full-depth penetration in the preheating case confirmed a plate thickness reduction at the tool shoulder's bottom. The red arrow in Figs. 5.8 (a-b) indicates a lack of penetration at the bottom area of the weld zone in conventional FSW. However, the advancing side of the bottom portion of the weld in the conventional FSW shows a defect like a wormhole, indicated with the black arrow, as shown in Fig. 5.8 (b). The presence of defects at high traverse speed (i.e., 140 mm/min) may be due to insufficient heat input causing abnormal mixing of materials. Whereas no wormhole defect at high traverse speed (i.e., 140 mm/min) and 310 ^{o}C preheated FSW case were observed. In contrast, defects like wormholes can be observed at high preheating temperatures (i.e., 410 ^{o}C), which may be excess heat input supplied by preheating leads to insufficient bond formation, as shown in Figs. 5.8 (e-f). The macrograph of the welded sample at a high preheating temperature (i.e., 700 ^{o}C) could not be seen due to a large groove and crack defect formation that produced an improper weld.

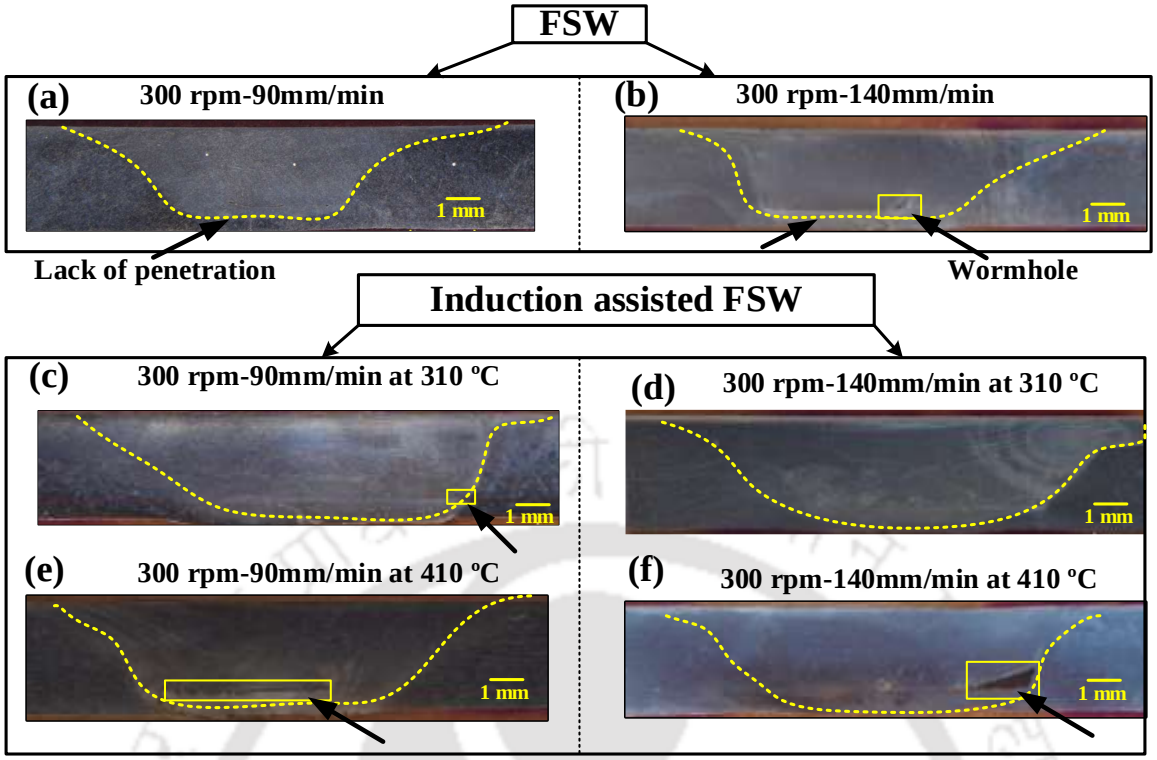

Fig. 5.8 The cross-sectional macrostructure of the FS welds was obtained at (a-b) without and (c-f) with preheating

Figure 5.9 displays the details of the macrograph of a welded sample that was obtained with a high traverse speed of 140 mm/min and a preheating temperature of 310 ºC. Figure 5.9 (a) shows the presence of different weld zones based on grain structure and material flow pattern in the welded sample. From the microscopic image of the base material (BM), as shown in Fig. 5.9 (b), it can be seen that the size of the grains is coarse, and it exists with MC-type carbide particles in the grain and its boundaries [62]. The black-colored MC-type carbide particles enriched with Ni and Ti elements were confirmed with the EDS spectrum. Figure 5.9 (c) shows the center of the weld, known as the stir zone (SZ), which exists with fine grain and fine distribution of carbide particles. Figure 5.9 (d) shows the thermomechanical affected zone (TMAZ), which exists adjacent to SZ in a very narrow region, whereas Fig. 5.9 (e) shows the flow pattern near the bottom of the advancing side (AS). No clear heat-affected zone (HAZ) was observed in the weld zone because of the absence of grain growth near the TMAZ. Song et al. [91] also reported the absence of HAZ in the study of joining Inconel 600 with lesser assisted FSW.

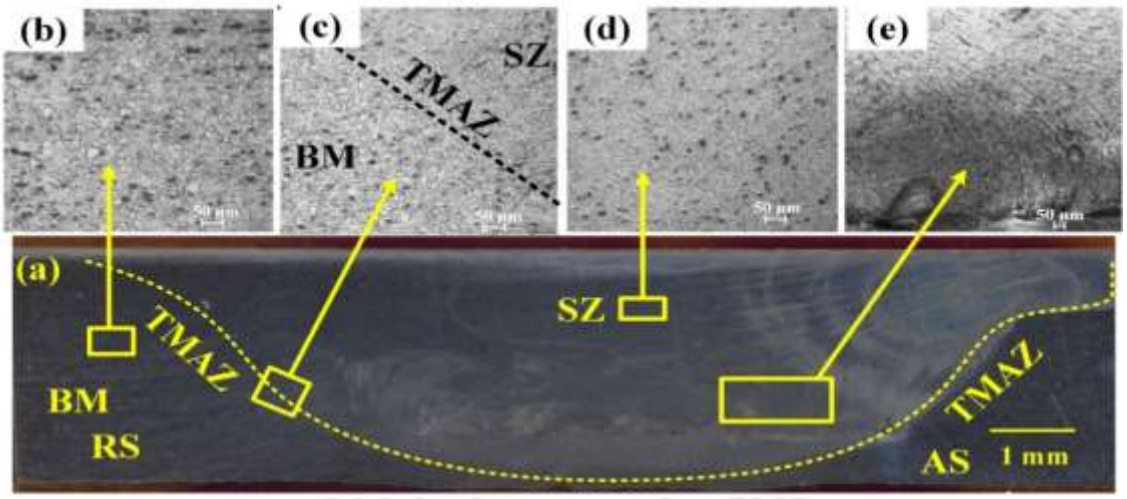

Fig. 5.9 Microscopic views contain (a) cross-sectional view, (b) BM, (c) SZ, (d) TMAZ, and (e) flow pattern view.

For the observation of the weld joint properties in different welding parameters and conditions, the stir zone (SZ) study is significant. Figure 5.10 shows the variation of SZ microstructures obtained with conventional and preheated FSW at traverse speeds of 90 mm/min and 140 mm/min. From Fig. 5.9 (b), it can be observed that the base material (BM) has a coarse grain with an average grain size of 75 µm. In comparison, the grain refinement in the weld zone was observed due to the application of FSW on the Inconel 718. In the conventional FSW process, the SZ's average grain size was 10.5 µm and 7 µm at traverse speeds of 90 mm/min and 140 mm/min, respectively, as shown in Figs. 5.10 (a) and (d). The effect of preheating on the SZ microstructure in the weld was seen in Figs. 5.10 (b, f, c, and e). The grain size of the SZ of the weld obtained at preheating temperature 310 ^{o}C was 13 µm and 9.5 µm at traverse speed 90 mm/min and 140 mm/min, whereas it was 15 µm and 11.5 µm at 410 ^{o}C preheating, respectively.

The microstructural observation obtained in conventional FSW reveals that the average grain size obtained at high traverse speed (i.e., 140 mm/min) was finer than at low traverse speed (i.e., 90 mm/min). At high traverse speed, low heat input and high cooling rate were responsible for the formation of small grain size [113,144]. Under the preheated FSW, the obtained grain size was slightly larger than the conventional FSW. As depicted in Fig. 5.4, the peak temperature variation at the same traverse speed can be seen in the with and without induction preheating FSW temperature curve. The temperature variation was observed due to additional local preheating during the welding, resulting in high peak temperature and taking more time to cool after the welding. The area near the weld zone had also been heated by local preheating,

and it took more time to cool the weld zone. The grain size in the stir zone was slightly larger than the without preheating case due to the decrease in cooling rate. The above grain size observation shows that its variation was not highly affected by preheating compared to dynamic recrystallization during the FSW. The grain size variation in the weld zone at different welding parameters is mainly caused by the dynamic recrystallization, stirring action, and cooling effect [77].The variation of the TMAZ region was also observed in the microstructure obtained at conventional and preheated FSW. A small region of TMAZ at the interface between SZ and BM was found in the conventional FSW, as shown in Fig. 5.10 (g). However, the microstructure variation in the TMAZ region due to preheating was more significant in I-FSW, as shown in Figs. 5.10 (h) and (i). Due to the slow cooling rate in I-FSW, the grain size in the TMAZ region was larger, and no clear boundary between the BM and SZ was observed. In the (TMAZ), partial recrystallization and recovery occurred, resulting in a deformed microstructure with slightly smaller grains than the (BM). Ji et al. [71] and Sun et al. [159] reported a similar result in their preheated FSW study.

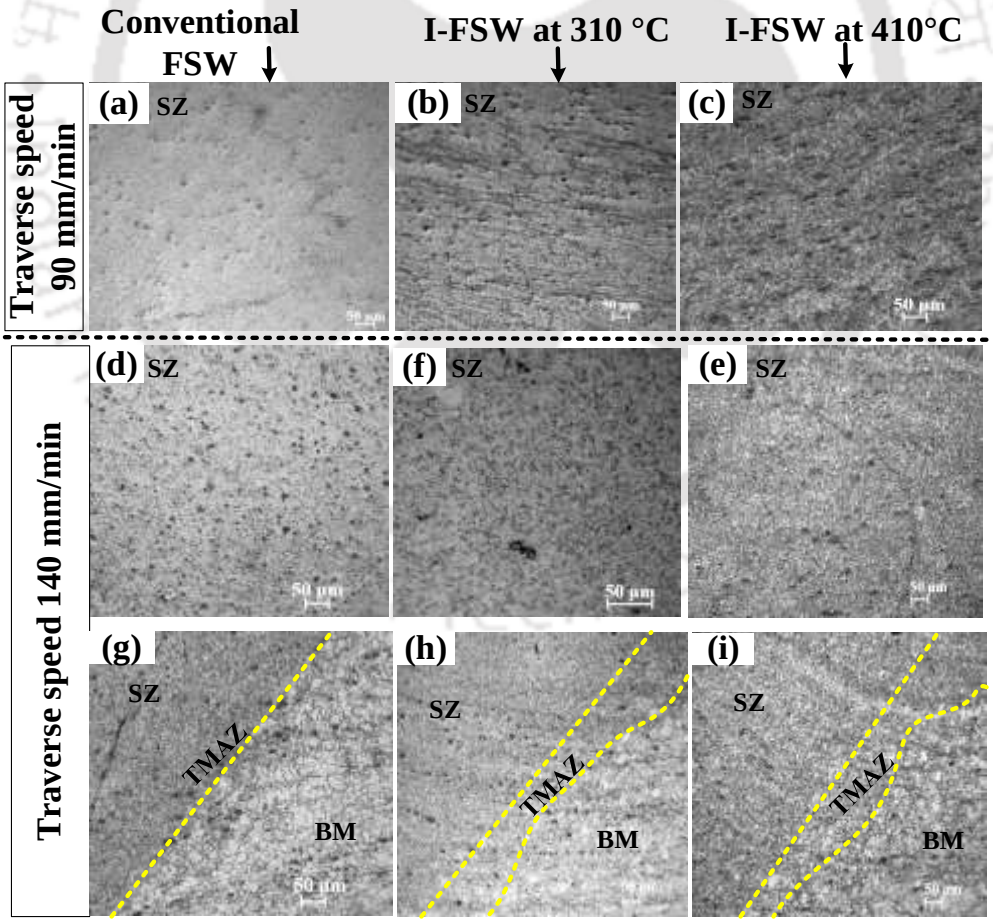

Fig. 5.10 Microscopic views of SZ obtained in (a and d) conventional, (b and f) I-FSW at 310 ^{o}C, (c and f) I-FSW at 410 ^{o}C, and corresponding (g, h, and i) TMAZ at different parameters.

The presence of the external elements and microvoid near the bottom area of the weld nugget zone was analyzed with the FESEM micrographs and the EDS analysis, as shown in Fig. 5.11. The cross-sectional analysis of the macrostructure obtained at high traverse speed (i.e., 140 mm/min) was defect-free. Therefore, in the present investigation, the detailed analysis of the bottom area of the stir zone, obtained at high traverse speed during the conventional FSW and I-FSW, was performed. EDS analysis of the SZ shows the presence of external W and Co elements detected, illustrating the tool's degradation during the FSW process. During the welding of high-strength material, the tool's degradation occurred due to high temperature and high strain rate in the weld zone [66]. Song et al. [37] and Tiwari et al. [77] also reported similar results for high tool wear during the FSW of high-strength material. The SEM image of the stir zone microstructure obtained in conventional FSW reveals the high presence of tungsten (W) particles compared with the stir zone of the I-FSW joint, which was confirmed by the EDS spectrum, as shown in Figs. 5.11 (a) and (b). The EDS results (Fig. 5.11 (c)) showed 2.5 wt.% of the tungsten (W) element in the case of conventional FSW, whereas it was 0.3 wt.% and 0.08 wt.% in the case of I-FSW at preheating temperature 310 ^{o}C and 410 ^{o}C, respectively, as shown in Figs. 5.11 (d) and (e). The less wt.% of tungsten (W) element in the preheated FSW joints can be explained by softening the base material (BM) through preheating. In addition, some microvoids in the microstructure image of the SZ were obtained at a high traverse speed of 140 mm/min in the conventional FSW, as shown in the magnified image of Fig. 5.11 (a). In contrast, the microvoids in the SZ under the I-FSW were not observed at a high traverse speed. Insufficient heat input and insufficient intermixing between the particles resulted in the existence of microvoids [160]. The presence of microvoids in the weld zone results in a decrease in weld properties [161].

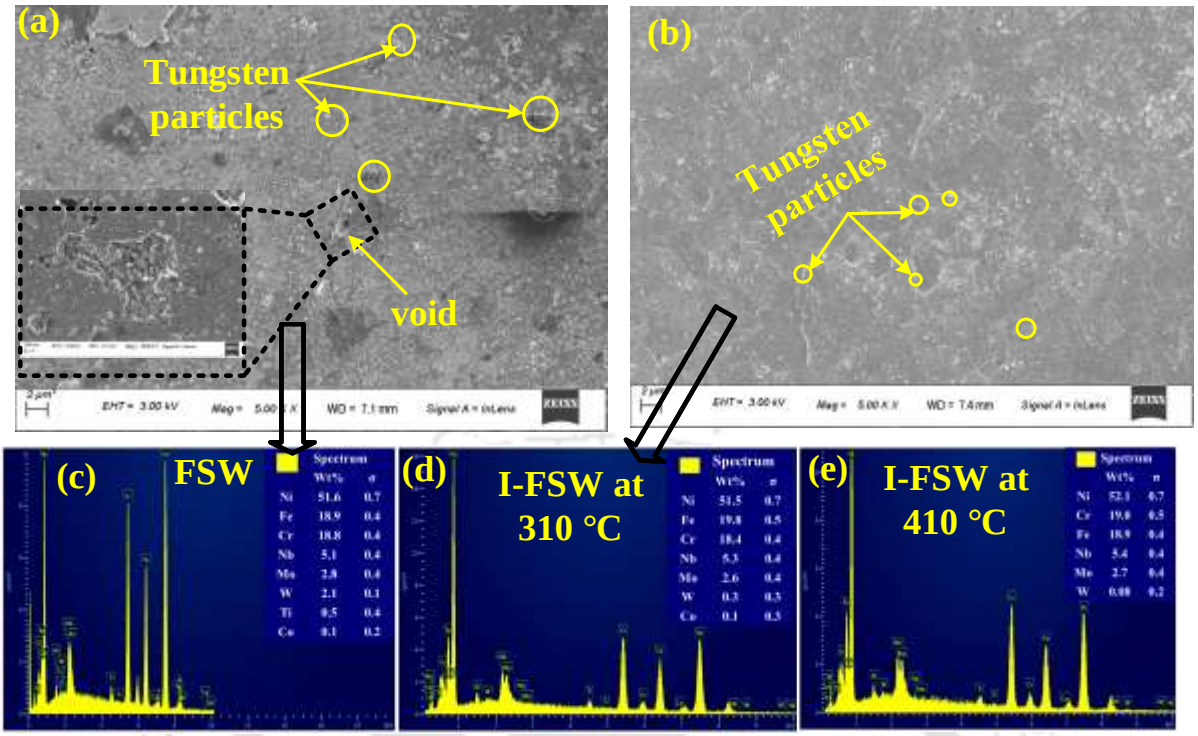

Fig. 5.11 FE-SEM and EDS analysis near the bottom area of the SZ obtained at traverse speed 140 mm/min under (a) conventional FSW and (b) I-FSW.

The presence of carbide particles and intermetallic phases in the stir zone obtained with and without preheated FSW joint at 140 mm/min traverse speed were analyzed with FESEM-EDS, as shown in Fig. 5.12. The optical microstructure image (Fig. 5.9 (b)) of the base material shows the consistency of coarse grains and MC-type carbide ranging between 15 to 20 µm dispersed at the grain boundary. In contrast, the size of the carbide particles in the SZ was found to be more refined and uniformly distributed than the BM due to dynamic recrystallization, as shown in Figs. 5.12 (a-b). The presence of MC-type carbide particles such as (Nb)C, (Ti, Nb)C and (Nb, Ni, Ti, Cr)C were confirmed with the EDS point spectrum 1 & 5, 2 and 3, respectively. However, some oxide particles in the SZ of the weld joint fabricated using an induction-assisted FSW process were observed and confirmed with the EDS point spectrum 4. Oxide formation on the top surface, which was forged in the stir zone by the tool shoulder, may cause local preheating of the base material. Thus, the change in metallurgical properties of the weld may be caused by excess localized preheating.

Figure 5.13 shows the TEM images, and selected area diffraction (SAD) patterns of the stir zone were obtained with and without induction preheated FSW. Figure 5.13 (a) presents the bright field (BF) image of the precipitates Ni_3Nb (ϒ'') and carbide particles (i.e., $M_{23}C_6$) of the stir zone obtained in conventional FSW at traverse speed 140 mm/min. Figures 5.13 (e-f) show

the point EDS spectrum 1 and 2 identified the corresponding precipitates and carbide particles. The random distribution of round-shaped carbide particles existed inside the grain boundaries with a diameter of 30-50 nm. The presence of very fine round-shaped strengthening precipitates Ni_3Nb (ϒ'') was also observed inside the grain boundaries with a diameter of 18 nm. Figure 5.13 (b) shows a low-magnified TEM image of the accumulation of higher dislocation densities at the grain boundaries because of dynamic recrystallization during conventional FSW.

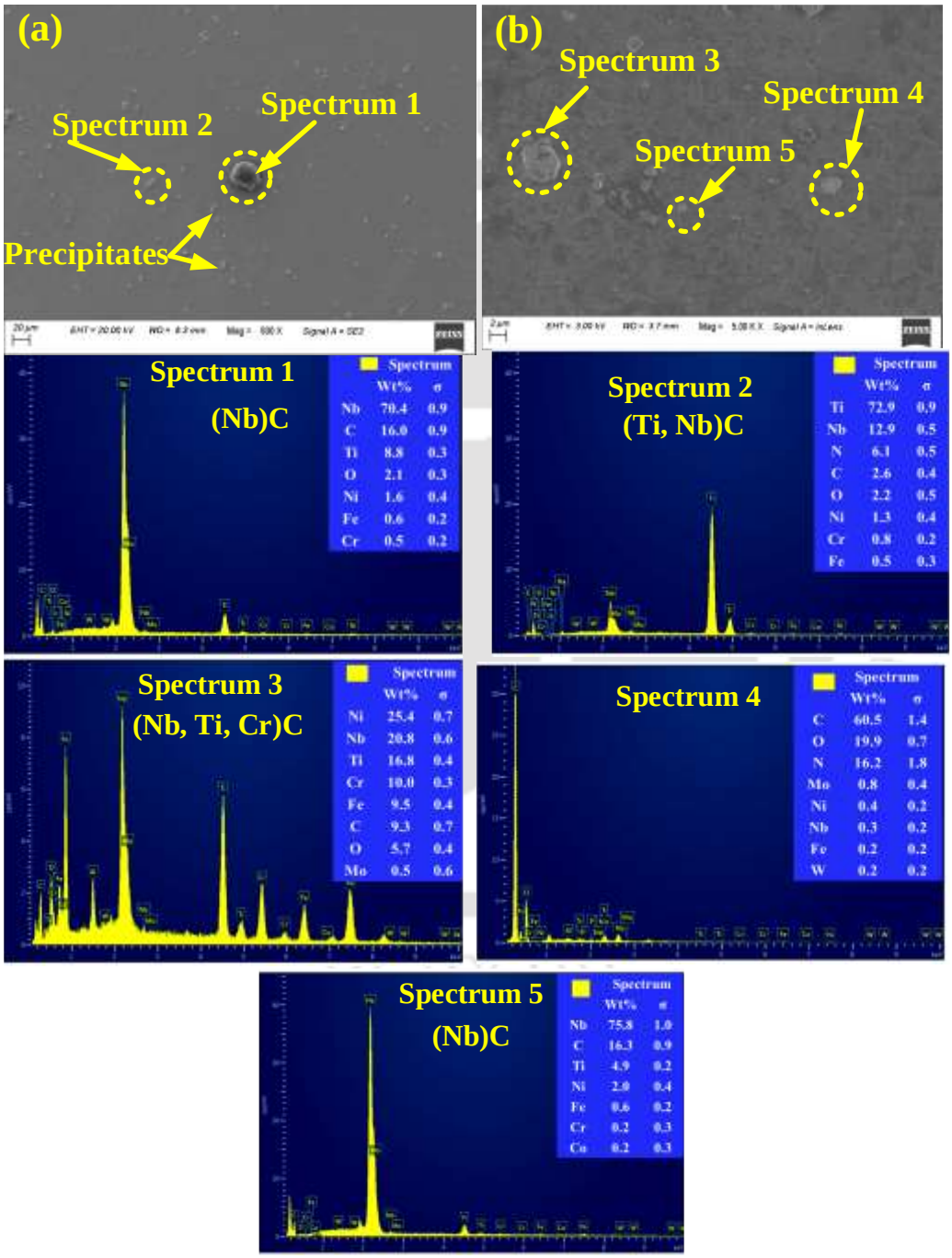

Fig. 5.12 FESEM and EDS analysis of the SZ obtained (a) with and (b) without induction-assisted FSW.

The effect of induction preheating (at temperature 310 ^{o}C) was also observed with the grain size and the carbide particles. MC-type carbide particles had a spherical shape with a small increased diameter of 50-80 nm, whereas more precipitates were found inside the grain. The cluster distribution of carbide particles with the fine spherical shaped precipitates was observed in the grain and grain boundaries, as shown in Fig. 5.13 (c). Figure 5.13 (d) shows the low dislocation densities at the grain boundaries generated from dynamic recrystallization in the induction-assisted FSW. The corresponding selected area diffraction patterns (SAD) identified the $M_{23}C_6$ carbide particle (i.e., (Ni, Cr)C) and intermetallic phase Ni_3Nb (Y") in the bright field images of SZ. In the SAD pattern, the bright and big spots are related to carbide particles, and small spots are related to the intermetallic phase with a [011] zone axis. The diffraction pattern also conformed to the face-centered cubic crystalline nature of the intermetallic phase (i.e., Ni_3Nb) with $(11\bar{1})$ and $(02\bar{2})$ index. Prasad [162] also reported a similar result in their study of carbide and secondary phases in the grains.

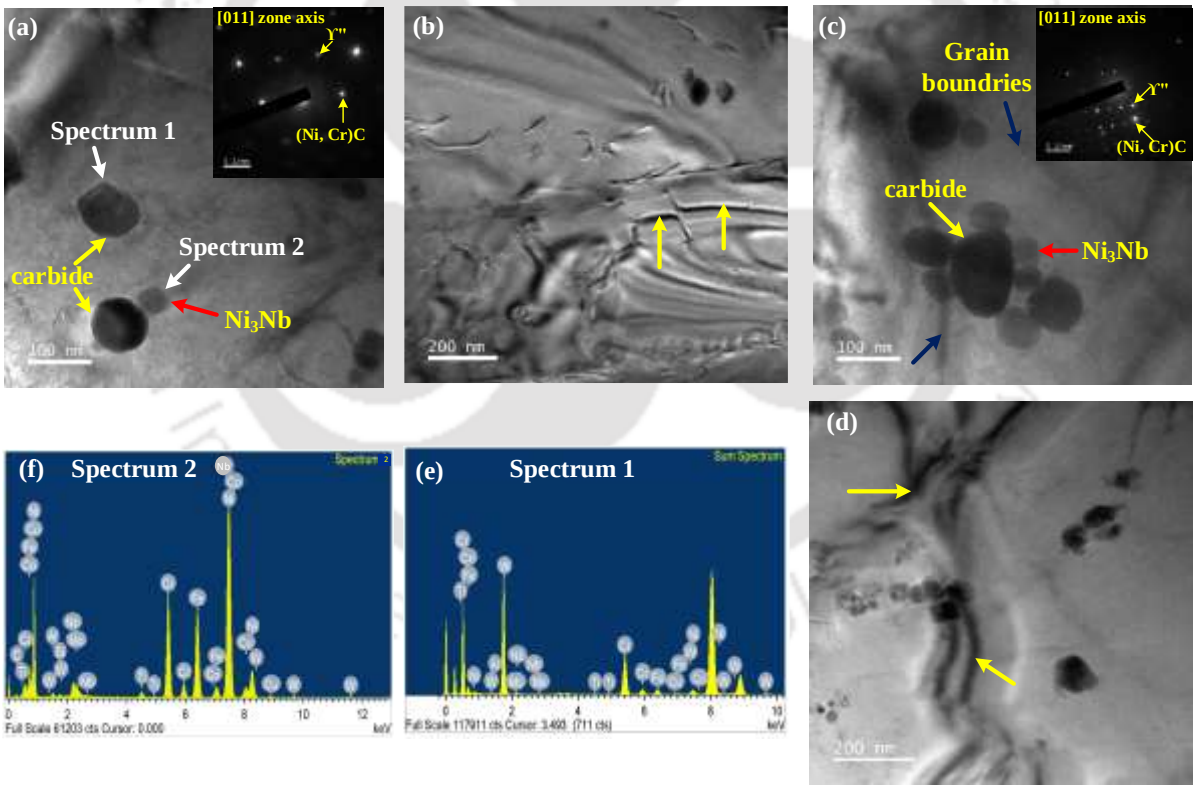

Fig. 5.13 TEM micrographs of SZ and corresponding SAD pattern of the phases and carbide particles observed during (a-b) Conventional FSW and (c-d) I-FSW process at 310 ^{o}C.

5.3.4 Mechanical properties

Figure 5.14 displays the microhardness profile curves generated on the joints prepared by the conventional and induction-assisted FSW (I-FSW) process. Figure 5.14 (a) represents the schematic diagram for the microhardness traverse position. Figs. 5.14 (b-c) shows the hardness distribution curves obtained in the middle of the cross-sectional weld zone area, whereas the hardness variation along the weld thickness is shown in Fig. 5.14 (d). In all the cases, the average hardness value of the SZ was observed to be higher than the BM (230 $HV_{0.5}$). The variation of microhardness profile in different weld zones was highly influenced by the grain size distribution observed in these regions. The rise in microhardness in the SZ was a result of the formation of a microstructure consisting of small grains, brought about by the dynamic recrystallization process and the presence of precipitates inside the grain.

On the other hand, the hardness value of TMAZ was lower than the SZ, and it was lowest in the preheating case. The decrease of hardness value at the TMAZ was found due to coarser grains induced in this zone by the thermal cycle effect during the welding. Using conventional FSW, it was observed in the SZ that with the increase of the traverse speed from 90 to 140 mm/min, the hardness value increased from 350 $HV_{0.5}$ to 375 $HV_{0.5}$., as shown in Fig. 5.14 (b). The variation of hardness value with traverse speed was due to the variation of microstructure obtained at different welding parameters [77].

Compared with conventional FSW joint, the hardness value of induction-assisted FSW joint was observed slightly decreased because of the small increase in the microstructure. The microhardness of the joint obtained under the I-FSW process at 140 mm/min with low preheating temperature (i.e., at 310 ^{o}C) was higher than the high preheating temperature (i.e., at 410 ^{o}C). In contrast, it was lower at a low preheating temperature under 90 mm/min traverse speed. However, A sudden increase in hardness curve value was also observed in the weld zone due to fine carbide particles and the generation of some phases during the I-FSW process [37,91,146]. Thus, from the microhardness curves, it may be observed that the hardness values of the weld joint increase with the decrease of preheating temperature and increases in the traverse speed. The variation of hardness value in the SZ was also analyzed through the weld thickness, as shown in Fig. 5.14 (d). The average hardness value near the top surface (350 $HV_{0.5}$) was lower than the bottom (370 $HV_{0.5}$). The high hardness value on the bottom side was due to the generation of more fine grains at the bottom area during the FSW process than at the

upper surface of the weld. Song et al. [91] have also reported a similar trend of variation of hardness values along with the weld thickness in their literature.

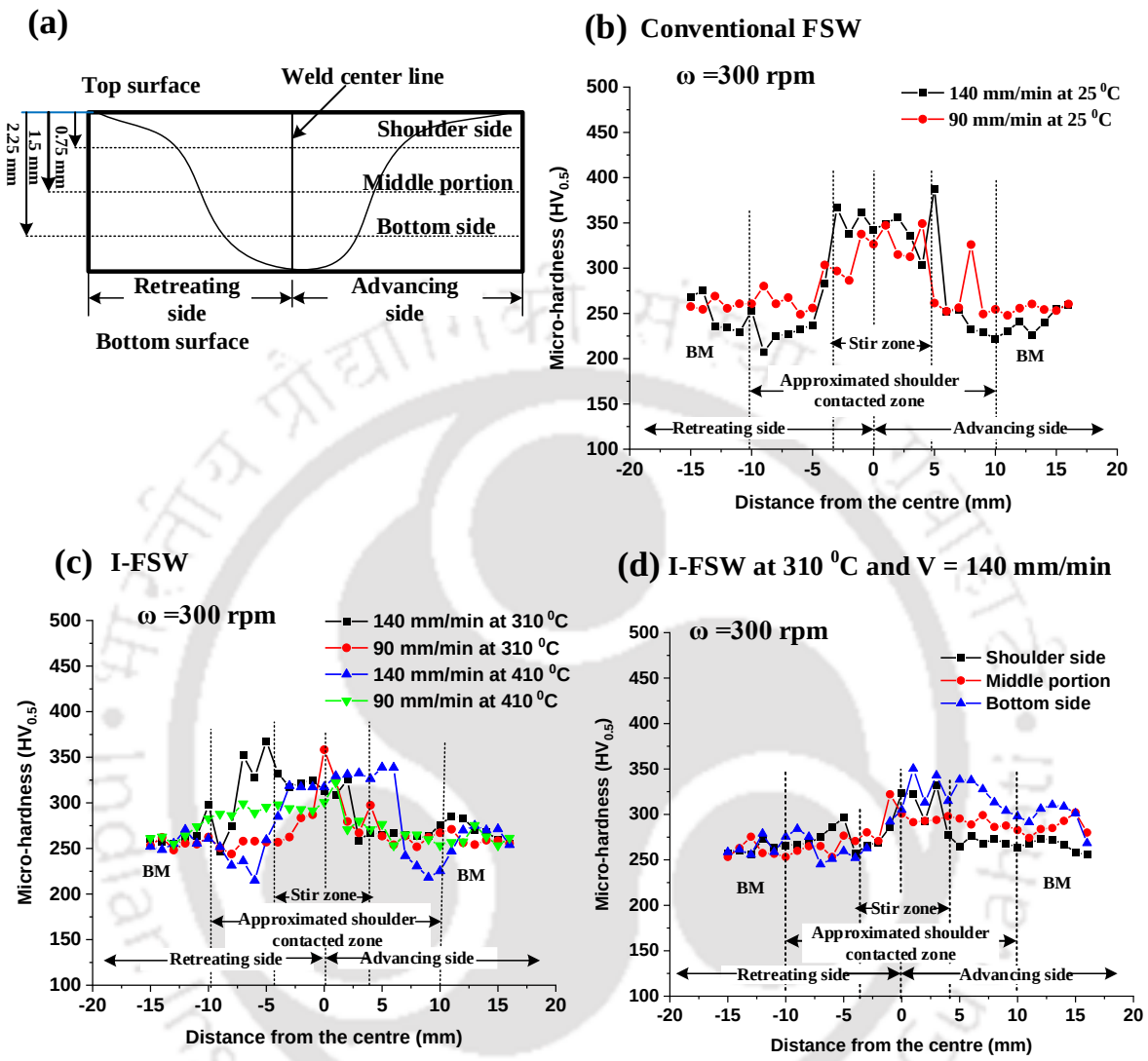

Fig. 5.14 (a) Schematic representation of hardness measuring line and Hardness distribution curve obtained during the (b) conventional FSW, (c) I-FSW, and (d) its variation through the thickness.

Figure 5.15 shows the top views of tensile-tested specimens with the stress-strain curve obtained at different welding parameters and preheating conditions. Under the conventional FSW, Figs. 5.15 (a-b) shows the fracture location of welded samples obtained at a traverse speed of 90 mm/min in the base material, whereas it was in the weld region at 140 mm/min. However, in all the induction-assisted FSW, the fracture location of tensile specimens was in the TMAZ except for samples welded at 140 mm/min under the preheating temperature of 310 ^{o}C, as shown in Figs. 5.15 (c to f). The fractured location of the tensile sample welded under

high traverse speed (i.e., 140 mm/min) and low preheating temperature (i.e., 310 ^{o}C) was observed in the base material, as shown in Fig. 5.15 (d). The fracture location of the tensile specimens in the base material conforms to the higher joint strength than the fracture in the weld zone.

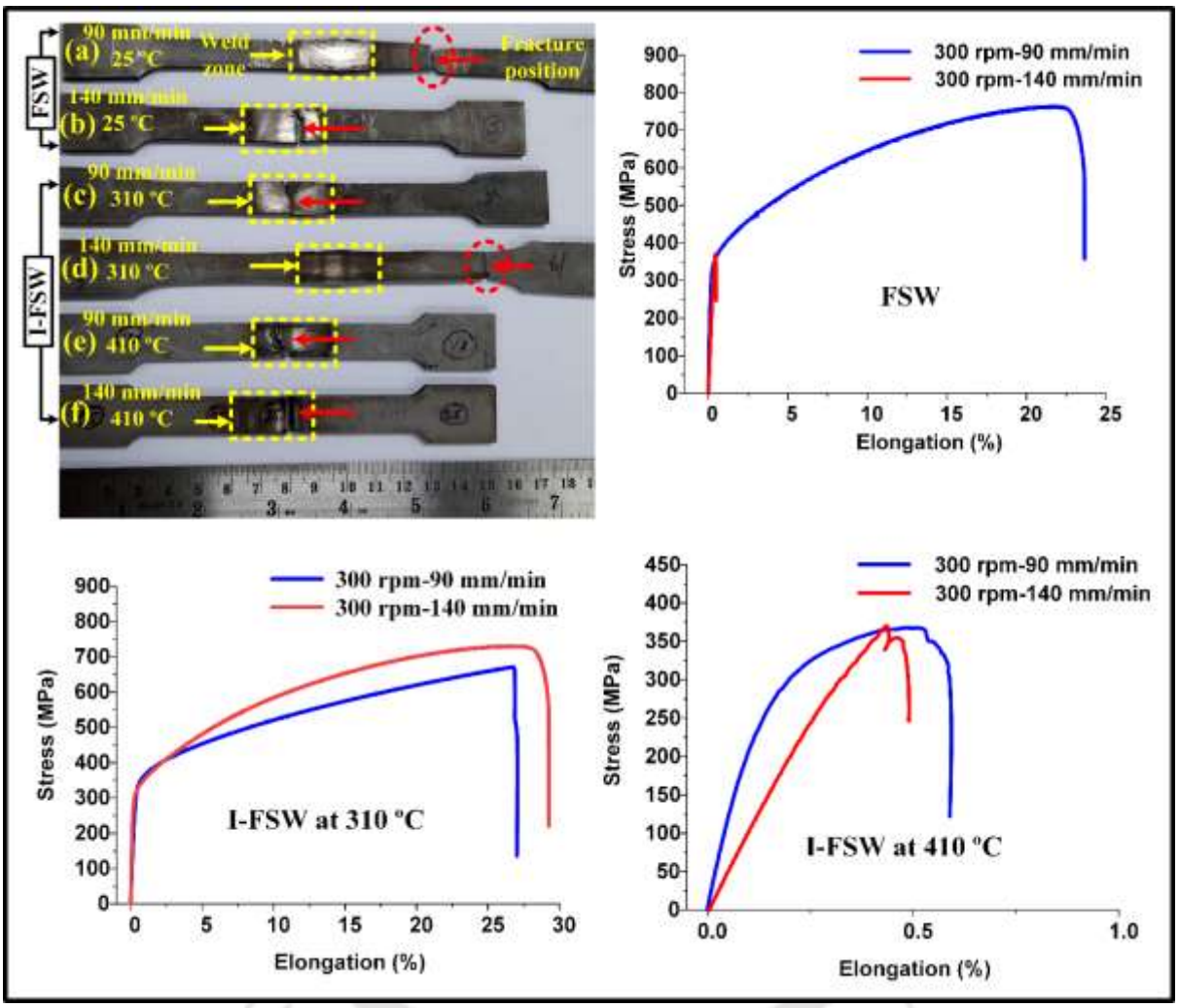

Fig. 5.15 Top view of the welded tensile samples and their corresponding tensile curve obtained at different weld conditions.

The average tensile strength with corresponding elongation results of the welded joints obtained in conventional and preheated FSW at different weld parameters are presented in Fig. 5.16. It is well known that defects such as micro-voids, cracks, and wormholes are responsible for producing stress concentration during the tensile test of welded specimens. The ultimate tensile strength (UTS) and elongation of the base material under the tensile load were recorded at 745 MPa and 35%, respectively. Under the conventional FSW process, the maximum tensile strength with high elongation (i.e., 750 MPa & 27%) was recorded at 90 mm/min traverse speed. The increase in weld strength may be caused by defect-free weld with a fine grain size

in the weld zone. The decreased weld strength with minimum elongation (i.e., 0.5%) was observed with increasing the traverse speed (i.e., above 140 mm/min). At high traverse speed (i.e., above 140 mm/min), the wormhole defect on the advancing side was found due to insufficient heat input and improper material mixing, resulting in decreased weld strength [113].

The weld strength under the I-FSW process was observed to be significantly affected by the preheating temperature. The ultimate tensile strength and elongation of the weld joint obtained at traverse speed 90 mm/min and 310 ^{o}C preheating temperature were 698 MPa and 26%, respectively, slightly lower than the conventional FSW. Whereas at high traverse speed (i.e., 140 mm/min) with the same preheating (i.e., 310 ^{o}C), improved weld strength (i.e., 740 MPa) and elongation (i.e., 28%) were recorded. At high traverse speed and low preheating temperature, 98.9 % weld strength and 26% elongation of the base material were recorded. The combined effect of traverse speed and local preheating caused excess heat generation, resulting in flash generation and the formation of a coarser microstructure. The increase of weld strength at high traverse speed (i.e., 140 mm/min) under the I-FSW process may be caused by fine grain structure with the cluster of fine carbide particles and the formation of intermetallic phases in the weld nugget zone. The proper intermixing of the material particles at a traverse speed of 140 mm/min compared with the 90 mm/min makes its defect-free joint which highly influences the weld strength. The change of microstructure and weld thickness reduction highly affected the weld strength obtained at different traverse speeds. Besides, a significant decrease in joint strength and elongation at 410 ^{o}C preheating temperatures were recorded under both traverse speeds (i.e., 90 and 140 mm/min). A sudden reduction of tensile strength and ductility of the weld joint was observed when used at a high preheating temperature above 310 ^{o}C. The generation of thick flash during the welding under excess local preheating decreased the weld zone thickness, and the formation of a large cavity with coarser grain in the TMAZ highly affected the weld strength. Ji et al. [71] also reported a similar report for the weld strength under the back heated FSW.

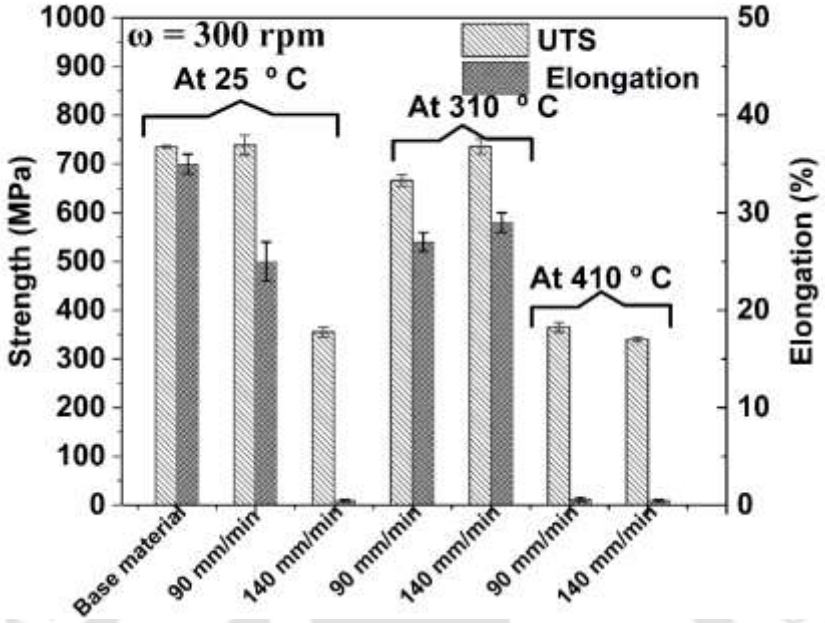

Fig. 5.16 Tensile strength and the corresponding elongation of the FS welded sample were obtained under different weld conditions.

Furthermore, in order to investigate fracture features of tensile tested specimens under conventional and preheated FSW were investigated with FESEM. Figure 18 shows the SEM micrograph of the tensile fractured surface, which was welded at a 140 mm/min traverse speed under the conventional and preheated (310 ^{o}C) FSW. The mode of fracture in the weld nugget zone under conventional FSW was examined by the elongation results (from Fig. 5.16) and the SEM micrographs of the fractured tensile specimens. The presence of flat surfaces and small dimples can be observed in the SEM micrograph, resulting in a mixed mode of fracture, as shown in Fig. 5.17 (a). The tensile curve (Fig. 5.16) indicates that the weld fractured with only 0.5% elongation, i.e., significantly less plastic deformation confirmed the dominant fracture mode was brittle. Compared with conventional FSW, the welded samples obtained at a preheated temperature of 310 ^{o}C and 140 mm/min traverse speed were fractured with 26% elongation. The fractured surface of the I-FSW joint in Fig. 5.17 (b) shows plenty of dimples with small size carbide particles. The presence of dimples with high elongation indicates a typical ductile mode of fracture.

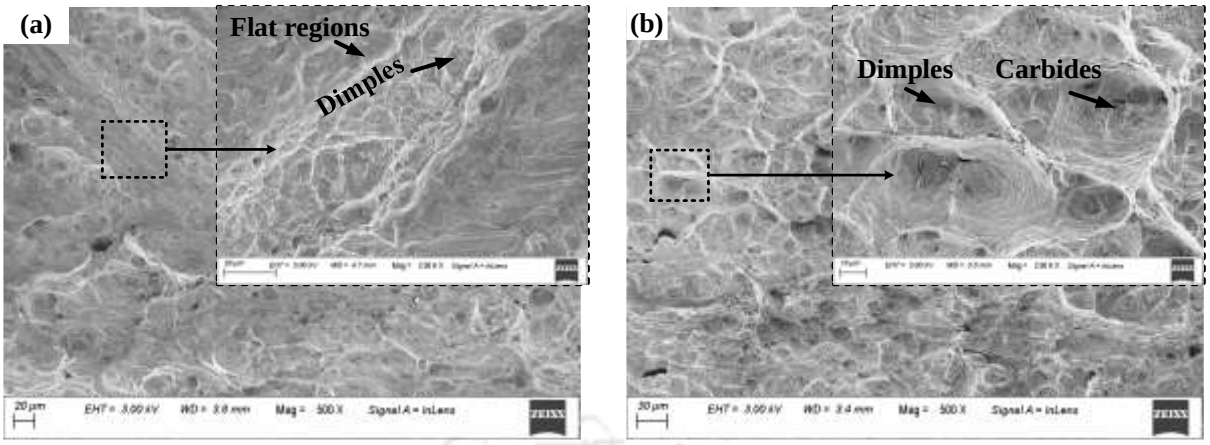

Fig. 5.17 SEM micrograph of the fractured tensile surfaces of welds obtained at 140 mm/min traverse speed in (a) Conventional FSW and (b) I-FSW

5.3.5 Tool wear during conventional and induction-assisted FSW

Welding high-strength materials such as nickel, titanium, and steel is very challenging regarding tool life, which directly affects the cost of the welding process. During the FSW process, the generation of high frictional heat due to rotational and traverse motion of the tool and the generation of high axial thrust on the FSW tool are highly responsible for wear, plastic deformation, and failure causes the diminishing of the tool life [77]. Hence, studying tool wear to improve tool life is key in selecting welding processes and parameters.

Figure 5.18 shows the top and front macrographic views of the WC-Co tool used in all cases during the welding of Inconel 718. Visual inspections of the deformation of the tool in terms of pin height and weight loss were performed. The observation was conducted under the tool rotational speed of 300 rpm, traverse speed of 140 mm/min, and preheating temperature of 310 ^{o}C. Figure 5.18 (a) shows the tool pin height of 2.7 mm before welding. After the completion of the welding process in conventional and preheated FSW, the observation shows that the tool shoulder and pin height lost their original geometry.

The maximum wear was observed in the tool pin, reducing its length in every weld length (i.e., 200 mm). Under the conventional FSW, it can be seen that after the 3rd weld length (i.e., after 600 mm), the tool pin height reduced to 1.9 mm, which was 71% of the original height, as shown in Fig. 5.18 (b). The loss of the tool pin height after 600 mm weld length was found less in induction preheating FSW than in the conventional FSW. From Fig. 19 (c), it is clearly observed that the height of the pin after the 3rd weld was 2.4 mm, which was 89% of the original tool pin size used in the I-FSW process.

The difference in tool weight under the conventional and induction preheated FSW process is shown in Fig. 5.18 (d). The weight loss of the tool was measured with micro balance before and after every weld length. The initial weight of the tool before the welding was 245 g. In the conventional FSW after 600 mm weld length, the loss of weight was found high (i.e., loss of 0.32 g) compared to the preheated FSW (i.e., loss of 0.05 g). The main cause of the weight loss was the reduction of tool pin height, shoulder wear, and an oxide layer formation near the shoulder edge. EDS analysis of the tool shoulder was performed near the pin base area, as shown in Figs. 5.18 (e, f). It can be seen that the reduction of wt.% of W (tungsten) element and the formation of an oxide layer occur on the contact surface of the tool after welding. In addition, the presence of Ni, Mo, Al and Cr elements on the shoulder surface was found from the base material due to the adhesion nature of the WC tool element. The carbide fracture and cobalt extrusion at high temperature and pressure during the welding is the primary mechanism of wear of the tool reported by Tiwari et al. [144] in their research study. Saving of tool wear in preheated FSW process was found due to the reduction of axial force on the tool and improved thermo-plasticization of the Inconel 718 material. In their research study, Ramkumar et al. [160] reported that an external preheating process reduced the generated torque and tool deformation during the welding.

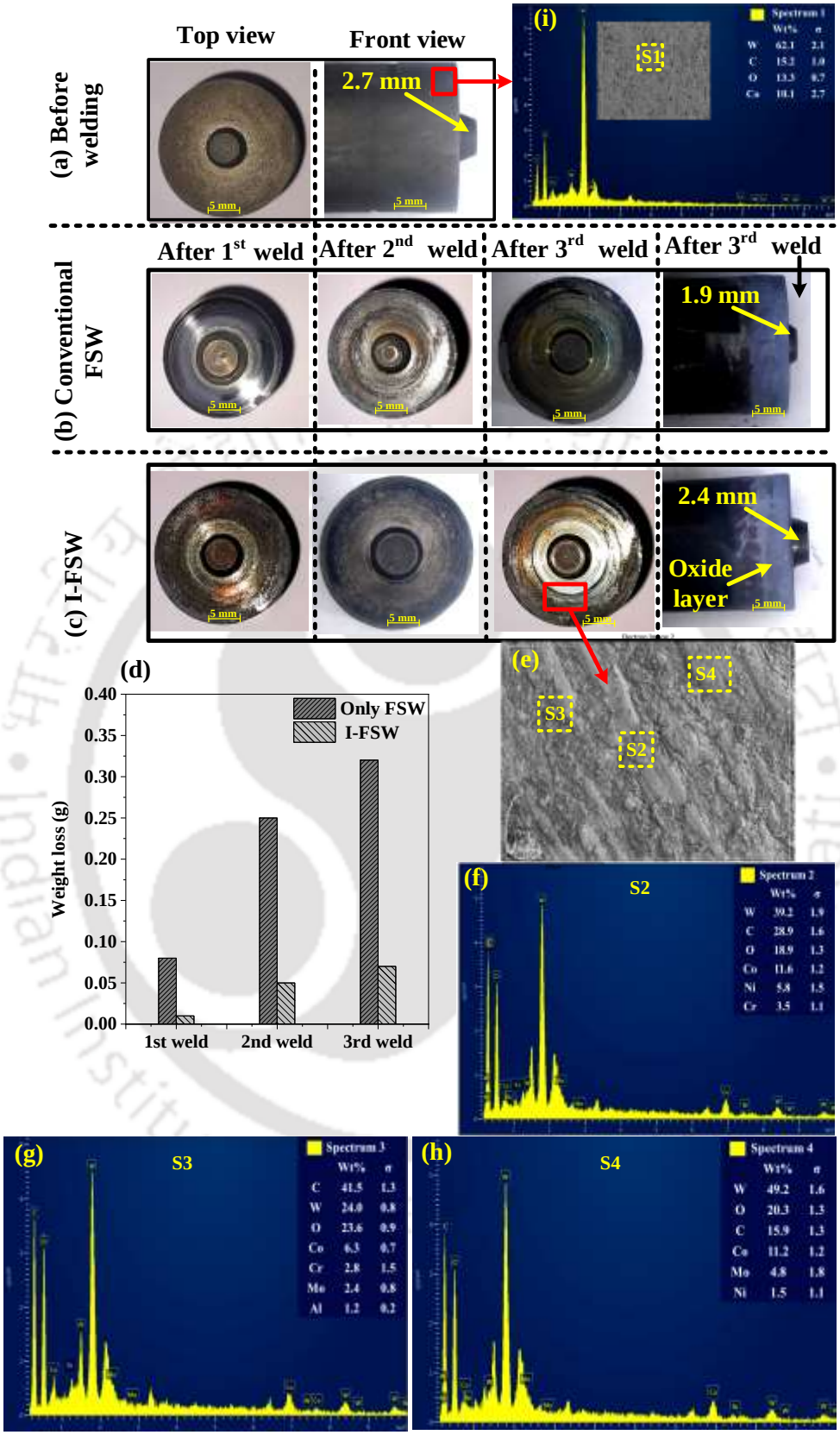

Fig. 5.18 Top and front views of the FSW tool (a) before welding, (b) after conventional welding, (e) after I-FSW, and its analysis represented in (d) weight loss graph, (e) tool shoulder portion and (f-i) EDS analysis of tool shoulder.

5.4 Brief scientific discussion

The application of the induction preheating during the FSW process at high traverse speed (140 mm/min) soften the material which gives proper intermixing of the material. The rise in microhardness in the SZ was a result of the formation of a microstructure consisting of small grains, brought about by the dynamic recrystallization process and the presence of precipitates inside the grain. Compared with conventional FSW joint, the hardness value of induction-assisted FSW joint was observed slightly decreased because of the small increase in the microstructure. A sudden increase in hardness curve value was also observed in the weld zone due to fine carbide particles and the generation of some phases during the I-FSW process. Similarly, the combined effect of traverse speed and local preheating caused excess heat generation, resulting in flash generation and the formation of a coarser microstructure. The increase of weld strength at high traverse speed (i.e., 140 mm/min) under the I-FSW process may be caused by fine grain structure with the cluster of fine carbide particles and the formation of intermetallic phases in the weld nugget zone.

5.5 Summary

The present work emphasizes the effect of high-frequency induction heating on the temperature distribution, microstructure and mechanical properties during the joining of the Inconel 718 plate by the FSW process. Also, axial force and tool wear analysis in the conventional and induction-assisted FSW process was performed. Thus, the following conclusions are summarized based on the results and discussion:

- Under the fixed position, the high-frequency induction heating device achieved a sample surface temperature of 310 ^{o}C, 410 ^{o}C and 700 ^{o}C at 7 kW, 12 kW, and 18 kW output power within 30 sec, respectively. During the transport condition of the induction device at a feed rate of 140 mm/min, a sample surface temperature achieved 310 ^{o}C at 12 kW output. Thus, the material surface temperature was proportional to the output power of the heating device and inversely to the feed rate.
- The generation of flash during the welding was directly proportional to the induction preheating temperature, which highly affected the weld strength.
- The use of high-frequency induction preheating reduced the axial force of FSW by 26%, which operated under 140 mm/min traverse speed. This reduction of axial force effectively reduced the tool wear and improved the tool life due to the softening of the material.

- Due to dynamic recrystallization during the conventional FSW, highly deformed grain structure and uniform distribution of carbide particles in the weld zone led to good weld quality at 90 mm/min traverse speed. The preheating effect observed a slight increase in grain structure with cluster distribution of primary and secondary carbide particles (i.e., NbC and $M_{23}C_6$) in the grain. A slow cooling rate resulted in good weld quality at a high traverse speed of 140 mm/min, which was 1.55 times faster than the normal FSW.
- The preheating effect reduces the external tungsten (W) element in the weld nugget zone. In contrast, the Oxide formation in the stir zone due to local heating resulted in a change in metallurgical properties.
- With the induction preheating, the mechanical properties were improved at high traverse speed (i.e., 140 mm/min) due to grain refinement and proper bond formation compared with conventional welding. The maximum hardness value in the SZ increased by 63% from the base material during the conventional FSW at a 140 mm/min traverse speed. In contrast, a small reduction in microhardness was observed under the preheated FSW. The tensile strength increased from 360 MPa (FSW) to 748 MPa (I-FSW), i.e., 98.6% of base material strength. The tensile fracture surface exhibited a presence of high dimples with small-size carbide particles, confirming the ductile mode of failure.

----------*----------*----------*:

CHAPTER 6

6. Friction Stir Welding of Dissimilar Inconel 718 and AISI 204cu Steel

6.1 Introduction

This study explored the feasibility of friction stir welding of dissimilar butt joints of Ni-based superalloy Inconel 718 and low-cost austenitic stainless AISI 204Cu. The conventional welding of dissimilar alloy poses different challenges due to differences in chemical and physical properties, such as proper filler material selection, weld zone cracking, and segregation defects, ultimately resulting in unfavourable weldability and mechanical properties. Therefore, producing high-quality joints between Ni-alloy and stainless steel by controlling heat input requires systematically investigating a promising alternative advance joining technique, friction stir welding. The primary area of interest is to investigate the process parameters of the FSW to obtain a defect-free weld. In previous literature, the complex relationship between microstructure and mechanical properties of dissimilar weld joints of Inconel 718 with AISI 204Cu is not studied systematically. After welding, the mechanical and microstructural properties of joints were analyzed.

6.2 Materials and methodology

Experiments have been carried out on Inconel 718 and austenitic stainless-steel AISI 204Cu sheets having dimensions of 200 mm × 80 mm × 3 mm by the conventional FSW process in annealed condition using WC-10wt.%Co tool. According to the supplier, the average alloy composition (in wt.%) and mechanical properties are discussed in chapter 3, Table 3.1. The used cylindrical tool had a 20 mm diameter flat shoulder and a 2.7 mm long tapered pin, as shown in Fig. 6.1 (a). A tapered pin geometry was 7–5 (shoulder side - free end). The schematic outline of the FSW process is shown in Fig. 6.1 (b). The experimental setup, working principle, and methodology used in this experiment are explained in chapter 3, Sections 3.2 and 3.3.

The input process parameters used in this experiment were chosen based on the visual inspection, and the macrograph of the joints obtained in several experimental trials is depicted in Table 6.1. The experiment was conducted at varying traverse speeds of 40, 70, 90 and 140 mm/min while keeping the rotational speed constant, i.e. 300 rpm. Providing the low rotational speed was based on the experimental trials and the author's previous study based on the similar

welding of Inconel 718. Kanhazian et al. [116] and Shamanian et al. [109] reported that positioning of higher tensile strength material (i.e., stainless steel) on the advancing side gives good strength. The higher heat on the advancing side is helpful to the flow of material from the advancing side (AS) to the retreating side (RS). In this study, the AISI 204Cu plate was placed on the advancing side (AS) and Inconel-718 on the retreating side (RS). This was done to avoid the formation of cavities or groove-like defects in AS.

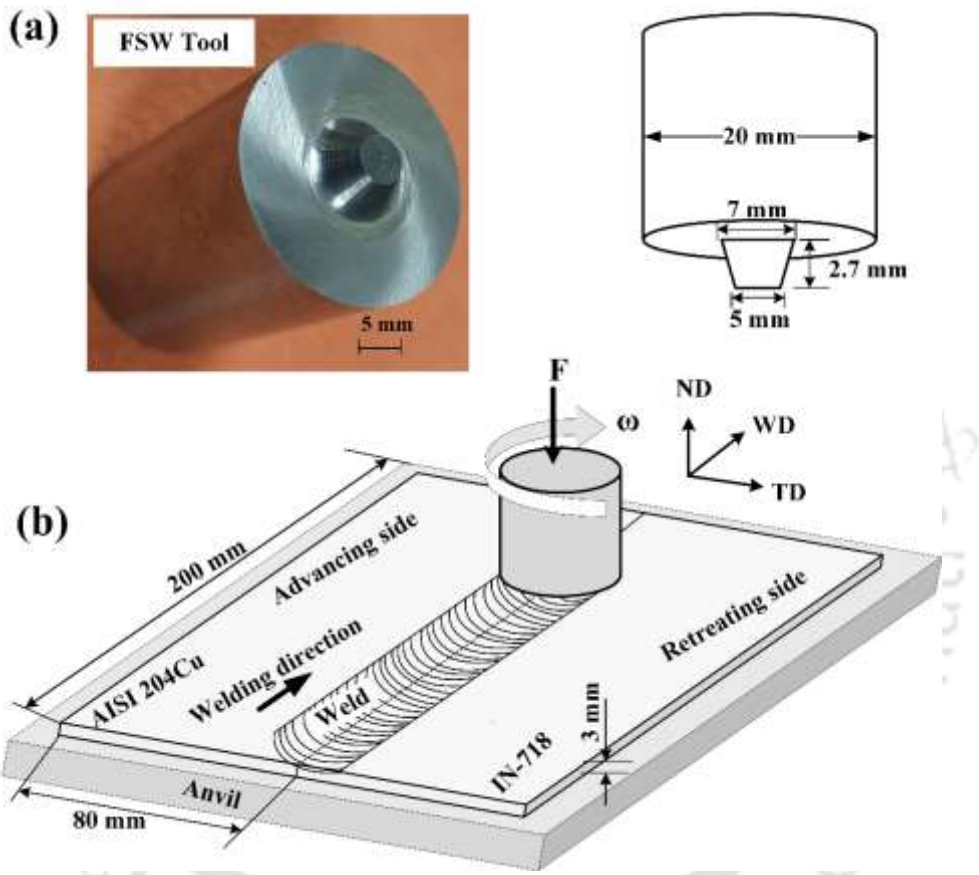

Fig. 6.1 (a) FSW tool and its schematic view and (b) Schematic diagram of FSW process.

Table 6.1 Process parameters used in dissimilar FSW.

Test number	Tool rotational speed (ω; rpm)	Welding speed (v; mm/min)	Retreating side (RS)	Advancing side (AS)
Test 1	300	40	IN-718	AISI 204Cu
Test 2	300	70	IN-718	AISI 204Cu
Test 3	300	90	IN-718	AISI 204Cu
Test 4	300	140	IN-718	AISI 204Cu

6.3 Results and discussion

This section discusses the microstructural and mechanical analysis outcomes in detail.

6.3.1 Macro and microstructural evolutions

6.3.1.1 Microstructure of the base materials

Figure 6.2 displays the microstructure of the base materials utilized in this study, namely Inconel 718 and AISI 204Cu alloys, both of which were annealed. In Fig. 6.2 (a), the ϒ austenitic matrix of IN718 clearly exhibits the presence of twin boundaries and carbide particles. The existence of MC-type carbide particles (where M: Nb, (Nb, Ti) or (Ni, Nb, Ti, Cr)) in the grains and their boundaries were previously ascertained by means of FESEM-EDS spectroscopy. The presence of these twin boundaries and strengthening precipitates impede dislocation movement, which increases the strength of Inconel 718 [55]. Similarly, Fig. 6.2 (b) shows little twin boundaries with full ϒ, austenitic matrix, with MC-type carbide particles in AISI 204Cu alloy. Grain size analysis of the microstructure of both the BMs- IN718 and AISI 204Cu showed coarse grain with an average grain size of 55 μm and 30 μm, respectively.

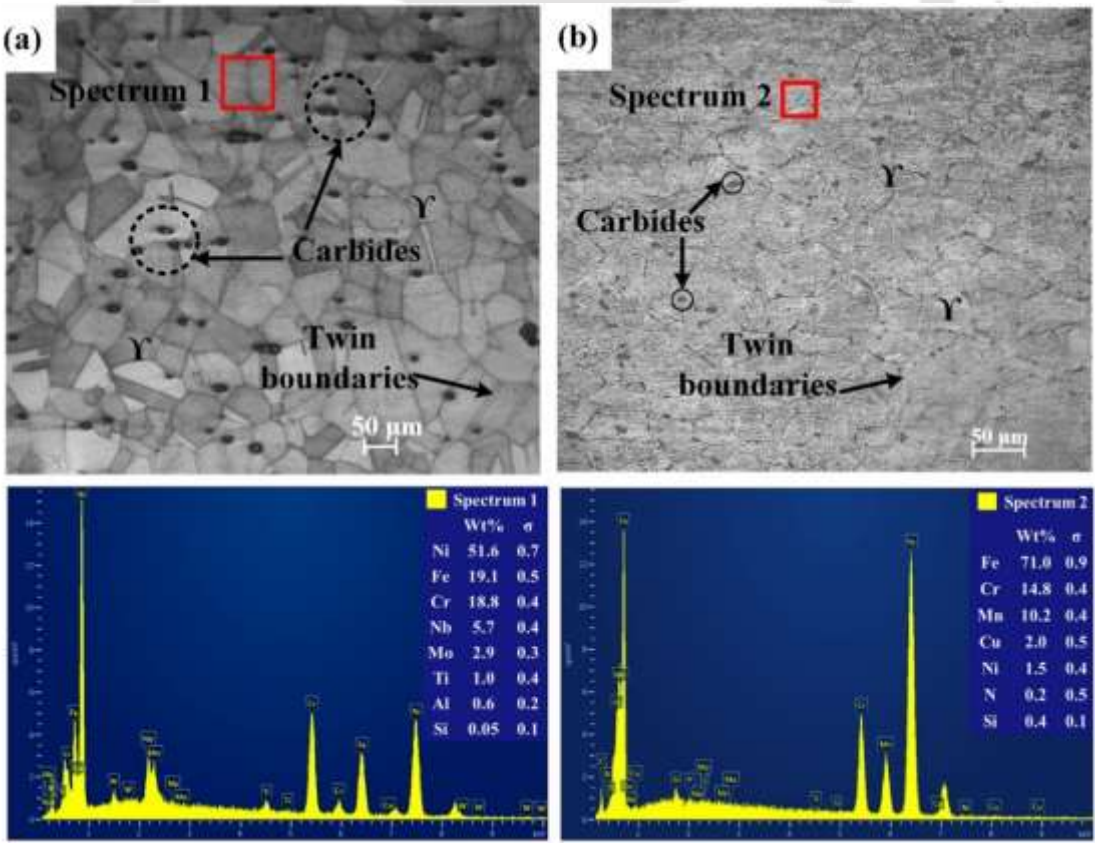

Fig. 6.2 Microstructure of the base material (a) Inconel 718 and (b) AISI 204Cu.

6.3.1.2 Macrostructure and microstructure observation of the welded joints

Figure 6.3 shows the top and cross-sectional macrostructure views of the friction stir welded dissimilar Inconel 718 - AISI 204Cu joints obtained at various welding parameters. Figs. 6.3 (b) and (c) show the smooth surface appearance with defect-free FSWed joint obtained at traverse speed 70 and 90 mm/min and constant rotational speed 300. However, weld surface defects like macro-grooves were found at 40 mm/min and 140 mm/min traverse speed, as shown in Figs. 6.3 (a) and (d). Apart from this defect, reduction of weld thickness (i.e., weld thinning) due to a plunging depth of the tool shoulder and keyhole defect at the end of the weld caused by retraction of the tool pin was also observed in all the weld parameters. The inherent issues such as keyhole, weld thinning, and internal defects always affect joint formation [163].

The welding was performed at a constant rotational speed of 300 rpm, which was chosen based on several experimental trials and the visual inspection of the welded surface. The flash generation and welded surface quality at a rotational speed of 300 rpm were observed as minimum and smooth, respectively. Our previous investigation (discussed in chapter 4) also observed that the FSW of Inconel 718 resulted in a sound weld at low rotational speed (i.e., 300 rpm).

The transverse cross-sectional views (in Fig. 6.3) of all the FS welded samples illustrate the effect of traverse speed on the material flow patterns. In this figure, the dark region or RS is Inconel 718, whereas the light region or AS is stainless steel 204Cu. The optical macroscopic observation of the welded samples shows the formation of basin-shaped morphology with the vortex-like shape of material flow in the weld zone. Similar morphology has also been observed by Kangazian et al. [116] in dissimilar FSW of Inconel 625 with mild steel. The plastic deformation and material flow caused by the tool rotation and movement during welding are generally responsible for weld strength. Cross-sectional observation revealed that certain sections of the Inconel 718 material were pulled from the RS to the AS. At 70 and 90 mm/min traverse speeds, Inconel material fully moved to the steel region in the upper part of the SZ. In contrast, the movement of the Inconel material from the RS to the AS in the SZ was partially at traverse speeds of 40 and 140 mm/min. At low and high traverse speeds (i.e., 40 and 140 mm/min), the gap between the dragged Inconel material and extreme part of SZ in the AS was 0.8 and 2 mm, respectively, whereas it was 0.2 and 0.1 mm in the case of 70 and 90 mm/min traverse speed, respectively. Inconel material which is inside the SZ obtained at 70 and 90 mm/min traverse speed, was observed in a layered manner (represented by yellow arrow),

whereas it was negligible at 40 and 140 mm/min. The difference in heat input at varying traverse speeds generates a difference in the volume of Inconel material in the SZ. At low traverse speed, the accumulation of heat is high and the cooling rate low, whereas at high traverse speed, the accumulation of heat is low, and the cooling rate is high [115]. A macrocrack at the extreme lower portion in the AS of the welded joint was observed at 40 mm/min, which is represented by a black arrow, affecting the weld strength. The lack of material mixing at very low traverse speed and moderate weld joint formation during the FSW of Inconel 718 was also reported in previous work. From the surface appearance and the cross-sectional view of Test 2 and Test 3, we could say that materials were completely intermixed, and no defects were displayed.

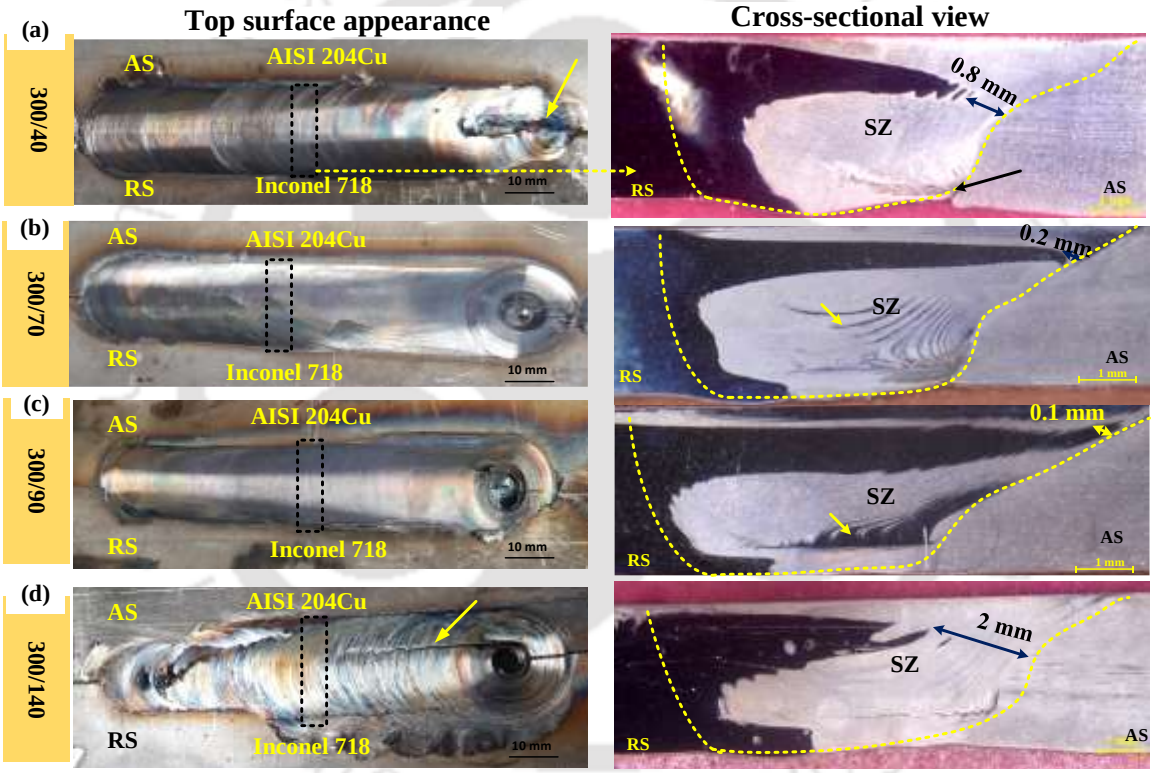

Fig. 6.3 Welded top surface view with a corresponding cross-sectional view at a varying traverse speed.

The details of distinct regions obtained with optical microstructure in Test 2 (i.e., obtained at 70 mm/min) sample is shown in Fig. 6.4. The cross-section of the weld shows the base metal (BM), which is outside of the basin-shaped region. At the centre of the weld region, the stir zone (SZ) and the thermo-mechanical affected zone (TMAZ) were observed adjacent to the SZ. The presence of heat affected zone (HAZ) was not clearly observed for both alloys. This could be the combined effect of the fast cooling rate during FSW and the physical properties

of the parent metals. Shamanian et al. [109] also observed the presence of different regions during the study of dissimilar FSW joints of Inconel 825/SS316L. The generation of distinct microstructural regions was observed caused by the variation of grain structure and the material flow pattern. The microstructure of the base metal of both alloys shows a coarse grain, which is explained in section 6.3.1.1. The microstructure of the SZ of Inconel 718 and AISI 204Cu are shown in Fig. 6.4 (c) and (d), respectively, which shows a more refined grain structure than the base metal. Mishra et al. [5] reported that a combined effect of high strain and high temperature results in dynamic recrystallization phenomena in the nugget zone. The distribution of grains in the SZ was found in the range of 2 to 23 μm in Inconel 718, whereas it was 2 to 14 μm in the case of AISI 204Cu. Fig. 6.4 (b) and (f) represent a narrow region of TMAZ microstructure, where the distribution of grain size was in the range of 5 to 35 μm in the Inconel 718 region, and it was 6 to 25 μm in the AISI 204Cu region. From the observation of TMAZ of AISI 204Cu, the fine equiaxed grains with some elongated grains were observed compared to the fine equiaxed grains in TMAZ of Inconel 718. The grain microstructure of TMAZ on both sides (i.e., in AS and RS) was deformed and found to be slightly larger than the SZ. The grain size variation was observed due to the difference in thermal cycles, and plastic deformation in the SZ was higher than in the TMAZ, resulting in incomplete recrystallization in the TMAZ region. Shamanian et al. [109] and Fernandez et al. [164] also reported similar observations about TMAZ formation during the FSW of Ni-based alloy with stainless steel. In the SZ, the material flow pattern at the bottom portion near the AS is shown in Fig. 6.4 (e) and at the upper portion in Fig. 6.4 (g). The macrostructure at the bottom portion of the SZ had a vortex-like pattern, and the lamella pattern was observed at the upper part. The difference in temperature distribution and the difference in mechanical properties of dissimilar materials may cause disruptive material flow in the SZ. Pankaj et al. [113] also reported a similar material flow pattern during the FSW of DH36 with the AISI-1008 steel.

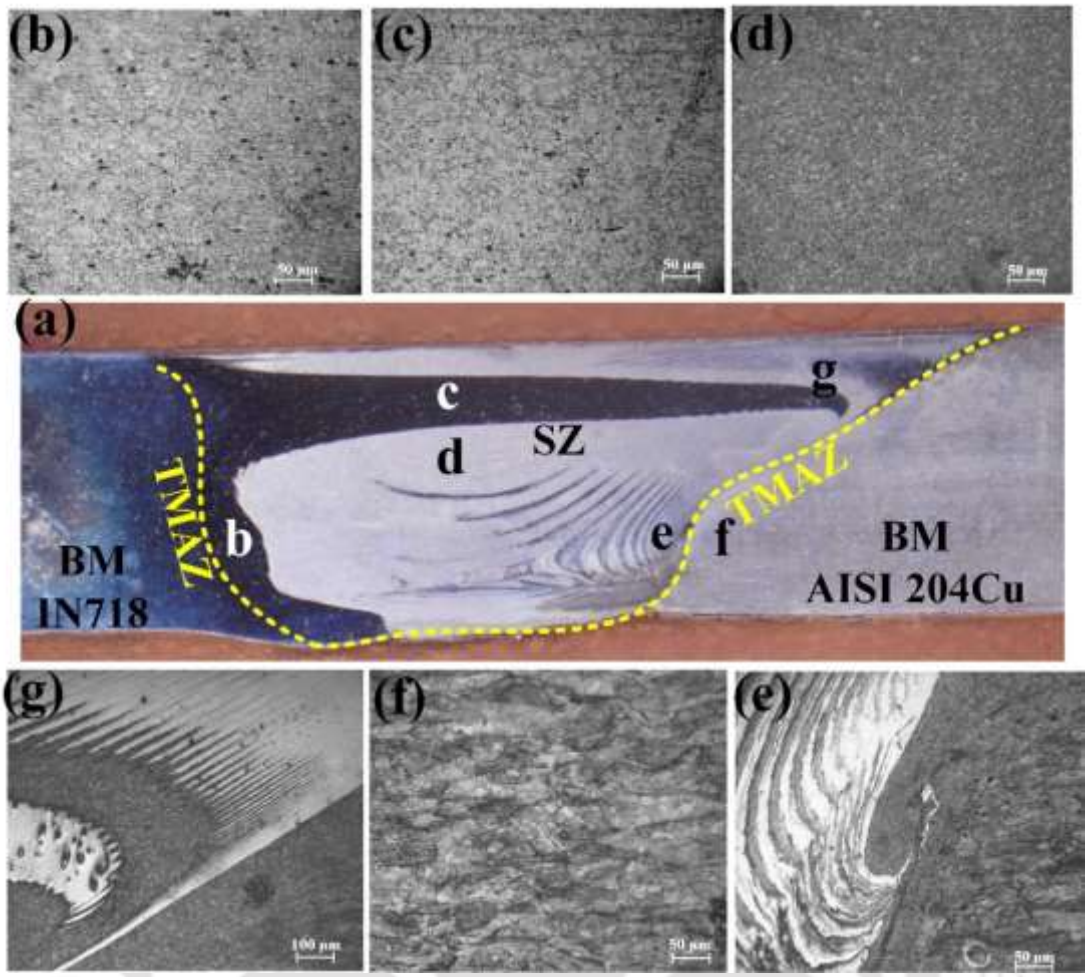

Fig. 6.4 Microstructure of welded joint obtained at traverse speed 70 mm/min in a different region (b) TMAZ of Inconel 718, (c) SZ of Inconel 718, (d) SZ of AISI 204Cu, (f) TMAZ of AISI 204Cu and (e and g) material flow behaviour.

The microstructure of SZs obtained at the different traverse speeds 40, 70, 90 and 140 mm/min were analyzed to study the significant effect of varying traverse speeds on the grain refinement. The measured average grain size of Inconel 718 was 5.5, 4.3, 3.2 and 2.6 µm, whereas it was 7.15, 7.04, 6.07 and 6.2 µm for AISI 204Cu at traverse speeds 40, 70, 90 and 140 mm/min, respectively, as shown in Fig. 6.5. In the weld nugget zone, both the materials' average grain size was observed fine at 40 mm/min, whereas it was finest at 140 mm/min. The grain size variation with traverse speed was observed due to the difference in heat input and cooling rate during the FSW.

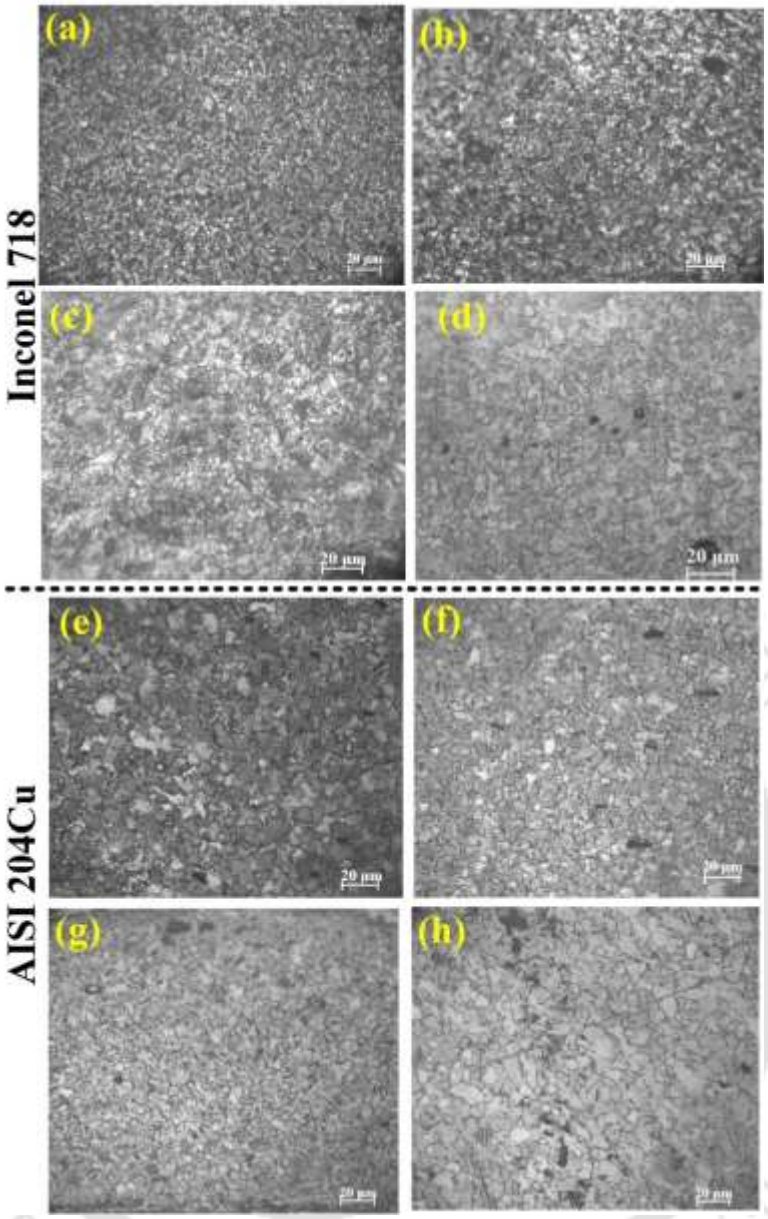

Fig. 6.5 Optical microstructure of (a-d) Inconel 718 SZs and (e-h) AISI 204Cu SZs, both obtained at varying traverse speeds (40, 70, 90 and 140 mm/min), respectively.

6.3.1.3. Metallurgical characterization of welded joints

Figure 6.6 shows the microstructure of the weld nugget zone of the Test 2 sample obtained at 70 mm/min. The cross-sectional view of the nugget zone reveals the alternate layer of steel corresponds to the dark-etching regions, and Ni-alloy corresponds to the light-etching regions, as shown in Fig. 6.6 (a). SEM analysis was performed corresponding to the borders of steel and Ni-alloys, SZ of steel and Ni-alloy and deformed zone, which is distinct from the similar FSW joint. Figures 6.6 (b) and (c) show typical SEM images of two different interface regions

found in the stir zone. The formation of the intermetallic layer at the interface regions was not observed, which is generally formed in dissimilar FSW welding of low melting point (Al/Mg) with steel [25,165]. In the Ni-alloy region corresponding to the stir zone, some more refined carbide particles than base material were observed, as shown in Fig. 6.6 (c). The point EDS spectrum 1 confirmed the presence of (Nb)C carbide particles. In contrast, a magnified SEM image of the selected area (Fig. 6.6 (c)) corresponding to spectrum 2 confirmed (Ti, Nb)C particles. The presence of low-temperature carbide particles was also observed by Song et al. [40] during the FSW of Inconel 718.

However, the microstructural details of fine-grained AISI 204Cu and Inconel 718 of different regions d & e (in Fig. 6.6 (a)) were examined with Fig. 6.6 (d) and (e), respectively. The microstructures of the Inconel 718 show more refined grains (i.e., 4.3 µm) than those of the base material grains (i.e., 55 µm). The random distribution of the fine carbide particles (marked with a yellow arrow) within the grain and its boundaries were observed, as shown in Fig. 6.6 (e). The grain refinement in the SZ resulted from the combined effect of high strain and high temperature produced during the FSW. The dynamic recrystallization (DRX) mechanism inside the weld nugget zone is generally influenced by the stacking fault energy (SFE), deformation temperature, strain rate and initial microstructure of grains of the material [166]. It is well reported that Ni-alloy has low stacking fault energy (SFE) face-centered cubic (FCC) material due to the presence of alloying elements [167]. Mishra [5] and Song et al. [40] reported that alloys with low SFE lead to discontinuous dynamic recrystallization (DDRX) mechanisms. In contrast, the high SFE lead to continuous dynamic recrystallization (CDRX) during the FSW. Material with low SEF exhibits accumulation of dislocation inside the grains because of the difficulty of the cross-slip and climb mechanism, leading to grain refinement. Similarly, the grain refinement of the AISI 204Cu alloy in the nugget zone was observed with optical microstructure (Fig. 6.5 (f)), which was an average grain size of 7.04 µm compared to the base material (average grain 35 µm). The presence of the delta ferrite in the matrix of ϒ austenite can be observed in a high-magnification SEM image, as shown in Fig 6.6 (d). Shamanian et al. [109] and Cui [166] reported that during the FSW of austenitic stainless steel, ferrite (as low SFE) and austenite (as high SFE) phases undergoes CDRX and DDRX mechanism, respectively. In the SS 224Cu region, some ferrite phase was also observed in the austenite matrix, which is represented with a red arrow inside Fig 6.6 (d). The little ferritic phase was confirmed by the point EDS spectrum 3, which was chromium-rich crystallization within the original austenitic structure. In the previous chapter 5 authors mentioned the weld centre

temperature during FSW of 3 mm thick Inconel 718 at 140 mm/min and reported that the nugget zone temperature reached 937 ^{o}C. Furthermore, Rodriguez et al. [60] reported that the peak temperature during the dissimilar FSW of mild steel/ Inconel 625 reached as high as 1200 ^{o}C under 300 rpm and 100 mm/min parameters. In this study, the tool traverse speed (70 mm/min) is lower than the speed which was used by Rodriguez et al. [60] and the previous study. The lower traverse speed with the same tool rotational speed (300 rpm) would result in a higher temperature in the weld centre zone. Therefore, the materials in the nugget zone experienced severe plastic deformation and possibly achieved the transformation of austenite to the ferrite phase. The incorporation of copper in the austenitic structure of AISI 204Cu was also observed, which was confirmed with the EDS spectrum 4 (Fig. 6.6 (d)). The presence of some spherical-shaped particles of copper leads to an austenite stabilizer and reduces the work hardening problem [168].

A particular SEM microstructure of the layered mixing pattern obtained in the nugget zone near the bottom of the advancing side is shown in Fig 6.6 (f). A magnified image of the layered mixing pattern illustrates the dark and light etched band pattern was AISI 204Cu and Inconel 718, respectively. The point EDS analysis performed the elemental analysis of the dark band (spectrum 5) and light band (spectrum 6). In the layered pattern region of AISI 204Cu, some nickel (Ni) element was observed, which could come from the nearest Inconel 718 material. However, inside the Inconel 718 layered pattern, the presence of AISI 204Cu material was not found, whereas some refined (Ni, Nb, Ti)C carbide particles were confirmed with spectrum 6.

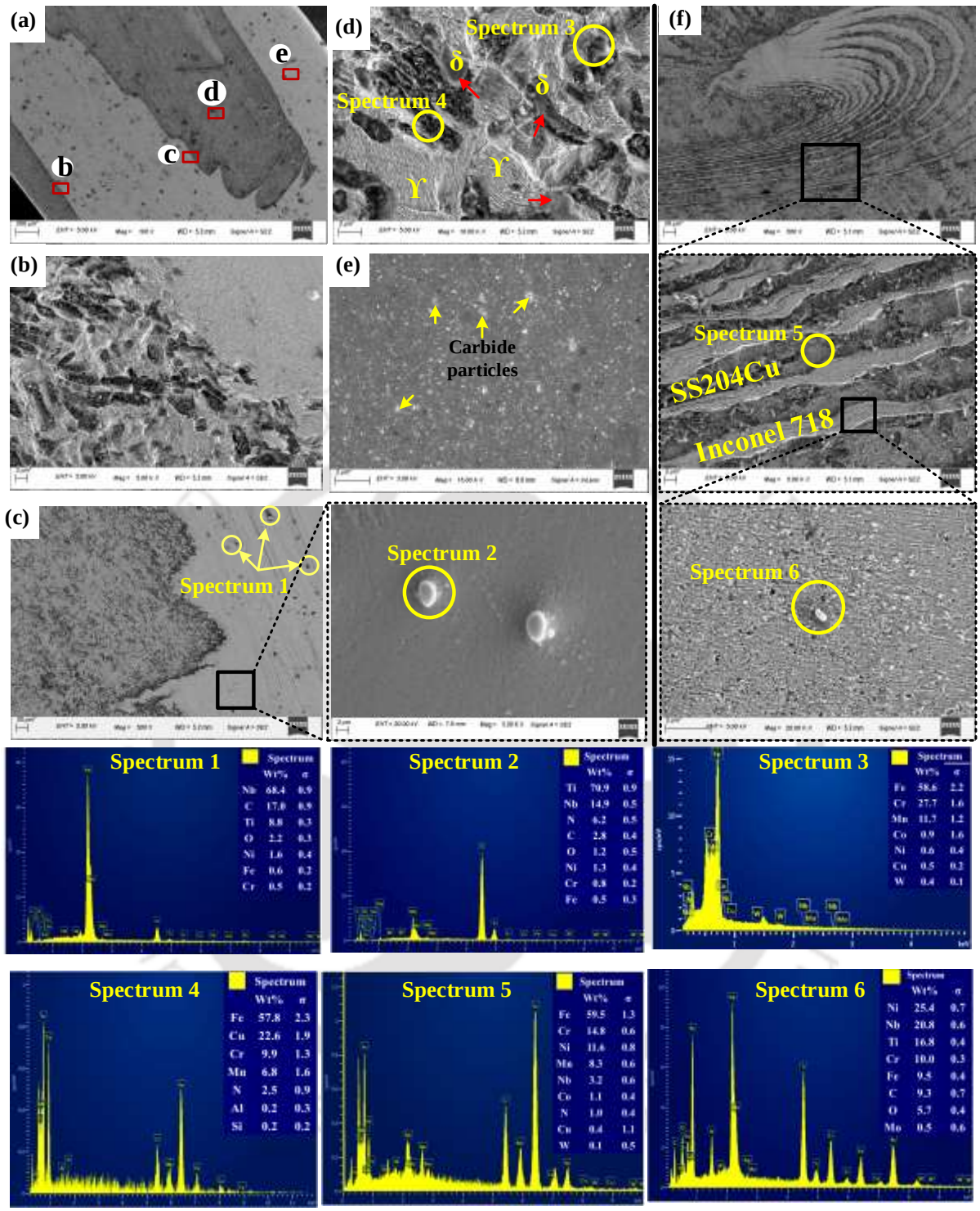

Fig. 6.6 SEM examination of the nugget zone of Test 2 specimen: (a) cross-section view of joint, (b-e) Magnified view of the area marked in (a), (f) Material flow pattern near AS of the joint, and EDS result of the corresponding spectrum 1to 6.

EDS mapping on the separated region in the stirring zone of the welded sample was used to analyze the distribution of elemental particles. For Test 2, the concentration of Fe and Mn elements in the central region was detected as high, which shows the stainless steel 204Cu, as

shown in Fig. 6.7. However, the distribution of Ni elements in the U-shaped region was maximum, and it was negligible in the steel region. A clear separate boundary of Inconel 718 and AISI 204Cu was observed at the interface region. The concentration of Cr elements in both areas was observed to be almost equal. Therefore, this analysis shows that both materials were fully separated in the stir zone. The EDS map analysis shows that the distribution of W and Co elements in both the region of the stir zone was found, which shows the presence of external elements from the tool wear.

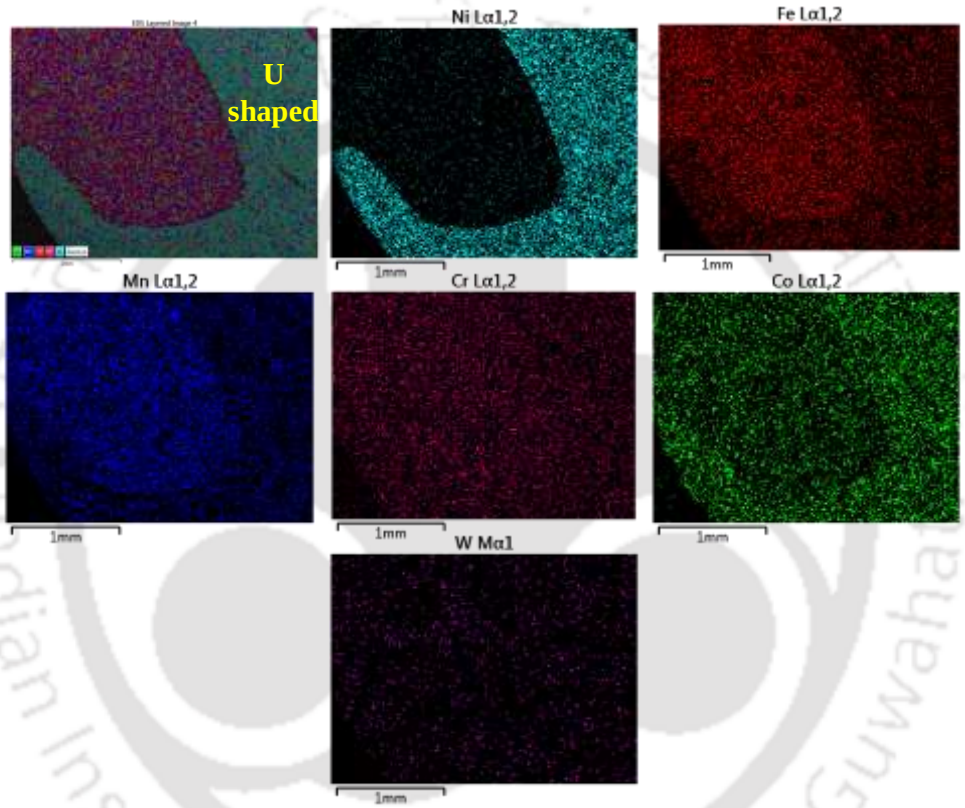

Fig. 6.7 EDS mapping in the nugget zone of the welded sample Test 2.

In the stir zone, an EDS line scan at the interface was also performed in the form of a chemical composition profile, as shown in the FESEM micrograph (Fig. 6.8 (a)). Two distinct positions at the joint interface region of steel and Ni-based alloy have been taken better to analyze the chemical composition and differentiated phase morphology. Fig. 6.8 (b) and (c) represent the EDS line scan results of the large scan region (denoted by Δ) and small scan region (denoted by *), respectively. The large scan region shows the distribution profile of all major elements (i.e., Ni, Fe, Cr, Mn, Nb and Mo) across the interface. In contrast, the small scan region shows the distribution profile of Ni, Fe and Mn elements. The line scan profile shows that an increase of Fe and Mn and a decrease of Ni, Cr, Nb and Mo were observed in the steel. The diffusion

of main elements at the interface region was 18-25 wt.% Ni, 15 wt.% Cr, 6 wt.% Mn and 50-60 wt.% Fe and its width were 1.5 µm. The EDS scan results show the high percentage of Ni elements at the interface resulted in an austenite stabilizer with an fcc structure.

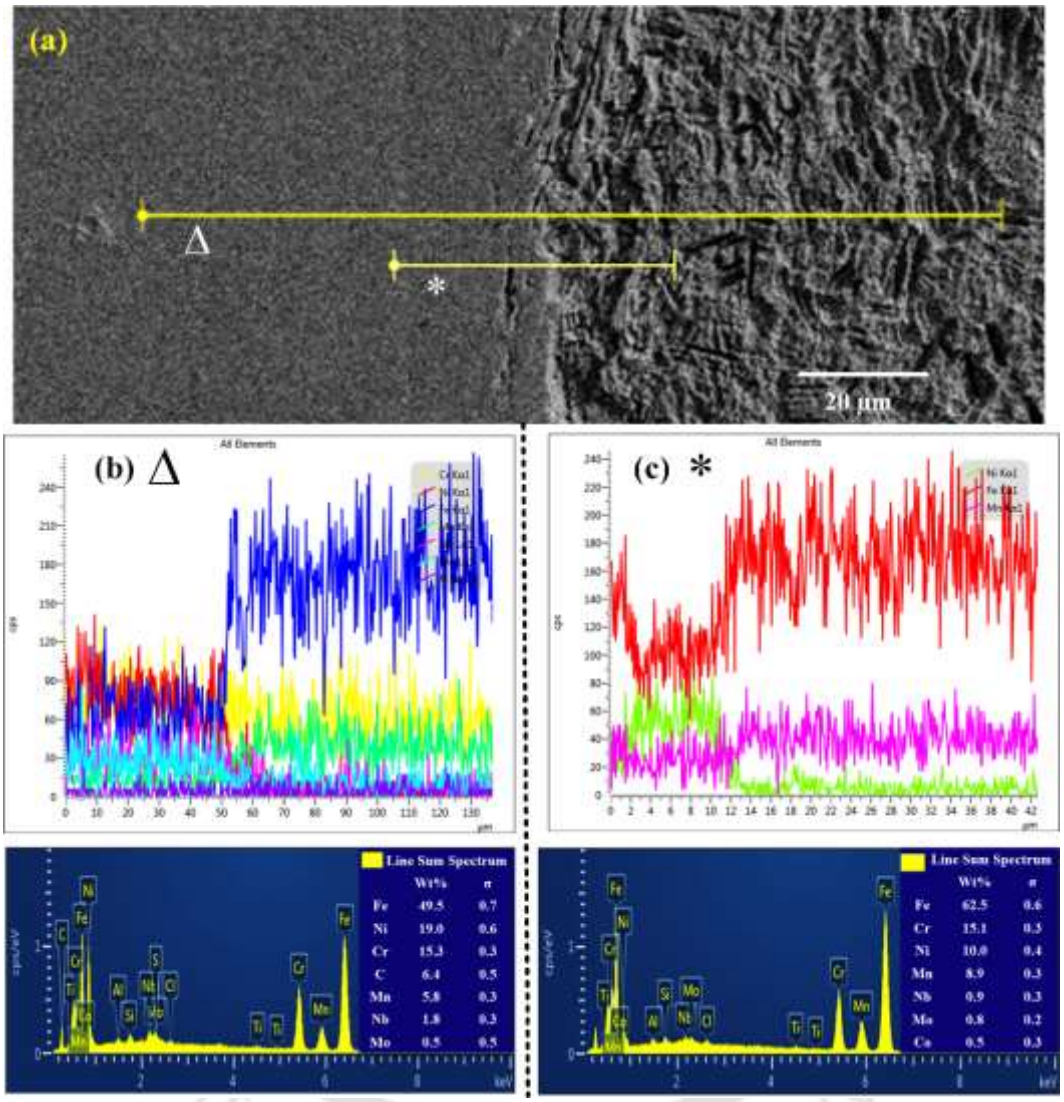

Fig. 6.8 EDS line scan analysis in the interface region. (a) SEM image (b) All chemical composition profiles present in the large scan region and (c) Chemical composition profiles for Ni, Fe and Mn elements in the small region.

In this study, XRD analysis was executed to confirm the presence of bulk-phase composition and different phases. The combined XRD pattern of the weld nugget zone with Inconel 718 and AISI 204Cu base materials is represented in Fig. 6.9. The base material's XRD pattern exhibited only the major peak of face-centered cubic (FCC) ϒ austenite. A clear indication of major and minor peaks was observed in the weld joint. The XRD pattern of the weld joint depicts the $M_{23}C_6$ carbide, ferrite and ϒ austenite phases.

Moreover, the presence of $(Fe_{12}W)_{0.15}$ phase having face centered cubic (fcc) structure with a lattice parameter a = 2.56 Å confirmed the existence of external element W (tungsten) in the SZ. Previous studies have also reported the presence of external elements caused by the WC-Co tool wear during the FSW process [40].

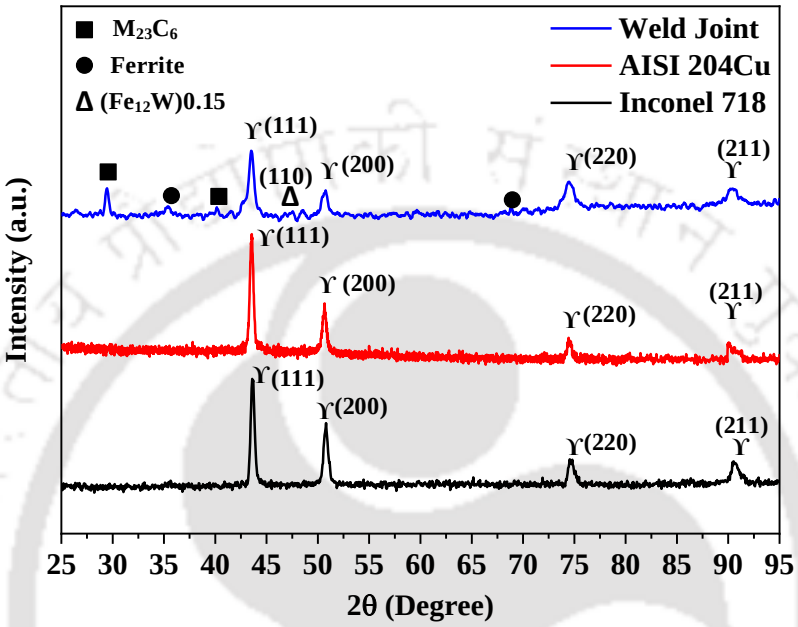

Fig. 6.9 XRD pattern of the weld joint and as received base material.

Figure 6.10. represents the typical TEM micrographs of the stir zone obtained at 70 mm/min traverse speed. Figure 6.10 (a) presents the bright field image and selected area diffraction (SAD) pattern of an austenite matrix with carbide precipitates. EDS peaks of spectrum 1 confirm the presence of (Fe, Mn, Cr)C precipitates (i.e., $M_{23}C_6$) in the austenitic stainless steel. Long needle-shaped carbide precipitates around the grain boundaries were observed in the bright field image. The generated temperature (around 1050 ^{o}C) during the FSW process was sufficient to precipitate the carbide particle [169]. Fig. 6.10 (b) shows that some spherical particles with a mean diameter of 40 nm near the grain boundary were observed at the Ni-base region. The EDS peaks of spectrum 2 results show that these particles belong to the (Ni, Cr)C carbide phase.

Furthermore, Fig. 6.10 (c) shows the random distribution of round-shaped carbide particles with external tungsten (W) and cobalt (Co) particles inside the grain. The high resolution of region A (Fig. 6.10 (c)) confirms the morphology of these particles, and spectrum 3 reveals the existence of Co particles. The tool wear caused the presence of external elements (i.e., W and

Co) during the FSW process [62]. Apart from the carbide particles, high dislocation densities with the presence of the delta (δ) phase were observed, as shown in Fig. 6.10 (c). The heat input per unit length in the stir zone increases at a lower traverse speed and lowers the cooling rate. The high temperature decomposed the δ phase in the stir zone, and a very small amount of δ-ferrite was observed (marked as a black arrow).

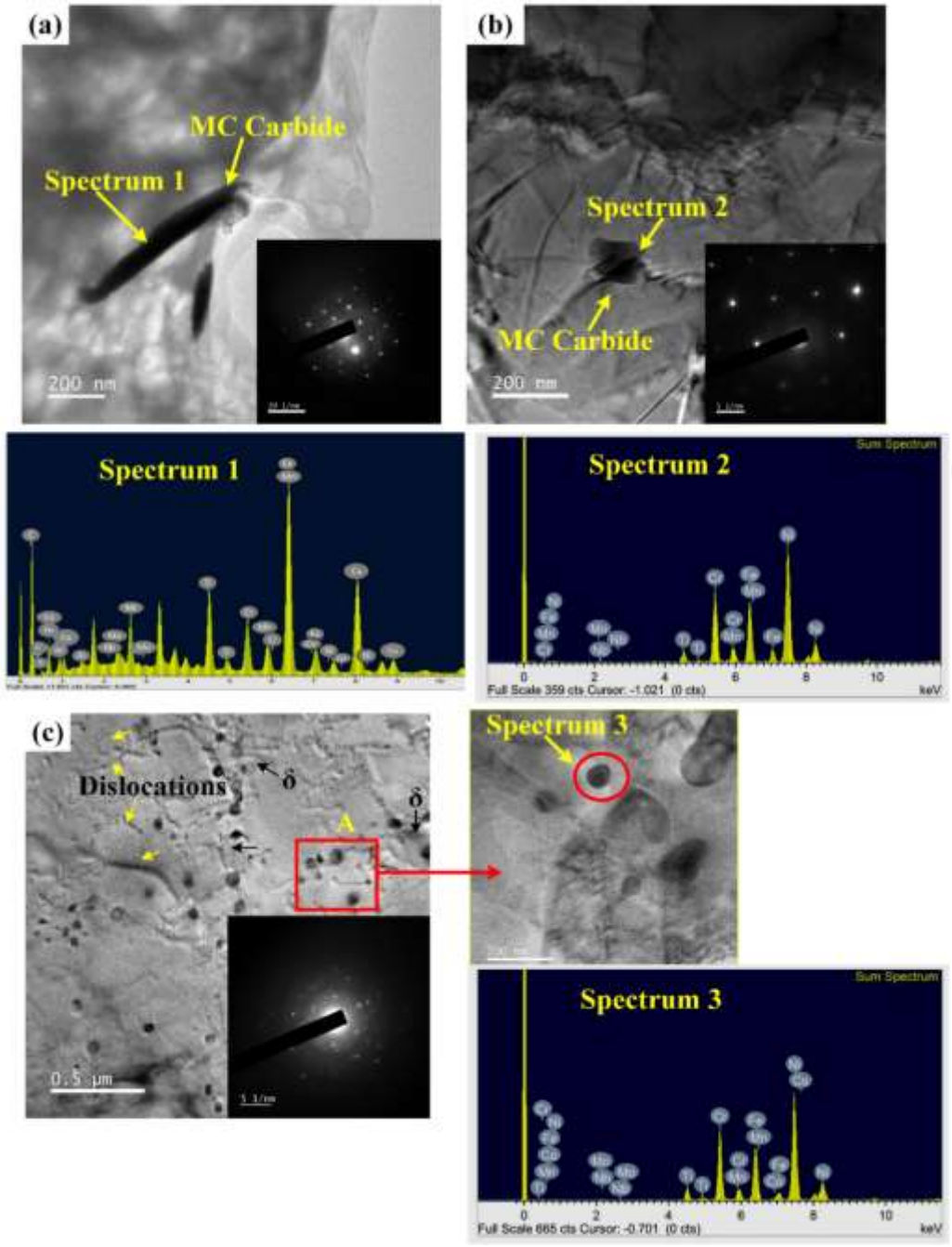

Fig. 6.10 TEM micrographs of the stir zone showing bright-field image and SAD pattern of (a) $M_{23}C_6$ carbide particle, (b) (Ni, Cr)C carbide phase and (d) morphology of the external elements.

The microstructural characterization of the joint interface of Inconel 718 and AISI 204Cu, which was obtained at a traverse speed of 70 mm/min, is shown in Fig. 6.11. The bright-field image of the interface region shows that no intermetallic layer was generated during the FSW, and these alloys were separate with a clear boundary at the interface region. The EDS spectrum in the region of Ni-base alloy (marked as A) and austenitic steel alloy (marked as B) confirmed the presence of separate regions. Figure 6.11 (a) shows the presence of some deformed $M_{23}C_6$ carbide phase particles with a size of 40 nm at the interface region with dislocation (marked as a red arrow) in the deformed grains. The SAD pattern at the interface region reveals that the diffused grains are crystalline with an fcc structure. The cubic structure having (111), (200), (220) and (211) planes with the d-spacing value 2.083, 2.042, 1.89 and 1.802 A^o, respectively, also matched with the XRD analysis. The high presence of the Fe and Ni elements at the interface region reveals the fcc structure. The main elements Ni, Fe, Cr, and Mn, were also analyzed with line spectrum, as shown in Fig. 6.8.

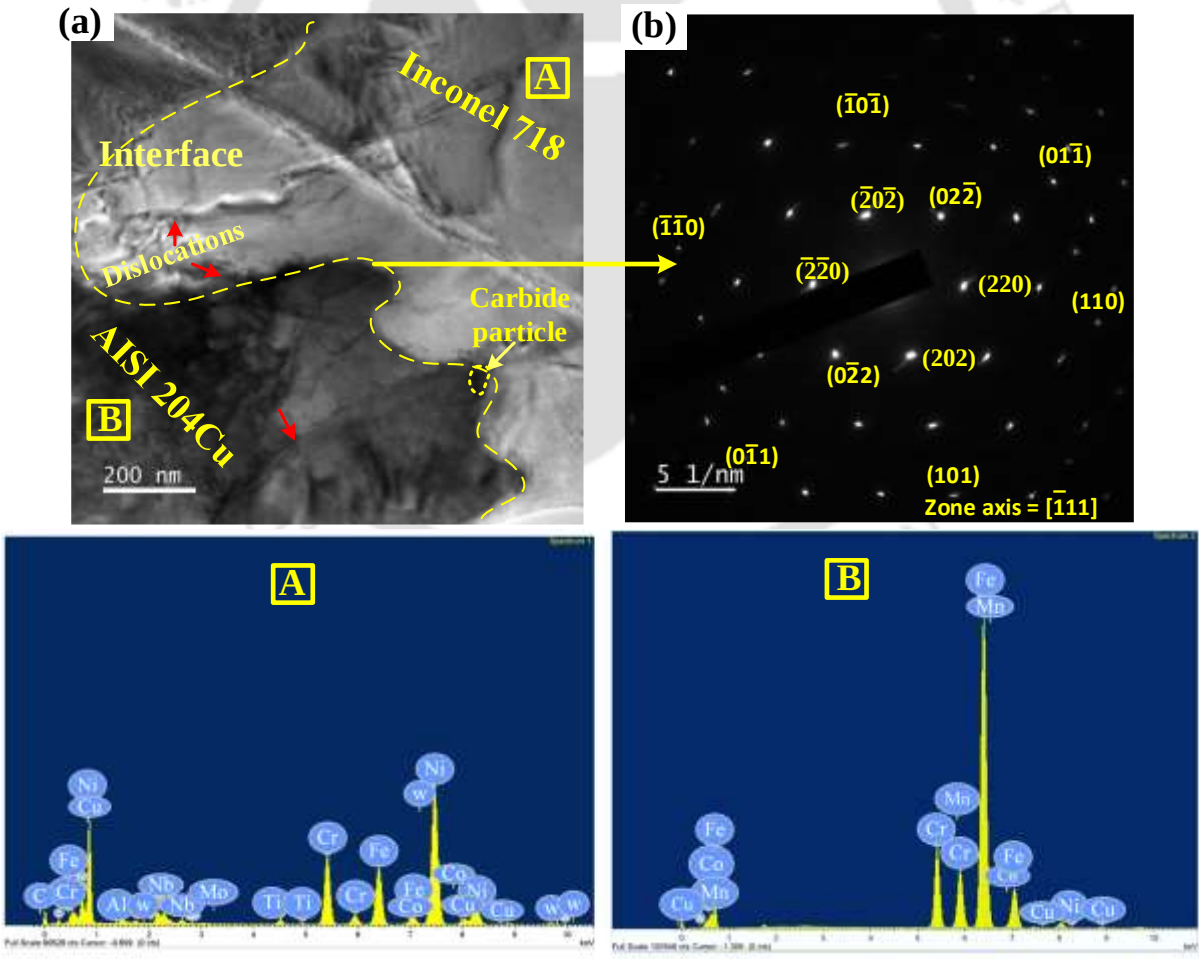

Fig. 6.11 TEM micrograph at the (a) interface region and its (b) corresponding SAD pattern.

6.3.2. Mechanical properties

6.3.2.1. Hardness

Figure 6.12 shows the micro-hardness profile of the welded sample obtained at a varying traverse speed. The average microhardness value of the base metals was 210 $HV_{0.5}$ and 280 $HV_{0.5}$ for Inconel 718 and AISI 204Cu, respectively. The microhardness tests of the welded samples were performed at the shoulder side, a middle portion and the bottom side, which was perpendicular to the joint line, as shown in Fig. 6.12 (a). Figures 6.12 (b-e) shows the inhomogeneous distribution of the hardness curve obtained at varying traverse speeds (i.e., 40, 70, 90 and 140 mm/min). In all the welded samples, the microhardness values of the nugget zone were higher than those of the base metal. It was also observed that the hardness value at the bottom side (i.e., 2.25 mm from the surface) was higher than the shoulder side (i.e., 0.75 mm from the surface). In the Inconel 718 region, a slight increase in hardness value in the TMAZs was observed (220-240 $HV_{0.5}$), whereas, in the SZ, the hardness distribution curve revealed the maximum value. The average values at 40 and 140 mm/min were shown 310 $HV_{0.5}$ and 345 $HV_{0.5}$, respectively. In the SZ, the average hardness value of the Inconel side increased with the increase in traverse speed.

In contrast, the increase of hardness value with the traverse speed in the stainless-steel weld region was slightly lower than in the Inconel weld region. It could be seen that a slight increase of hardness values in the TMAZs of steel was found in the range of 290 to 310 $HV_{0.5}$, whereas in the SZ, significantly higher hardness (350 $HV_{0.5}$ at 140 mm/min) was observed than the parent metal. An increase of average hardness value in the TMAZs and SZ of both materials can be explained in terms of grain refinement induced by FSW. According to the Hall-Petch relation, the decrease in the grain size increases the hardness of the crystalline material [60]. As the welding speed increases from 40 to 140 mm/min, the grain refinement in both materials was observed, as shown in the previous section (Fig. 6.5), which could increase the hardness value. Indeed, the fluctuation of hardness value observed in the nugget zone could be related to the presence of fine carbide particles, chromium precipitation and the generation of some phases (i.e., austenite to ferrite) [62,115]. Shamanian et al. [109] and Song et al. [62] reported similar trends for microhardness values in the study of dissimilar FSW of Ni-based alloy with stainless steel.

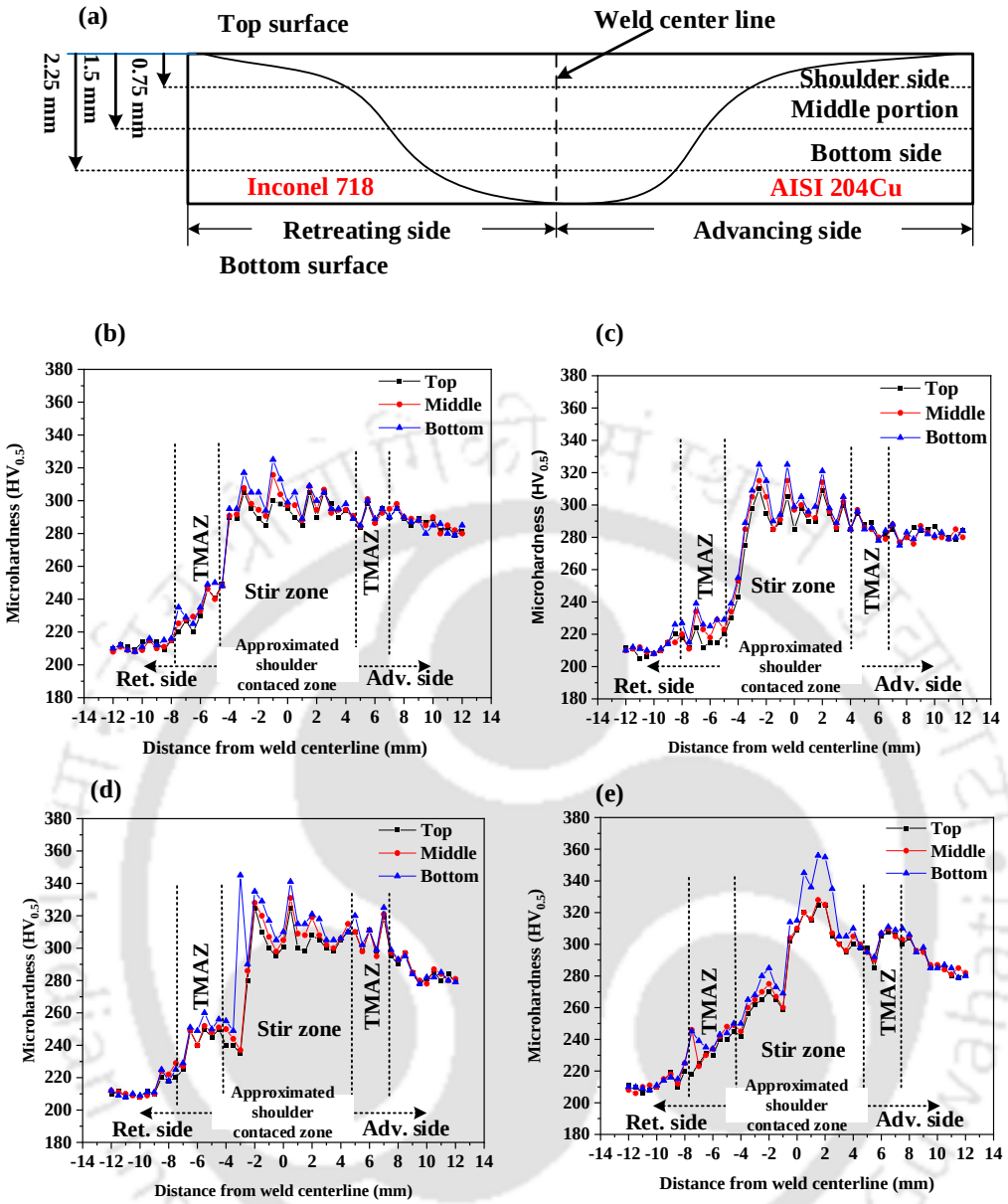

Fig. 6.12 Microhardness variation across the centerline of the welded sample obtained at different traverses peed.

6.3.2.2 Tensile test results

Mechanical properties in terms of the average ultimate tensile strength (UTS) and the 0.2% offset yield strength (YS) for all specimens with corresponding error bands are shown in Fig. 6.13 (a). Figure 6.13 (b) shows the top view of fractured tensile-tested samples of welded joints obtained at various parameters. From the plotted test results, the average ultimate tensile strength was 731, 856, 550, 735, 725, and 186 MPa, and yield strength was 310, 465, 307, 325, 337 and 110 MPa for base metal Inconel 718 and AISI 204Cu, and tested sample 1, 2, 3 and 4,

respectively. The tensile strength of all the welded samples was lower than the tensile strength of both the base metals except for the sample welded at 70 mm/min. The obtained UTS and yield strength of Test 2 were 735 MPa and 325 MPa, respectively, higher than the Inconel 718 and lower than the AISI 204Cu. The fractured tensile specimens showed that all fractures were located inside the weld zone on the AS, except for the Test 2 sample. The Test 2 sample fractured away from the weld zone on the RS. The fractured Test 2 specimens indicate that FSW could achieve the dissimilar Ni-base/steel sound joint.

The effects of traverse speed on the grain refinement, flow of material and defects like voids and groove formation were discussed in previous sections. When the traverse speed was set to 40 mm/min, dissimilar joints showed lower tensile strength compared to the base materials. This could be due to the presence of a crack in the TMAZ near AS, which was observed in the cross-sectional view (Fig. 6.3). The dissimilar joint welded at a traverse speed of 140 mm/min exhibited the lowest strength due to the generation of large groove defects during welding. This defect is generally formed by improper mixing of material caused by low heat input and high cooling rate obtained at the high traverse speed. On the contrary, the tensile strength of the weld obtained at 70 and 90 mm/min traverse speed resulted from 100.5% and 99.1% of the Ni-based alloy material, respectively. The obtained high weld strength at 70 and 90 mm/min traverse speed was due to the welding thermal cycle effect, which highly influences the proper mixing of material, grain refinement and phase precipitation in the SZ. High weld strength may be due to the welding cycle thermal effect which significantly affects the proper mixing of material, grain refinement and phase precipitation in the SZ. Furthermore, the microstructure observations of the nugget zone near the AS showed a high density of fine-grained dragged Inconel 718 material (shown in Fig. (6.3)), which may also improve mechanical strength.

Figure 6.14 shows the SEM fractography of fractured tensile samples of weldments obtained at welding speed 70 and 90 mm/min, which was performed to examine the fracture characteristics. The deformed Test 2 tensile specimen fractured with necking in the Ni-base alloy region, shown in Fig. 6.13 (b). From the fractography image (Fig. 6.14 (a)) of Test 2, no crack boundaries and/or cleavage facets were seen on the fracture surface. In contrast, inhomogeneous distribution of dimples was observed on the fracture surface, which demonstrates the quality of fracture was ductile modes of fracture. The cause of failure initiation was deep dimples like voids, and some large carbide particles present in the base material act as the crack initiation. However, the fracture location of the welded tensile sample of Test 3 was inside the weld zone, which is demonstrated with two different regions marked

as A and B, as shown in Fig. 6.14 (b). At high magnification, of fractured surface marked as A showed cleavage facets, whereas the surface marked as B showed fine and deep dimples with carbide particles. This sample has experienced mixed modes of failure.

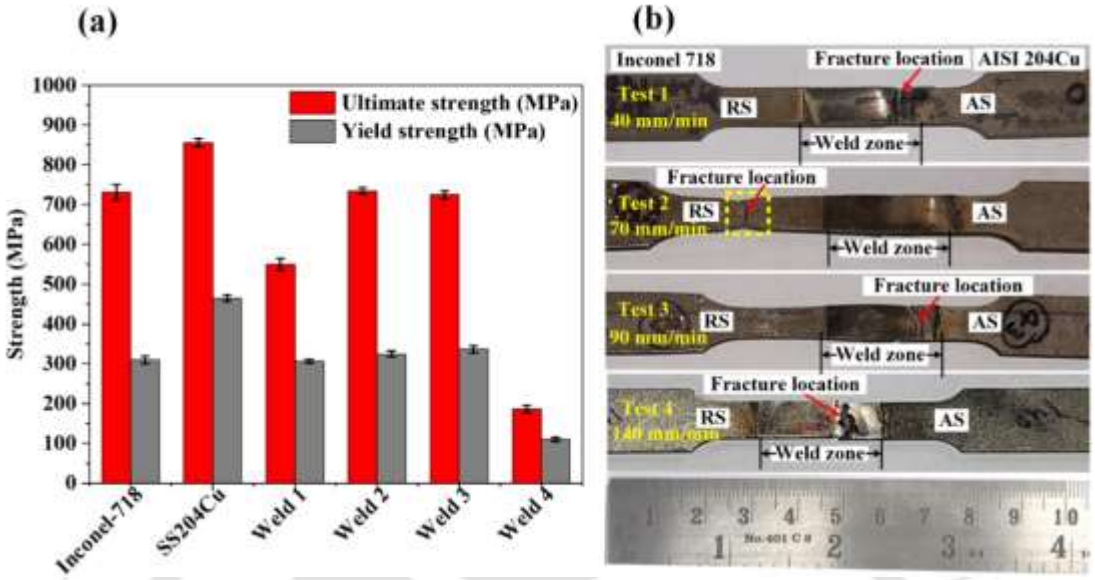

Fig. 6.13 (a) UTS and 0.2% YS of the base material and welded sample, and (b) top view of the fractured tensile sample.

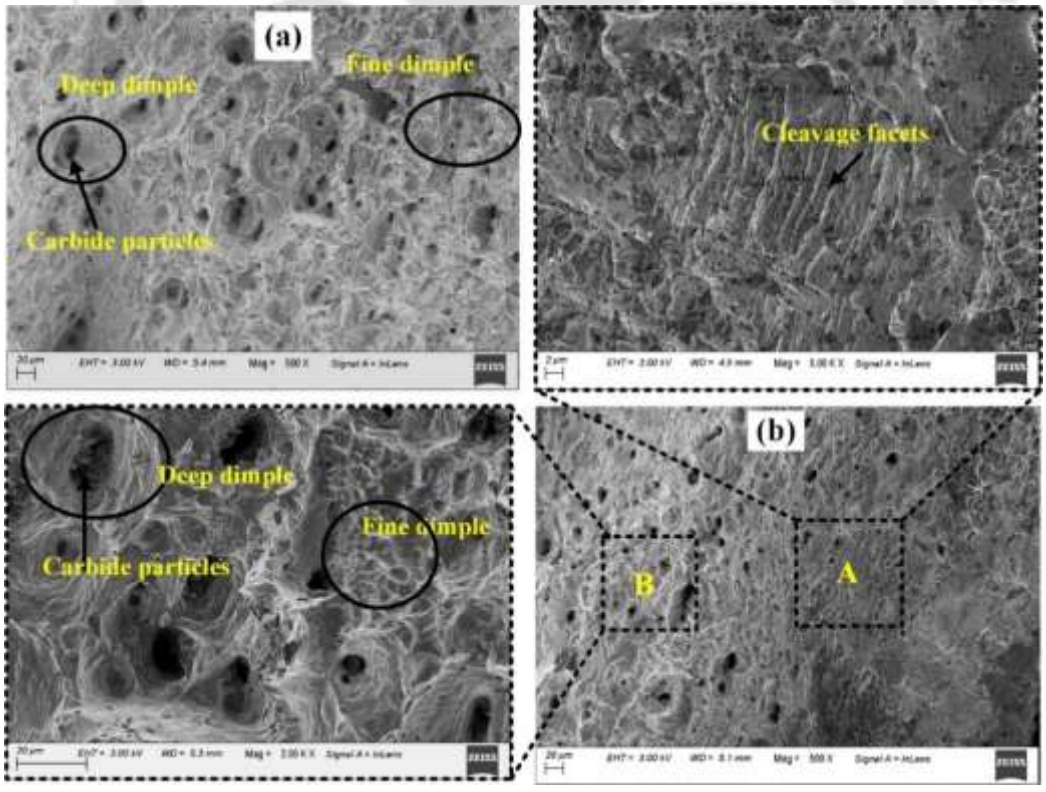

Fig. 6.14 SEM fractography of (a) tensile sample of Test 2 and (b) Test 3.

6.3.2.3 Impact test

Impact studies on the dissimilar weld joints were also performed to estimate the mechanical impact response. The fractured samples and test results are shown in Fig. 6.15. Visual inspection of broken samples reveals that the all-welded samples were completely separated from the centre of the V-notch due to the impact test, as shown in Fig. 6.15 (a). The impact toughness test results of the base material and the welded joints obtained at various traverse speeds are shown in Fig. 6.15 (b). The result shows that the average impact value of welded joint obtained at 40 and 140 mm/min traverse speed was lower than the measured impact value of the parent Inconel 718 (i.e., 55 J) and AISI 204Cu (i.e., 32 J) metals. The average toughness value of the welded joints obtained at 70 and 90 mm/min traverse speed was 32.5 J and 34 J, respectively, which was higher than the AISI 204Cu and lower than the Inconel 718. The impact toughness value increased with increasing traverse speed and was found to maximum (34 J) at 90 mm/min. At high traverse speed, a minimum value (15 J) was observed due to the presence of groove defect in the AS of the improper welded joint. SEM fractography analysis of the highest (i.e., Test 3) and the lowest (i.e., Test 4) impact-valued fractured surface was carried out in this work, as shown in Figs. 6.15 (c) and (d), respectively. The high impact fractured surface morphology clearly shows a more fined dimple population with some voids, resulting in a typical plastic fracture. However, the low impact valued sample shows elongated dimples and cleavage with some cracks resulting in a mixed fracture mode. Fig. 15 (d) also shows the groove-like surface (denoted by red arrow) with the fibrous region found in the fractured surfaces of welded joints obtained at high traverse speeds, resulting in a minimum impact value. The result showed that the grain refinement and precipitated phase highly influenced the impact toughness value. Fine grain with a highly distorted precipitate phase restricts dislocation movement and crack propagation [170].

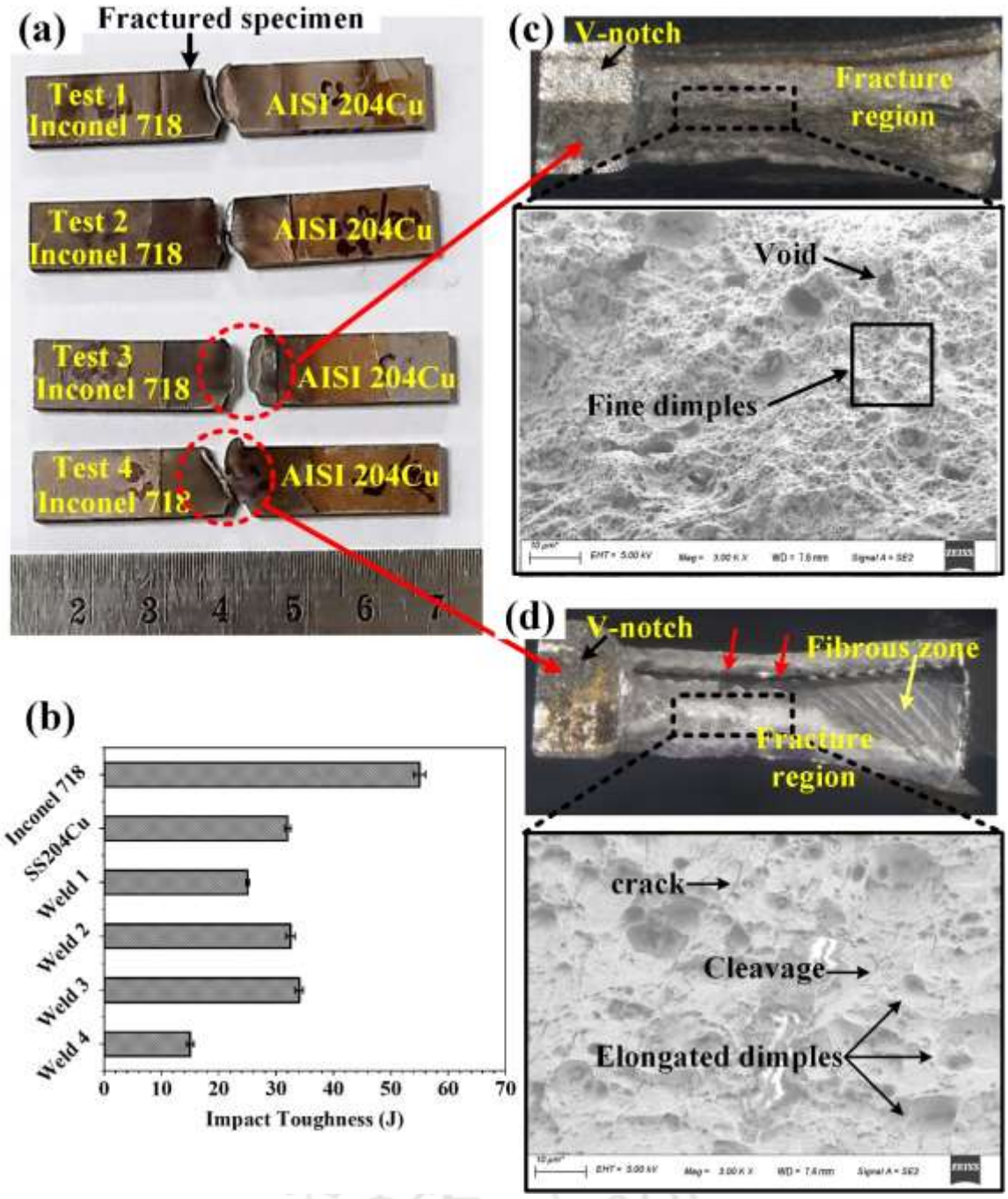

Fig. 6.15 (a) Fractured impact tested specimens with corresponding (b) measured toughness value and SEM micrograph of the fractured region of (b) high toughness weld and (c) low toughness weld.

6.3.2.4 Tool wear characterization

The wear of welding tools always happens during the FSW of high strength materials such as steel and nickel alloy. During the FSW process, the generation of high welding temperature and high load on the FSW tool is highly responsible for the degradation of the welding tool

[144]. Figure 6.16 shows the top views of the WC-Co tool surface with the EDS analysis. Figure 6.16 (a) shows the tool pin height of 2.7 mm before the welding process, whereas, Fig. 6.16 (b) illustrates the tool pin height was 2.5 mm after the welding used in traverse speed 70 mm/min. The magnified views of the tool shoulder portion illustrate the change of original surface geometry after the weld. After a single pass of the weld, the maximum wear position of the tool was observed in the tool pin height. The formation of an oxide layer was also observed near the tool shoulder edge, as shown in Fig. 6.16 (b). EDS area scan analysis on the tool shoulder was performed before and after the weld, shown in spectrum 1 and 2, respectively. It can be observed that a reduction of wt.% of tungsten (W) and cobalt (Co) elements and an increment of oxygen (O) and carbon (C) elements occurred after the welding. In addition, analysis of spectrum 2 of the tool shoulder surface shows the presence of Ni, Fe and Mo elements apart from the base WC-Co tool elements due to the adhesion nature of WC-Co tool elements [122]. In order to reduce tool wear and extend the tool's lifespan, it is essential for future research to gain a deeper understanding of the mechanism behind tool degradation during the joining of dissimilar high strength materials.

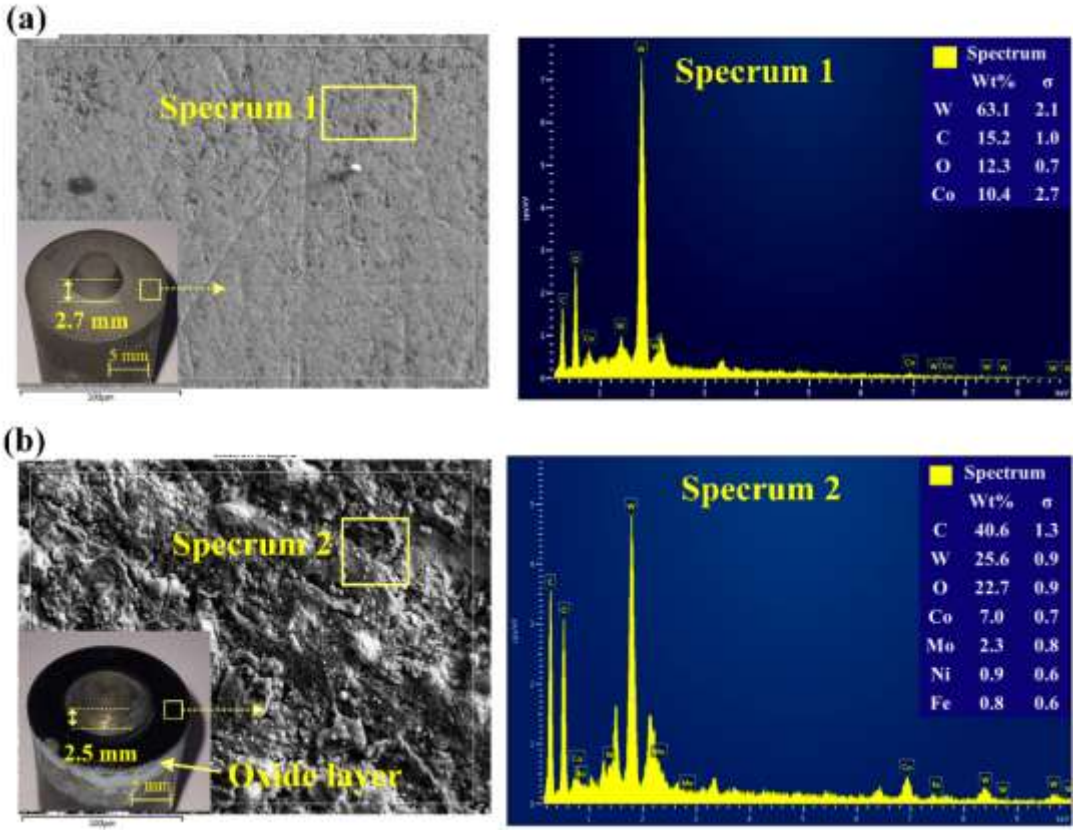

Fig. 6.16 FSW WC-Co tool surface analysis (a) before welding and (b) after welding.

6.4 Brief scientific discussion

From the above results of dissimilar FSW, the microhardness profiles across the welded region were observed directly affected by the microstructures. The microhardness of a material refers to its resistance to penetration or indentation, and it can be influenced by factors such as grain size, phase distribution, and dislocation density. The results in all the welded samples shows, the microhardness values of the nugget zone were higher than those of the base metal. An increase of average hardness value in the TMAZs and SZ of both materials can be explained in terms of grain refinement induced by FSW. According to the Hall-Petch relation, the decrease in the grain size increases the hardness of the crystalline material. Similarly, the tensile strength variation in the FSW of dissimilar materials, such as Inconel 718 and stainless steel AISI 204Cu, has a critical aspect that affects the mechanical performance of the welded joint. The obtained high weld strength at 70 and 90 mm/min traverse speed was due to the welding thermal cycle effect, which highly influences the proper mixing of material, grain refinement and phase precipitation in the SZ. High weld strength may be due to the welding cycle thermal effect which significantly affects the proper mixing of material, grain refinement and phase precipitation in the SZ.

6.5 Summary

In this study, the Inconel 718 Ni-based superalloy plate was successfully joined with the AISI 204Cu stainless steel by friction stir welding using the WC-10wt.%Co tool. Also, the effect of traverse speed on the surface appearance, microstructure and mechanical properties of the dissimilar FSWed joints was widely investigated. Thus, based on the results and discussion, the most prominent points are summarized as follows:

- A sound weld can be obtained with an FSWed dissimilar joint on Inconel 718 to AISI 204Cu at medium traverse speed (i.e., 70-90 mm/min) under the rotational speed of 300 rpm.
- Microstructural characterization at the cross-section view determines only SZ and TMAZ on both metals. The application of FSW led to grain refinement in the nugget zone, resulting in an increment of hardness value directly proportional to the traverse speed. These features were attributed to dynamic recrystallisation.

- In the nugget zone, a soundly mechanically joined weld interface with homogeneously distributed primary (NbC, (NbTi)C)) and secondary ($M_{23}C_6$) carbide particles across ϒ matrix were formed, which improved the mechanical properties of joints.
- The EDS and XRD analysis confirmed the presence of external elements, i.e., W and Co, inside the nugget zone caused by the wear of FSW tool material during joining.
- The weldments obtained at a traverse speed of 70 mm/min showed a higher ultimate and yield strength, which was higher than the Inconel 718 parent metal but lower than the AISI 204Cu parent metal.
- The impact toughness value of the weldments increases with the increase of traverse speed due to grain refinement. The obtained maximum impact value (at 90 mm/min) was higher than the AISI 204Cu base metal but lower than the Inconel 718 base metal. However, the toughness value at high traverse speed was lowest due to weld defects.

……..*……..*…….. :

CHAPTER 7

7. Comparative Study of Conventional and Induction-Assisted Friction Stir Welding of Dissimilar Alloy, i.e., Inconel 718 and SS316L

7.1 Introduction

In this study, conventional and induction heating-assisted friction stir welding (I-FSW) in joining dissimilar Inconel 718 and stainless steel (SS316L) alloy using the WC-10wt.%Co tool was experimentally investigated. Nowadays, the welding of dissimilar materials is becoming increasingly popular in manufacturing because of flexible design considerations. Several fusion welding processes have been used in joining Ni-alloy with stainless steel. Conventional welding presents numerous challenges, including the need to accurately select appropriate filler materials, the risk of liquation and solidification cracking in the fusion zone, and the development of intermetallic phases that may undermine the weld's overall quality. FSW is a solid-state joining technique that has been used to minimize the major difficulties associated with the inconsistency of chemical and physical properties of distinct IN718 and SS316L materials. In addition, an induction preheating source has been used for customizing the FSW process in high-strength material and minimizing the degradation of the FSW tool. The primary area of interest is to check the feasibility of the FSW process and examine the effect of induction preheating on temperature distribution, axial force, mechanical properties, and microstructure of dissimilar joints made by FSW of Inconel 718 and SS316L alloy. Additionally, the study investigated the influence of induction preheating on tool wear.

7.2 Materials and methodology

In this study, annealed Inconel 718 and stainless steel SS316L sheets with identical dimensions of 200 mm length, 80 mm width, and 3 mm thickness were joined. The joining process was performed in position control mode on a FSW machine fitted with a WC-10wt.%Co tool and the auxiliary induction preheating system (I-FSW). The average chemical compositions and mechanical properties of the as-received base materials from the supplier (Shanti metal supply corporation, India) are mentioned in the methodology section in chapter 3. The specification of the high-frequency induction heating machine and FSW tool, the experimental setup, the working principle, and the methodology used in this experiment are explained in chapter 3, sections 3.2 and 3.3. The welding was performed at a constant rotational of 300 rpm and

traverse speed of 70 and 140 mm/min, respectively. The welding parameters were based on our previous investigation and experimental trials. The transient temperature distribution was measured during the welding with the K-type thermocouples. It was spot welded on either side of the base plate at 20 mm (i.e., marked as TC1 & TC2) and 23 mm (i.e., marked as TC3 & TC4) distances from the weld center line in the advancing side (AS) and retreating side (RS), respectively, as shown in Fig. 7.1. In addition, tool wear after 600 mm weld length was measured in terms of weight loss and tool pin length shortage with a micro balance and Vernier caliper, respectively.

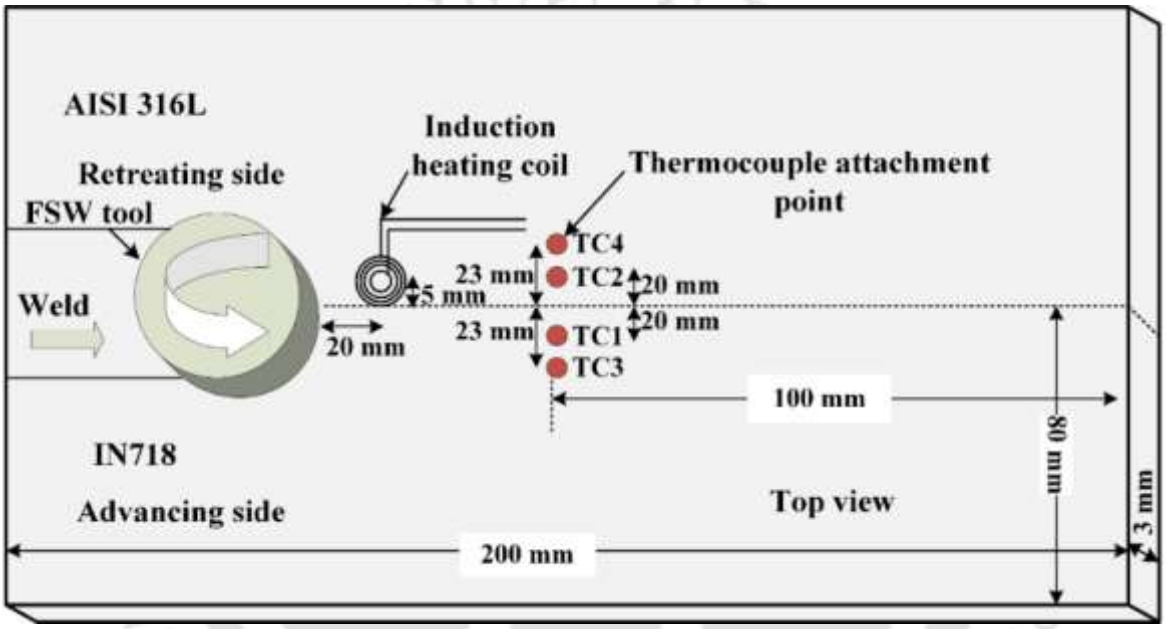

Fig. 7.1 Schematic diagram of thermocouple wire positioning on the base plate.

7.3 Results and discussion

This section discusses the thermal, microstructural and mechanical analysis outcomes in detail.

7.3.1. Thermal analysis

7.3.1.1. Temperature distribution due to induction heating under the stationary case.

To evaluate the heating performance of a high-frequency induction machine, first, we determined the variation of temperature profile with the output power on the stationary Inconel and stainless-steel plates. Fig. 7.2 (a-b) shows different temperature profiles with the variable output power of 9 kW, 11 kW and 13 kW under the fixed coil position (5 mm) above the workpiece surface and fixed heating time (40 s). From the temperature profile, it was observed

that the maximum surface temperature of both the workpiece plates changed according to the output power of the induction machine. The generated maximum temperature in the Inconel plate was higher than the stainless steel under the same output power. The maximum temperature of the Inconel 718 plate changed from 400 ^{o}C to 480 ^{o}C, whereas it changed from 300 ^{o}C to 380 ^{o}C in the stainless-steel plate under the same induction output power. The high heat generation in the Inconel 718 plate compared to the stainless steel under the same output power may be caused by the high electrical resistivity of the Inconel material [171].

7.3.1.2. Temperature distribution under the moving case.

After getting the temperature variation of the stationary workpiece with the induction output parameter, the thermal analysis was conducted on the moving plate under the parameters 70 and 140 mm/min to find out the inline preheating effect in the FSW process. Figures 7.2 (c) and (d) show the temperature profile variation with the moving plate at parameters 70 and 140 mm/min, respectively. In this analysis, 9 kW induction output power was used because the heating temperature goes above 300 °C, which confirm from the above Figs. 7.2 (a-b). The yield strength of the Inconel 718 and stainless steel 316L began to decrease above 350 ^{o}C and 200 ^{o}C, respectively [172]. The temperature profile shows, in both cases, that the generated temperature at the center of the induction coil was higher than the coil periphery, and it was higher in the case of 70 mm/min (i.e., 300 ^{o}C or more) than the 140 mm/min (i.e., 200 ^{o}C or more) due to the more heating time. The generated maximum temperature on the moving plate confirmed that the heating temperature was adequate, at which the yield strength of the material started to diminish.

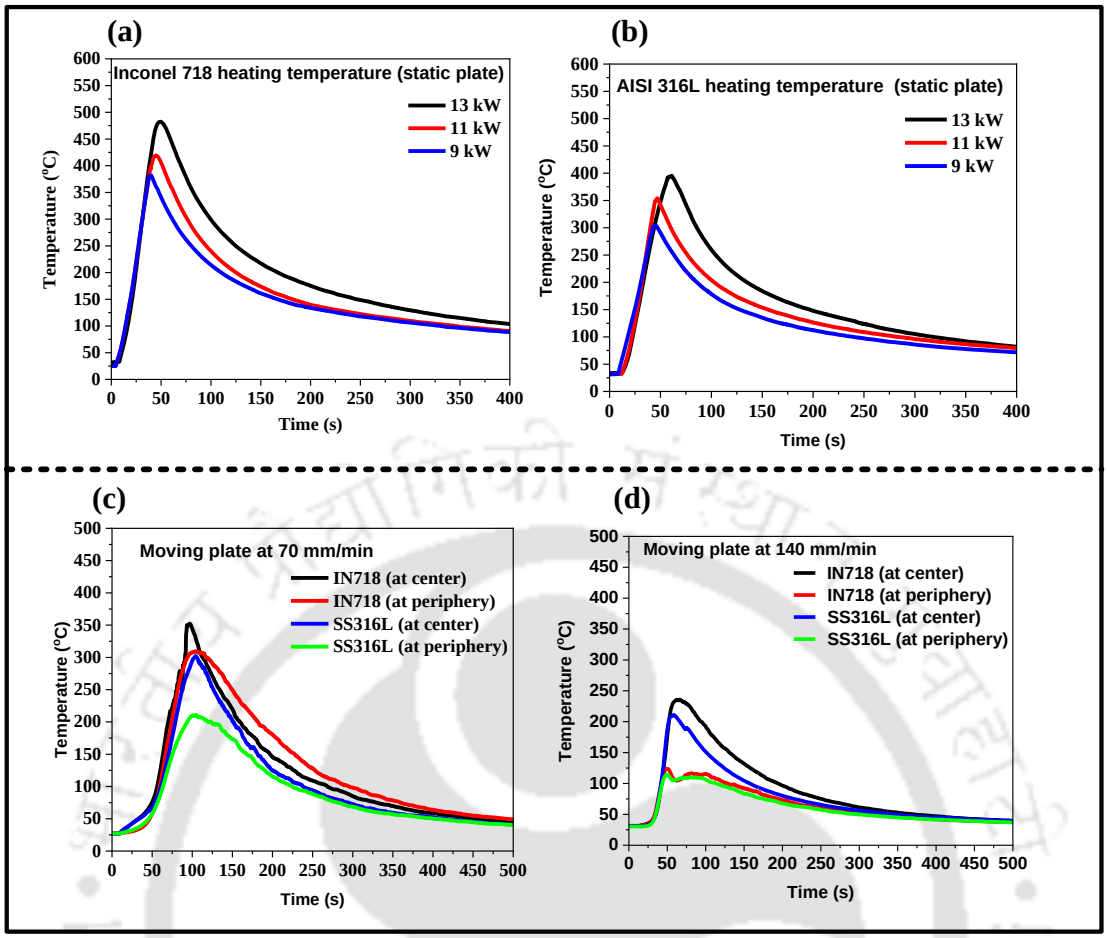

Fig. 7.2 The variation of temperature with output power under the (a-b) stationary workpiece condition and (c-d) moving workpiece condition.

After finding out the temperature variation in the moving plate by the high-frequency induction heating, we proceeded with this thermal analysis experiment with/ without the Induction FSW process to find the inline preheating effect. Figures 7.3 (a-b) and 7.3 (c-d) show the transient temperature profiles obtained using the conventional FSW and induction-assisted FSW processes, respectively, at a constant rotational speed of 300 rpm and traverse speed of 70 and 140 mm/min. The temperature curve analysis shows that the obtained temperature on the advancing side (i.e., TC1 and TC3) was higher than the retreating side (i.e., TC2 and TC4) in all conditions. In the FSW process, the generated maximum temperature in the Inconel 718 (i.e., AS) plate and SS316L (i.e., RS) plate at 70 mm/min was 250 ^{o}C and 140 ^{o}C, respectively, whereas it was 220 ^{o}C and 130 ^{o}C at 140 mm/min. The cause of higher temperature in the AS is mainly due to the beginning of the transformation of solid material into semi-solid and the flow of material on the AS experiencing additional frictional heat [173]. Also, the generated temperature at a high traverse speed (i.e., at 140 mm/min) was lower than the low traverse speed (i.e., at 70 mm/min) because of the low rate of heat input and less tool stirring time.

Furthermore, two peaks in the heating step were noticed from the temperature profile created in the induction-assisted FSW process, as illustrated in Figs 7.3 (c-d). The first peak at the beginning of the heating stage was generated due to induction heating, and the second peak at the end of the heating stage was due to tool rotation. The generated maximum temperature in the AS (i.e., TC1) reached 530 ^{o}C and 400 ^{o}C, during the I-FSW process at the welding speed of 70 and 140 mm/min, respectively, which was 2.12 and 1.8 times the conventional FSW temperature. The use of induction heating as an external energy source in the FSW process showed a remarkable increase in material temperature than the conventional FSW. The measured temperature results in the stainless steel and Inconel 718 plates during the conventional and induction-assisted FSW process were almost similar to the previous study [72].

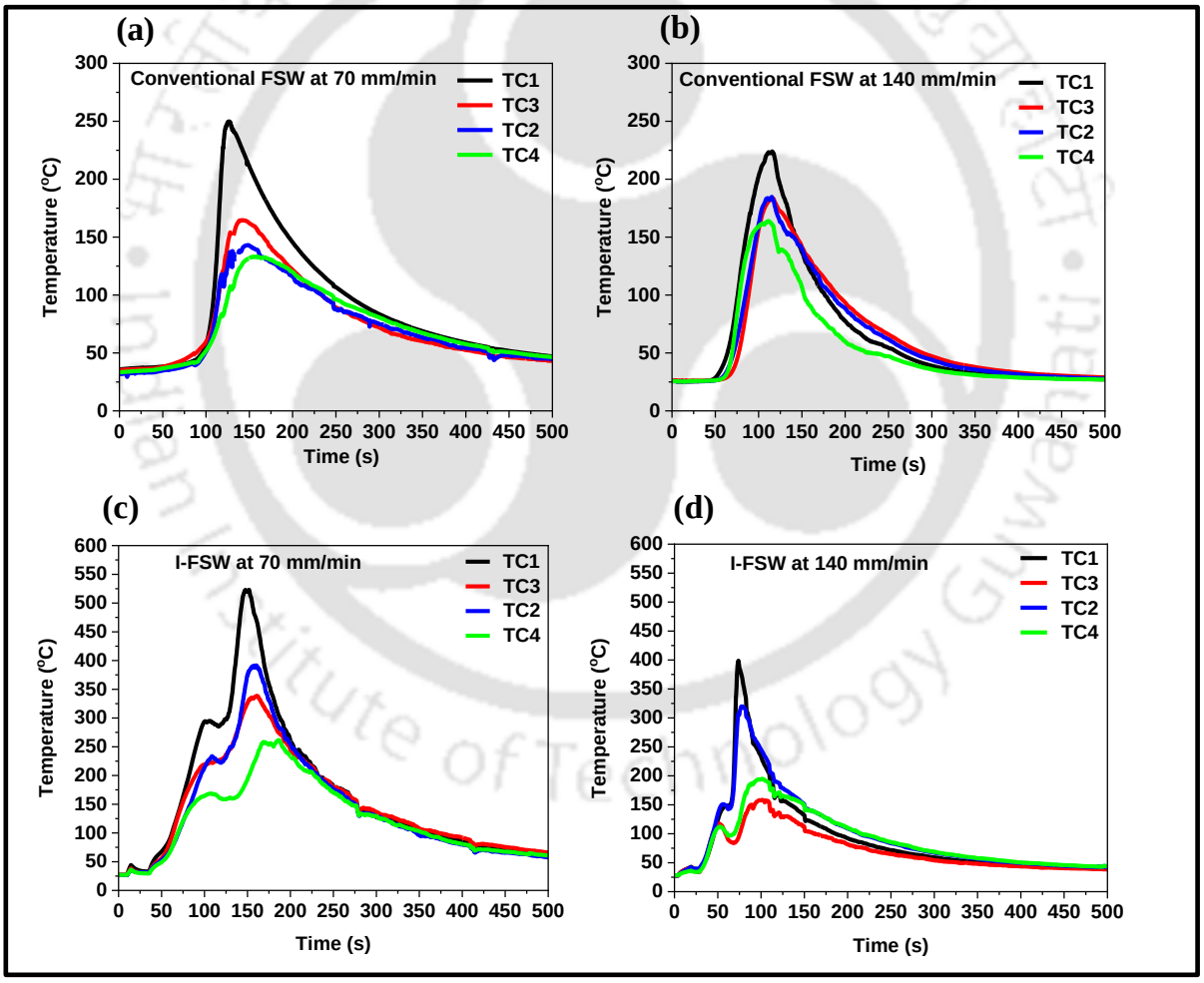

Fig. 7.3 The variation of temperature distribution under (a-b) FSW and (c-d) I-FSW.

7.3.2 Weldment surface and force analysis

Figure 7.4 (a) shows the top and cross-sectional views of the dissimilar FSW welds obtained at a constant rotating speed of 300 rpm with varying welding speeds of 70 and 140 mm/min under conventional and induction-assisted FSW. The welded surface appearance obtained under the conventional FSW at 70 mm/min was smooth with defect-free joint and insignificant flash, whereas it had surface defects like macro-groove at 140 mm/min. The generation of surface defects like grooves and cracks is formed because of insufficient heat input resulting in the inadequate flowing of materials [24]. However, the surface appearance under the induction-assisted FSW process at 70 and 140 mm/min was very smooth with generated thick (thickness ~0.30 mm) and thin flash (thickness ~0.22 mm), respectively. The preheating temperature and traverse speed significantly influence flash generation in the AS of the weld. Welding at a high traverse speed of 140 mm/min with a preheating temperature of ~300 ^{o}C (i.e., generated at 9 kW) appeared smooth surface without grooves or crack defects. Additional heat input facilitated the proper intermixing and flow of materials resulting in good welding at a high traverse speed [72]. Previous investigation shows (mentioned in chapter 5) that joining the Inconel 718 sheets with the I-FSW process under a preheating temperature above 400 ^{o}C resulted in excess thinning of the weld plate and large groove defects. Therefore, this experiment was conducted at low (i.e., 9 kW) output power gives a better result. Apart from grooves and flash defects, plate thinning due to tool plunging and end keyhole defects were also observed in all the weld conditions.

The optical macrograph of the cross-sectional views of all the joints obtained in the FSW and I-FSW process shows a basin-shaped morphology due to the tapered shape of the tool pin, as shown in Fig. 7.4 (a). Material flow patterns in the cross-sectional image showed the impact of welding speed and induction preheating. The bright region (RS) in the cross-sectional images is SS316L, whereas the dark region (AS) is Inconel 718. The material flow pattern in all the cross-sections shows a vortex-like shape. The weld strength in the FSW process generally depends on the plastic deformation and intermixing of the material. Under the conventional FSW, the weld macrograph obtained at 70 mm/min shows that some portion of stainless-steel material pulled from RS to the AS, whereas, at a welding speed of 140 mm/min, layers of steel material inside the Inconel material were observed. The weld cross-sectional image obtained at 140 mm/min reveals a large cavity defect in the bottom area of the AS. The presence of cavity defect at high speed may be due to less heat input resulting in insufficient material flow and abnormal mixing. However, the material flow pattern obtained in the induction-preheated

FSW process under the same welding parameters was almost the same as the conventional FSW process. The macrograph of the welded sample obtained in the I-FSW process at 70 mm/min shows a wormhole defect near the AS, which might be caused by excess heat supply by the mutual effect of induction heating and low traverse speed resulting in insufficient bond formation. However, the macrograph of the weld obtained at high traverse speed (i.e., at 140 mm/min) under the I-FSW process does not appear defects like a wormhole. At high traverse speed, the combined effect of heat accumulation by the tool movement and induction heating was low, and the cooling rate was high, resulting in the proper weld. From the visual examination of the joined surface and the macrograph of the weld, obtained under FSW at 70 mm/min and I-FSW at 140 mm/min, we could say that the weld obtained under these parameters, there was no defect with complete intermixed material.

Figure 7.4 (b) depicts the generated downward axial force during the dissimilar FSW and I-FSW welding of Inconel 718 with SS316L. The axial force profile was obtained under the welding parameters, i.e., a constant rotational speed of 300 rpm and variable traverse speed of 70 and 140 mm/min. The generated force profile over time contains plunge, dwell and weld zone. In the initial welding stage, as the rotating tool pin penetrates into the workpiece, the axial force increases sharply, known as the plunge stage. In the plunge stage, maximum force is generated due to inadequate thermal softening of the material. After this, the rotating tool steadily rotates for some time (i.e., 15 s) at a fixed position known as the dwell period generating higher frictional heat, resulting in softening of the material, causing the reduction of vertical force. Following this, the rotating tool moves along the weld line as per the given traverse speed and produces welding known as the weld zone, where axial force continuously produces a steady manner. The traverse speed and induction preheating significantly affected the axial force profile, as shown in Fig. 7.4 (b).

In the conventional FSW process, the generated average axial force during the welding stage at 70 mm/min and 140 mm/min was 25 kN and 28 kN, respectively. On the other hand, in the preheated (i.e., I-FSW) case, the average axial force was 18 kN and 20 kN at 70 mm/min and 140 mm/min, respectively, which decreased by 28% and 24% compared to the conventional FSW. Based on the previous thermal analysis results, it could be noted that the temperature distribution in the I-FSW process was higher than the conventional FSW process, and it was higher on the Inconel 718 plate than on the steel plate. Also, the Inconel plate was used on the advancing side in this experiment, where the generated frictional temperature was higher than on the retreating side. Therefore, using an induction preheating source before the FSW tool

gives the additional thermal softening of the material, which naturally reduces the material's plastic deformation resistance and flow stress, resulting in a reduction of axial force. Some researchers [88] reported that using induction preheating during friction stir welding lowers the axial force. Furthermore, in all circumstances, the average axial force with high welding speed was larger than with low welding speed. At a higher traverse speed, the thermal softening and materials flow occurs less due to a decrease in stirring time and frictional heat input than at the lower traverse speed, causing the increment of the average axial force.

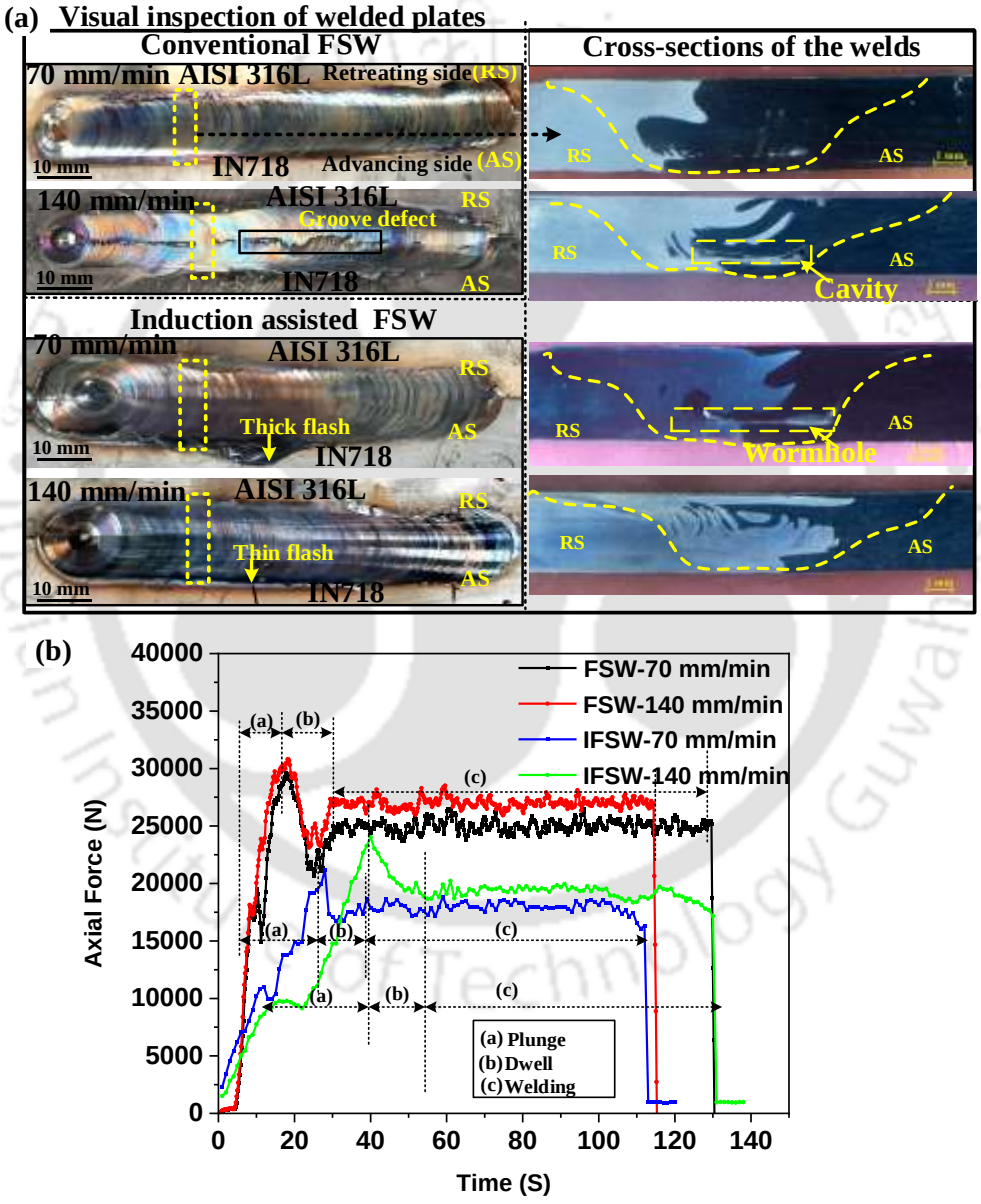

Fig. 7.4 (a) Visual inspection of the welded plate with their cross-sectional views and (b) corresponding generated axial force diagram during the FSW and I-FSW at different parameters.

7.3.3 Microstructure characterization

Figure 7.5 (a) shows the macrograph of the welded joint obtained at 140 mm/min using the induction-assisted FSW technique, in which various weld zone based on grain structure was observed, as highlighted in Figs. 7.5 (b-g). The optical microstructure of the base material (BM) SS316L and IN718 are shown in Figs. 7.5 (b) and (g), respectively, which are outside the nugget zone. Some circular-shaped carbide particles could be seen in the base material of SS316L. Whereas the presence of MC-type carbide particles (as blackspot) enriched with Ti and Ni elements with some twin boundaries in the fully equiaxed ϒ austenitic matrix might be seen in the Inconel 718 base material. The existence of the carbide particles in the grain and its boundaries were examined with the FESEM-EDS spectroscopy. From the microstructure study of the base materials, the BMs-SS316L and IN718 had coarse grain with average grain sizes of 35 µm and 65 µm, respectively.

However, the details of the microstructure obtained inside the basin-shaped region are illustrated in Fig. 7.5 (c-f). As stated by Mishra and Ma [5], the areas (at the weld centre) where materials underwent high deformation and recrystallization phenomenon are typically known as the stir zone (SZ), and adjacent to this is the thermo-mechanical affected zone (TMAZ), where the materials are affected by the thermal cycle and plastic deformation. Figs. 7.5 (c) and (f) show the narrow region of TMAZ generated near the parent material of SS316L and Inconel 718, respectively. In contrast, Figs. 7.5 (d) and (e) show the full SZ in the flow region of SS316L and Inconel 718 at the centre of the weld, respectively, which exhibits a more refined grain structure than the other weld zones. Due to changes in the material flow pattern and grain structure produced during the FSW process, several microstructural zones appear. The average grain size in the TMAZ at the SS316L and Inconel 718 side was found to be 17 µm and 22 µm, respectively, whereas it was 8 µm and 11 µm in the SZ. In the TMAZ of SS 316L, some elongated grains with fine grains were found, compared to entirely fine equiaxed grains in the TMAZ of IN718. The differential in heat generation and cooling rate during the FSW led to the grain size variation that was seen. In this research, the heat-affected zone (HAZ) near the base metals was not observed in both SS316L and Inconel 718 sides because there is a fast cooling rate during the FSW process that does not affect the microstructure [109]. In the weld nugget zone, observing the flow patterns reveals the flow of SS316L material from the RS to the AS was high. The upper section was in a lamellar pattern, while the below portion was in a vortex-like pattern. According to Kangazian et al. [116], variations in flow patterns in the

weld zone are mainly caused by differences in temperature distribution and material mechanical and physical characteristics.

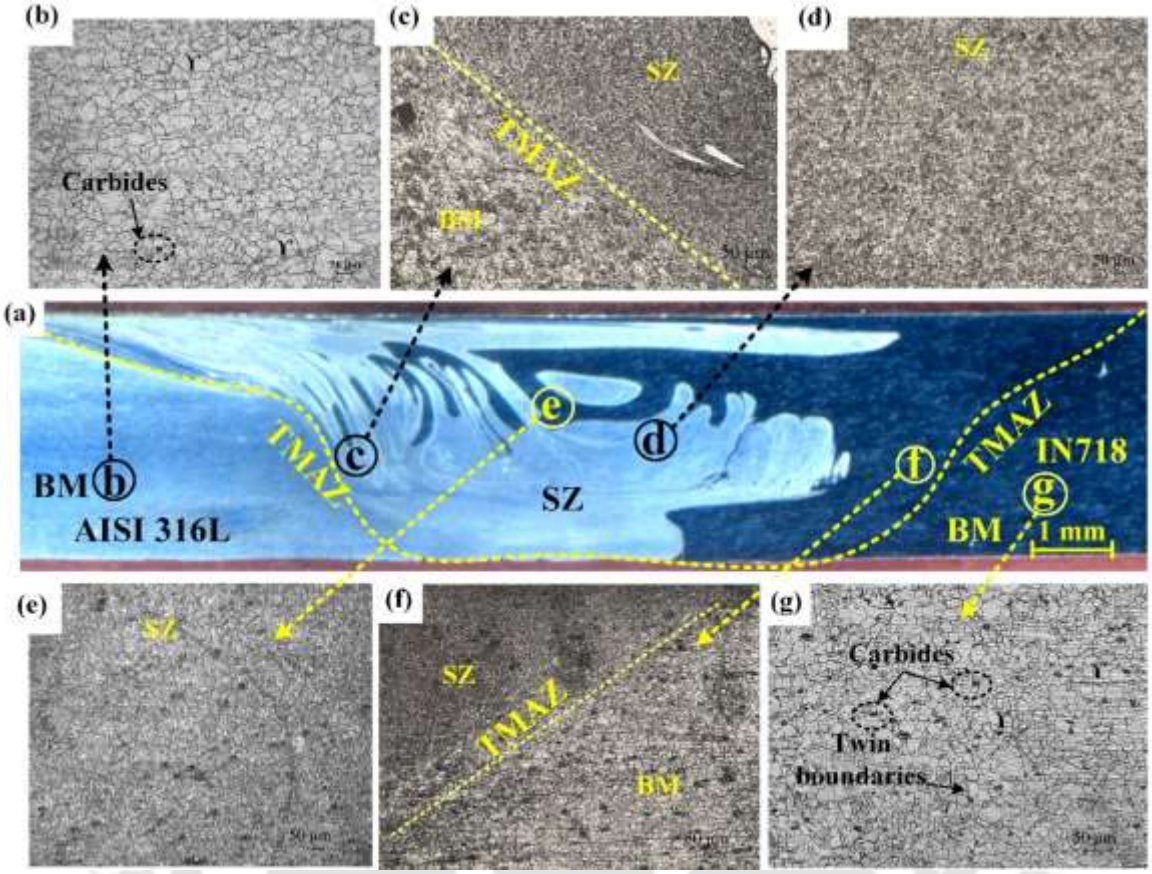

Fig. 7.5 Cross-sectional view of dissimilar I-FSWed joints under 140 mm/min.

To better understand the effect of induction preheating and welding parameters on the welded joint, the study of TMAZs and SZs is significant. Figure 6 shows the optical microscopic views of the TMAZ and SZ microstructures obtained at 70 and 140 mm/min under the conventional and induction-assisted FSW process. Under the conventional FSW, the average grain size of the SZ at welding speeds of 70 and 140 mm/min was 7.2 and 5.5 µm, respectively, for the SS316L, whereas it was 10 and 7.5 µm for Inconel 718. A narrow region of the TMAZ (between the marked yellow line) between the base and the SZ was observed in the conventional FSW, as shown in Fig. 7.6. The measured average grain size of the TMAZ in the SS316L was 15.6 and 14 µm, whereas it was 22 and 16.2 µm for the Inconel 718.

In comparison, the effect of induction preheating on the grain refinement was also observed under the joint obtained at the same traverse speed. The microstructural observation of the I-FSW joint obtained at 300 ^{o}C preheating temperature reveals that the measured average grain size of the SZ in the SS316L was 8.6 and 7.2 µm, at 70 and 140 mm/min, respectively, whereas

it was 11 and 8.7 µm in the Inconel 718. Also, the average grain size of the TMAZ was 16 and 15.5 µm in the region of SS316L, and it was 23 and 17 µm in the region of Inconel 718. The microstructure observation shows that the grains of the SZ and TMAZ were more refined at high traverse speed (i.e., 140 mm/min) than at low traverse speed (i.e., 70 mm/min) under the constant rotational speed of 300 rpm. The region of the TMAZ was found larger in the case of I-FSW than the conventional FSW, and it was higher on the Inconel 718 side than on the SS316L side. The difference in the TMAZ region could be the relatively low temperature, variations in the materials' physical characteristics, and variations in cooling rates.

The generated temperature highly influences the nugget zone's microstructure during the FSW. The temperature recorded (mentioned in chapter 5) during the FSW and I-FSW of Inconel 718 at 140 mm/min was 937 ^{o}C and 1055 ^{o}C, which was sufficient to recrystallize the grains of Inconel 718 and stainless steel 316L. Apart from temperature, the rate of heat generation and rate of deformation was also responsible for the microstructure growth. The responsible cause for forming small grains at high traverse speed was the high cooling rate and low heat input per unit length, giving less grain growth time [116]. At low welding speed, the rate of heat generation dominates over the deformation resulting in the grain coarsening. However, the grains obtained in both Inconel 718 and SS316L with the I-FSW case were slightly larger than in the FSW case. This shows that local preheating significantly improved the recrystallization process. The effect of preheating resulted in sufficient heat input and a high strain rate at high welding speeds resulting in successful dynamic recrystallization of the grains. In addition to the material's temperature, strain rate and initial grain size, the stacking fault energy (SFE) influences the dynamic recrystallisation mechanism. The materials used in this investigation were Ni-alloy and stainless steel, which have low stacking fault energy and lead to discontinuous dynamic recrystallization (DDRX) mechanisms [174]. Material with low stacking fault energy can easily form recrystallization nuclei than the material (i.e., Al) of high SFE. Ji et al. [71] have also reported similar results on the effect of preheating in their research.

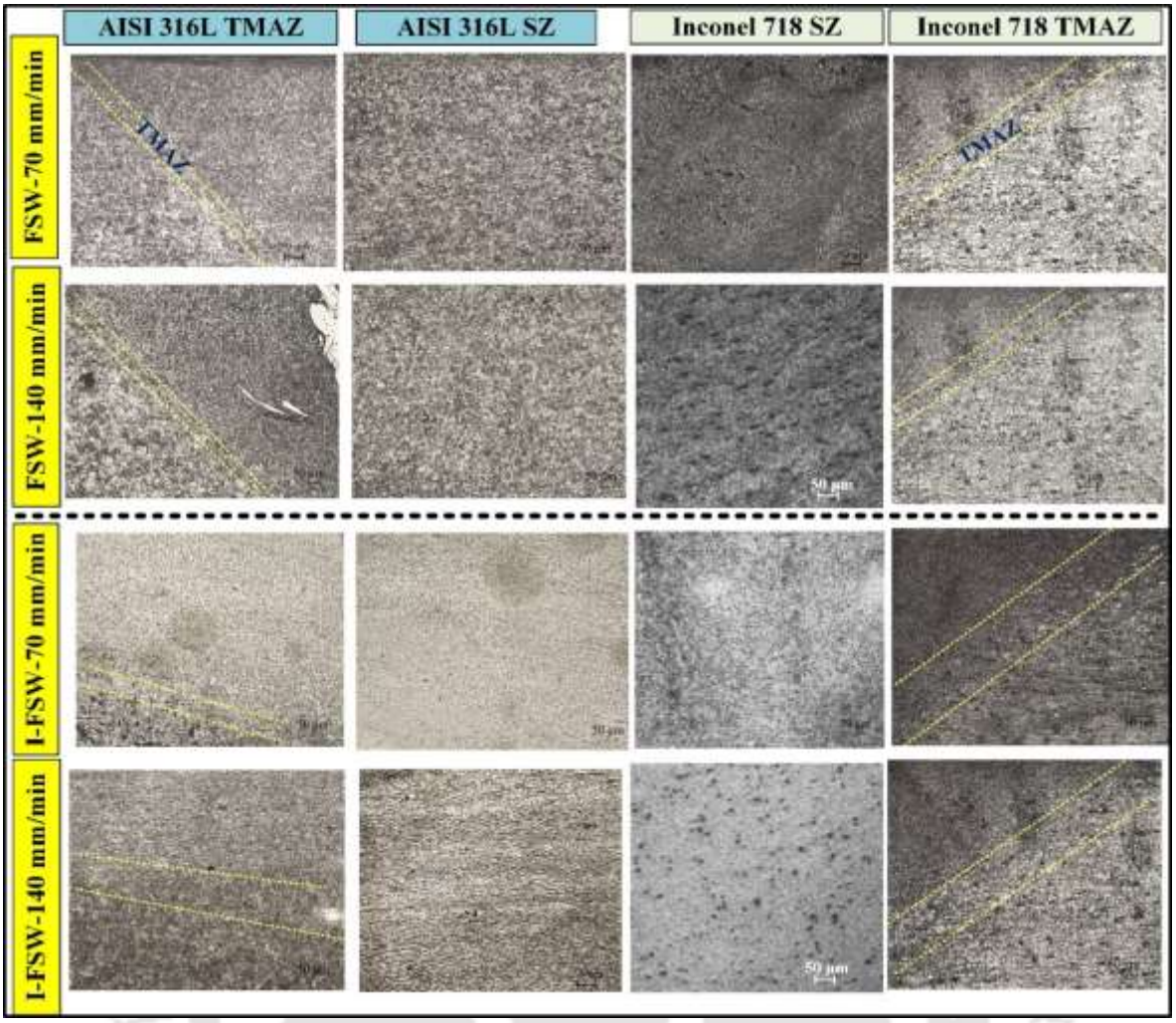

Fig. 7.6 Optical microstructure of TMAZ and SZ of the welded sample obtained under conventional and induction-assisted FSW.

7.3.4. Bonding characterization.

The study of the material flow and bond formation in the nugget zone of the joint obtained under the FSW and I-FSW process at a welding speed of 140 mm/min was performed with the help of the FESEM-EDS micrographs, as shown in Fig. 7.7. SEM images of the nugget zone of the joint corresponding to the FSW process are shown in Fig. 7.7 (a), whereas images obtained under the I-FSW process are shown in Fig. 7.7 (e). The cross-sectional view illustrates the layer of the SS316L and Inconel 718 in the nugget zone. The detailed analysis of the SEM images obtained under the FSW process corresponding to the stir zone of the IN718, interface regions between IN718 and SS316L and the stir zone of SS316L are shown in Figs. 7.7 (b), (c) and (d), respectively. Similarly, the corresponding regions obtained under the I-FSW process are shown in Figs 7.7 (f), (g) and (h). The occurrence of refined MC-type carbide particles and

intermetallic phases in the SZ of the IN718 region under the FSW and I-FSW cases was observed. The magnified stir zone image of the Ni-alloy region reveals the uniform distribution of the carbide particles ranging between 5- 12 μm, as shown in Fig. 7.7 (b) and (f). The EDS point spectrum 1 and 2 confirm the presence of low-temperature carbide particles such as (Nb, Ti)C and (Nb)C in the SZ of the weld. The magnified image (Fig. 7.7 (d)) of the SZ of the SS316L region shows the presence of some microvoids in the conventional FSW joint, whereas it was not found (in Fig. 7.7 (h)) in the I-FSW joint. The presence of the microvoid in the nugget zone is generally observed due to insufficient heat input and improper intermixing of the materials, which decrease the weld strength [24]. Figs. 7.7 (c) and (g) show the SEM images of the interface regions of IN718 and SS316L corresponding to the SZ obtained under FSW and I-FSW, respectively. In both cases, no intermetallic compounds were observed at the interface regions, which is often observed with dissimilar FSW of low melting alloys [120]. In addition, the EDS analysis of the SZ shows the existence of some external elements like tungsten (W) and cobalt (Co), which were found due to tool wear that occurred during the FSW. The EDS result of the SZ obtained under the FSW shows 1.7 wt.% of tungsten elements (spectrum 3 and 4), whereas it was 0.1 wt.% of tungsten elements (spectrum 6) in the case of I-FSW. The presence of low wt.% of tungsten element in the I-FSW joint reveals less wear to the tool due to softening of the base material. The microstructural analysis of the SZ of the SS316L region explored the presence of some ferrite phase between the austenite grain boundary. The EDS spectrum 5 confirms the appearance of delta ferrite in the stainless-steel region, which shows less amount of austenite stabilizing element Ni and high ferrite stabilizing elements Cr and Mo compared with the base steel. The result of EDS spectrum 7 at the interface layer of the I-FSW joint shows the existence of some oxide particles, which may be caused by local preheating of the BM.

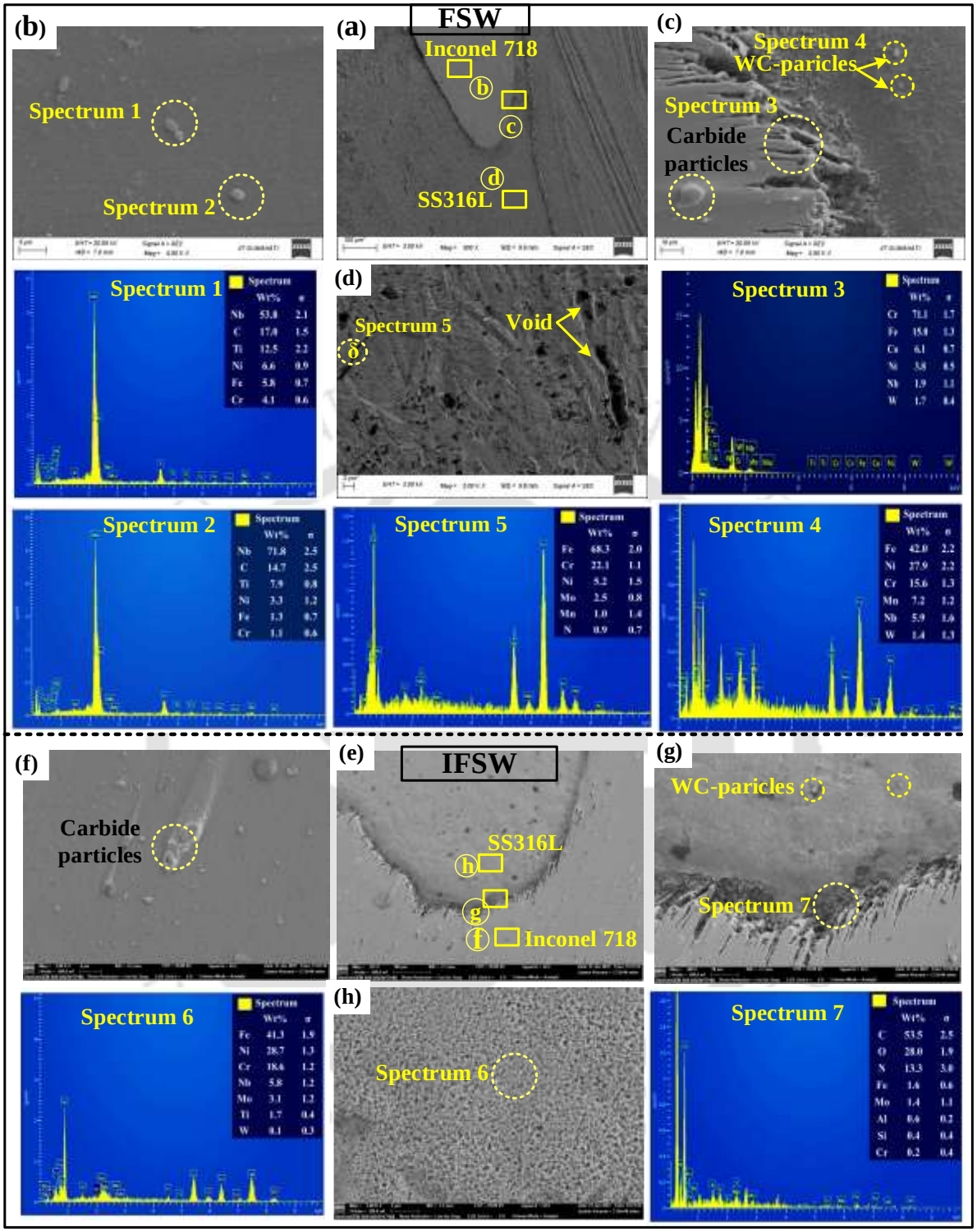

Fig. 7.7 SEM examination of SZ obtained under (a) FSW and (e) I-FSW processes with corresponding EDS spectrum.

Furthermore, the EDS area mapping on the interface region of Ni-alloy and steel in the nugget zone of the I-FSW sample was performed to analyze the element diffusion. The EDS mapping reveals the high concentration of Ni and Fe elements in two separate regions, confirming

Inconel 718 and SS316L regions, as shown in Fig. 7.8. A clear boundary in the interface region was observed, revealing the good diffusion of the Ni and Fe elements. The high concentration of the Mo and Nb elements in the region of high Ni concentration was observed, whereas the concentration of the Cr was almost the same in both regions.

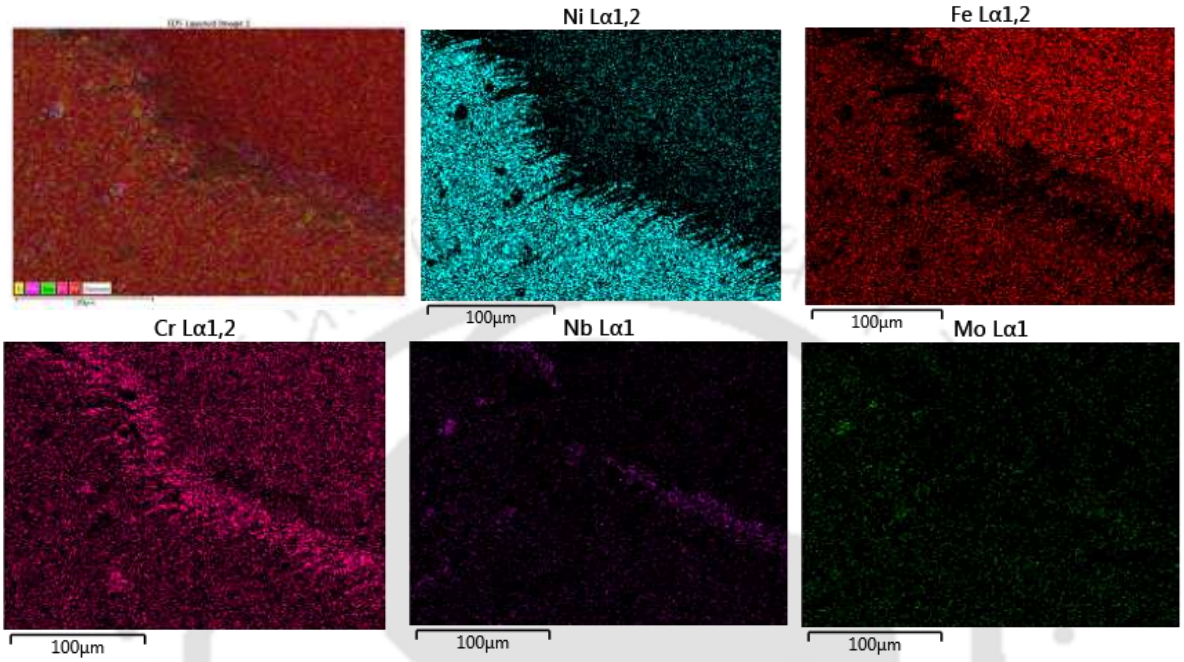

Fig. 7.8 EDS mapping in the SZ was obtained under the I-FSW process.

Moreover, the EDS line scanning across the interface was used to investigate the chemical composition of the diffused elements. Figures 7.9 (a) and (b) show the FESEM image and EDS line scan results of the interface region obtained under the FSW and I-FSW joint, respectively. The EDS line scan results show that no intermetallic compound layer is formed at the interface region. The distribution profile of the elements across the interface shows the presence of major elements Fe, Cr, Ni, Mo, and Nb. In both cases, the chemical composition profile shows a decrease in Fe and Cr and an increase in Ni and Nb in the diffusion zone. At the interface region, the chemical composition (in wt.%) of the major diffused elements Ni, Cr, Fe and Nb was 12%, 22%, 60% and 1% in the FSW joint, respectively, whereas, in the I-FSW joint, it was 11%, 28%, 64% and 0.9%. The width of the diffusion zone of the joint obtained under the FSW joint was approximately 1.9 µm, whereas, in the I-FSW joint, it was 2.4 µm. The enhanced atomic diffusion zone with the I-FSW may be explained by the additional heat input resulting in more materials' softening. Li et al. [140] also observed the variation of the diffusion zone in the electrically assisted pressure welding of the Ni-alloy and steel. Additionally, the high concentration of the Cr and Nb elements in the interface region, especially for the I-FSW joint,

indicates the segregation of secondary phases like carbides. Because of the high concentration of Fe and Ni elements, the EDS scan findings show that the structure of the interface region is fcc.

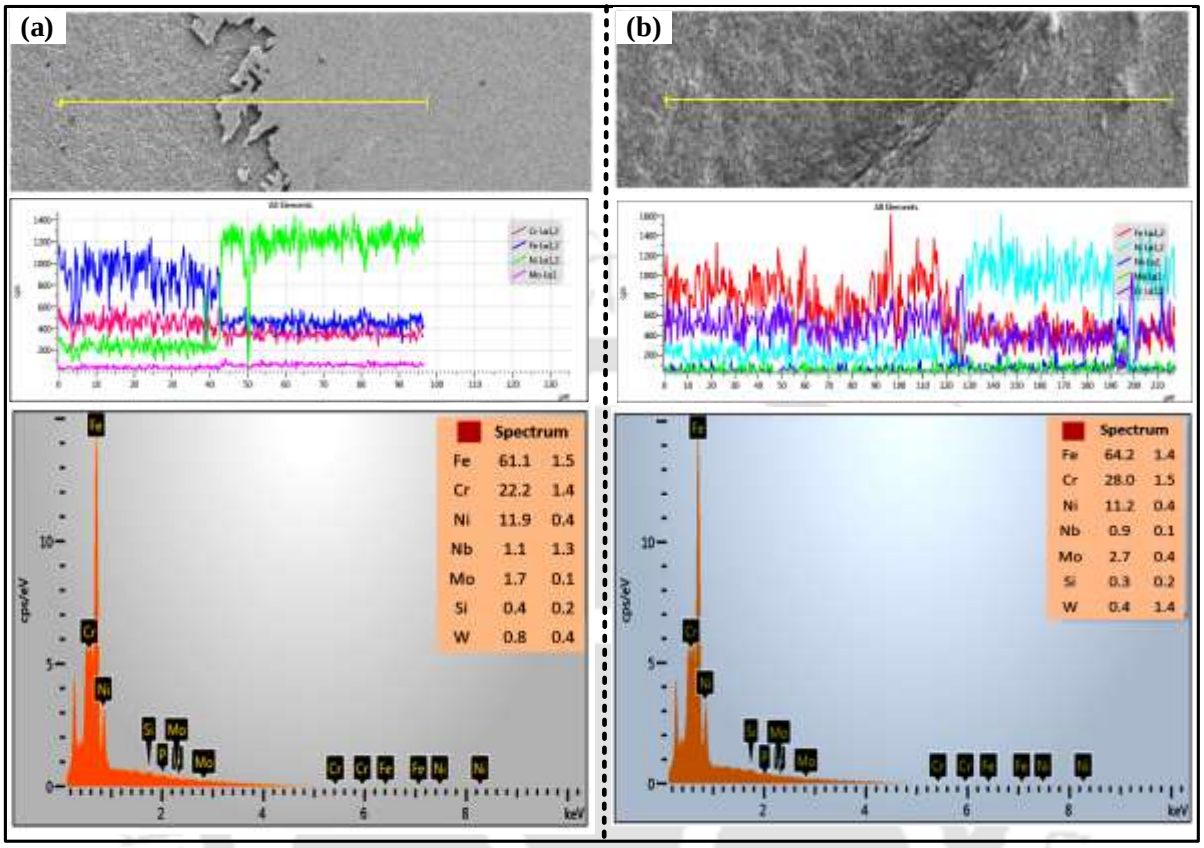

Fig. 7.9 EDS line scan at the joint interface was obtained with (a) FSW and (b) I-FSW.

Figure 7.10 displays the combined X-ray diffraction pattern of the welded sample under the FSW and I-FSW joint with the base materials. The base material, i.e., Inconel 718 and SS316L, shows only the diffraction pattern of the face-centered cubic austenitic (ϒ) matrix with a 2θ value of 43.4º, 50.58º, 74.50º and 90.51º. The diffraction pattern of the welded samples obtained under the FSW and I-FSW shows some minor peaks with the ϒ austenitic peak. The presence of $(Fe_{12}W)0.15$ and $CrNi_3$ phases with an fcc structure were found in the welded sample. The XRD pattern of the welded joint reveals a low-intensity peak, which confirms the presence of components (such as W and Co) with carbide phases. The existence of external elements in both cases confirms the occurrence of tool wear during the welding.

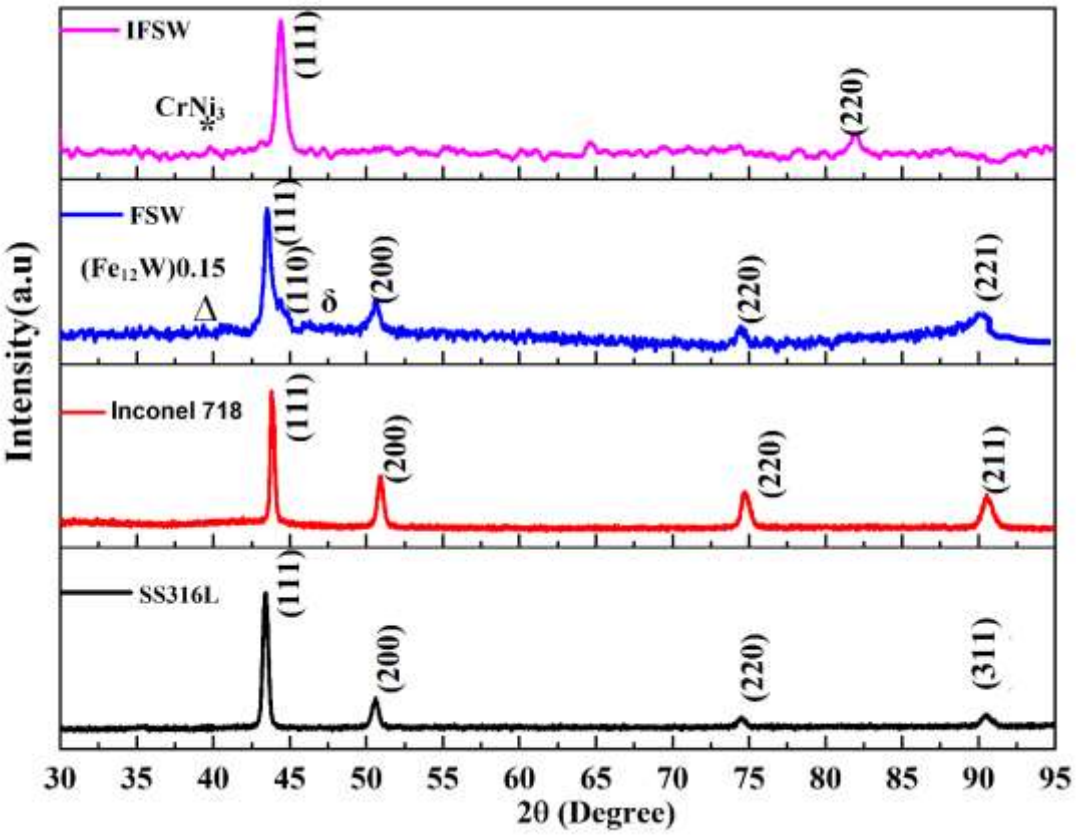

Fig. 7.10 XRD patterns of the welded sample under the FSW and I-FSW with parent materials.

More details of the microstructure and phases present in the SZ of the joint obtained at 140 mm/min under the FSW and I-FSW process were studied by transmission electron microscopy (TEM) observations. Figures 7.11 (a) and (c) show the TEM image and the corresponding selected area diffraction (SAD) pattern (Figs. 7.11 (b) and (d)) taken from the FSW joint. The TEM image and the corresponding SAD pattern obtained under the I-FSW are shown in Figs. 7.11 (e) and (f). The presence of primary carbide $(Ni_3Nb)C$ particles with some precipitates $M_{23}C_6$ was observed with the magnified bright-field TEM image (Fig. 7.11 (a)). These precipitates had circular and long needle-like morphology observed in the grains and at their boundary. The existence of primary carbide particles and the precipitates (Fe, Cr, Mo, Mn)C, i.e., $M_{23}C_6$ in the ϒ austenite matrix, was confirmed by the results of EDS point spectrums 1 and 2. The previous investigation (mentioned in chapter 4) showed that during the FSW of Inconel 718, the generated temperature in the SZ reached around 1050 ^oC. This temperature was sufficient for generating the low-temperature carbide particles, which are generated between 760 to 980 ^oC [175]. The comparative study of induction-assisted FSW with

conventional FSW was performed with the bright-field image, as shown in Figs. 7.11 (c) and (e). The effect of preheating on the carbide particles and grain size, along with dislocation densities, was observed. In the grain study, the microstructural grain size of the nugget zone in the case of I-FSW was observed to be slightly larger grain size than the FSW, which also generated the difference in the dislocation density. The dislocation density near the grain boundaries in the case of preheating was higher than convention FSW because of the more dynamic recrystallisation observed in I-FSW. The TEM image of SZ obtained with FSW (i.e., Fig 7.11 (c)) shows a round-shaped carbide particle with an average diameter of 80 nm, whereas it was found between 25 to 45 nm in the SZ obtained with I-FSW (i.e., Fig. 7.11 (e)). In the corresponding SAD pattern, the big and small spots related carbide and intermetallic phase were observed with a [001] zone axis. The diffraction pattern corresponding to the bright field image of the carbide particles is illustrated in Figs. 7.11 (c) and (e) observed in the face-centered cubic crystalline (fcc) structure with the [221] and [211] index.

Furthermore, Figs. 7.11 (g) and (h) show the HRTEM image and the corresponding d spacing value taken from the SZ obtained under the I-FSW. The GATAN graph showed the d-spacing value of the selected area of the HRTEM was 2.8 Å. These analyses confirm the crystalline structure nature of the intermetallic phase, which matched the result obtained in the XRD analysis. The binary and ternary phase diagram of the SS316L exhibits the most commonly precipitate phases $M_{23}C_6$, σ, η and χ, whereas the phase diagram of Inconel 718 shows carbides (i.e., MC, M_6C, $M_{23}C_6$ and M_7C_3), δ and Υ'' [24,172]. The composition, thermomechanical treatment and temperature generally influence the characteristics of the phases. The existence of high-temperature carbide (i.e., MC, M_6C), σ, η, χ and δ in the weld zone generally require high energy with a long ageing time and temperature [176]. In this study, it should be noted that only low-temperature carbide precipitates were observed during the FSW process. This might be due to the low heat input, short thermal cycle, and different properties of the precipitates.

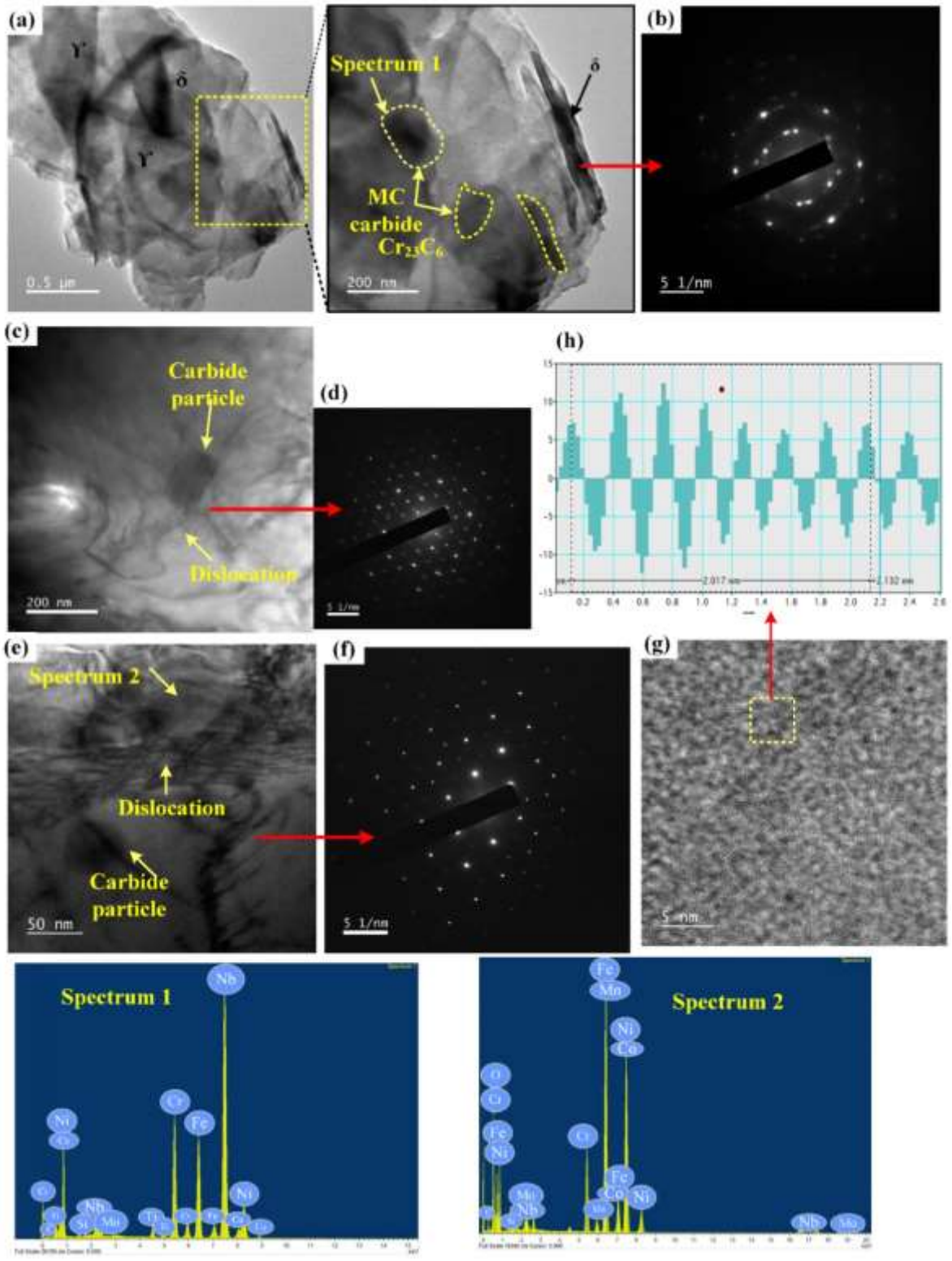

Fig. 7.11 A bright-field TEM image with the SAD pattern of the SZ was obtained under (a, c) FSW and (e) I-FSW, along with the HRTEM image.

Furthermore, the microstructural analysis of the interface region of Inconel 718 and SS316L joint obtained under the I-FSW process was performed with the TEM image, which is shown

in Fig. 7.12. The TEM bright-field image shows that it consists of two separate regions of Inconel 718 (noted by A) and SS316 (noted by B), confirmed by the XEDS analysis. At the interface layer, no intermetallic layer was observed. The bright-field image also shows the presence of carbide particles and deformed and recrystallised grains. The presence of deformed $M_{23}C_6$ precipitates with 35 nm was seen at the interface region. Moreover, the HRTEM of the bright filed interface region was analyzed to calculate the d-spacing value. The measured d value at three different positions near the interface region was 2.6, 2.8 and 2.6 Å. The SAD pattern of the interface region shows the fundamental reflection of the ϒ matrix along with the intermetallic phase, an fcc crystalline structure.

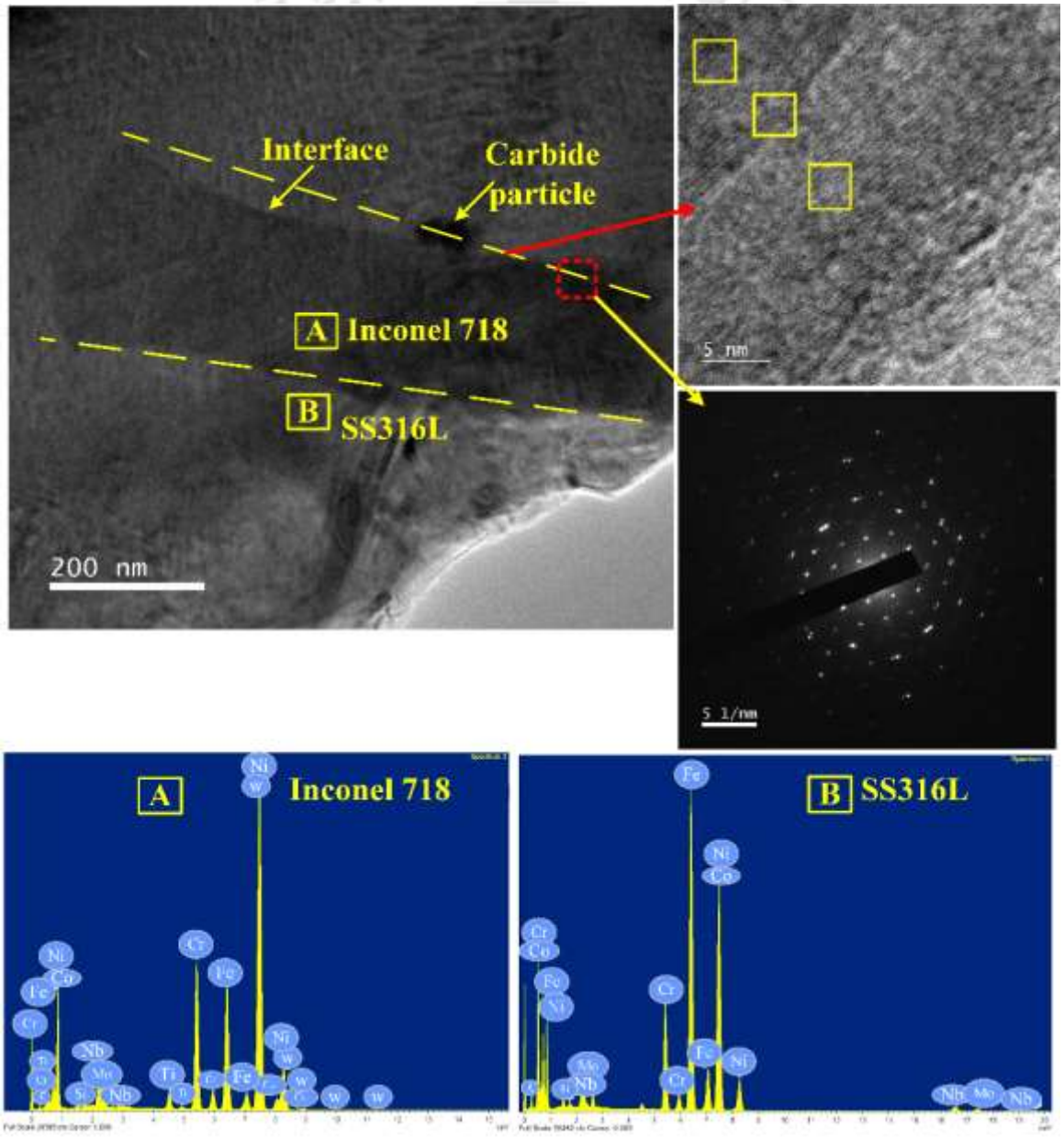

Fig. 7.12 TEM Images and SAD pattern of the interface region under the I-FSW process.

7.3.5 Mechanical properties

The mechanical properties of FSW and I-FSW joints produced at 70 and 140 mm/min are tested to demonstrate the advantages of induction preheating in the FSW joints. Figure 7.13 (a) shows the microhardness measurement position along the weldments' transverse cross-sectional position at 0.75 mm, 1.5 mm and 2.75 mm below the top surface. Figures 7.13 (b) and (c) show the inhomogeneous average hardness distribution curve obtained at the FSW and I-FSW joints, respectively. The microhardness values of the BM of Inconel 718 and SS316L were obtained from the combined Figs. 7.13 (b) and (c) are 260 ± 5 and 190 ± 5 $HV_{0.5}$, respectively. It is important to note that the average microhardness value of the nugget zone in all cases was higher than the base metals, and it was maximum in the Inconel region. The average microhardness values in the SZ of the FSW joint at 70 and 140 mm/min were 315 and 325 $HV_{0.5,}$ respectively. The variation of hardness value with traverse speed was due to grain size variation at different welding parameters [42]. In the FSW joints, a slight increment of the hardness value in the TMAZ of the stainless-steel region was observed, whereas it was lower in the Inconel region. According to previous work [42,115], the microhardness value in the weld zone was highly influenced by the refined recrystallized grains and refined carbide precipitates caused by dynamic recrystallisation during the FSW of Ni-alloy and stainless-steel joints.

Compared with the FSW joint, the measured average hardness value in the nugget zone of the induction preheated I-FSW joint was found to increase slightly due to the more refined carbide microstructure, as shown in Fig. 7.13 (c). The hardness value in the SZ of the I-FSW joint at 70 and 140 mm/min was 325 and 355 $HV_{0.5}$. Furthermore, fluctuation of the hardness curve in the nugget zone was observed because of some refined carbide particles and the generation of some fine precipitates in the nugget zone of the I-FSW joint [91]. Thus, an increase in hardness value in the weld zone of both materials in the FSW and I-FSW can be explained by grain refinement. According to the Hall-Petch equation [60], the microhardness of crystalline materials increases as grain refinement improves. Li et al. [140] also observed similar trends of variation of microhardness in the FSW joints of stainless steel with Ni-alloy.

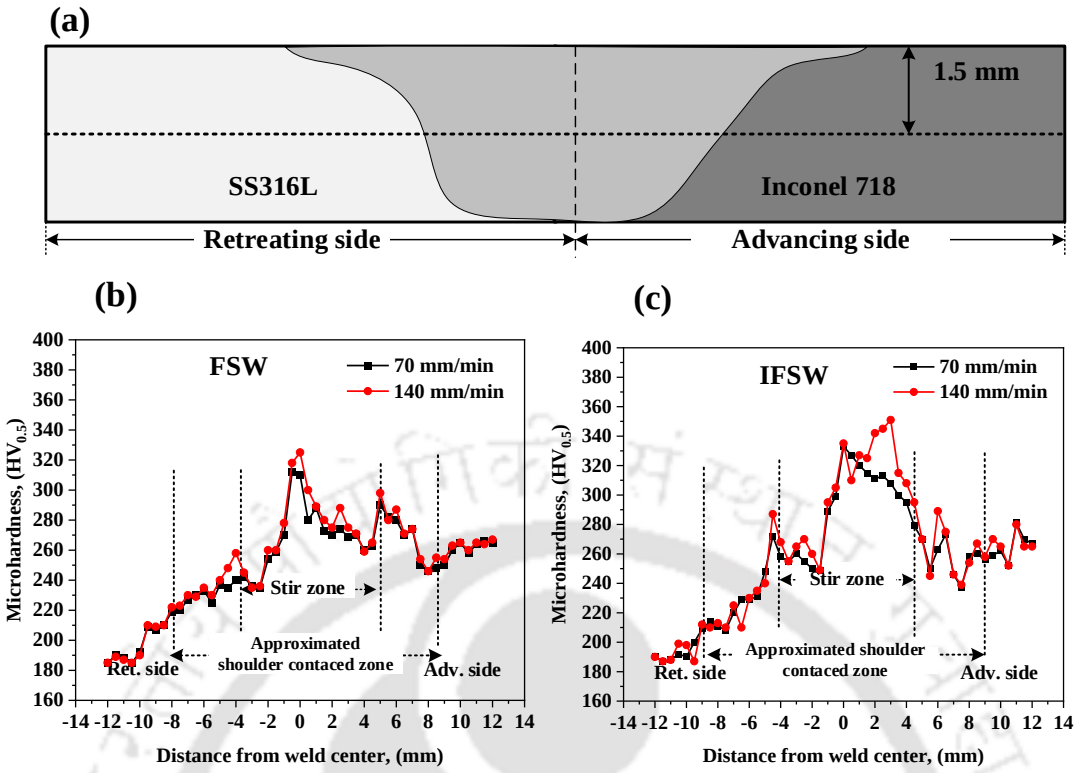

Fig. 7.13 (a) Schematic representation of measured hardness position with hardness distribution curved obtained under (b) FSW and (c) I-FSW joints.

The ultimate tensile strength (UTS) and 0.2% offset yield strength (YS) of the base material with the welded sample obtained at various parameters are shown in Fig. 7.14 (a). Figure 7.14 (b) shows the engineering stress-strain curves of FSW and I-FSW joints obtained at optimal parameters. The UTS of the base materials Inconel 718 and SS316L were 945 ± 5 and 680 ± 5 MPa, respectively. Under the conventional FSW, the tensile strength of the welded sample was maximum (i.e., 688 MPa) at low traverse speed (i.e., at 70 mm/min), whereas it was minimum (i.e., 210 MPa) at high traverse speed (i.e., 140 mm/min). The high tensile strength at low speed may be caused by a defect-free weld joint with refined grains in the weld zone. In contrast, at high traverse speed, weld defect like a large cavity in the bottom of the joint was observed (as shown in Fig. 7.4), which was highly responsible for the decrease in weld strength. The defects like micro-voids, cavities and wormholes produce stress concentration during the tensile test, which is generally responsible for the strength of the welded specimens [77]. On the other hand, in the I-FSW joint, the maximum tensile strength (i.e., 683 MPa) was observed at the high traverse speed, whereas it was 559 MPa at the low traverse speed. The yield strength of the welded samples obtained at low and high traverse was 336 and 380 MPa, respectively.

However, the optimal tensile strength of the welded samples obtained with the FSW at 70 mm/min and the I-FSW at 140 mm/min was lower than the Inconel 718 and higher than the SS316L. Compared with the FSW, the I-FSW gives better advantages in enhancing the mechanical properties at high speed. The dissimilar I-FSW joint welded at high traverse speed (i.e., 140 mm/min) exhibited good weld strength because a defect-free joint with proper intermixing of material in the nugget zone was observed, as discussed in the previous section. The formation of more refined carbide particles with phase precipitation in the SZ due to local preheating may be caused enhancement of the mechanical properties of the joint.

Furthermore, fracture characteristics of the defect-free joints obtained under conventional FSW (70 mm/min) and preheated I-FSW (140 mm/min) were examined to establish the correlation between their mechanical and microstructure properties. To examine the tensile fracture characteristics, the fractured surfaces were analyzed by the FESEM. Figure 7.15 shows the welded joint's tensile fracture position and SEM surface morphologies. The macroscopic observation shows that the conventional FSW failure joint crack passes through the SS316L base metal. In contrast, the position of a crack in the I-FSW failure joint passes through the weld nugget zone (see Figs. 7.15 (a) and (c)). The observation of the SEM fractography image (Fig. 7.15 (b)) shows the formation of the neck in the region of base stainless steel before the failure. The magnified image of the fractured surface reveals the inhomogeneous distribution of deep and shallow dimples and carbide particles (marked yellow arrow), which shows the ductile mode of failure. Whereas the observation of the fractured tensile sample of the preheated I-FSW shows the fracture surface of the joint exists from two different morphological surfaces (denoted A and B region in Fig. 7.15 (d)). The magnified view of region A shows the fracture surface of dense shallow dimples and a few refined carbide particles dispersed in the Ni-alloy matrix. This observation indicates that this Ni-region underwent high plastic deformation. In contrast, the magnified view of region B shows that the fractured surface consists of some tear ridges with deep dimples. This indicates that region B (i.e., stainless steel) undergoes a mixed mode of deformation. The initiation of failure in the weld zone may be caused by the joint root failure and some carbide precipitates acting as the initiation of crack.

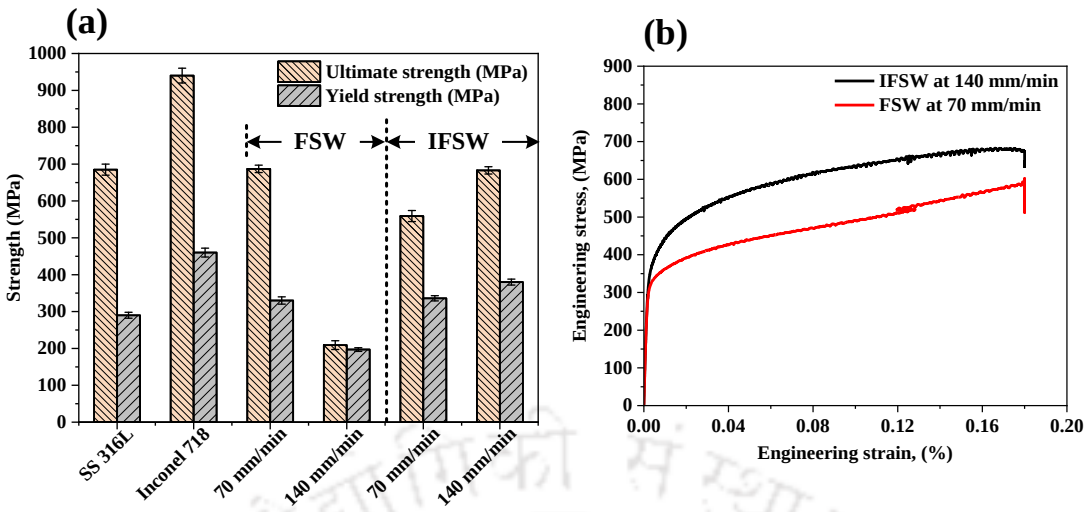

Fig. 7.14 (a) Tensile strength and corresponding 0.2% yield strength of the base and welded sample, and (b) engineering stress-strain curves of optimal FSW and I-FSW joints.

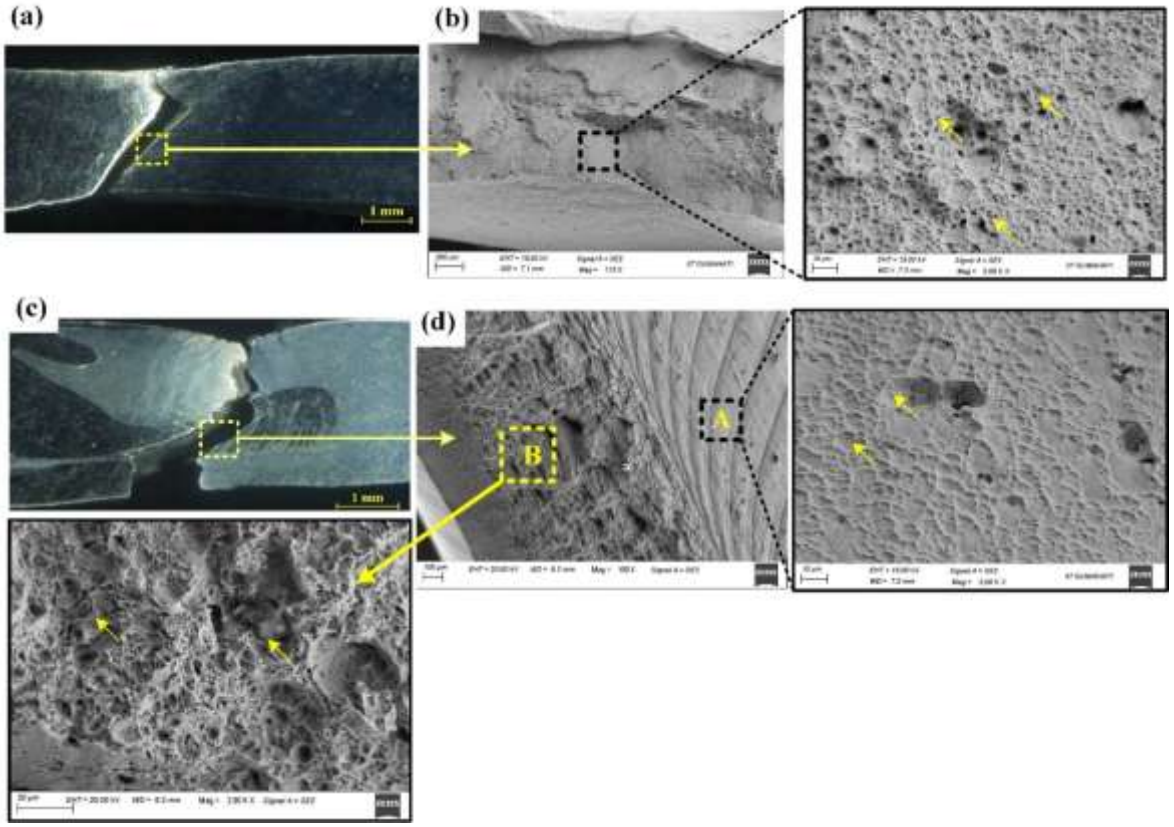

Fig. 7.15 Fracture morphologies of tensile tested specimen: cross-sections of (a) FSW (300 rpm-70 mm/min) and (b) I-FSW (300 rpm-140 mm/min) failure joints and their corresponding (b and d) FESEM images.

7.3.6 Estimation of tool wear

Rapid tool wear is commonly observed during the FSW of high strength materials like Ni-alloys and steel, which poses a significant challenge for defect-free joints. This study used the tungsten carbide with cobalt (WC-10wt.% Co) binder phase for the with and without preheated dissimilar FSW joints. The analysis was conducted after the joining of 400 mm weld length obtained under the FSW parameters 300 rpm and 140 mm/min and preheating temperature 300 ^{o}C. Figure 16 shows the qualitative and quantitative tool analysis used in the conventional and induction-preheated FSW process. Figure 7.16 (a) shows the initial tool pin height of 2.7 mm with EDS analysis at the shoulder and contact tool surface. After the welding, tool pin height was observed at 0.8 mm and 2.4 mm under the FSW and I-FSW process, as shown in Fig. 7.16 (b) and (c), respectively. The visual inspection of the deformed tool showed a change in the original tool geometry with the reduction of pin length and shoulder wear. The reduction of tool pin height after 400 mm weld length was observed at maximum (i.e., 70%) with conventional FSW, whereas it was minimum (i.e., 7.4%) with I-FSW.

However, the degradation of the tool in terms of weight loss in grams (g) under FSW and I-FSW was also weighted with microbalance before and after welding. After the welding, the residual base materials adhered to the surface of the shoulder and pin were eliminated and cleaned in the ultrasonic bath before the tools were weight. The initial weight of the received tool was 227.97 g, whereas, after 400 mm weld length, its reduced weight was 226.70 g and 227.915 g in FSW and I-FSW, respectively. The maximum reduction of tool weight in the case of FSW compared with I-FSW was observed because of high shoulder wear, pin height reduction, and oxide layer formation with the FSW observed. EDS area mapping with point analysis of the FSW tool shoulder near the pin base area (marked as A) was performed, as shown in Fig. 7.16 (b) and spectrum A. The result indicates that a high reduction of wt.% of tungsten (W) element and increment of carbon and oxygen elements were observed. Furthermore, external elements such as Fe, Ni, and Mo were also found in the base metal due to the adhesion nature of the WC tool element [122]. The EDS spectrum B of the I-FSW tool shows the presence of a higher wt.% of W than the FSW but less than the as-received tool. Applying an external heat source reduces the generated stress on the tool by softening the base material [27]. During the welding, a high rate of heat is generated and reaches an elevated temperature of tool material leading to adhesion wear and oxidation of the tools [177]. In addition, tool shoulder surface roughness observation was performed, as shown in Fig. 7.16 (d). The result shows the roughness value was high (R_a: 0.76) in the FSW tool and (R_a: 0.54)

in the I-FSW compared with the as-received tool (R_a: 0.16) due to high wear on the shoulder surface. Saving of tool degradation in the case of I-FSW was observed due to preheating, reducing axial force and softening of the base material. Understanding the tool wear during high strength dissimilar material is essentially required for future work to increase tool life.

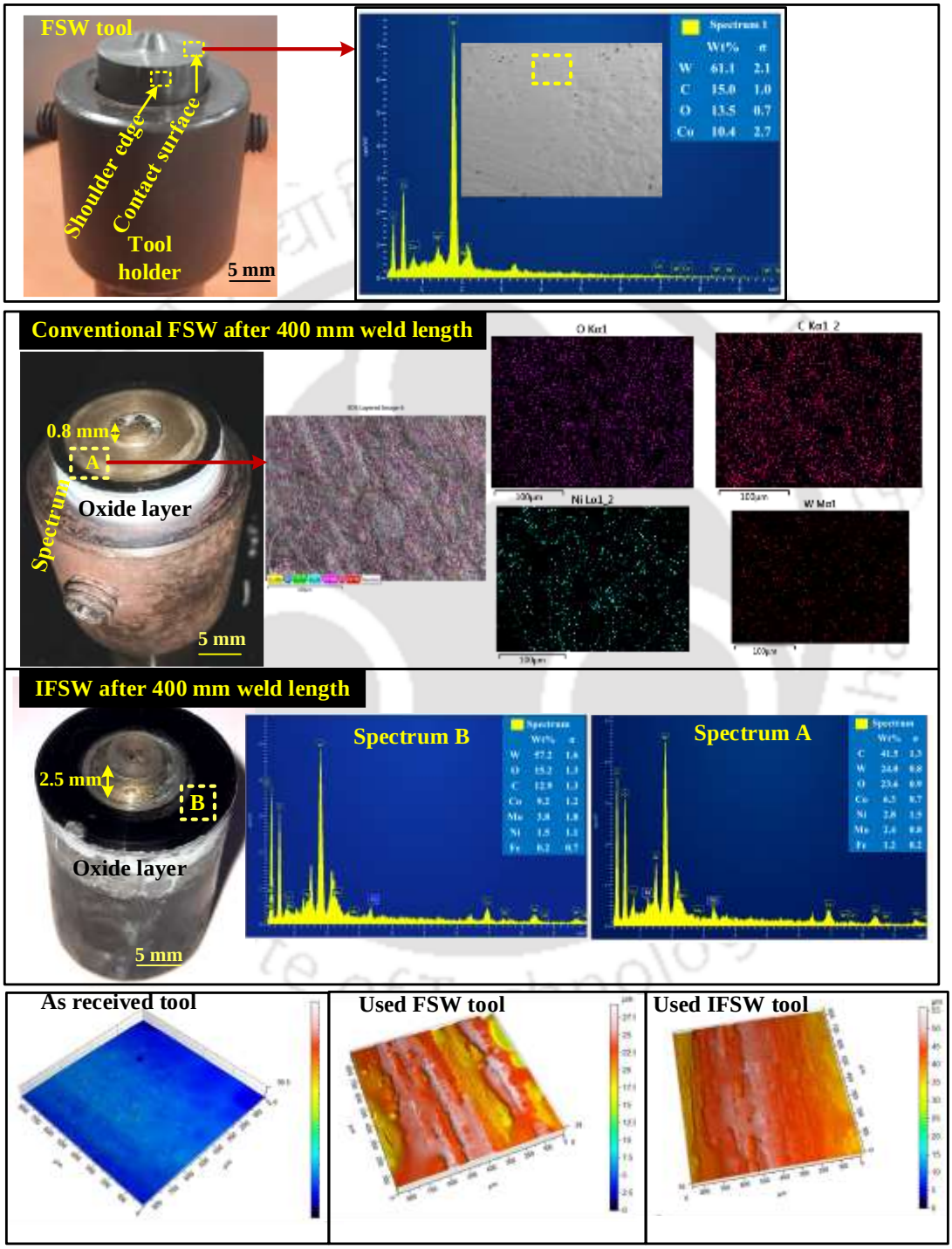

Fig. 7.16 Top view of friction stir welding tool (a) as received, (b) used in FSW, (c) used in I-FSW and (d) its corresponding surface topology.

7.4 Brief scientific discussion

The observation of the results obtained during the dissimilar I-FSW of Inconel 718 with SS316L, shows that the mechanical properties of the joint with preheating significantly improved at a high welding speed (i.e., at 140 mm/min). In this study, it should be noted that only low-temperature carbide precipitates were observed during the FSW process. This might be due to the low heat input, short thermal cycle, and different properties of the precipitates. In the FSW joints, a slight increment of the hardness value in the TMAZ of the stainless-steel region was observed, whereas it was lower in the Inconel region. Increase in hardness value in the weld zone of both materials in the FSW and I-FSW can be explained by grain refinement. According to the Hall-Petch equation, the micro- hardness of crystalline materials increases as grain refinement improves. Similarly, during the tensile test, defects like micro- voids, cavities and wormholes produce stress concentration, which is generally responsible for the strength of the welded specimens. Compared with the FSW, the I-FSW gives better advantages in enhancing the mechanical properties at high speed. The dissimilar I- FSW joint welded at high traverse speed (i.e., 140 mm/min) exhibited good weld strength because a defect-free joint with proper inter- mixing of material in the nugget zone was observed.

7.5 Summary

In the present study, the stainless steel SS316L plate was successfully joined with the Inconel 718 plate by using with and without heated friction stir welding process. The effect of induction preheating on the temperature distribution, applied axial force, microstructure characteristics, mechanical properties and tool wear analysis during the FSW process were performed. Thus, the following conclusions are summarized below based on the results and discussion.

- Friction stir butt joints can be successfully obtained on Inconel 718 and SS316L under a constant rotational speed of 300 rpm and at 70 mm/min with conventional and at 140 mm/min with induction-assisted FSW.
- Analyzing the output power of the induction heating device and temperature confirmed that material surface temperature was proportional to the output power and inversely to the feed rate. Besides, the generated surface temperature on Inconel 718 was higher than on the SS316L.
- The use of preheating reduces the axial force experienced by the tool by 24% under 140 mm/min traverse speed. Induction preheating reduced the tool wear by 62% because of the reduction of axial force and improvement of material softening.

- Microstructural observation showed a highly deformed grain structure with refined carbide particles occurred in the SZ of both materials due to dynamic recrystallization. The combined effect of external preheat and welding speed resulted in more refinement in grain structure. Moreover, high dislocation densities near the grain boundaries in the SZ were noticed under the TEM of the preheated sample. In the SZ, the distribution of refined primary (NbC) and secondary ($M_{23}C_6$) carbide particles in the ϒ austenitic matrix was observed, which improved weld strength.
- Besides mechanically intermixing, an increase in temperature during the I-FSW process led to increasing the width of the diffusion zone at the interface layer; however, no intermetallic compound layer was formed at the interface region.
- Compared with the FSW, the I-FSW process significantly improved mechanical properties at a high traverse speed of 140 mm/min. The optimal tensile strength of the I-FSW joint was 683 MPa, being 473 MPa higher than that of the FSW joint. Reduction of the carbide precipitates size, along with grain refinement and proper intermixing of the materials, causes the primary mechanism for improvement of mechanical properties of the I-FSW joints.

……..*……..*……

CHAPTER 8

8. Corrosion Behaviour of Dissimilar Joints Formed with and without Induction-Assisted Friction Stir Welding

8.1 Introduction

Previous chapter 7 has discussed the feasibility of the FSW process and the effect of induction preheating on microstructure and mechanical properties of the FSWed dissimilar joint of Inconel 718 and SS316L. An improved joint strength at a traverse speed of 140 mm/min with the induction-assisted FSW process was observed. Generally, stainless steel and Ni-based alloys are utilized in severe environments such as aerospace, nuclear engineering, oil and gas production parts, and submarine parts, where high corrosion resistance and high-temperature mechanical properties are required. Therefore, a detailed analysis of the corrosion behavior of the friction stir welded joint of Ni-alloy and stainless steel is needed. The present work thoroughly investigated the electrochemical properties under the acidic and salt solutions of the dissimilar joint formed by the conventional and assisted FSW (I-FSW) processes. In addition, the influence of induction preheating on microstructural features as well as corrosion properties has been deeply studied and finding the relationship between the microstructure of the joint and corrosion behavior.

8.2 Materials and methodology

This experimental work used 3 mm thick Inconel 718 and SS316L sheets to perform dissimilar butt joints by the FSW and I-FSW process and performed a corrosion test. The average chemical composition and mechanical properties of the as-received plate are mentioned in chapter 3, Table 3.1. The details of the FSW tool, the experimental setup, the working principle, and the metallurgical investigation procedure used in this experiment are explained in chapter 3, sections 3.2 and 3.3. Based on the previous work, the optimum parameters used in this study were the traverse speed of 140 mm/min and rotational speed of 300 rpm along with 9 kW output power of the high frequency (i.e., 120 kHz) induction heating machine.

The electrochemical studies on the weldments obtained with and without the induction-assisted FSW along with the base metal (BM) were conducted in a conventional three-electrode cell arrangement. In the electrochemical test, two solutions, 1 M HCl and 3.5 wt.% NaCl was used for the analysis of the corrosion behaviour of the welded joint and the base metal. The details

of the electrochemical test setup and used methodology are explained in chapter 3, section 3.3.3.

8.3. Results and discussion

This section discusses the microstructural and corrosion behavior of the joints.

8.3.1. Microstructural characterization of the base materials

The microstructure of the as-received base material SS316L and Inconel 718 alloys consisting of ϒ austenitic matrix is illustrated in Figure 8.1. The existence of small twin grains with some carbide particles and precipitates ϒ"(Ni_3Nb) in the grains and at the boundaries of a full austenitic (ϒ) matrix of Inconel 718 is depicted in Figure 8.1 (a). The presence of carbide particles and precipitates was previously confirmed by means of the EDS spectrum. Figure 8.1 (b) shows the existence of a tiny amount of ferrite phase in the austenite matrix with some carbide and twin boundaries in the SS316L alloy. Shamanian et al. [109] stated that the formation of the delta ferrite phase in the matrix of the austenite phase is observed during the solidification, where ferrite-promoting elements segregate. Furthermore, both base materials IN718 and SS31L showed naturally coarse microstructure with a distribution of 15-70 µm and 10-52 µm, respectively.

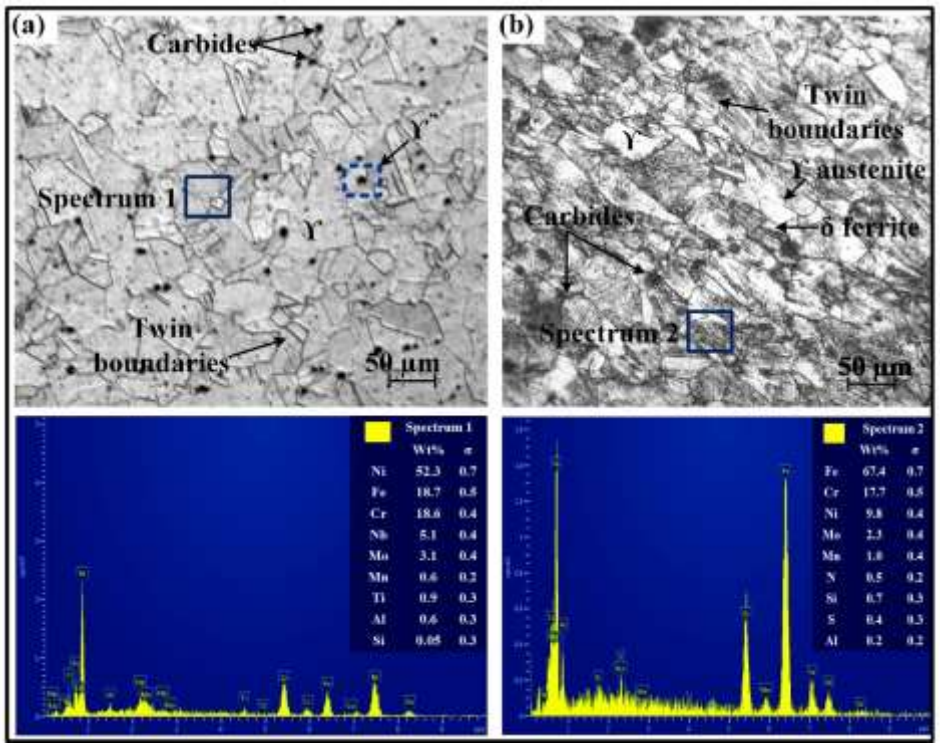

Fig. 8.1 Microstructure and EDS spectrum of parent metal (a) IN718 and (b) SS316L.

8.3.2. Macro and microstructural characterization of the welded samples

The macrostructure across the cross-section of the joint obtained through the conventional FSW and preheated friction stir welding (I-FSW) processes is shown in Figures 8.2 (a) and (b), respectively. The whitish region or RS of the image is stainless steel, whereas the blackish region or AS is IN718. Similar to the previous different weld zone, three typical zones containing base metal (BM), thermo-mechanical affected zone (TMAZ), and stir zone (SZ) can be observed. This investigation should note that heat affected zone (HAZ) in both materials has not been found. The joint obtained through the FSW process was in the basin-like shaped stir zone (SZ) and found to have wormhole defects near the bottom of the SZ, whereas the joint formed under the I-FSW process shows no macro defects. The appearance of wormhole defects in the joint may be a result of inadequate heat input and inadequate mixing of the materials due to high traverse speed during the FSW process. Further observation on the mixing of stainless-steel material from the left side (RS) to the right side (AS) in the case of I-FSW was found to be more than the FSW process. The high volumetric region of the stainless steel in the SZ (Fig. 8.2 (b)) of I-FSW joints might be ascribed to excess heating, causing excessive plastic deformation.

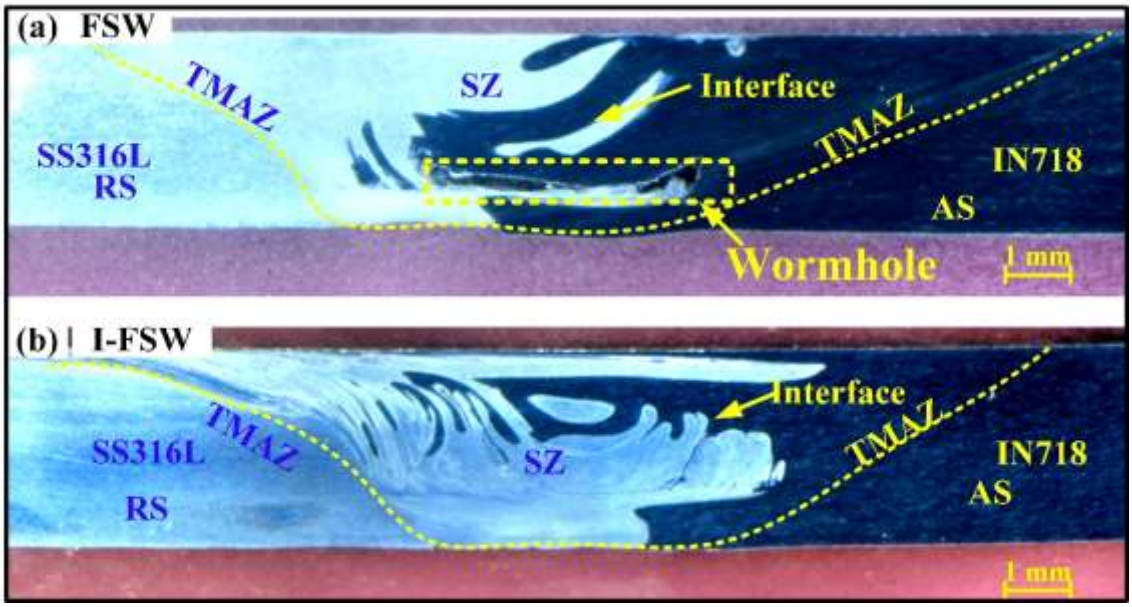

Fig. 8.2 Dissimilar cross-sectional view obtained during (a) conventional FSW and (b) assisted FSW process.

Figure 8.3 illustrates the optical micrographs of the stir zone of the joints obtained by the conventional and assisted-FSW process. In both processes, the microstructure of the stir zone (SZ) revealed a highly distorted grain structure compared to the base material. During FSW,

the rotating tool generates high temperature and intense plastic deformation in the stir zone, which cause dynamic recrystallization (DRX) of the material. Under the FSW process, the deformed grains in the SZ of the IN718 (Fig. 8.3 (a)) and SS316L (Fig. 8.3 (b)) were within the 2 to 12 µm and 3 to 8 µm, respectively. However, the microstructure of the SZ of the joints produced by the I-FSW process, which operated at 300 ^{o}C preheating temperature and traverse speed of 140 mm/min, displayed a relatively slight increase in particle size. In the SZ of IN718 (Fig. 8.3 (c)) and SS316L (Fig. 8.3 (d)), the observed grain size ranged from 3 to 15 µm and 4 to 12 µm, respectively. The responsible cause for the slight increase in the grains under the I-FSW could be attributed to the combined effect of induction preheating and the FSW tool pin, which generates high heat and results in a longer cooling time. The previous research showed that the weld cooling time of the I-FSW joint was found higher than the FSW joint. The strength of the I-FSW joint was not highly affected by the little increment of the grain size. The tensile strength of the I-FSW joint was higher than the FSW joint due to the proper intermixing of material and defect free joint formation.

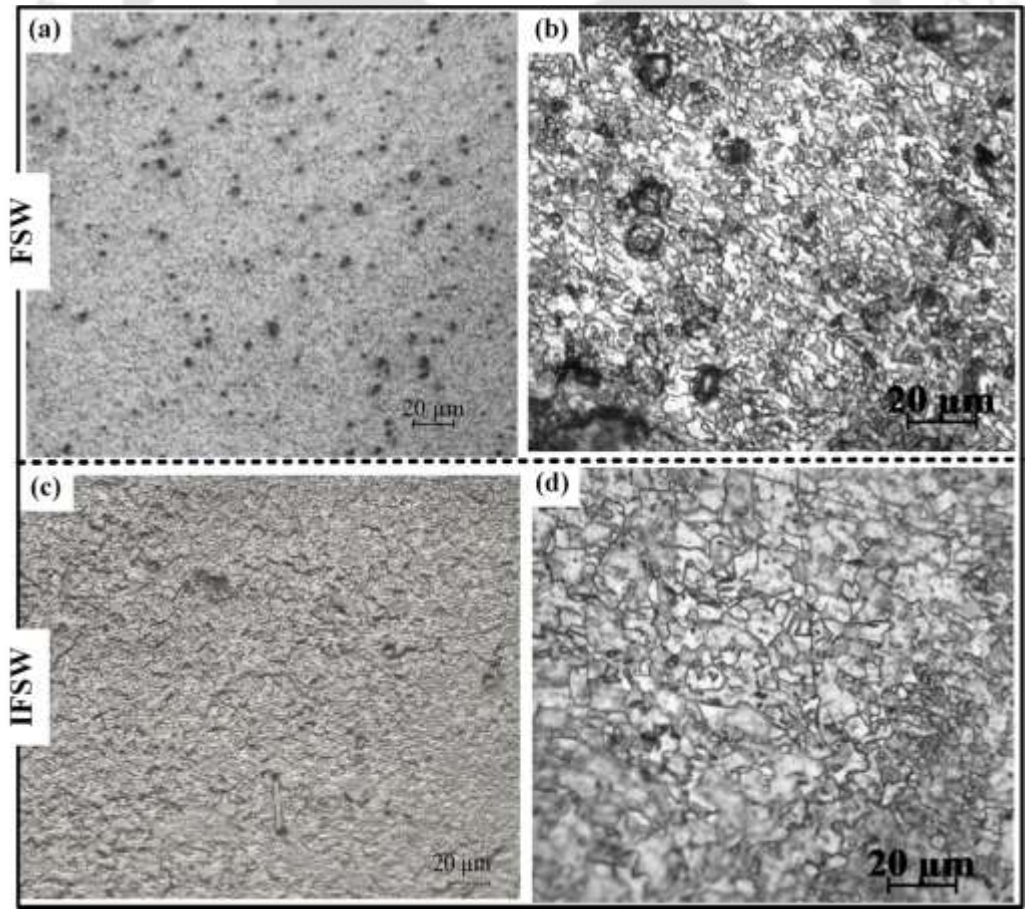

Fig. 8.3 Microstructure of stir zone obtained under the different conditions: (a) FSW-IN718, (b) FSW-SS316L, (c) I-FSW-IN718 and (d) I-FSW-SS316L.

Figure 8.4 shows the FESEM micrographs of the SZ of the joints obtained with and without induction-assisted FSW. Figure 8.4 (a) shows the SZ of the FSW joints, and it can be clearly seen that inside the nugget zone, a separate layer of IN718 (denoted by A) and SS316L (denoted by B) are presented. The magnified SEM image of SS316L material clearly shows the existence of distorted carbide particles $M_{23}C_6$ with an average size of 0.5 µm dispersed in the grains, confirmed with the EDS spectrum 1. Similarly, the magnified SEM image of Inconel material shows the existence of deformed carbide particles like (Nb, Ti, Cr)C and (Nb, Ti)C were distributed in the grains and grain boundaries, which was established by the EDS spectrum 2 and 3, respectively. Additionally, the presence of external elements such as tungsten (W) and cobalt (Co) in the stir zone was confirmed through the EDS spectrum analysis, resulting from tool wear in the FSW joints. The FE-SEM images of the stir zone in the joints produced by the I-FSW process, as depicted in Fig. 8.4 (b), showcase alternate Inconel and stainless-steel layers. The magnified view of IN718 (denoted by C) and SS316L (denoted by D) shows a refined grain structure with carbide and intermetallic particles uniformly distributed in the SZ than the microstructure obtained under the FSW process. The existence of carbide particles and intermetallic phase were also revealed with the EDS spectrum 4 and 5.

Figure 8.5 illustrates the SEM image of the I-FSW joint interface with the EDS line scan profile, which was performed to check the existence of the intermetallic phases. The result showed that at the interface region nickel (Ni) element profile from the IN718 surface to the SS316L surface side drastically decreased, and a similarly sharp increase of the Fe element profile in the SS316L region was observed. For all samples, the interface regions did not exhibit the formation of intermetallic compounds, which is a common occurrence in dissimilar FSW of low-melting alloys [178]. It is worth noting that the application of the external heat source during the FSW resulted in a more intermixing and flow of material than the conventional FSW, improving the joints' mechanical properties [77,91]. As depicted in Fig. 8.6, X-ray analysis confirmed the presence of precipitates and carbide particles in both the FSW and I-FSW joints. The additional external element tungsten (W) peaks in the FSW joint may be attributed to the tool material. Hanke et al. [43] reported similar tool wear phenomena in the FSW of Ni-base alloy. The intensity of the external elements was not observed under the assisted FSW joint.

According to the previous analysis, the maximum temperature in the region of the SZ reaches up to 950 to 1000 ^{o}C during the FSW of the Inconel 718 and SS316L and is also reported that FSW is a fast cooling process than other welding methods. Under the analysis of the FESEM

micrographs and XRD of the joint, no delta phase (δ) in the SZ was detected, which is generally formed above the solvus temperature of 1010 °C with sufficient cooling time. In the region of the SZ, only a few small gammas double prime (γ") phase (Ni_3Nb) and refined MC-carbide particles were detected. The TTT diagram of the Inconel 718 shows that the temperature reached above 910 °C caused the development of the gamma double prime γ" phase. Previous studies have also noted that the FSWed joints of Inconel 718 and SS316L are significantly affected by deformed grains, precipitates, and carbide particles. The observation of the microstructure of the joint under the use of induction preheating showed that the external heat source did not highly influence it. The application of an external heat source increased the flow of material, and little increment of the grain size was observed.

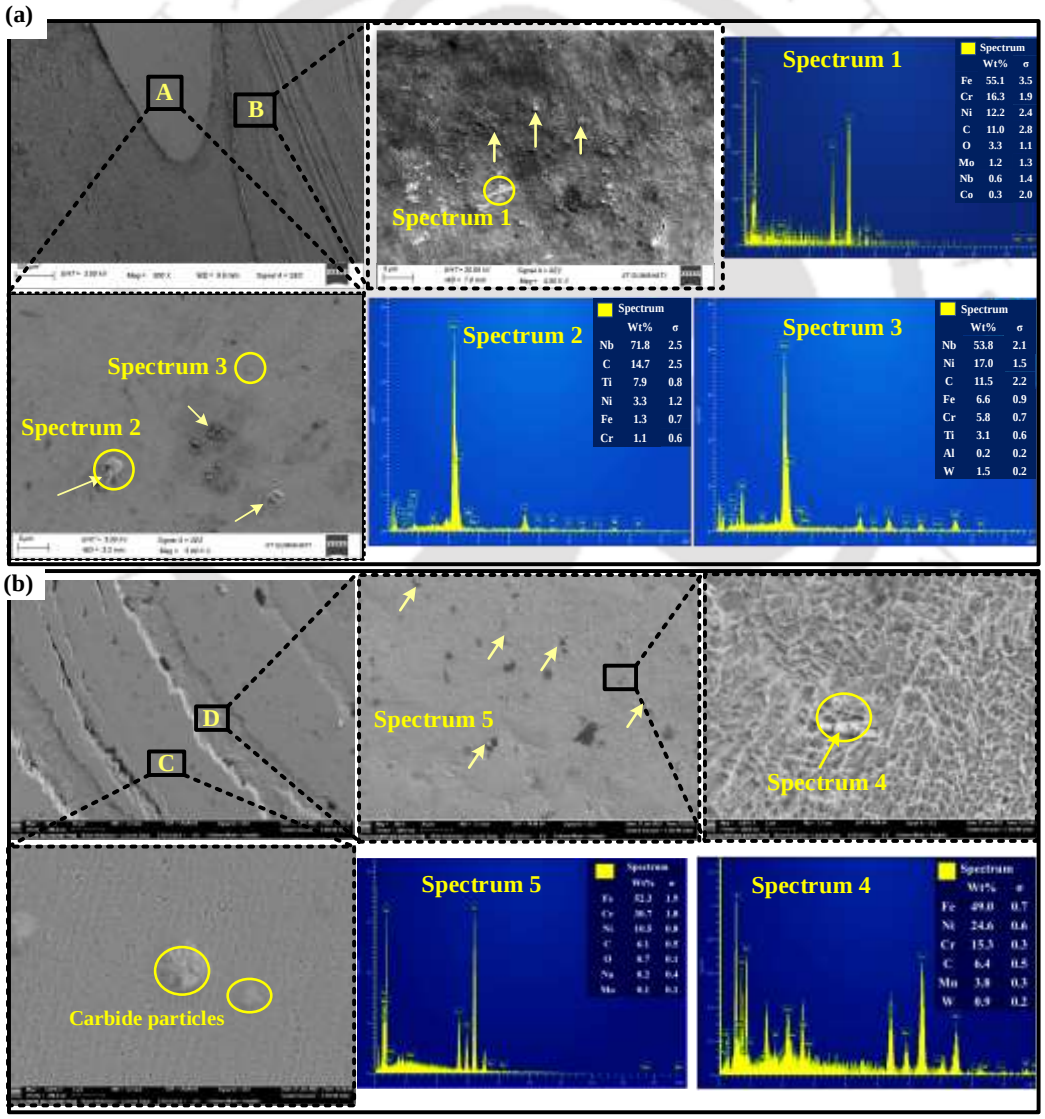

Fig. 8.4 FESEM images with EDS analysis of the nugget zone of the (a) conventional and (b) assisted-FSW joint.

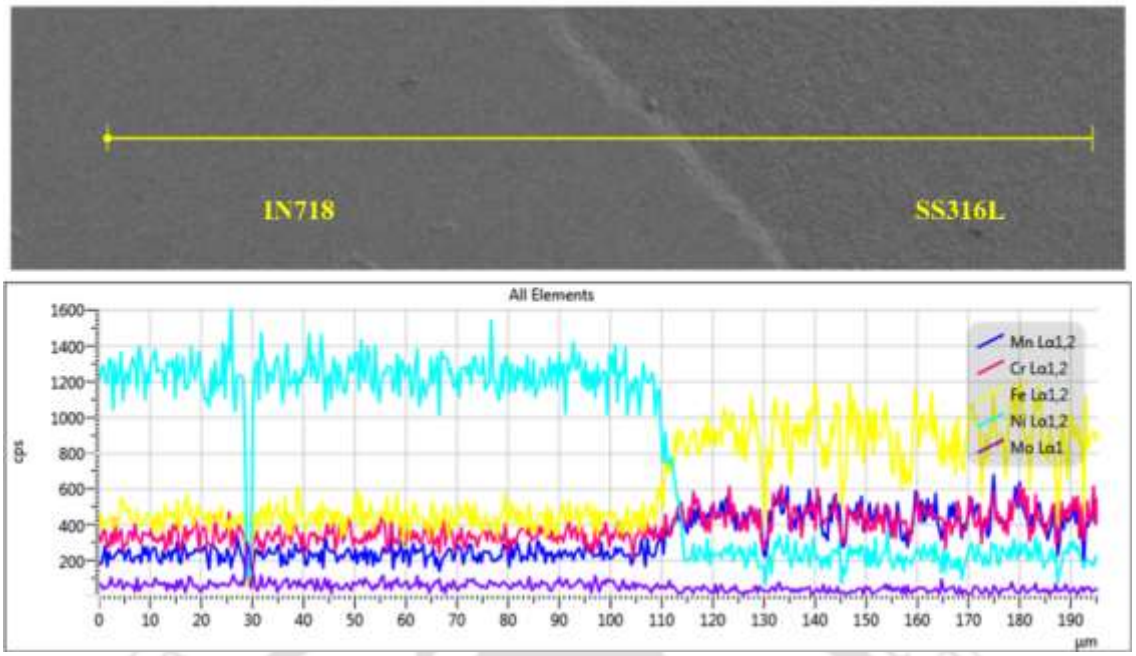

Fig. 8.5 EDS line scan analysis result obtained across the interface of IN718 and SS316L.

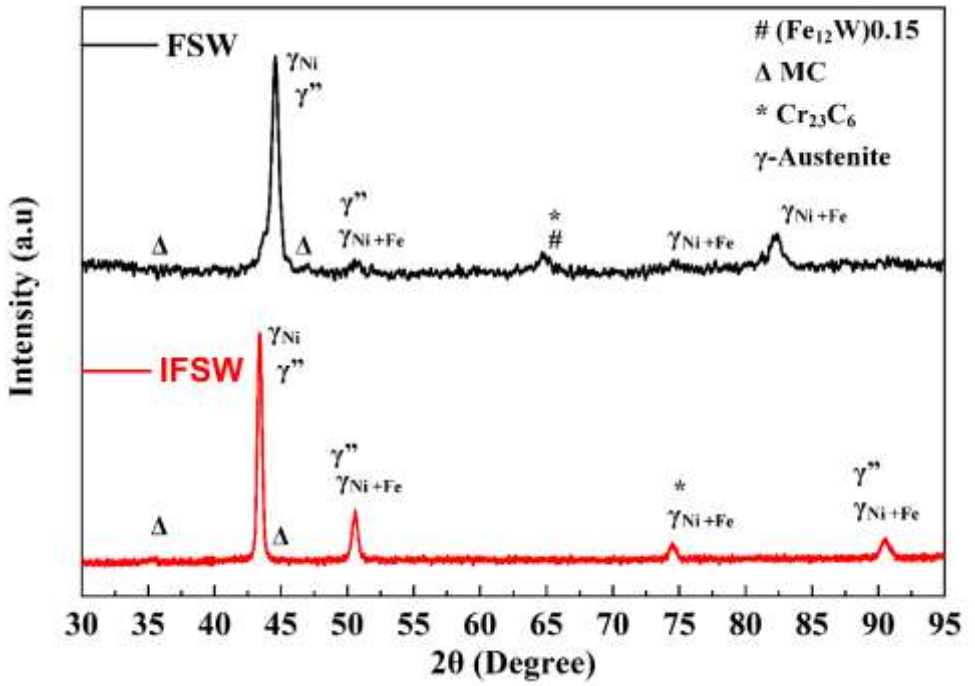

Fig. 8.6 The X-ray diffraction (XRD) patterns of the nugget zones of the I-FSW and FSW joint.

Figures 8.7 (a) and (b) show the typical TEM images of the SZ obtained with and without preheated FSW. Bright-field TEM images in both cases revealed the existence of carbide (Nb, Cr)C particles with some precipitates $M_{23}C_6$, which was confirmed by the EDS spectra 1 and

2, respectively. The morphology of the carbide particles in both cases was circular shaped, with an average diameter of 90 nm (under FSW) and 45 nm (under I-FSW) observed. The dislocation densities in the I-FSW joints were found to be higher than in the FSW joints due to the increased dynamic recrystallization observed in the I-FSW process, as shown in the bright images obtained through TEM analysis. The use of an induction preheating source leads to an increase in temperature in the weld zone, which in turn increase in dynamic recrystallization. This can lead to the formation of new grains, which can in turn lead to an increase in the dislocation density. Under the I-FSW process, high heat input per unit length and slow cooling rate due to external heating make the nugget zone a slight increase of grains with high dislocation densities.

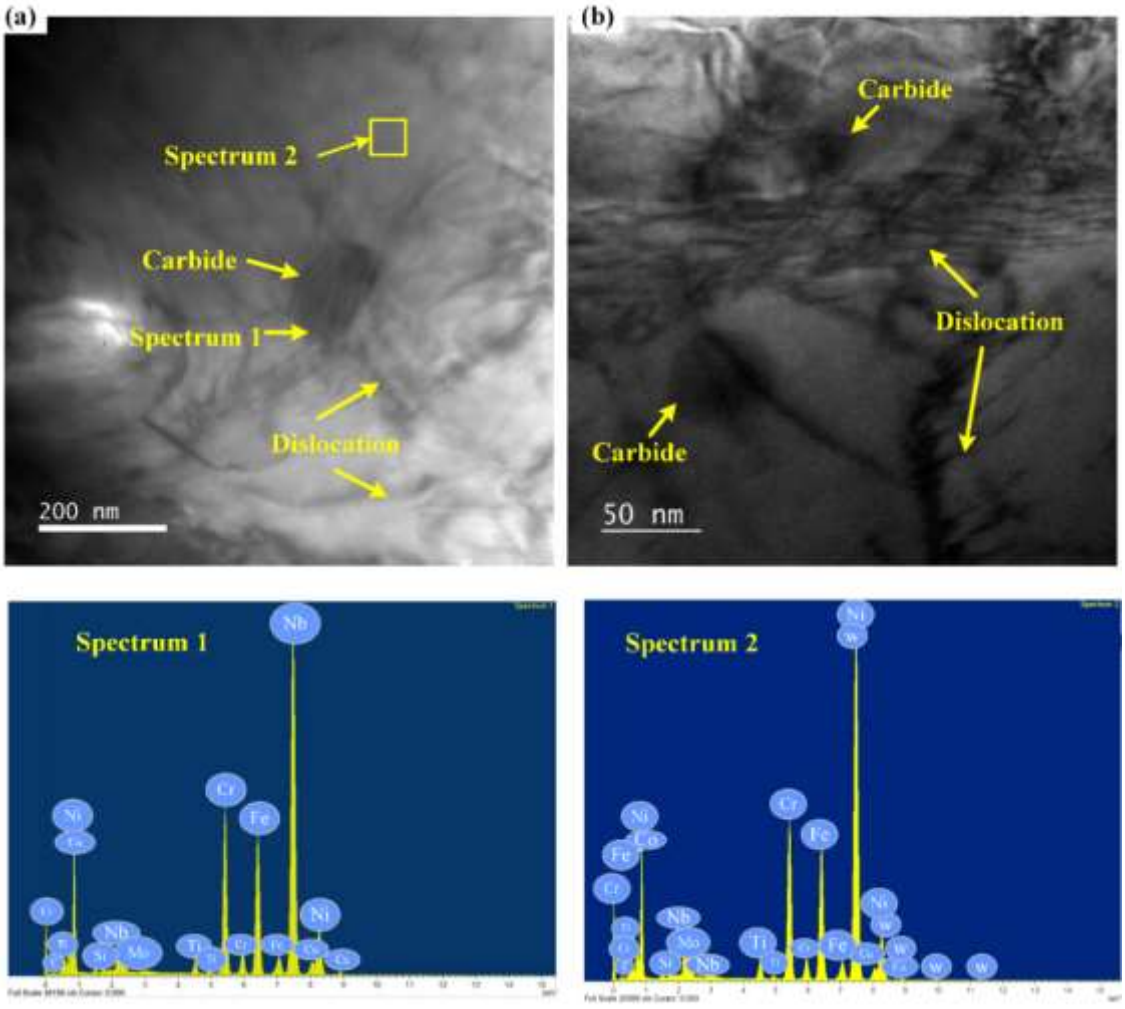

Fig. 8.7 TEM images showing the carbide particles with dislocation densities for (a) conventional and (b) preheated FSW joints.

8.3.3. Corrosion behaviour

The resistance to corrosion of conventional and assisted friction stir welded joints was studied in both HCl and NaCl solutions through immersion corrosion testing, DC current-based potentiodynamic polarization testing, and AC current-based electrochemical impedance spectroscopy.

8.3.3.1. Weight loss method

The performance of the joint in terms of weight reduction under the immersion corrosion test was evaluated by exposing the samples to the solutions at room temperature. Table 8.1 depicts the normalized weight deviations of the welded and base samples while exposed to the 1M HCl and 3.5 wt.% NaCl solution. The weight loss at the end of the immersion test (i.e., after 240 h) was found maximum in the HCl solution (0.0155 g) and minimum in the NaCl solution (0.0009 g) for the SS316L-BM, whereas it was lowest for IN718. The weight loss of the samples was detected to be highest with HCl solution compared with NaCl solution. However, the immersion test also shows the weight loss of the FSWed joint was lower than the I-FSWed joint sample in both solutions.

Table 8.1 Experimental results of the normalized weight loss and normalized corrosion rate.

	Specimen	Initial weight w_o (g)	Final weight w_1 (g)	Weight loss w (g)
HCL media	IN718	3.2845	3.2772	0.0073
	SS316L	2.8289	2.8134	0.0155
	I-FSW	3.0640	3.0492	0.0148
	FSW	2.9578	2.9464	0.0114
NaCl media	IN718	3.2740	3.2739	0.0001
	SS316L	2.8079	2.8070	0.0009
	I-FSW	3.0312	3.0304	0.0008
	FSW	2.9570	2.9564	0.0006

Macrographs of the corroded surface of the BM, I-FSW and FSW joints after 240 h immersion in 1M HCl and 3.5 wt.% NaCl solution is shown in Fig. 8.8. The optical micrographs of the corroded surface showed a major corrosion attack under the acidic medium (HCl) (Figs. 8.8 (a-d)) compared to the salt solution (NaCl) (Figs. 8.8 (e-h)). Severe corrosion attack on the stainless-steel surfaces was observed in both solutions, and it was fewer on the Inconel surface.

The acidic corrosion attack on the weld joint clearly reflects an alternate layer of corroded steel and Inconel surface (Figs. 8.8 (c-d)), which was not observed under the salt solution (Figs. 8.8 (g-h)). The observation of the micrograph images shows corrosion attack on the SS316L surfaces was severe compared to the Inconel surface.

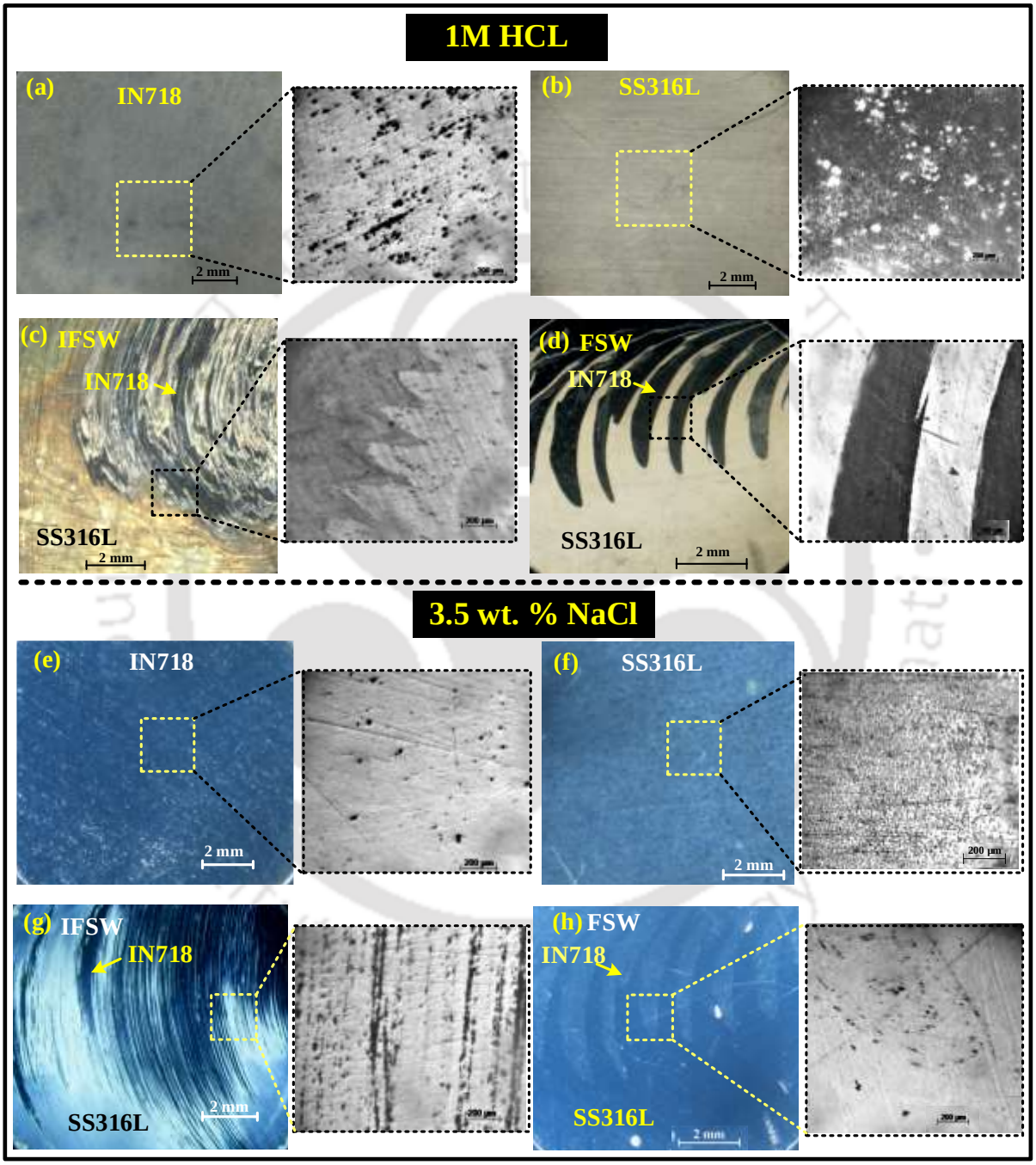

Fig. 8.8 Images of the base metal and weld joints after being subjected to immersion testing in HCl (a-d) and NaCl (e-h) solution media were taken at both macro and micro levels.

8.3.3.2 Electrochemical techniques

The electrochemical studies were conducted to gain insight into the welded samples' corrosion mechanisms and electrochemical behaviour in different conditions.

In order to assess the potential difference between the working electrodes and the environment under the zero-current condition, first, the open circuit potential was determined. Before performing the electrochemical experiments, the stable potential of the working electrodes is required for the constant rate of corrosion reaction [179]. The graphs of the OCP for the base and dissimilar joint metals, as recorded in a 1M HCl solution and a 3.5 wt.% NaCl solution at a temperature of 22 ± 5 °C are shown in Figures 8.9 (a) and (b), respectively. Figure 8.9 shows that the FSW sample required more time in both solutions to achieve a stable OCP value than the I-FSW sample. At the same time, both BM in the NaCl solution takes less time to reach a steady state than the HCl solution. The time taken to reach the stable OCP value indicates the material's corrosion behaviour, which resists the action of the electrolyte.

Furthermore, it can be seen that in the HCl solution, the OCP value of welded sample shifted towards the positive value compared to the SS316L-BM but found more negative values compared to the IN718-BM. Therefore, the friction stir welded sample shows enhanced corrosion susceptibility than the SS316L base metal. Also, observing the OCP value in both solutions suggests that the IN718-BM sample shows the highest thermodynamic stability.

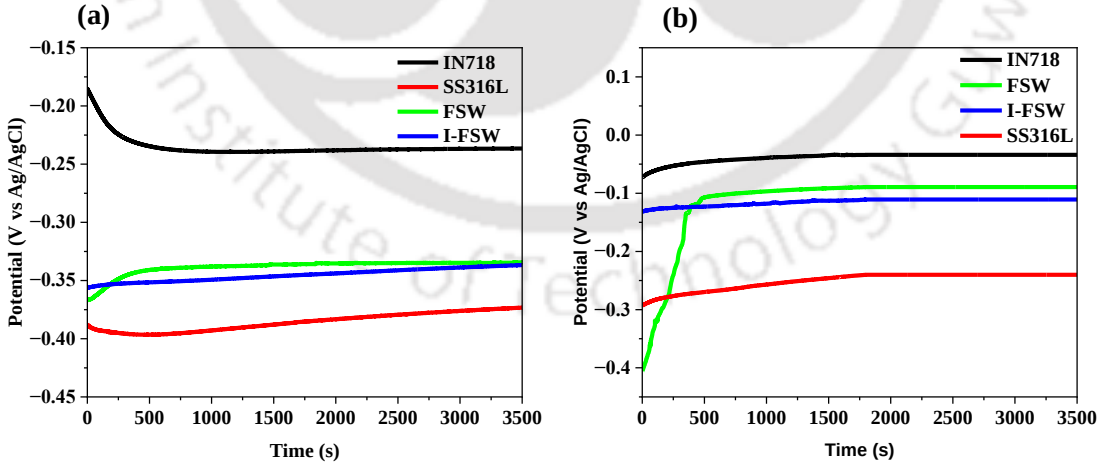

Fig. 8.9 Open circuit potential of the BM and welded sample in (a) 1M HCl and (b) 3.5% of NaCl solution.

Additionally, potentiodynamic polarization (PDP) tests were conducted on the base metal, FSWed joints, and I-FSWed joints to know the kinetics of electrochemical reactions that occur on the materials' surface. Figures 8.10 (a) and (b) show the Tafel plot obtained from the PDP test under the 1M HCl and 3.5 wt.% of NaCl solution, respectively. Moreover, Table 8.2 summarizes the corrosion potential (E_{corr}), corrosion current density (I_{corr}) and polarization resistance (R_p) obtained by Tafel extrapolation. As shown in Fig. 8.10, all the curves were almost identical and exhibited a negative hysteresis in both solutions. A close observation of Table 8.2 revealed that in both the solutions, the E_{corr} of the IN718-BM was less negative value than that of the SS316L-BM, while the corrosion potential of the welded sample (nugget zone) was between the base metals. Moreover, the welded sample exhibited a lower I_{corr} value and higher polarization resistance (R_p) than the BM in acidic solution, whereas it was lower than BM-SS316L in salt solution media. In general, metals with less negative potential and low corrosion current density offer higher corrosion resistance [180]. The observation of the E_{corr}, I_{corr}, and R_p value of the welded sample gives that the corrosion rate of the I-FSW sample is less than the corrosion rate of the FSW sample. Also, the corrosion rate of the samples under the 1M HCl solution media was higher than the 3.5 wt.% NaCl solution media. Mortezaie et al. [54] also observed similar results for Inconel and austenitic steel corrosion resistance under the 3.5 wt.% NaCl solution media.

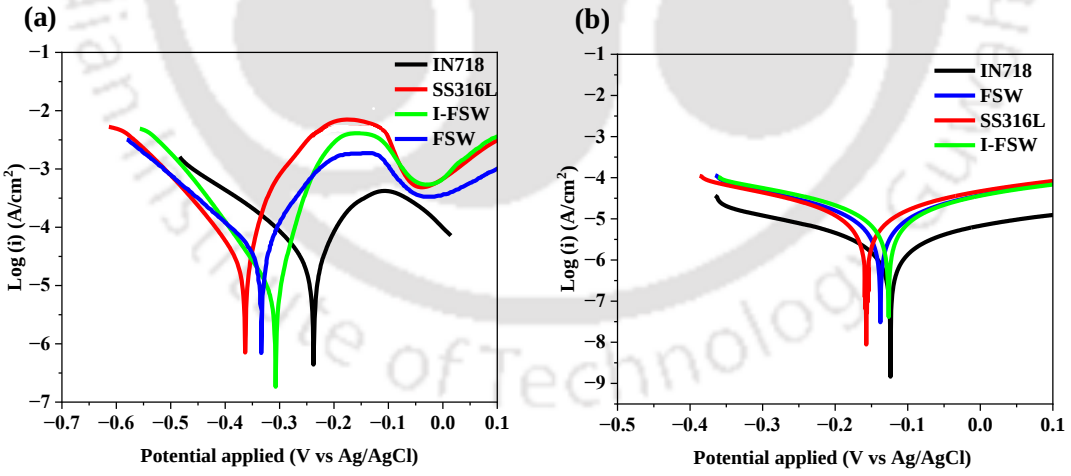

Fig. 8.10 PDP curve of BM and welded sample under the (a) 1M hydrochloric acid (HCl) and (b) 3.5 weight percent (wt.%) sodium chloride (NaCl).

Table 8.2 Potentiodynamic polarization results of the BM and welded sample in acidic and salt solution.

	Sample	E_{corr} (V vs AgCl)	I_{corr} ($\mu A/cm^2$)	R_p (Ωcm^2)
1M HCl	IN718	-0.2386	16.6111	785
	SS316L	-0.3648	30.7184	386
	I-FSW	-0.3067	6.6895	1379
	FSW	-0.3353	9.0211	1492
3.5 wt.% NaCl	IN718	-0.1242	0.5391	24310
	SS316L	-0.1587	3.3978	5105
	I-FSW	-0.1226	2.2080	5367
	FSW	-0.1304	2.5804	4679

Electrochemical impedance spectroscopy was also performed in addition to the potentiodynamic polarization test in order to evaluate the detailed mechanism of corrosion or any charge transfer processes within a short testing time [180,181]. This technique confirmed the results obtained from weight reduction under the immersion corrosion test and potentiodynamic polarization test by providing an average electrochemical response.

The representation of the EIS as the Nyquist and Bode plots of the BM, I-FSW and FSW joint obtained in 1M HCl and 3.5 wt.% NaCl solution is displayed in Fig. 8.11. The joint region of the dissimilar weld used for the EIS measurements comprised only the nugget zone. The obtained Nyquist plots of all the samples in the HCl (Fig. 8.11 (a)) and NaCl (Fig. 8.11 (c)) solution displayed a similar semicircular pattern in both media except a linear plot of the IN718 base metal in the NaCl media. Because of the limited charge transfer capacity between the oxide layer and solution, the curve is semicircular, whereas a linear curve indicates a diffusion mechanism of ions through the metal/ solution interface [137,182]. The Nyquist plots of all samples show a single semi-circle which reflects the obtained impedance data had a high-frequency single time constant. However, on the real impedance line, low frequencies are represented on the right side of the semi-circle, while high frequencies are represented on the left. The existence of large capacitive loops at higher frequencies suggests a formation of a capacitive layer on the surface. In a Nyquist diagram, the diameter of the capacitive loop is an indication of the polarization resistance at the metal-electrolyte interface [183]. From the Nyquist plots, we can observe that the IN718-BM joint sample showed a larger loop as compared to the remaining sample in both solution media, which shows higher corrosion

resistance. Additionally, in both solutions, the capacitive loop diameter of the welded sample was larger than that of SS316L-BM.

Bode plots of impedance and phase angle vs. frequency are also represented in Figs. 8.11 (b) and (d). In bode plots, the phase angle represents the lead or lag by the current. Generally, a negative phase angle indicates the capacitive nature of the system, i.e., lagging the current, whereas a positive phase angle leads the current. The obtained phase angle in all the experimental data shows the capacitive electrochemical nature of the system. The impedance value at high-frequency (10^4–10^5 Hz) indicates the solution resistance, whereas at low frequency (10^{-2}–10^0 Hz) represents the polarization resistance of the sample [134]. The obtained polarization resistance of the samples followed a specific order: BM-IN718 > I-FSW > FSW > SS316L, which is consistence with the PDP curves in both the solution media. Figure 8.9 (e) shows the equivalent electric circuit (EEC) was used to fit the EIS spectra of different samples using Nova 2.1.5 software. For fitting, a simple Randles circuit consisting of constant phase elements (CPE), charge transfer resistance (R_{ct}) and solution resistance (R_s) was used. The capacitor in the actual electrochemical processes does not behave ideally because of the inhomogeneity of the electrode geometry or surface roughness [184]. Constant phase elements (CPE) of the double-layer capacitor were used as a non-ideal capacitor capacitance in the equivalent circuit model, which represents the deviations from an ideal capacitance behaviour. The impedance of the CPE is expressed as $Z_{CPE} = [Y_o (j\omega)^n]^{-1}$, where Y_o is the capacitance, ω is the angular frequency, j is an imaginary number, and n is the power index number. The CPE transforms into an inductor, resistor, and capacitor, depending on the value of n, at n = −1, 0 and 1, respectively [185]. After fitting in the equivalent circuit, the outcome of the extracted EIS parameters is provided in Table 8.3. The value of n observed from Table 8.3 was less than 1 (n = 0.73 – 0.99), indicating the circuit behaves like the non-ideal capacitive properties of an oxide film. Table 8.3 shows that the solution resistance (R_s) of both the solution media is less than the charge transfer resistance (R_{ct}), which was lowest in the HCl solution media. It can be seen that the R_{ct} value of the samples in the NaCl solution was higher than the HCl solution. Higher R_{ct} indicates better corrosion resistance [186]. The R_{ct} value of the I-FSW and FSW samples in both solutions is larger than the SS316L-BM and lower than the IN718-BM sample, whereas the CPE (Y_o) value is lower than both base materials. These parameters (R_{ct}, Y_o) indicate that the corrosion resistance of all the samples in the HCl solution was lower than the NaCl solution, whereas, in the case of the welded sample, the corrosion resistance of the I-

FSW sample was higher than the FSW. This result was consistent with the experimental weight loss and PDP test.

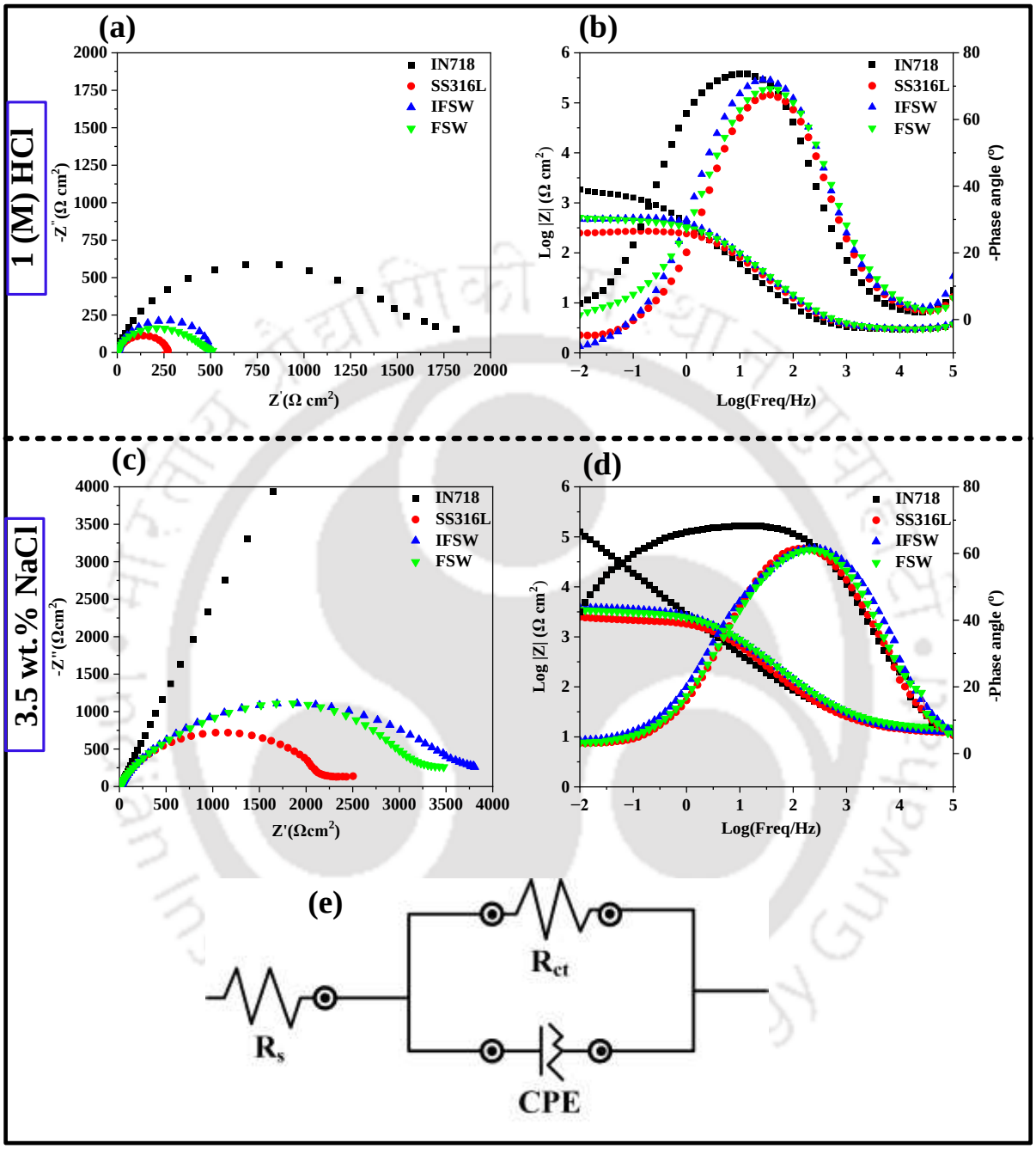

Fig. 8.11 EIS test result of the BM and the welded sample as Nyquist plot (a and c), and Bode plot (b and d) under acidic (a and b) and salt solution (c and d), and their equivalent circuit (e).

Table 8.3 Electrochemical impedance spectroscopy (EIS) parameters for BM and welded corrosion sample in the HCl and NaCl solution.

	Sample	R_s (Ω cm^2)	R_{ct} (Ω cm^2)	CPE parameters	
				Y_o (μ Ω^{-1} cm^{-2} s^n)	n
1(M) HCl	IN718	2.7727	1484.5	438	0.852
	SS316L	2.9412	275.01	222	0.872
	I-FSW	3.0308	516.46	217	0.9951
	FSW	3.0602	493.49	192	0.9985
3.5 wt.% NaCl	IN718	13.531	302,329	35.182	0.7589
	SS316L	11.761	2231.2	38.104	0.7517
	I-FSW	11.292	3619.2	32.438	0.7306
	FSW	13.903	3142.1	30.291	0.738

In the current study, the immersion test, PDP, and EIS results indicate that the base IN718 material exhibits more corrosion resistance compared to the other samples tested in both solution environments. The high nickel (52 wt.%) and high chromium (18.6 wt.%) content make this alloy highly corrosion resistant in chloride solution and oxidizing environment [187]. The corrosion properties of the metals are generally affected by several factors, including temperature, concentration, diffusion, oxidizing agents etc. Apart from the factors mentioned above, the corrosion properties are also affected by the grain size [188] and precipitated particles [189].

In the FSW process, significant plastic deformation and dynamic recrystallization result in grain refinement in the nugget zone, impacting the material's bulk and surface characteristics. The results of the microstructural characterization in section 3.2 showed that the grain size in the nugget zone of the dissimilar welded joint was finer than in the base metal. Additionally, the FSW joints (Figs. 8.3 (a-b)) had a finer grain size compared to the I-FSW joints (Figs. 8.3 (c-d)). The corrosion resistance of the I-FSW joint was higher than the FSW, which had the slightly bigger grain size. The large grain boundary area produced by the small grain size increases passivation and reduces the corrosion current [181]. Sarlak et al. [137] and Ralston et al. [188] have also stated that grain refinement prevents the initiation rate of local pitting corrosion, which improves the material's corrosion resistance.

Moreover, the presence of secondary particles like MC-carbide particles, ϒ'-Ni_3(Al, Cr, Ti) and ϒ"- Ni_3Nb in the welded joint also affects the corrosion behaviour. According to Chen et al. [190], the existence of the precipitates and carbide phases in the ϒ matrix of Inconel 718 decreases its pitting corrosion resistance due to the galvanic effect. Carbide particles create a galvanic cell with the Ni and Fe-matrix because of the large potential difference. Therefore, intermetallic particles/precipitates form a preferential site for the galvanic effect. The corrosion resistance of the FSW sample was found to be slightly lower than the I-FSW, but it was better than the BM-SS316L sample. The use of induction preheating revealed a decrease in carbide particle size and the elimination of external particle contaminations (i.e., tool partials). Also, increased the volumetric presence of stainless steel in the nugget zone (as shown in Fig. 8.2 (b)), which may have caused a slight increase in corrosion resistance.

Furthermore, the pitting corrosion tendency of the weld joints (FSW and I-FSW) after the potentiodynamic polarization test in both solutions was studied, as shown in Fig. 8.12. After the PDP test of the FSW weld joints in the HCl solution, large circular-shaped isolated (370 µm) (Fig. 8.12 (a)) pits were detected in the region of the SS316L surface, whereas the IN718 region surfaces were comparatively smooth. At the interface region, some semicircular (Fig. 8.12 (b)) pits in the SS316L region were observed. In addition, corrosion morphology in the stir zone of the I-FSW joint was found same as that of the FSW joint with small pits (105 µm) (Fig. 8.12 (c)). As a comparison, after the PDP test in the NaCl solution, the weld (FSW) sample surface displays very small pitting corrosion (3 to 5 µm), which was a relatively smooth surface as compared with the acidic solution, as shown in Fig. 8.12 (d). It was noted that the diameter of the pits on the IN718 surface was very small in both the solutions, and it was very large on the SS316L surface, which shows more severe pitting corrosion on the steel surface. The wt.% variation of the element inside the pits was analyzed for the conformation of the phases. EDS point spectrum 1 and 2 of the pits display the variation of the wt.% of the Fe and Cr elements, which form an oxide layer after the corrosion. The magnified views (Figs. 8.12 (a) and (c)) of the corrosion pits reveal the morphology of the pits, which shows the breakdown of the oxide film and the presence of some precipitates confirmed with the EDS spectrum 3. The formation of the small corrosion pits inside the SS316L surface after the polarization test with the NaCl reveals the formation of the oxide film, verified by the EDS spectrum 4.

Stainless steel 316L and Inconel 718 alloy contain $M_{23}C_6$ as major carbide precipitates, which could act as a preferable site for the corrosion pits. Wei et al. [191] reported that the existing carbide precipitates have high interfacial energy, and a large difference in phase composition

in the austenite matrix shows the preferable site for the corrosion pits. The electrochemical potential of the joint that formed with the Ni-alloy and steel was more active (anode) than the carbide precipitates (cathode), which ultimately caused the dissolution of the austenite matrix adjacent to the carbide precipitates and caused the pits corrosion. Figure 8.13 illustrates the schematic mechanism of pitting corrosion of SS316L and IN718 under the acidic solution. Besides this, the size and number of pits reduction under the I-FSW joint sample may be attributed to the microstructure change. The microstructure observation of the preheated joint compared with the conventional (FSW) joint revealed the presence of a slight increase of grains and carbide precipitates which was confirmed with the TEM analysis, as shown in Fig. 8.6. Chen et al. [190] explored the impact of compressive residual stresses on the formation of corrosion pits. According to their findings, a combination of compressive residual stress, alterations in microstructure, and the presence of ϒ’/ϒ” precipitates and carbide particles significantly contributes to pitting corrosion.

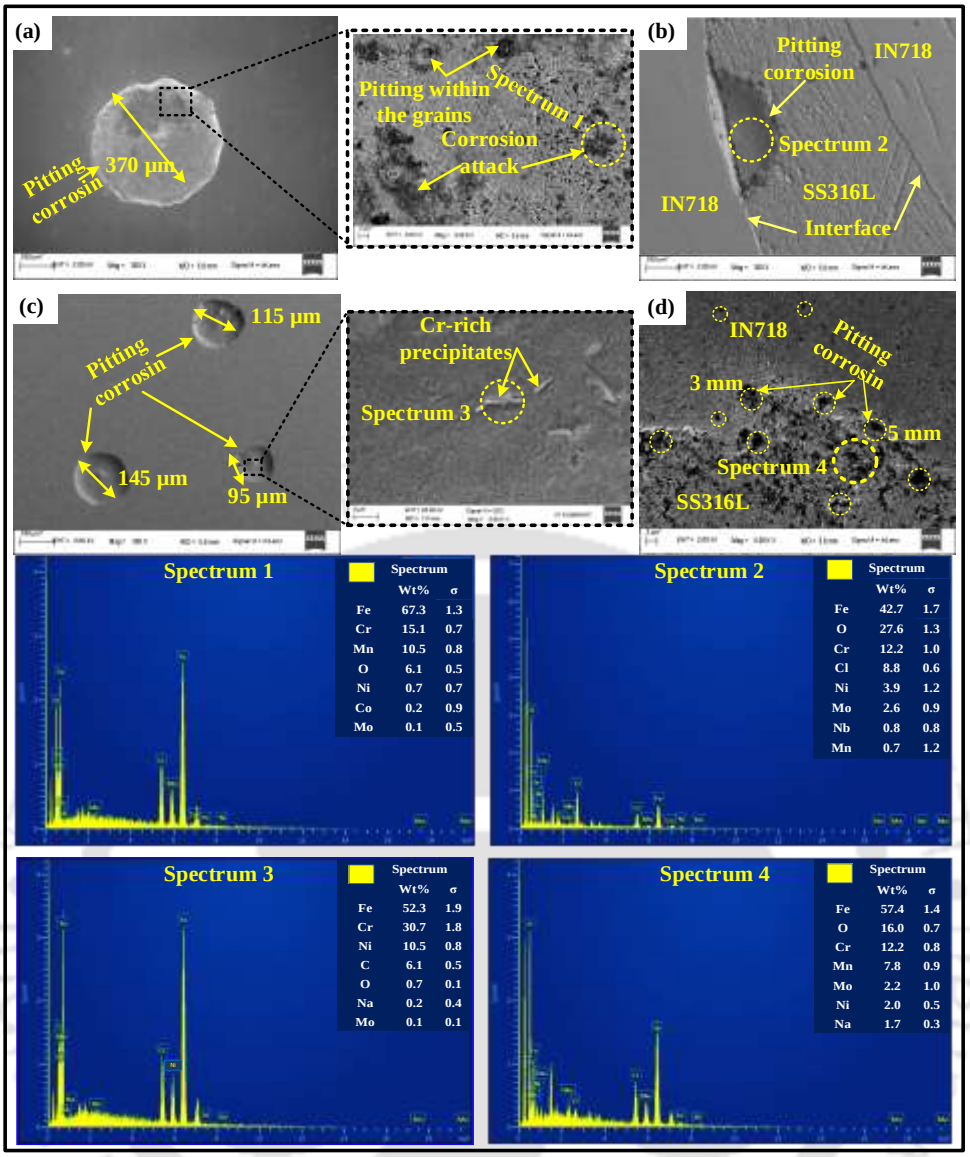

Fig. 8.12 Surface morphologies after potentiodynamic polarization test of FSW joint under (a-b) HCl solution, I-FSW joint under (c) HCL solution and FSW joint under (d) NaCl solution and their related EDX spectrum.

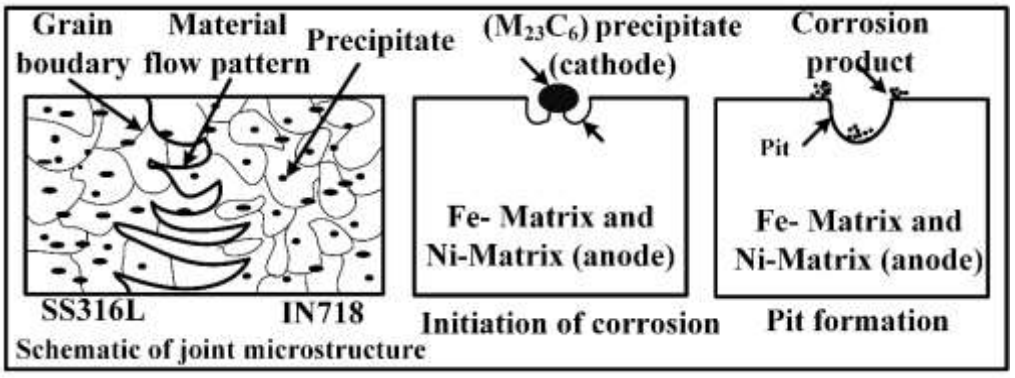

Fig. 8.13 Schematic pitting corrosion mechanism of a weld joint.

The XPS high resolution spectra taken from the interface surface of both IN718 and SS316L specimens, produced through FSW and I-FSW, are displayed in Figure 8.14. An XPS analysis was conducted to examine the oxide films that formed on the welded surface after exposure to an acidic environment where severe corrosion of the specimens in previous testing was observed. A comparison of the XPS peaks of the I-FSW surface (Fig. 8.14 (a)) and the FSW surface (Fig. 8.14 (b)) reveals differences in the intensities of peaks associated with Ni2p, Fe2p, Cr2p, Mo3d, Nb3d, and O1s, indicating varying chemical states within the surface layer. The observation shows that the corrosion resistance of the welded specimen is primarily attributed to the formation of a passive film rich in Ni, Fe, Cr, Mo, and Nb. Chen et al. [190] and Zhong et al. [192] conducted XPS analysis on Inconel 718 and SS316L material, respectively, and confirmed that the oxides of Ni, Cr, Nb, Mo, and Fe protect the surface of Inconel 718, while Ni, Fe, and Cr oxides protect SS316L.

The core level spectra of Cr, Fe, Ni, and Nb revealed the presence of a passive layer composed of oxides and hydroxides. This result is consistent with previous XPS data [190,192–194] reported for Ni-based alloys and stainless steel 316L. The main peaks of Cr_2O_3, Cr $(OH)_3$, Fe_2O_3, FeOOH, $Ni(OH)_2$, Mo^{6+}, and $Ni_{15}O_{16}$ oxide film were observed, which agree with the previous investigation [193] and act as a corrosion inhibitor. Moreover, little difference in the relative intensities of the peak of Cr, Mo, and Nb at the same binding energy of the FSW and I-FSW was observed. The peaks associated with metallic NbO oxide in the FSW specimen were no longer present. The atomic percentage of the passive film formed on the interface surfaces of the FSW and I-FSW specimens is listed in Table 8.4. It could be noticed that the surface films primarily involved Cr, Ni, and Fe-enriched oxide, and their concentration in the I-FSW specimen is higher than in the FSW specimen. The changes in atomic concentration may stem from the variations in carbide precipitates and grain size previously discussed in Section 8.3.2. According to Wei et al. [191], carbide particle distribution influenced the surface elements' distribution, leading to local variations in electrochemistry.

Table 8.4. Employing XPS analysis, observed atomic concentrations (%).

	O	Cr	Ni	Fe	Nb
I-FSW	94	5.13	2.05	1.45	0.48
FSW	89.96	2	3.72	0.47	-

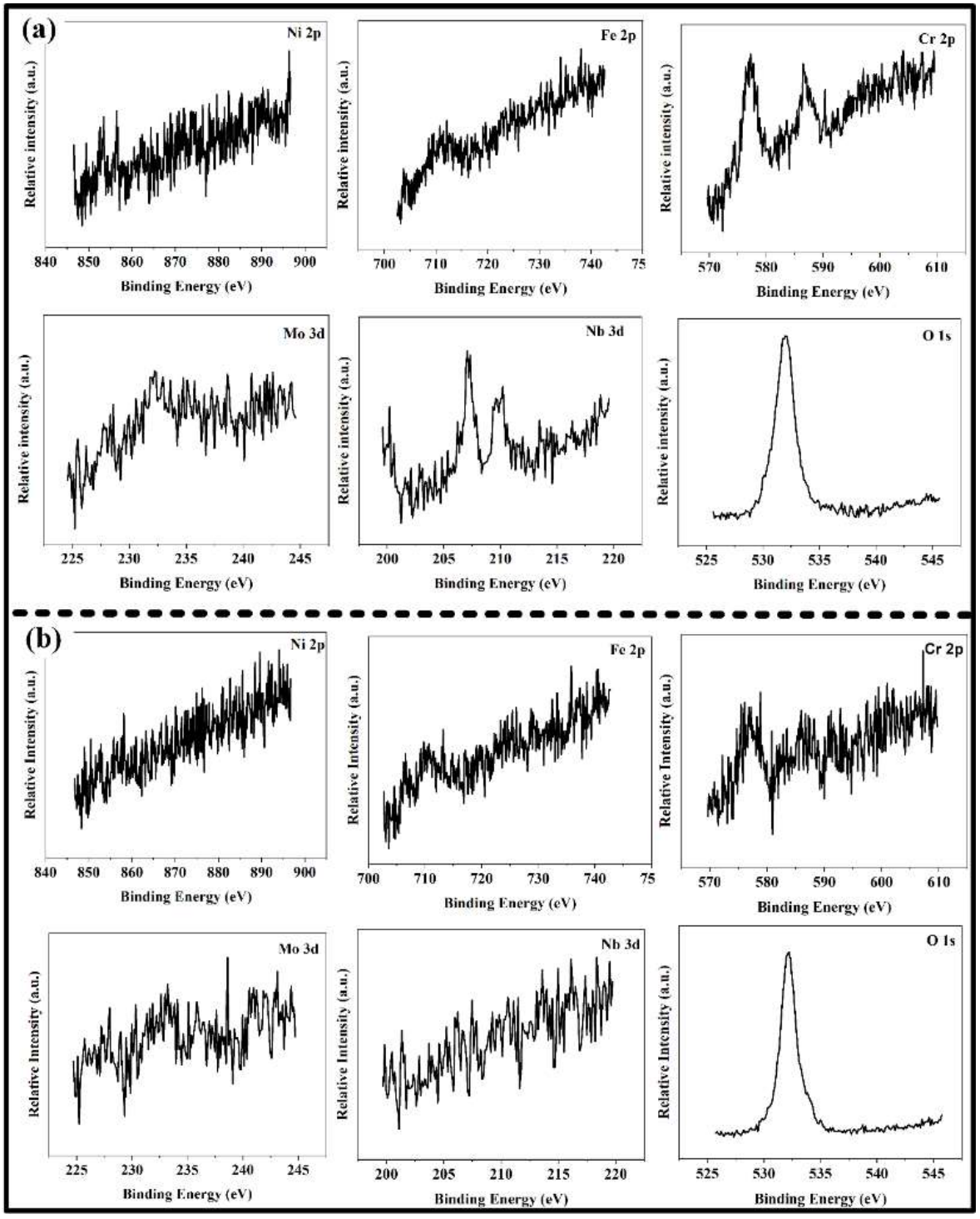

Fig. 8.14 The high resolution of the XPS spectra obtained on the (a) preheated and (b) conventional FSW sample after immersion in 1M HCl solution.

8.4 Brief scientific discussion

In the current study, the results from the immersion test, PDP, and EIS indicate that the base IN718 material exhibits more corrosion resistance compared to the other samples tested in both solution environments. The presence of secondary particles like MC-carbide particles, ϒ'-

Ni_3(Al, Cr, Ti) and ϒ”- Ni_3Nb in the welded joint affected the corrosion behavior. The existence of the precipitates and carbide phases in the ϒ matrix of Inconel 718 decreases its pitting corrosion resistance due to the galvanic effect. Carbide particles create a galvanic cell with the Ni and Fe-matrix because of the large potential difference. Therefore, intermetallic particles/precipitates form a preferential site for the galvanic effect. The corrosion resistance of the FSW sample was found to be slightly lower than the I-FSW, but it was better than the BM-SS316L sample. The use of induction preheating revealed a decrease in carbide particle size and the elimination of external particle contaminations. Increased the volumetric presence of stainless steel in the nugget zone, which caused a slight increase in corrosion resistance.

8.5. Summary

This study aimed to examine the influence of induction preheating on the microstructure development and corrosion resistance of dissimilar friction stir welding joints between IN718 and SS316L materials. The key insights derived from the study are:

- Microstructural observation showed more refinement of the grains in the FSW nugget zone than in the I-FSW nugget zone. The combination of external preheat and welding speed resulted in little increment of the grain structure and increased flow of SS316L into the IN718 region.
- The grain size of the $M_{23}C_6$ carbide particles and Ni_3(Nb, Ti) precipitates decreased in the nugget zone by the use of preheating during the FSW.
- The immersion corrosion test, potentiodynamic polarization test, and electrochemical impedance spectroscopy all showed a lower level of corrosion resistance in all the samples when exposed to 1M HCl solution compared to 3.5 wt.% NaCl solution
- In agreement with the results of the immersion corrosion test, PDP and EIS in both the solution, corrosion resistance of the BM-IN718 > I-FSW joint > FSW joint > BM-SS316L. More refinement of carbide particles and absence of external elements improves the corrosion resistance of the I-FSW joints than the FSW joints.
- High pitting corrosion with the HCl solution in the region of SS316L is mainly related to the refined $M_{23}C_6$ carbide particles in the nugget zone, which act as cathodes relative to the ϒ-austenite matrix.
- Welded samples showed signs of the formation of Cr_2O_3, Fe_2O_3, FeOOH and $Ni(OH)_2$ oxide film after the corrosion test, which acts as a corrosion inhibitor.

……..*……..*……

CHAPTER 9

9. Conclusions and Scope of the Future Work

9.1 Conclusions

In this thesis, research work has been carried out on providing an alternate and effective joining technique (FSW) to tackle disadvantages being faced by a conventional joining of 3 mm thick similar (Inconel 718) and dissimilar (Inconel 718 - SS316L/AISI 204Cu) materials. In addition, measures have been taken to minimize the problems associated with tool wear during FSW of high strength materials. To continue supporting this current research trend and rapid growth of FSW for high strength material, it needs to have a deeper understanding of the effects of preheating on mechanical, microstructural and corrosion properties evaluation as well as the tool wear. This deeper understanding is important because it will help to optimize the FSW process and improve the quality of the welded joints. The following important conclusions and recommendations from the thesis work are summarized below.

- A high-strength joint between similar Inconel 718 sheets without defects was achieved using the FSW method at low rotational and medium traverse speeds.
- Grain refinement in the SZ increased with increasing traverse speed and decreasing rotational speed due to stirring deformation accompanied by dynamic recrystallization.
- Under the conventional FSW, highly deformed grain structure and uniform distribution of carbide particles in the weld zone led to good weld quality.
- The application of a high-frequency induction preheating system during the hybrid FSW of Inconel 718 reduces the axial force of conventional FSW by 26% and increases its weld speed by 55%. This reduction of axial force effectively reduces tool wear and improves the tool life due to the softening of the material.
- Preheating during FSW retarded the cooling rate, which gives a slight increase in the grain structure in the stir zone and the presence of cluster distribution of carbide particles (i.e., NbC and $M_{23}C_6$) in the grain. Compared to conventional welding, this approach resulted in improved weld quality at around two times higher traverse speed.
- For the dissimilar joint of Ni-based alloy and Ni-free austenitic steel, in the nugget zone, a mechanically sound weld interface with uniformly distributed primary (NbC, (NbTi)C)) and secondary ($M_{23}C_6$) carbide particles across ϒ matrix were formed, which improved the mechanical properties of joints.

- For the dissimilar joints between Inconel 718/AISI 204Cu, the ultimate and yield strength of the good quality weldments reached higher than the Inconel 718 parent metal but lower than the AISI 204Cu parent metal.
- For the experimental investigation on the dissimilar FSW of Inconel 718 with SS316L, the use of preheating reduces the axial force experienced by the tool by 24%. Induction preheating reduced the tool wear by 62% due to the reduction of axial force and material softening.
- For the dissimilar FSW joints of Inconel 718 with SS316L, besides mechanically intermixing, an increase in temperature during the I-FSW process led to increase the width of the diffusion zone at the interface layer; however, no intermetallic compound layer was formed at the interface region.
- The micro-hardness and tensile properties of I-FSW joints improved due to reduction of the carbide precipitates size, along with grain refinement and proper intermixing of the materials.
- The corrosion test of dissimilar Inconel 718/SS316L joint revealed a lower level of corrosion resistance in all the samples when exposed to 1M HCl solution compared to 3.5 wt.% NaCl solution.
- In agreement with the results of the immersion corrosion test, PDP and EIS in both the solution, corrosion resistance of the BM-IN718 > I-FSW joint > FSW joint > BM-SS316L.
- More refinement of carbide particles and absence of external elements improved the corrosion resistance of the I-FSW joints than the FSW joints.
- High pitting corrosion with the HCl solution in the region of SS316L is mainly related to the refined $M_{23}C_6$ carbide particles in the nugget zone, which act as cathodes relative to the ϒ-austenite matrix.

Overall the current work proposes a detailed experimental investigation and concludes that the FSW process is advantageous for creating similar and dissimilar joints. The use of an induction preheating system improves tool life and increases weld speed. Finally, by applying the preheating source, one can commercialize this process for the joining of high strength similar and dissimilar materials

9.2 Scope of future work

The present research confirmed the feasibility of friction stir welding of high strength material by implanting preheating source. However, this experiment opens the door for future investigators to explore many other aspects regarding developments of the process, which may allow one to use this process commercially.

- The present work mainly focused on the experimental investigation of joining, a numerical simulation model for the I-FSW process can be proposed for the current work for a better understanding of the material particle deformation and flow behaviour.
- Determination of residual stresses as well as fatigue analysis using numerical and experimental techniques during FSW of Inconel 718 and SS316L, is also important for further investigations.
- Furthermore, to adopt the I-FSW process for high-strength materials in the industries, more improvement of tool life is essential. Therefore, a detailed investigation of the tool's life with other methods, like the use of another external heat source or configuration change, is required.

……*……..*…….. :

List of publications

❖ **International Journal (Published/Accepted)**

1. Sanjay Raj, Pankaj Biswas (2022), "Mechanical and microstructural characterizations of friction stir welded dissimilar butt joints of Inconel 718 and AISI 204Cu austenitic stainless steel", Materials Characterization, Volume 185:111763, https://doi.org/10.1016/j.matchar.2022.111763
2. Sanjay Raj, Pankaj Biswas (2021), "High-Frequency Induction Assisted Hybrid Friction Stir Welding of Inconel 718 Plates", ASME Journal of Manufacturing Science and Engineering Volume 144(4): 041014, https://doi.org/10.1115/1.4052357
3. Sanjay Raj, Pardeep Pankaj, Pankaj Biswas (2021), "Friction Stir Welding of Inconel-718 Alloy Using a Tungsten Carbide Tool", Journal of Materials Engineering and Performance volume 31, pages 2086–2101" https://doi.org/10.1007/s11665-021-06331-w
4. Sanjay Raj, Pankaj Biswas (2022), "Effect of induction preheating on microstructure and mechanical properties of friction stir welded dissimilar material joints of Inconel 718 and SS316L", CIRP Journal of Manufacturing Science and Technology, https://doi.org/10.1016/j.cirpj.2022.12.014
5. Pardeep Pankaj, Avinish Tiwari, Lakshmi Narayan Dhara, Sanjay Raj, Pankaj Biswas (2021), "Investigations on the Effect of Sheets Positioning in Advancing & Retreating Side for Dissimilar FSW of DH36 Steel and Aluminum Alloy 6061" Journal of The Institution of Engineers (India): Series C volume 103, pages5–20, https://doi.org/10.1007/s40032-021-00714-7
6. Sanjay Raj, Pankaj Biswas "Experimental investigation of the effect of induction preheating on the microstructure evolution and corrosion behaviour of dissimilar FSW (IN718 and SS316L) joints". Journal of Manufacturing Processes, https://doi.org/10.1016/j.jmapro.2023.04.021
7. **Sanjay Raj,** Pankaj Biswas "Friction Stir Welding of Inconel 718 Reinforced with Carbon Nanotubes". Archives of Metallurgy and Materials. (Under review)
8. **Sanjay Raj**, Pankaj Biswas "Simulation and experimental investigation on thermomechanical behavior of induction assisted dissimilar FSW of Inconel 718 and SS316L.". (Under preparation)

❖ **Book chapters**

1. Sanjay Raj, Pankaj Biswas, (2022) "Friction Stir Welding of Heat-Treated Inconel 718 Alloy, and Its Mechanical and Microstructural Analysis", Recent Advances in Manufacturing Processes and Systems, Lecture Notes in Mechanical Engineering, Springer, Singapore, http://doi.org/10.1007/978-981-16-7787-8_42
2. Sanjay Raj, Pardeep Pankaj, Pankaj Biswas, (2021) "Microstructure and Mechanical Characterization of Friction Stir Welded Inconel 718 Alloy", Recent Advances in Mechanical Engineering pp 611–618, Lecture Notes in Mechanical Engineering, https://doi.org/10.1007/978-981-15-7711-6_61

❖ **International conferences/ Research conclave**

1. Sanjay Raj, Pardeep Pankaj, Pankaj Biswas, (07-09 February 2020), "Microstructure and mechanical characterization of friction stir welded Inconel 718 alloy", The 1st International Conference on Recent Advancement of Mechanical Engineering, **ICRAME 2020**, NIT Silchar, India.
2. Sanjay Raj, Pankaj Biswas, (10-12, June 2021) "Friction Stir Welding of Heat-treated Inconel 718 alloy, & its Mechanical and Microstructural Analysis", 2nd International Conference on Recent Advances in Manufacturing (**RAM-2021**), S.V.NIT Surat, India.
3. Sanjay Raj, Pardeep Pankaj, Pankaj Biswas, (19-20 December 2021) "Effect of Traverse Speed on Mechanical and Microstructure Properties of Friction Stir Welded Inconel 718 alloy", 8th International Conference on Advancements and Futuristic Trends in Mechanical and Materials Engineering, (**AFTMME-2020**), Organised by Society of Materials & Mechanical Engineers (SOMME), India.
4. Sanjay Raj, Pankaj Biswas, (20-22, May 2022) "Microstructure and mechanical characterizations of friction stir butt-welded Inconel 718 alloy by considering the effect of welding speed", North-East Research Conclave, Sustainable Science and Technology (**NERC-2022**) IIT Guwahati, India.
5. Sanjay Raj, Pankaj Biswas, (20-22, April 2023) "Friction Stir Welding of Inconel 718 Reinforced with Carbon Nanotubes" 2nd International Conference on Advances in Mechanical Engineering and Material Science (**ICAMEMS-2023**), The School of Mechanical Engineering, VIT-AP University, India.

……..*……..*…….. :

REFERENCES

[1] P. Ramakrishnan, Welding Metallurgy, 1972. https://doi.org/10.22486/iwj.v4i3.150243.

[2] R.W. Messler, PRINCIPLES OF WELDING, n.d.

[3] D.H. Phillips, Welding engineering: an introduction, 2023.

[4] W.M.U. Thomas, E.D. Nicholas, A. Hall, C. Cb, Friction stir welding for the transportation industries, 18 (1998) 269–273.

[5] R.S. Mishra, Z.Y. Ma, Friction stir welding and processing, 50 (2005) 1–78. https://doi.org/10.1016/j.mser.2005.07.001.

[6] S. Ahmed, P. Saha, Selection of optimal process parameters and assessment of its effect in micro-friction stir welding of AA6061-T6 sheets, Int. J. Adv. Manuf. Technol. 106 (2020) 3045–3061. https://doi.org/10.1007/s00170-019-04840-6.

[7] P.L. Threadgill, Terminology in friction stir welding, Sci. Technol. Weld. Join. 12 (2007) 357–360. https://doi.org/10.1179/174329307X197629.

[8] Z.A.K. Noor Zaman Khan, Arshad Noor Siddiquee, Friction Stir Welding Dissimilar Aluminum Alloys, 2013.

[9] A. Thomas, M. El-wahabi, J.M. Cabrera, J.M. Prado, High temperature deformation of Inconel 718, 177 (2006) 469–472. https://doi.org/10.1016/j.jmatprotec.2006.04.072.

[10] M. Jambor, O. Bokůvka, F. Nový, L. Trško, J. Belan, Phase transformations in nickel base superalloy INCONEL 718 during cyclic loading at high temperature, Prod. Eng. Arch. 15 (2017) 15–18. https://doi.org/10.30657/pea.2017.15.04.

[11] J.T. Tharappel, J. Babu, Welding processes for Inconel 718- A brief review, IOP Conf. Ser. Mater. Sci. Eng. 330 (2018). https://doi.org/10.1088/1757-899X/330/1/012082.

[12] M. Talha, C.K. Behera, O.P. Sinha, A review on nickel-free nitrogen containing austenitic stainless steels for biomedical applications, Mater. Sci. Eng. C. 33 (2013) 3563–3575. https://doi.org/10.1016/j.msec.2013.06.002.

[13] D. Rasouli, A. Kermanpur, A. Najafizadeh, Developing high-strength, ductile Ni-free Fe-Cr-Mn-C-N stainless steels by interstitial-alloying and thermomechanical processing, J. Mater. Res. Technol. 8 (2019) 2846–2853. https://doi.org/10.1016/j.jmrt.2018.12.026.

[14] W. Chuaiphan, L. Srijaroenpramong, Evaluation of microstructure, mechanical properties and pitting corrosion in dissimilar of alternative low cost stainless steel grade 204Cu and 304 by GTA welding joint, J. Mater. Res. Technol. 9 (2020) 5174–5183. https://doi.org/10.1016/j.jmrt.2020.03.034.

[15] A.K. Sahu, S. Bag, Probe Pulse Conditions and Solidification Parameters for the Dissimilar Welding of Inconel 718 and AISI 316L Stainless Steel, Metall. Mater. Trans. A Phys. Metall. Mater. Sci. 51 (2020) 2192–2208. https://doi.org/10.1007/s11661-020-05705-4.

[16] M.B. Henderson, D. Arrell, R. Larsson, M. Heobel, G. Marchant, D. Arrell, R. Larsson, M. Heobel, G.M. Nickel, M.B. Henderson, D. Arrell, R. Larsson, M. Heobel, G. Marchant, Nickel based superalloy welding practices for industrial gas turbine applications Nickel based superalloy welding practices for industrial gas turbine

applications, 1718 (2013). https://doi.org/10.1179/136217104225017099.

[17] I.E. Locci, C.L. Bowman, T.P. Gabbs, B. Rd, I.E.L. Got, Development of High Temperature Dissimilar Joint Technology for Fission Surface Power Systems, 4th Int. Brazing Solder. Conf. 718 (2009) 165–175.

[18] S. Ferretti, G. Valenzano, W. Cugno, International space station external active thermal control system lines manufacturing, in: AIAA 57th Int. Astronaut. Congr. IAC 2006, American Institute of Aeronautics and Astronautics Inc., 2006: pp. 2952–2955. https://doi.org/10.2514/6.iac-06-b4.2.09.

[19] S. Guo, D. Xu, G. Jiang, W. Kuang, Corrosion behavior and mechanism of Ni-based alloys Hastelloy C2000 and Inconel 740 in chloride-containing supercritical water oxidation, J. Alloys Compd. 907 (2022). https://doi.org/10.1016/j.jallcom.2022.164452.

[20] H. Zhou, Z. Tian, C. Liao, Corrosion behaviour characterisation of 316L stainless steel and Inconel 625 in supercritical water containing hydrochloric acid and high oxygen, Corros. Eng. Sci. Technol. (2022). https://doi.org/10.1080/1478422X.2022.2112931.

[21] T. Ramkumar, M. Selvakumar, P. Narayanasamy, A.A. Begam, P. Mathavan, A.A. Raj, Studies on the structural property, mechanical relationships and corrosion behaviour of Inconel 718 and SS 316L dissimilar joints by TIG welding without using activated flux, J. Manuf. Process. 30 (2017) 290–298. https://doi.org/10.1016/j.jmapro.2017.09.028.

[22] S. Gas, G. Geometry, W. Section, P.M. Di-, M. Branch, Some Problems in Welding Inconel 718, (1971) 480–484.

[23] F.C. Liu, Y. Hovanski, M.P. Miles, C.D. Sorensen, T.W. Nelson, A review of friction stir welding of steels: Tool, material flow, microstructure, and properties, J. Mater. Sci. Technol. 34 (2018) 39–57. https://doi.org/10.1016/j.jmst.2017.10.024.

[24] A.I. Albannai, Review The Common Defects In Friction Stir Welding, Int. J. Sci. Technol. Res. 9 (2020) 318–329. www.ijstr.org.

[25] A. Abdollahzadeh, A. Shokuhfar, J.M. Cabrera, A.P. Zhilyaev, H. Omidvar, In-situ nanocomposite in friction stir welding of 6061-T6 aluminum alloy to AZ31 magnesium alloy, J. Mater. Process. Tech. 263 (2019) 296–307. https://doi.org/10.1016/j.jmatprotec.2018.08.025.

[26] A.K. Lakshminarayanan, V. Balasubramanian, Understanding the parameters controlling friction stir welding of AISI 409M ferritic stainless steel, Met. Mater. Int. 17 (2011) 969–981. https://doi.org/10.1007/s12540-011-6016-6.

[27] Y.F. Sun, Y. Konishi, M. Kamai, H. Fujii, Microstructure and mechanical properties of S45C steel prepared by laser-assisted friction stir welding, Mater. Des. 47 (2013) 842–849. https://doi.org/10.1016/j.matdes.2012.12.078.

[28] D.K. Yaduwanshi, S. Pal, S. Bag, Effect of Preheating on Mechanical Properties of Hybrid Friction Stir Welded Dissimilar Joint, (2014) 1–6.

[29] S. Zinn, L. Semiatin, Elements of Induction Heating: Design, Control, and Applications, ASM Int. (1988) 335. https://www.asminternational.org/search/-/journal_content/56/10192/06522G/PUBLICATION.

[30] X. Xie, C. Xu, G. Wang, J. Dong, W. Cao, R. Kennedy, H. Temperature, T. Beijing, TTT Diagram of a Newly Developed Nickel-Base, TMS (The Miner. Met. Mater. Soc.

(2005) 193–202.

[31] A. Benoit, S. Jobez, P. Paillard, V. Klosek, T. Baudin, Study of inconel 718 weldability using MIG CMT process, Sci. Technol. Weld. Join. 16 (2011) 477–482. https://doi.org/10.1179/1362171811Y.0000000031.

[32] G.D.J. Ram, A.V. Reddy, K.P. Rao, G. Madhusudhan, G.D.J. Ram, A.V. Reddy, K.P. Rao, G.M. Reddy, Control of Laves phase in Inconel 718 GTA welds with current pulsing Control of Laves phase in Inconel 718 GTA welds with current pulsing, 1718 (2013). https://doi.org/10.1179/136217104225021788.

[33] Y. Mei, Y. Liu, C. Liu, C. Li, L. Yu, Q. Guo, H. Li, Effect of base metal and welding speed on fusion zone microstructure and HAZ hot-cracking of electron-beam welded Inconel 718, JMADE. 89 (2016) 964–977. https://doi.org/10.1016/j.matdes.2015.10.082.

[34] N. Anbarasan, S. Jerome, S.G.K. Manikandan, Hydrogen and molybdenum control on laves phase formation and tensile properties of inconel 718 GTA welds, Mater. Sci. Eng. A. 773 (2020) 138874. https://doi.org/10.1016/j.msea.2019.138874.

[35] L. Li, G. Peng, J. Wang, J. Gong, H. Li, Experimental study on weld formation of Inconel 718 with fi ber laser welding under reduced ambient pressure, Vaccum. 151 (2018) 140–147. https://doi.org/10.1016/j.vacuum.2018.02.008.

[36] J. Gordine, Some Problems in Welding Inconel 718, Weld. Res. Suppl. November (1971) 480-s. http://files.aws.org/wj/supplement/WJ_1971_11_s480.pdf.

[37] K.H. Song, K. Nakata, Effect of precipitation on post-heat-treated Inconel 625 alloy after friction stir welding, Mater. Des. 31 (2010) 2942–2947. https://doi.org/10.1016/j.matdes.2009.12.020.

[38] F. Ye, Æ.H. Fujii, Æ.T. Tsumura, Friction stir welding of Inconel alloy 600, (2006) 5376–5379. https://doi.org/10.1007/s10853-006-0169-6.

[39] M.M.Z. Ahmed, B.P. Wynne, J.P. Martin, Effect of friction stir welding speed on mechanical properties and microstructure of nickel based super alloy Inconel 718, Sci. Technol. Weld. Join. 18 (2013) 680–687. https://doi.org/10.1179/1362171813Y.0000000156.

[40] K.H. Song, K. Nakata, Microstructural and mechanical properties of friction-stir-welded and post-heat-treated Inconel 718 alloy, J. Alloys Compd. 505 (2010) 144–150. https://doi.org/10.1016/j.jallcom.2010.06.016.

[41] G.V.B. Lemos, A.B. Farina, R.M. Nunes, P.H.C.P. Da Cunha, L. Bergmann, J.F. Dos Santos, A. Reguly, Residual stress characterization in friction stir welds of alloy 625, J. Mater. Res. Technol. 8 (2019) 2528–2537. https://doi.org/10.1016/j.jmrt.2019.02.011.

[42] Y.S. Sato, P. Arkom, H. Kokawa, T.W. Nelson, R.J. Steel, Effect of microstructure on properties of friction stir welded Inconel Alloy 600, 477 (2008) 250–258. https://doi.org/10.1016/j.msea.2007.07.002.

[43] S. Hanke, G.V.B. Lemos, L. Bergmann, D. Martinazzi, J.F. Santos, T.R. Strohaecker, Degradation mechanisms of pcBN tool material during Friction Stir Welding of Ni-base alloy 625, Wear. 376–377 (2017) 403–408. https://doi.org/10.1016/j.wear.2017.01.070.

[44] G.V.B. Lemos, S. Hanke, J.F. Dos Santos, L. Bergmann, A. Reguly, Progress in friction

stir welding of Ni alloys, 1718 (2017). https://doi.org/10.1080/13621718.2017.1288953.

[45] M.D.M. das Nevesa, A. Lottob, J.R. Berrettac, W. de Rossid, N.D. V. Júniord, Microstructure development in Nd:YAG laser welding of AISI 304 and Inconel 600, Weld. Int. 24 (2010) 104–113. https://doi.org/10.1080/09507110903568877.

[46] D.R. K., D. Sidharth, P.P. Phani, R. Rajendran, G.M. K., S. Narayanan, Microstructure and properties of inconel 718 and AISI 416 laser welded joints, J. Mater. Process. Technol. 266 (2019) 52–62. https://doi.org/10.1016/j.jmatprotec.2018.10.039.

[47] G. Li, J. Huang, Y. Wu, An investigation on microstructure and properties of dissimilar welded Inconel 625 and SUS 304 using high-power CO2 laser, Int. J. Adv. Manuf. Technol. 76 (2015) 1203–1214. https://doi.org/10.1007/s00170-014-6349-7.

[48] L. Yan, J.E. Jam, M.H. Beni, M.J. Kholoud, D. Baleanu, M.E. Shahraki, F. Ghaemi, Effect of laser welding parameters on the temperature distribution, microstructure and mechanical properties of dissimilar weld joint of Inconel 625 and stainless steel 304, Int. Commun. Heat Mass Transf. 131 (2022) 105859. https://doi.org/10.1016/j.icheatmasstransfer.2021.105859.

[49] X.L. Gao, J. Liu, L.J. Zhang, Dissimilar metal welding of Ti6Al4V and Inconel 718 through pulsed laser welding-induced eutectic reaction technology, Int. J. Adv. Manuf. Technol. 96 (2018) 1061–1071. https://doi.org/10.1007/s00170-018-1633-6.

[50] K.D. Ramkumar, S.D. Patel, S.S. Praveen, D.J. Choudhury, P. Prabaharan, N. Arivazhagan, M.A. Xavior, Influence of filler metals and welding techniques on the structure – property relationships of Inconel 718 and AISI 316L dissimilar weldments, J. Mater. 62 (2014) 175–188. https://doi.org/10.1016/j.matdes.2014.05.019.

[51] C.M. Lin, T.L. Su, K.Y. Wu, Effects of parameter optimization on microstructure and properties of GTAW clad welding on AISI 304L stainless steel using Inconel 52M, Int. J. Adv. Manuf. Technol. 79 (2015) 2057–2066. https://doi.org/10.1007/s00170-015-6875-y.

[52] Y. Aghayar, A.R. Naghashzadeh, M. Atapour, An assessment of microstructure and mechanical properties of inconel 601/ 304 stainless steel dissimilar weld, Vacuum. 184 (2021) 109970. https://doi.org/10.1016/j.vacuum.2020.109970.

[53] K. Devendranath Ramkumar, P. Siva, G. Kumar, V. Radha Krishna, A. Chandrasekhar, S. Dev, W.S. Abraham, S. Prabhakaran, S. Kalainathan, R. Sridhar, Influence of laser peening on the tensile strength and impact toughness of dissimilar welds of Inconel 625 and UNS S32205, (2016). https://doi.org/10.1016/j.msea.2016.08.104.

[54] A. Mortezaie, M. Shamanian, An assessment of microstructure, mechanical properties and corrosion resistance of dissimilar welds between Inconel 718 and 310S austenitic stainless steel, Int. J. Press. Vessel. Pip. 116 (2014) 37–46. https://doi.org/10.1016/j.ijpvp.2014.01.002.

[55] S. Dev, K.D. Ramkumar, N. Arivazhagan, R. Rajendran, Investigations on the microstructure and mechanical properties of dissimilar welds of inconel 718 and sulphur rich martensitic stainless steel, AISI 416, J. Manuf. Process. 32 (2018) 685–698. https://doi.org/10.1016/j.jmapro.2018.03.035.

[56] R. Cortés, N.K. Rodríguez, R.R. Ambriz, V.H. López, A. Ruiz, D. Jaramillo, Fatigue and crack growth behavior of Inconel 718–AL6XN dissimilar welds, Mater. Sci. Eng.

A. 745 (2019) 20–30. https://doi.org/10.1016/j.msea.2018.12.087.

[57] A.K. Maurya, C. Pandey, R. Chhibber, Dissimilar welding of duplex stainless steel with Ni alloys: A review, Int. J. Press. Vessel. Pip. 192 (2021) 104439. https://doi.org/10.1016/J.IJPVP.2021.104439.

[58] G. Dak, C. Pandey, A critical review on dissimilar welds joint between martensitic and austenitic steel for power plant application, J. Manuf. Process. 58 (2020) 377–406. https://doi.org/10.1016/j.jmapro.2020.08.019.

[59] J. Kangazian, M. Shamanian, Microstructure and mechanical characterization of Incoloy 825 Ni-based alloy welded to 2507 super duplex stainless steel through dissimilar friction stir welding, Trans. Nonferrous Met. Soc. China (English Ed. 29 (2019) 1677–1688. https://doi.org/10.1016/S1003-6326(19)65074-0.

[60] J. Rodriguez, A.J. Ramirez, Materials Characterization Microstructural characterisation of friction stir welding joints of mild steel to Ni-based alloy 625, Mater. Charact. 110 (2015) 126–135. https://doi.org/10.1016/j.matchar.2015.10.023.

[61] M. Shamanian, A. Mirzaei, J. Kangazian, J.A. Szpunar, Characterization and mechanical behavior of AISI 316L/Incoloy 825 dissimilar welds processed by friction stir welding, J. Manuf. Process. 55 (2020) 66–77. https://doi.org/10.1016/J.JMAPRO.2020.03.045.

[62] K.H. Song, W.Y. Kim, K. Nakata, Evaluation of microstructures and mechanical properties of friction stir welded lap joints of Inconel 600/SS 400, Mater. Des. 35 (2012) 126–132. https://doi.org/10.1016/j.matdes.2011.09.054.

[63] R.M. Landell, C.R. de Lima Lessa, L. Bergmann, J.F. dos Santos, C.E.F. Kwietniewski, B. Klusemann, Investigation of friction stir welding process applied to ASTM 572 steel plate cladded with Inconel®625, Weld. World. (2020) 393–403. https://doi.org/10.1007/s40194-020-01007-w.

[64] A. Aghaei, K. Dehghani, Characterizations of friction stir welding of dissimilar Monel400 and stainless steel 316, Int. J. Adv. Manuf. Technol. 77 (2015) 573–579. https://doi.org/10.1007/s00170-014-6467-2.

[65] B. Vicharapu, G. Vieira, B. Lemos, L. Bergmann, H. Geesthacht, A. De, Probing underlying mechanisms for pcBN tool decay during friction stir welding of nickel-based alloys Probing underlying mechanisms for PCBN tool decay during friction stir welding of nickel-based alloys, (2021). https://doi.org/10.4322/2176-1523.20202455.

[66] A. Fall, M.H. Fesharaki, A.R. Khodabandeh, M. Jahazi, Tool wear characteristics and effect on microstructure in Ti-6Al-4V friction stir welded joints, Metals (Basel). 6 (2016). https://doi.org/10.3390/met6110275.

[67] O.S. Salih, H. Ou, W. Sun, Heat generation, plastic deformation and residual stresses in friction stir welding of aluminium alloy, Int. J. Mech. Sci. 238 (2022) 107827. https://doi.org/10.1016/j.ijmecsci.2022.107827.

[68] L. Shi, C.S. Wu, H.J. Liu, The effect of the welding parameters and tool size on the thermal process and tool torque in reverse dual-rotation friction stir welding, Int. J. Mach. Tools Manuf. 91 (2015) 1–11. https://doi.org/10.1016/j.ijmachtools.2015.01.004.

[69] K.P. Mehta, V.J. Badheka, Journal of Materials Processing Technology Hybrid approaches of assisted heating and cooling for friction stir welding of copper to aluminum joints, J. Mater. Process. Tech. 239 (2017) 336–345.

https://doi.org/10.1016/j.jmatprotec.2016.08.037.

[70] X. Liu, S. Lan, J. Ni, Journal of Materials Processing Technology Electrically assisted friction stir welding for joining Al 6061 to TRIP, J. Mater. Process. Tech. 219 (2015) 112–123. https://doi.org/10.1016/j.jmatprotec.2014.12.002.

[71] S. Ji, Z. Li, Y. Wang, L. Ma, Joint formation and mechanical properties of back heating assisted friction stir welded Ti – 6Al – 4V alloy, JMADE. 113 (2017) 37–46. https://doi.org/10.1016/j.matdes.2016.10.012.

[72] J. Cheon, T. Park, J. Yoon, C. Kim, Evaluation of a High-Frequency Induction Heating Assisted Friction Stir Welding Process on Carbon Steel Sheets, J. Weld. Join. 37 (2019) 501–507. https://doi.org/10.5781/jwj.2019.37.5.10.

[73] W. Zhao, C.S. Wu, L. Shi, Acoustic induced antifriction and its effect on thermo-mechanical behavior in ultrasonic assisted friction stir welding, Int. J. Mech. Sci. 190 (2021) 106039. https://doi.org/10.1016/j.ijmecsci.2020.106039.

[74] A.I. Alvarez, V. Cid, G. Penal, J. Sotel, D. Verdera, Assisted friction stir welding of carbon steel: Use of induction and laser as preheating techniques, (2013) 117–125.

[75] B. Vijendra, A. Sharma, Induction heated tool assisted friction-stir welding (i-FSW): A novel hybrid process for joining of thermoplastics, J. Manuf. Process. 20 (2015) 234–244. https://doi.org/10.1016/j.jmapro.2015.07.005.

[76] G. Casalino, S. Campanelli, A.D. Ludovico, N. Contuzzi, A. Angelastro, Study of a fiber laser assisted friction stir welding process, High Power Laser Mater. Process. Lasers, Beam Deliv. Diagnostics, Appl. 8239 (2012) 823913. https://doi.org/10.1117/12.912622.

[77] A. Tiwari, P. Pankaj, S. Suman, P. Singh, P. Biswas, S. Pal, A.G. Rao, Effect of plasma preheating on weld quality and tool life during friction stir welding of DH36 steel, Proc. Inst. Mech. Eng. Part B J. Eng. Manuf. 235 (2021) 1458–1472. https://doi.org/10.1177/0954405421990139.

[78] T. Yi, S. Liu, C. Fang, G. Jiang, Eliminating hole defects and improving microstructure and mechanical properties of friction stir welded joint of 2519 aluminum alloy via TIG arc, J. Mater. Process. Technol. 310 (2022) 117773. https://doi.org/10.1016/j.jmatprotec.2022.117773.

[79] Y. Kunnathur Periyasamy, A.V. Perumal, D. Rajasekaran, Effect of Material Position and Ultrasonic Vibration on Mechanical Behaviour and Microstructure of Friction Stir-Welded AA7075-T651 and AA6061 Dissimilar Joint, Trans. Indian Inst. Met. 71 (2018) 2575–2591. https://doi.org/10.1007/s12666-018-1389-6.

[80] Z. Zhang, C. He, Y. Li, L. Yu, S. Zhao, X. Zhao, Effects of ultrasonic assisted friction stir welding on flow behavior, microstructure and mechanical properties of 7N01-T4 aluminum alloy joints, J. Mater. Sci. Technol. 43 (2020) 1–13. https://doi.org/10.1016/j.jmst.2019.12.007.

[81] M. Ahmadnia, A. Seidanloo, R. Teimouri, Y. Rostamiyan, K.G. Titrashi, Determining influence of ultrasonic-assisted friction stir welding parameters on mechanical and tribological properties of AA6061 joints, Int. J. Adv. Manuf. Technol. 78 (2015) 2009–2024. https://doi.org/10.1007/s00170-015-6784-0.

[82] H.K. Ma, D.Q. He, J.S. Liu, Ultrasonically assisted friction stir welding of aluminium

alloy 6061, Sci. Technol. Weld. Join. 20 (2015) 216–221. https://doi.org/10.1179/1362171814Y.0000000275.

[83] Z. Liu, X. Meng, S. Ji, Z. Li, L. Wang, Improving tensile properties of Al/Mg joint by smashing intermetallic compounds via ultrasonic-assisted stationary shoulder friction stir welding, J. Manuf. Process. 31 (2018) 552–559. https://doi.org/10.1016/j.jmapro.2017.12.022.

[84] I. Heating, H. Treating, Theory of Heating by Induction, (2001).

[85] F. Dughiero, Induction Heating : fundamentals Induction heating fundamentals, (2018) 1–29.

[86] A.I. Álvarez, M. García, G. Pena, D. Verdera, Evaluation of an induction-assisted friction stir welding technique for super duplex stainless steels †, (2014) 892–896. https://doi.org/10.1002/sia.5442.

[87] N. Oeystein, G., Ove, K. A., Midling, O. T., & Hydro, Modified friction stir welding, (1999).

[88] Y.F. Sun, J.M. Shen, Y. Morisada, H. Fujii, Spot friction stir welding of low carbon steel plates preheated by high frequency induction, Mater. Des. 54 (2014) 450–457. https://doi.org/10.1016/j.matdes.2013.08.071.

[89] G.K. Padhy, C.S. Wu, S. Gao, Auxiliary energy assisted friction stir welding – Status review, Sci. Technol. Weld. Join. 20 (2015) 631–649. https://doi.org/10.1179/1362171815Y.0000000048.

[90] F. Palm:, Laser supported friction stir welding method, (2004).

[91] K.H. Song, T. Tsumura, K. Nakata, Development of Microstructure and Mechanical Properties in Laser-FSW Hybrid Welded Inconel 600, 50 (2009) 1832–1837. https://doi.org/10.2320/matertrans.M2009058.

[92] B. Ahmad, A. Galloway, A. Toumpis, Numerical optimisation of laser assisted friction stir welding of structural steel, Sci. Technol. Weld. Join. 24 (2019) 548–558. https://doi.org/10.1080/13621718.2019.1570682.

[93] S.L. Campanelli, G. Casalino, C. Casavola, V. Moramarco, Analysis and comparison of friction stir welding and laser assisted friction stir welding of aluminum alloy, Materials (Basel). 6 (2013) 5923–5941. https://doi.org/10.3390/ma6125923.

[94] M. Merklein, A. Giera, Laser assisted Friction Stir Welding of drawable steel-aluminium tailored hybrids, Int. J. Mater. Form. 1 (2008) 1299–1302. https://doi.org/10.1007/s12289-008-0141-x.

[95] X. Fei, X. Jin, Y. Ye, T. Xiu, H. Yang, Effect of pre-hole offset on the property of the joint during laser-assisted friction stir welding of dissimilar metals steel and aluminum alloys, Mater. Sci. Eng. A. 653 (2016) 43–52. https://doi.org/10.1016/j.msea.2015.11.101.

[96] A. Tiwari, P. Pankaj, S. Suman, P. Singh, P. Biswas, S. Pal, A.G. Rao, Effect of plasma preheating on weld quality and tool life during friction stir welding of DH36 steel, Proc. Inst. Mech. Eng. Part B J. Eng. Manuf. 235 (2021) 1458–1472. https://doi.org/10.1177/0954405421990139.

[97] H.S. Bang, H.S. Bang, G.H. Jeon, I.H. Oh, C.S. Ro, Gas tungsten arc welding assisted hybrid friction stir welding of dissimilar materials Al6061-T6 aluminum alloy and STS304 stainless steel, Mater. Des. 37 (2012) 48–55. https://doi.org/10.1016/j.matdes.2011.12.018.

[98] G.C. Sindo Kou, Arc-enhanced friction stir welding, (2004).

[99] P. Pankaj, A. Tiwari, P. Biswas, A.G. Rao, Plasma-Assisted Hybrid Dissimilar Friction Stir Welding for Joining of DH36 Steel and AISI 1008 Steel: Thermal Modelling and Experimental Analysis, Arab. J. Sci. Eng. 46 (2021) 7929–7952. https://doi.org/10.1007/s13369-021-05574-y.

[100] D.K. Yaduwanshi, S. Bag, S. Pal, Numerical modeling and experimental investigation on plasma-assisted hybrid friction stir welding of dissimilar materials, Mater. Des. 92 (2016) 166–183. https://doi.org/10.1016/j.matdes.2015.12.039.

[101] K.P. Mehta, V.J. Badheka, Hybrid approaches of assisted heating and cooling for friction stir welding of copper to aluminum joints, J. Mater. Process. Technol. 239 (2017) 336–345. https://doi.org/10.1016/j.jmatprotec.2016.08.037.

[102] Y. Miyano, H. Fujii, Y. Sun, Y. Katada, S. Kuroda, O. Kamiya, Mechanical properties of friction stir butt welds of high nitrogen-containing austenitic stainless steel, Mater. Sci. Eng. A. 528 (2011) 2917–2921. https://doi.org/10.1016/J.MSEA.2010.12.071.

[103] S. Du, H. Liu, Y. gao, Y. Hu, L. Zhou, Effects of process parameters on joint formation and tool wear behavior in friction stir welded TA5 alloy, Int. J. Adv. Manuf. Technol. (2022) 2531–2547. https://doi.org/10.1007/s00170-022-10366-1.

[104] M.R. Meshram, Influence of tool tilt angle on heat transfer and material flow in friction stir welding, J. Manuf. Process. 59 (2020) 98–112. https://doi.org/10.1016/j.jmapro.2020.09.038.

[105] M. Zhai, C. Wu, L. Shi, Tool tilt angle induced variation of shoulder-workpiece contact condition in friction stir welding, Sci. Technol. Weld. Join. (2021) 1–9. https://doi.org/10.1080/13621718.2021.2013709.

[106] S.S. Kumar, N. Murugan, K.K. Ramachandran, Effect of tool tilt angle on weld joint properties of friction stir welded AISI 316L stainless steel sheets, Meas. J. Int. Meas. Confed. 150 (2020) 107083. https://doi.org/10.1016/j.measurement.2019.107083.

[107] N.A. Muhammad, C.S. Wu, H. Su, Concurrent influences of tool offset and ultrasonic vibration on the joint quality and performance of dissimilar Al/Cu friction stir welds, J. Mater. Res. Technol. 14 (2021) 1035–1051. https://doi.org/10.1016/J.JMRT.2021.07.009.

[108] A. Tiwari, P. Singh, P. Pankaj, P. Biswas, S.D. Kore, S. Pal, Effect of Tool Offset and Rotational Speed in Dissimilar Friction Stir Welding of AISI 304 Stainless Steel and Mild Steel, J. Mater. Eng. Perform. 28 (2019) 6365–6379. https://doi.org/10.1007/s11665-019-04362-y.

[109] M. Shamanian, A. Mirzaei, J. Kangazian, J.A. Szpunar, Characterization and mechanical behavior of AISI 316L/Incoloy 825 dissimilar welds processed by friction stir welding, J. Manuf. Process. 55 (2020) 66–77. https://doi.org/10.1016/j.jmapro.2020.03.045.

[110] R. Nandan, T. Debroy, H.K.D.H. Bhadeshia, Recent advances in friction-stir welding – Process , weldment structure and properties, 53 (2008) 980–1023.

https://doi.org/10.1016/j.pmatsci.2008.05.001.

[111] P.K. Sahu, S. Pal, Effect of FSW parameters on microstructure and mechanical properties of AM20 welds, Mater. Manuf. Process. 33 (2018) 288–298. https://doi.org/10.1080/10426914.2017.1279295.

[112] M. Al-Moussawi, A.J. Smith, Defects in Friction Stir Welding of Steel, Metallogr. Microstruct. Anal. 7 (2018) 194–202. https://doi.org/10.1007/s13632-018-0438-1.

[113] P. Pankaj, A. Tiwari, P. Biswas, A.G. Rao, S. Pal, Experimental studies on controlling of process parameters in dissimilar friction stir welding of DH36 shipbuilding steel–AISI 1008 steel, Weld. World. (2020) 10–12. https://doi.org/10.1007/s40194-020-00886-3.

[114] R. Zettler, T. Vugrin, M. schmücker, Effects and defects of friction stir welds, Frict. Stir Weld. From Basics to Appl. (2010) 245–276. https://doi.org/10.1533/9781845697716.2.245.

[115] M.M.Z. Ahmed, B.P. Wynne, J.P. Martin, M.M.Z. Ahmed, B.P. Wynne, J.P. Martin, Effect of friction stir welding speed on mechanical properties and microstructure of nickel based super alloy Inconel 718., 1718 (2013). https://doi.org/10.1179/1362171813Y.0000000156.

[116] J. Kangazian, M. Shamanian, Microstructure and mechanical characterization of Incoloy 825 Ni-based alloy welded to 25 07 super duplex stainless steel through dissimilar friction stir welding, Trans. Nonferrous Met. Soc. China (English Ed. 29 (2019) 1677–1688. https://doi.org/10.1016/S1003-6326(19)65074-0.

[117] P. Pankaj, A. Tiwari, P. Biswas, Impact of varying tool position on the intermetallic compound formation , metallographic / mechanical characteristics of dissimilar DH36 steel , and aluminum alloy friction stir welds, Springer Berlin Heidelberg, 2021. https://doi.org/10.1007/s40194-021-01203-2.

[118] A.C. Somasekharan, L.E. Murr, Microstructures in friction-stir welded dissimilar magnesium alloys and magnesium alloys to 6061-T6 aluminum alloy, 52 (2004) 49–64. https://doi.org/10.1016/j.matchar.2004.03.005.

[119] O. Mypati, P. Srirangam, S. Sahu, S. Kanta Pal, An Investigation of the Effect of Intermetallic Compounds on the Mechanical and Electrical Properties of Friction Stir Welded Al and Cu Busbar for Battery Pack Applications, (2021). https://doi.org/10.21203/rs.3.rs-802948/v1.

[120] P. Kaushik, D.K. Dwivedi, Effect of tool geometry in dissimilar Al-Steel Friction Stir Welding, J. Manuf. Process. 68 (2021) 198–208. https://doi.org/10.1016/J.JMAPRO.2020.08.007.

[121] H. Shi, K. Chen, Z. Liang, F. Dong, T. Yu, X. Dong, L. Zhang, A. Shan, Intermetallic Compounds in the Banded Structure and Their Effect on Mechanical Properties of Al/Mg Dissimilar Friction Stir Welding Joints, J. Mater. Sci. Technol. 33 (2017) 359–366. https://doi.org/10.1016/j.jmst.2016.05.006.

[122] A. Tiwari, Tool performance evaluation of friction stir welded shipbuilding grade DH36 steel butt joints, Int J Adv Manuf Technol. 103 (2019) 1989–2005. https://doi.org/10.1007/s00170-019-03618-0.

[123] Y.N. Zhang, X. Cao, S. Larose, P. Wanjara, Y.N. Zhang, X. Cao, S. Larose, P. Wanjara,

Review of tools for friction stir welding and processing Review of tools for friction stir welding and processing, 4433 (2013). https://doi.org/10.1179/1879139512Y.0000000015.

[124] F.C. Liu, Y. Hovanski, M.P. Miles, C.D. Sorensen, T.W. Nelson, A review of friction stir welding of steels: Tool, material flow, microstructure, and properties, J. Mater. Sci. Technol. (2018). https://doi.org/10.1016/j.jmst.2017.10.024.

[125] K. Gangwar, M. Ramulu, Friction stir welding of titanium alloys : A review, Mater. Des. 141 (2018) 230–255. https://doi.org/10.1016/j.matdes.2017.12.033.

[126] R. Rai, H.K.D.H. Bhadeshia, T. Debroy, Review : friction stir welding tools Review : friction stir welding tools, 16 (2013) 325–342. https://doi.org/10.1179/1362171811Y.0000000023.

[127] K.J. Quintana, J. Luis, L. Silveira, Mechanistic models and experimental analysis for the torque in FSW considering the tool geometry and the process velocities, J. Manuf. Process. 30 (2017) 406–417. https://doi.org/10.1016/j.jmapro.2017.09.031.

[128] G. Buffa, J. Hua, R. Shivpuri, L. Fratini, Design of the friction stir welding tool using the continuum based FEM model, 419 (2006) 381–388. https://doi.org/10.1016/j.msea.2005.09.041.

[129] K. Kumar, S. V. Kailas, T.S. Srivatsan, Influence of tool geometry in friction stir welding, Mater. Manuf. Process. 23 (2008) 188–194. https://doi.org/10.1080/10426910701774734.

[130] G. Rambabu, D. Balaji Naik, C.H. Venkata Rao, K. Srinivasa Rao, G. Madhusudan Reddy, Optimization of friction stir welding parameters for improved corrosion resistance of AA2219 aluminum alloy joints, Def. Technol. 11 (2015) 330–337. https://doi.org/10.1016/j.dt.2015.05.003.

[131] S. Maggiolino, C. Schmid, Corrosion resistance in FSW and in MIG welding techniques of AA6XXX, J. Mater. Process. Technol. 197 (2008) 237–240. https://doi.org/10.1016/j.jmatprotec.2007.06.034.

[132] R.K. Jayaraj, S. Malarvizhi, V. Balasubramanian, Electrochemical corrosion behaviour of stir zone of friction stir welded dissimilar joints of AA6061 aluminium–AZ31B magnesium alloys, Trans. Nonferrous Met. Soc. China (English Ed. 27 (2017) 2181–2192. https://doi.org/10.1016/S1003-6326(17)60244-9.

[133] P. West, V.C. Shunmugasamy, C.A. Usman, I. Karaman, B. Mansoor, Part II.: Dissimilar friction stir welding of nickel titanium shape memory alloy to stainless steel – microstructure, mechanical and corrosion behavior, J. Adv. Join. Process. 4 (2021) 100072. https://doi.org/10.1016/j.jajp.2021.100072.

[134] H. Wang, C. Zhang, Z. Zhou, Y. Zhang, K. Wang, W. Wang, P. Han, Y. Lu, X. Li, Y. Liu, X. Zhang, Y. Zhou, X. Xu, Effect of the microstructure on the corrosion behavior of dissimilar friction stir-welded 304 austenitic stainless steel and Q235 low-carbon steel joints, Mater. Res. Express. 9 (2022). https://doi.org/10.1088/2053-1591/ac80a4.

[135] L.O. Osoba, A.M. Oladoye, V.E. Ogbonna, Corrosion evaluation of superalloys Haynes 282 and Inconel 718 in Hydrochloric acid, J. Alloys Compd. 804 (2019) 376–384. https://doi.org/10.1016/j.jallcom.2019.06.196.

[136] G.V.B. Lemos, A.B. Farina, H. Piaggio, L. Bergmann, J.Z. Ferreira, J.F. dos Santos, G.

Vander Voort, A. Reguly, Mitigating the susceptibility to intergranular corrosion of alloy 625 by friction-stir welding, Sci. Rep. 12 (2022) 1–9. https://doi.org/10.1038/s41598-022-07473-0.

[137] H. Sarlak, M. Atapour, M. Esmailzadeh, Corrosion behavior of friction stir welded lean duplex stainless steel, Mater. Des. 66 (2015) 209–216. https://doi.org/10.1016/j.matdes.2014.10.060.

[138] H.B. Li, Z.H. Jiang, H. Feng, S.C. Zhang, L. Li, P.D. Han, R.D.K. Misra, J.Z. Li, Microstructure, mechanical and corrosion properties of friction stir welded high nitrogen nickel-free austenitic stainless steel, Mater. Des. 84 (2015) 291–299. https://doi.org/10.1016/J.MATDES.2015.06.103.

[139] M. Atapour, H. Sarlak, M. Esmailzadeh, Pitting corrosion susceptibility of friction stir welded lean duplex stainless steel joints, Int. J. Adv. Manuf. Technol. 83 (2016) 721–728. https://doi.org/10.1007/s00170-015-7601-5.

[140] Y.F. Li, S.T. Hong, H. Choi, H.N. Han, Solid-state dissimilar joining of stainless steel 316L and Inconel 718 alloys by electrically assisted pressure joining, Mater. Charact. 154 (2019) 161–168. https://doi.org/10.1016/J.MATCHAR.2019.06.005.

[141] A. Tiwari, Tool Wear and Weld Quality Characterization in Friction Stir Welding of Similar and Dissimilar Steel, (2021). http://gyan.iitg.ac.in/handle/123456789/1886.

[142] K.H. Song, H. Fujii, K. Nakata, Effect of welding speed on microstructural and mechanical properties of friction stir welded Inconel 600, Mater. Des. 30 (2009) 3972–3978. https://doi.org/10.1016/j.matdes.2009.05.033.

[143] R.P. Mahto, R. Kumar, S.K. Pal, S.K. Panda, A comprehensive study on force , temperature , mechanical properties and micro-structural characterizations in friction stir lap welding of dissimilar materials (AA6061-T6 & AISI304), J. Manuf. Process. 31 (2018) 624–639. https://doi.org/10.1016/j.jmapro.2017.12.017.

[144] A. Tiwari, P. Singh, P. Pankaj, P. Biswas, S.D. Kore, FSW of low carbon steel using tungsten carbide (WC-10wt.%Co) based tool material, J. Mech. Sci. Technol. 33 (2019) 4931–4938. https://doi.org/10.1007/s12206-019-0932-7.

[145] B. Parida, S.D. Vishwakarma, S. Pal, Design and development of fixture and force measuring system for friction stir welding process using strain gauges †, 29 (2015) 739–749. https://doi.org/10.1007/s12206-015-0134-x.

[146] D.F. Huang, Investigation of Heterogeneity of FSW Inconel 718 Coupled with Welding Thermal Cycle, (2008).

[147] R. Palanivel, P. Koshy Mathews, N. Murugan, I. Dinaharan, Effect of tool rotational speed and pin profile on microstructure and tensile strength of dissimilar friction stir welded AA5083-H111 and AA6351-T6 aluminum alloys, Mater. Des. 40 (2012) 7–16. https://doi.org/10.1016/j.matdes.2012.03.027.

[148] H. Chen, L. Fu, P. Liang, Microstructure , texture and mechanical properties of friction stir welded butt joints of 2A97 Al e Li alloy ultra-thin sheets, 692 (2017) 155–169. https://doi.org/10.1016/j.jallcom.2016.08.330.

[149] J. Teimouri, S.R. Hosseini, K. Farmanesh, Effect of the As-Forged and Heat-Treated Microstructure on the Room Temperature Anisotropic Ductile Fracture of Inconel 718, J. Mater. Eng. Perform. 27 (2018) 2070–2080. https://doi.org/10.1007/s11665-018-

3302-1.

[150] H.T. Lee, W.H. Hou, Fine grains forming process, mechanism of fine grain formation and properties of superalloy 718, Mater. Trans. 53 (2012) 716–723. https://doi.org/10.2320/matertrans.M2011337.

[151] A. Mostafa, I.P. Rubio, V. Brailovski, M. Jahazi, M. Medraj, Structure, texture and phases in 3D printed IN718 alloy subjected to homogenization and HIP treatments, Metals (Basel). 7 (2017) 1–23. https://doi.org/10.3390/met7060196.

[152] A.K. Lakshminarayanan, C.S. Ramachandran, V. Balasubramanian, ScienceDirect Feasibility of surface-coated friction stir welding tools to join AISI 304 grade austenitic stainless steel, Def. Technol. 10 (2014) 360–370. https://doi.org/10.1016/j.dt.2014.07.003.

[153] X. Cao, M. Jahazi, Effect of welding speed on the quality of friction stir welded butt joints of a magnesium alloy, Mater. Des. 30 (2009) 2033–2042. https://doi.org/10.1016/j.matdes.2008.08.040.

[154] R. Guo, Y. Shen, G. Huang, W. Zhang, W. Guan, Microstructures and mechanical properties of thin 304 stainless steel sheets by friction stir welding, J. Adhes. Sci. Technol. 4243 (2018) 1–11. https://doi.org/10.1080/01694243.2017.1409064.

[155] G.V.B. Lemos, A.B. Farina, R.M. Nunes, P.H.C.P. Da Cunha, L. Bergmann, J.F. Dos Santos, A. Reguly, Residual stress characterization in friction stir welds of alloy 625, J. Mater. Res. Technol. 8 (2019) 2528–2537. https://doi.org/10.1016/j.jmrt.2019.02.011.

[156] K.D. Ramkumar, R.J. Sai, V.S. Reddy, S. Gundla, T.H. Mohan, V. Saxena, N. Arivazhagan, Effect of filler wires and direct ageing on the microstructure and mechanical properties in the multi-pass welding of Inconel 718, J. Manuf. Process. 18 (2015) 23–45. https://doi.org/10.1016/j.jmapro.2015.01.001.

[157] A.C. Razdolescu, M. Sahagia, A. Luca, S. Bercea, C. Dumitrescu, H. Schrader, Results obtained in the metrological certification of a commercially available radionuclide calibrator, 2002. https://doi.org/10.1016/S0969-8043(01)00146-4.

[158] H. Papahn, P. Bahemmat, M. Haghpanahi, I.P. Aminaie, Effect of friction stir welding tool on temperature , applied forces and weld quality, (2015) 475–484. https://doi.org/10.1049/iet-smt.2014.0150.

[159] S. Jianliang, L. Shuo, Q. Chouwu, P. Yan, Numerical and experimental investigation of induction heating process of heavy cylinder, 134 (2018) 341–352. https://doi.org/10.1016/j.applthermaleng.2018.01.101.

[160] K. Devendranath Ramkumar, S.D. Patel, S. Sri Praveen, D.J. Choudhury, P. Prabaharan, N. Arivazhagan, M.A. Xavior, Influence of filler metals and welding techniques on the structure-property relationships of Inconel 718 and AISI 316L dissimilar weldments, Mater. Des. 62 (2014) 175–188. https://doi.org/10.1016/j.matdes.2014.05.019.

[161] R.K. Gupta, H. Das, T.K. Pal, Influence of processing parameters on induced energy, mechanical and corrosion properties of FSW butt joint of 7475 AA, J. Mater. Eng. Perform. 21 (2012) 1645–1654. https://doi.org/10.1007/s11665-011-0074-2.

[162] K.S. Prasad, S.K. Panda, S.K. Kar, S.V.S.N. Murty, S.C. Sharma, Effect of solution treatment on deep drawability of IN718 sheets: Experimental analysis and metallurgical characterization, Mater. Sci. Eng. A. 727 (2018) 97–112.

https://doi.org/10.1016/j.msea.2018.04.110.

[163] X. Meng, Y. Huang, J. Cao, J. Shen, J.F. dos Santos, Recent progress on control strategies for inherent issues in friction stir welding, Prog. Mater. Sci. 115 (2021) 100706. https://doi.org/10.1016/j.pmatsci.2020.100706.

[164] J.R. Fernandez, A.J. Ramirez, Microstructural Evolution During Friction Stir Welding of Mild Steel and Ni-Based Alloy 625, (n.d.). https://doi.org/10.1007/s11661-016-3925-5.

[165] P. Pankaj, A. Tiwari, L.N. Dhara, S. Raj, P. Biswas, Investigations on the Effect of Sheets Positioning in Advancing & Retreating Side for Dissimilar FSW of DH36 Steel and Aluminum Alloy 6061, J. Inst. Eng. Ser. C. 103 (2022) 5–20. https://doi.org/10.1007/s40032-021-00714-7.

[166] G.M.X. a H.B. Cui a, R.D.K.M. b ∗, Z.A. Luo a, J. Ma a, G.D. Wang a, A, Microstructural evolution and mechanical properties of the stir zone in friction stir processed AISI201 stainless steel | Elsevier Enhanced Reader, Mater. Des. (2016) 463–475. https://doi.org/https://doi.org/10.1016/j.matdes.2016.05.106.

[167] A. Momeni, S.M. Abbasi, M. Morakabati, H. Badri, A Comparative Study on the Hot Working Behavior of Inconel 718 and ALLVAC 718 Plus, Metall. Mater. Trans. A Phys. Metall. Mater. Sci. 48 (2017) 1216–1229. https://doi.org/10.1007/s11661-016-3904-x.

[168] L. Freire, X.R. Nóvoa, G. Pena, V. Vivier, On the corrosion mechanism of AISI 204Cu stainless steel in chlorinated alkaline media, Corros. Sci. 50 (2008) 3205–3212. https://doi.org/10.1016/J.CORSCI.2008.08.029.

[169] M.J. Joseph, M.A. Jabbar, Effect of aging process on the microstructure, corrosion resistance and mechanical properties of stainless steel AISI 204, Case Stud. Constr. Mater. 11 (2019) e00253. https://doi.org/10.1016/j.cscm.2019.e00253.

[170] X. Wang, O. Sanchez-Mata, S.E. Atabay, J.A. Muñiz-Lerma, M. Attarian Shandiz, M. Brochu, Crystallographic orientation dependence of Charpy impact behaviours in stainless steel 316L fabricated by laser powder bed fusion, Addit. Manuf. 46 (2021) 102104. https://doi.org/10.1016/j.addma.2021.102104.

[171] W.D. Callister, D.G. Rethwisch, Fundamentals of materials science and engineering : an integrated approach, 2016. https://www.wiley.com/en-us/Fundamentals+of+Materials+Science+and+Engineering%3A+An+Integrated+Approach%2C+5th+Edition-p-9781119175506R120.

[172] A.S.M. International, A. Rights, ASM specialty handbook: nickel, cobalt, and their alloys, 2001. https://doi.org/10.5860/choice.38-6206.

[173] T. Küçükömeroğlu, S.M. Aktarer, G. Çam, Investigation of mechanical and microstructural properties of friction stir welded dual phase (DP) steel, IOP Conf. Ser. Mater. Sci. Eng. 629 (2019) 012010. https://doi.org/10.1088/1757-899X/629/1/012010.

[174] A. Hinojos, J. Mireles, A. Reichardt, P. Frigola, P. Hosemann, L.E. Murr, R.B. Wicker, Joining of Inconel 718 and 316 Stainless Steel using electron beam melting additive manufacturing technology, Mater. Des. 94 (2016) 17–27. https://doi.org/10.1016/j.matdes.2016.01.041.

[175] K.S. Prasad, S.K. Panda, S.K. Kar, M. Sen, S.V.S.N. Murty, S.C. Sharma, Microstructures , Forming Limit and Failure Analyses of Inconel 718 Sheets for

Fabrication of Aerospace Components, J. Mater. Eng. Perform. 26 (2017) 1513–1530. https://doi.org/10.1007/s11665-017-2547-4.

[176] J.K.L.Lai, A Review of Precipitation Behaviour in AISI Type 316 Stainless Steel, Mater. Sci. Eng. 61 (1983) 101–109.

[177] B. Vicharapu, H. Liu, Y. Morisada, H. Fujii, A. De, Degradation of nickel-bonded tungsten carbide tools in friction stir welding of high carbon steel, Int. J. Adv. Manuf. Technol. 115 (2021) 1049–1061. https://doi.org/10.1007/s00170-021-07159-3.

[178] M. Sarvghad-Moghaddam, R. Parvizi, A. Davoodi, M. Haddad-Sabzevar, A. Imani, Establishing a correlation between interfacial microstructures and corrosion initiation sites in Al/Cu joints by SEM-EDS and AFM-SKPFM, Corros. Sci. 79 (2014) 148–158. https://doi.org/10.1016/j.corsci.2013.10.039.

[179] A. Pal, C. Das, New eco-friendly anti-corrosion inhibitor of purple rice bran extract for boiler quality steel: Experimental and theoretical investigations, J. Mol. Struct. 1251 (2022) 131988. https://doi.org/10.1016/j.molstruc.2021.131988.

[180] E. McCafferty, Introduction to corrosion science, 2010. https://doi.org/10.1007/978-1-4419-0455-3.

[181] S. Sinhmar, D.K. Dwivedi, A study on corrosion behavior of friction stir welded and tungsten inert gas welded AA2014 aluminium alloy, Corros. Sci. 133 (2018) 25–35. https://doi.org/10.1016/j.corsci.2018.01.012.

[182] H.B. Li, Z.H. Jiang, H. Feng, S.C. Zhang, L. Li, P.D. Han, R.D.K. Misra, J.Z. Li, Microstructure, mechanical and corrosion properties of friction stir welded high nitrogen nickel-free austenitic stainless steel, Mater. Des. 84 (2015) 291–299. https://doi.org/10.1016/j.matdes.2015.06.103.

[183] Z.S. Mousavi, S. Karimi, A. Heidarpour, S.M. Hosseini, S. Ghasemi, Microstructural Variation and Corrosion Behavior of 60/40 Brass/Ti2SC Surface Composite through Friction Stir Processing, J. Mater. Eng. Perform. (2022) 0–11. https://doi.org/10.1007/s11665-021-06441-5.

[184] C. Wang, Y. Yu, J. Yu, Y. Zhang, Y. Zhao, Q. Yuan, Microstructure evolution and corrosion behavior of dissimilar 304/430 stainless steel welded joints, J. Manuf. Process. 50 (2020) 183–191. https://doi.org/10.1016/j.jmapro.2019.12.015.

[185] J.A. Moreto, M.S. dos Santos, M.O.A. Ferreira, G.S. Carvalho, R. V. Gelamo, I. V. Aoki, M. Taryba, W.W. Bose Filho, J.C.S. Fernandes, Corrosion and corrosion-fatigue synergism on the base metal and nugget zone of the 2524-T3 Al alloy joined by FSW process, Corros. Sci. 182 (2021) 109253. https://doi.org/10.1016/j.corsci.2021.109253.

[186] A. Pal, C. Das, A novel use of solid waste extract from tea factory as corrosion inhibitor in acidic media on boiler quality steel, Ind. Crops Prod. 151 (2020) 112468. https://doi.org/10.1016/j.indcrop.2020.112468.

[187] J. Wang, J. Xu, X. Zhang, X. Ren, X. Song, X. Chen, An investigation of surface corrosion behavior of Inconel 718 after robotic belt grinding, Materials (Basel). 11 (2018) 1–14. https://doi.org/10.3390/ma11122440.

[188] K.D. Ralston, N. Birbilis, Effect of Grain Size on Corrosion: A Review, Corrosion. 66 (2010) 075005-075005–13. https://doi.org/10.5006/1.3462912.

[189] L.C.M. Valle, A.I.C. Santana, M.C. Rezende, J. Dille, O.R. Mattos, L.H. de Almeida, The influence of heat treatments on the corrosion behaviour of nickel-based alloy 718, J. Alloys Compd. 809 (2019) 151781. https://doi.org/10.1016/j.jallcom.2019.151781.

[190] T. Chen, H. John, J. Xu, Q. Lu, J. Hawk, X. Liu, Influence of surface modifications on pitting corrosion behavior of nickel-base alloy 718. Part 1: Effect of machine hammer peening, Corros. Sci. 77 (2013) 230–245. https://doi.org/10.1016/j.corsci.2013.08.007.

[191] X. Wei, W.J. Zheng, Effect of carbides on sensitivity of pitting corrosion in Inconel 718 alloy, Anti-Corrosion Methods Mater. 67 (2020) 158–165. https://doi.org/10.1108/ACMM-10-2018-2025.

[192] Y. Zhong, Z. Zheng, J. Li, C. Wang, X. Wang, Effect of Ar-N2-He Shielding Gas on the Microstructure Evolution, Mechanical Properties and Corrosion Resistance of the Laser-Mig Hybrid Additive Manufactured 316l Stainless Steel, J. Mater. Process. Tech. 312 (2022) 117844. https://doi.org/10.2139/ssrn.4094533.

[193] J. Yang, S. Wang, Y. Li, X. Tang, Y. Wang, D. Xu, Y. Guo, Effect of salt deposit on corrosion behavior of Ni-based alloys and stainless steels in supercritical water, J. Supercrit. Fluids. 152 (2019) 104570. https://doi.org/10.1016/j.supflu.2019.104570.

[194] J. Nie, L. Wei, Y. Jiang, Q. Li, H. Luo, Corrosion mechanism of additively manufactured 316 L stainless steel in 3.5 wt.% NaCl solution, Mater. Today Commun. 26 (2021) 101648. https://doi.org/10.1016/j.mtcomm.2020.101648.

Appendix A

A.1 FSW machine specifications: (Model: BMacT, Universal Milling Machine- India)

Spindle	BT 40
Spindle motor	20 HP/440V
FSW tool holder	BT 40 Arbor
Feed motor	3 HP- preferably 960 RPM
Z axis thrust	6500 kgf/65kN (max.) (adjustable in steps of 100 kgf)
Feed Requirements:	
Quill stroke	100 mm by hydraulic pressure
X-axis stroke	1000 mm (feed rate 20 − 300)
X-axis feed	23-300 minimum 15−18 levels
Y-axis stroke	200 mm/manual
Z-axis stroke	300 mm (feed rate 2 mm −50 mm) 18 steps
Table size	1800 × 400 mm
Table surface	'T' Slot as per standard
Hydraulic System:	
Hydraulic power packmotor	Minimum 5HP/440V
Hydraulic tank capacity	liters
Hydraulic oil	ISO 68
Lubrication System	
Lubrication	Centralised lubrication system
Lubrication oil	SAE40
Vibration	Anti-vibration pad

A.2 High-frequency induction machine: (Model: KX-5188, Zhejiang, China)

Input voltage (v)	Single phase 220 V ± 10
Oscillation power (kW)	20 kW
Maximum input current	40 A
Maximum output supply current	750 A
Oscillation frequency (kHz)	100-120 kHz
Colling water desire	Hydraulic pressure > 0.2 MPa

Self-sucking water pump	370 W
Coil type	Copper made pancake type.

A.3 Machine specification used for characterization.

Machine Name	Make and Model	Specifications
Universal testing machine (UTM)	Instron, UK	• Hydraulic power pack pumping capacity 25 Ltr/min • Testing Method: Load control and position control (strain and displacement)
Micro hardness tester	Make: Buehler, Model: Micrometer-2101	• Indentation force 50, 100, 300, 500, 2000 gF • Dwell time: 5 to 60 s
Drop weight impact tester	Make: FIE group, Model: IT30	• Impact energy scale: 30−120 J • Height of impact: 0.3 −1.7 m • Test: Impact energy, impact force
Stereo microscope	Make: Nikon, Model: SMZ25	• Zoom ratio: 25: 1 • Magnification range: 0.63X −15.75X • Motorized zoom • Zooming observation: BF/DF/FL/Simplepolarizing
Optical microscope	Make: Carl Zeiss, Model: Axiotech-100HD, 3D	• Magnification: 50X−5000X • Table movement: 3- axis measuring system, reflecting light measuring step 75 mm ×55 mm ×50 mm • Lens: Binocular photo type, 20°/23 • Camera: Axio-Cam and Axiovision 4.8.2 software (inbuilt)
Field emission scanning electron microscope (FESEM) with EDS detector	Make: Zeiss, Model: Sigma 300	• Specimen chamber: 330 mm inner dia. 270 mm height • Specimen weight: up to 0.5 kg tilted; up to 2kg not tilted • Movement: X =125 mm, Y= 125 mm, Z =50 mm, T = −10° to 360°, R = 360° continues • Specimen stage: 5 axis motorized cartesian
Infrared (IR) camera	Make: INFRATECH, Model: Variocam-hr − 400	• Frequency range: 1−8 Hz • Emissivity range: 0.01−1

X-ray photoelectron spectroscopy (XPS)	Make: PHI 5000 Versaprobe	• High flux X-ray source with Aluminum anode for X-ray generation
XRD	Make: Rigaku Model: Smartlab	• 9 kW generator and direct optical positioning • Prefix incident and diffracted beam • X- ray lens with attenuator, fixed divergenceslits 1/32° • High-resolution goniometer with opticallyencoded sample positioning enables a minimum step of 0.0001^{o}
Field Emission Transmission Electron Microscope (FETEM)	Make: JEOL Model: 2100F	• Electron Source: Schottky Field Emitter • Operating Voltages: 200.0 keV and 120.0 keV • Objective Lens Polepiece: High Resolution (HR) • Resolution @ 200 keV: point = 0.23 nm and lattice = 0.14 nm • Tilt-ranges (Double Tilt Holder): X axis = +/-35^{o} and Y axis = +/- 30
Potentiostat/ Galvanostat instrument	Make: Metrohm Autolab - PGSTAT302N	• Maximum current +/- 2A • Maximum scan rate 1000 V/s • Application software: NOVA
Micro balance	Make: Sartorius Model: BSA4S-CW	• Accuracy 0.1 mg • Rated load 200g
Single disc polisher/grinder machine	Make: Chennai Metco Model: PVM 008 Banipol VT	• 8"disc dia. Standard • 0.5 HP high torque AC motor • Single phase input 220v/50Hz or 110v/60Hz • Speed: 50 to– 1000 RPM
High-speed precision cutter	Make: Buehler IsoMet 4000 USA	• Automated three-axis movement • ISOMET 4000, 85-264V, 50/60HZ
Strain gauge-based force-dynamometer	Make: MP31C09, DIGITECH, India	• 20×4 LCD display • ± 0.1% ± 1 digit • 200 to 250VAC ± 10%, 50 Hz • Range: ±10,000 micro strain